Journal of Polymer Science

Part A-2: Polymer Physics

Contents

INTERSCIENCE PUBLISHERS

		Average no. copies each issue during preceding 12 months	Single issue nearest of filing date
A.	Total no. copies printed (*net press run*)	2900	2900
B.	Paid circulation		
	1. Sales through dealers and carriers, street vendors and counter sales	—	—
	2. Mail subscriptions	2392	2392
C.	Total paid circulation	2392	2392
D.	Free distribution by mail, carrier or other means		
	1. Samples, complimentary, and other free copies Copies distributed to News Agents, but not sold	122 —	122 —
E.	Total distribution (*Sum of C and D*)	2514	2514
F.	Office use, left-over unaccounted, spoiled after printing	386	386
G.	Total (*Sum of E & F—should equal net press run shown in A*)	2900	2900

CONTENTS

Vol. 9, Issue Nos. 1–12

CONTENTS   v

ISSUE NO. 5, MAY

Issue No. 8, August

ISSUE NO. 10, OCTOBER

ISSUE No. 12, DECEMBER

Studies on Formaldehyde Condensation Resins. XII.   Gelation Theory for Tetrafunctional Amino Resins

TADASHI URAGAMI and MASAYOSHI OIWA, *Department of Applied Chemistry, Faculty of Engineering, Kansai University, Osaka, Japan*

Synopsis

General kinetic equations for the gelation reaction of tetrafunctional amino monomer with formaldehyde are formulated according to Case's gelation theory.   The ratio of the rate constant of the condensation reaction to that of the addition reaction is evaluated by applying a theoretical kinetic equation to the experimental measurements.   The ratio of the rate constant for addition of an imino group to that for an amino group is also determined by combining the kinetic equation, stoichiometric relation, and expression for the gel point.   The total yield of resin, the yield of sol, and the number-average molecular weight of the sol fraction are discussed.

Introduction

A theoretical treatment of gel formation was first applied to a polycondensation reaction by Flory.[1–4]   Papers by Stockmayer[5,6] on the gelation of high polymers appeared at around the same time.

Flory's gelation theory has been applied in the quantitative treatment of curing reactions of thermosetting resins including phenol–formaldehyde,[7,8] polyester,[9,10] and epoxy resins.[11,12]   Recently, Ishii et al.[13–16] reported on the kinetics of gel formation in phenol–formaldehyde resin, with consideration of the difference in reactivity of o- and p-phenol.

However, previous kinetic studies on the gelation of addition-condensation resins have been largely confined to reactions of the polycondensation type, involving reactions of monomer with hydroxymethylated or chlormethylated compounds.

The addition-condensation amino resins are formed by a combination of two different reactions, addition and condensation, as follows:

Addition:

$$-NH_2 + HCHO \rightarrow -N \overset{CH_2OH}{\underset{H}{\diagdown}}$$

$$>NH + HCHO \rightarrow >N-CH_2OH$$

1

ห้องสมุด กรมวิทยาศาสตร์

Condensation:

$$-NH_2 + HOCH_2- \rightarrow -N\begin{matrix}CH_2-\\ \\ H\end{matrix} + H_2O$$

$$>NH + HOCH_2- \rightarrow >N-CH_2- + H_2O$$
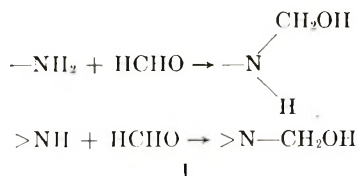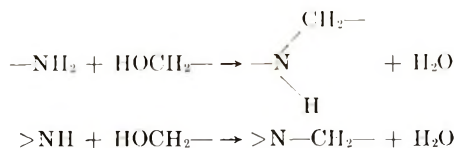
In the present paper, gelation as a consequence of both reactions, hydroxymethylation and methylene bond formation, is treated on the basis of Case's theory,[17] with emphasis on tetrafunctional amino resins involving urea, guanamine, etc.

Kinetic Treatment

In practice, the reactivity of an amino group of a tetrafunctional amino monomer (abbreviated as Am in this paper) may be different from that of the unreacted amino group, $H_2N-N\begin{matrix}H\\ \\ \end{matrix}$, where one amino group of Am has reacted. Also the reactivity of an imino group may differ in $H_2N-N\begin{matrix}CH_2OH\\ \\ H\end{matrix}$ and $H_2N-N\begin{matrix}CH_2-\\ \\ H\end{matrix}$. However, if these reactivities were considered in the kinetic treatment of gelation, the result would be very complex. Therefore, the usual assumptions must be made, namely, that no rings are formed and that the reactivity of each functionality is constant regardless of the size and structure of the molecule. Also, the condensation reaction is assumed to be due to methylene bond formation, and the rate of decomposition of methylol groups must be very small compared to the rate of hydroxymethylation.

With the above assumptions, the formation of Am resins can be simply represented by the above reactions.

The kinetic relations are given by:

$$dP_A/dt = k_A (1 - P_A) (1 - P_F) + \kappa_A (1 - P_A) (P_F - P_M) \quad (1)$$

$$dP_B/dt = k_B (P_A - P_B) (1 - P_F) + \kappa_B (P_A - P_B) (P_F - P_M) \quad (2)$$

$$dP_F/dt = k_A (1 - P_A) (1 - P_F) + k_B (P_A - P_B) (1 - P_F) \quad (3)$$

$$dP_M/dt = \kappa_A (1 - P_A) (P_F - P_M) + \kappa_B (P_A - P_B) (P_F - P_M) \quad (4)$$

Here, k_A, k_B, κ_A, and κ_B are rate constants; P_F is the extent of reaction of formaldehyde; P_A and P_B are defined by

$$P_A = \{[\text{secondary amino}] + [\text{tertiary amino}]\}/[\text{total amino}]$$

$$P_B = [\text{tertiary amino}]/[\text{total amino}]$$

where primary, secondary and tertiary amino refer respectively to nitrogens bearing one, two, and three N-C links; and P_M is the extent of reaction to form methylene linkages.

Additional assumptions, expressed as eqs. (5) and (6), are introduced here for the sake of simplification.

$$\kappa_A/k_A = \kappa_B/k_B = K \qquad (5)$$

$$k_B/k_A = k \qquad (6)$$

By combining eqs. (1) and (2), and eqs. (3) and (4) we obtain the following equations:

$$dP_B/dP_A = k(P_A - P_B)/(1 - P_A) \qquad (7)$$

$$dP_M/dP_F = K(P_F - P_M)/(1 - P_F) \qquad (8)$$

Solving eqs. (7) and (8) leads to eqs. (9) and (10) and eqs. (11) and (12), respectively:

$$1 - P_B = \frac{1 - P_A}{k - 1} \, [k - (1 - P_A)^{k-1}] \quad k \neq 1 \qquad (9)$$

$$1 - P_B = (1 - P_A) \, [1 - \ln(1 - P_A)] \; k = 1 \qquad (10)$$

$$1 - P_M = \frac{1 - P_F}{K - 1} \, [K - (1 - P_F)^{K-1}] \; K \neq 1 \qquad (11)$$

$$1 - P_M = (1 - P_F) \, [1 - \ln(1 - P_F)] \; K = 1 \qquad (12)$$
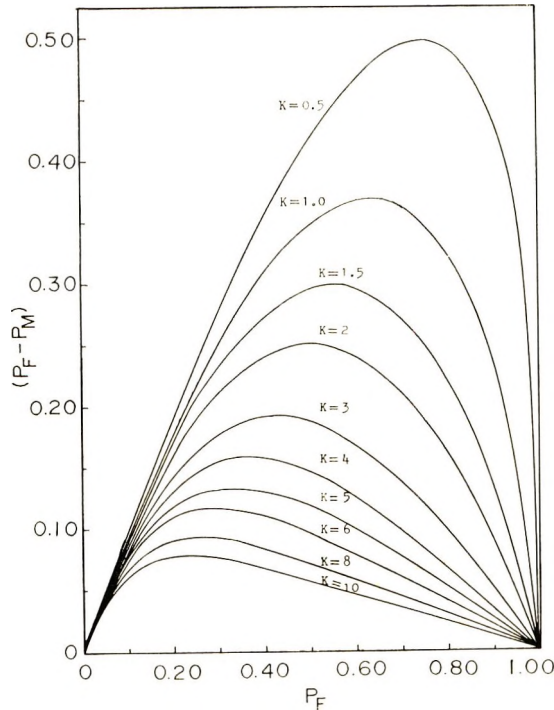
Fig. 1. Relation between the extent of reaction of formaldehyde P_F, and $P_F - P_M$, the probability of occurrence of methylol groups for different values of K.

In terms of the initial concentrations of formaldehyde and Am, i.e., $[F]_0$ and $[Am]_0$, respectively, the stoichiometric relation for the system is represented by

$$2(P_A + P_B) = r\,(P_F + P_M) \tag{13}$$

where

$$r = [F]_0 / [Am]_0$$

Accordingly, relations among four variables, i.e., P_A, P_B, P_F, and P_M, may be obtained by using eqs. (9)–(13).

The relation between the extent of reaction of formaldehyde P_F and the proportion of methylol groups present $(P_F - P_M)$ is plotted in Figure 1 as a function of the value of K, on the basis of eqs. (11) and (12). Thus, the value of K may be determined by comparing experimental measurements with this theoretical relation.

Distribution of Structural Units

The structural units which constitute the Am resin can be depicted as:
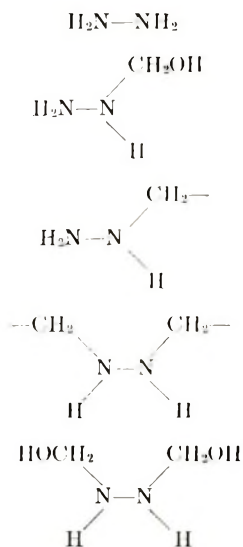
Expressions for the probabilities of formation of these structures follow. The probability of amino group reacting is P_A, and if an amino group reacts with formaldehyde, the probability for the formation of $-NH-CH_2OH$ is:

$$P_A \cdot P_M/(P_F + P_M)$$

This methylol group reacts further to form $-NH-CH_2-$, with the probability

$$P_A \cdot [P_F/(P_F + P_M)] \cdot (P_M/P_F) = P_A \cdot [P_M/(P_F + P_M)]$$

TABLE I

	Structure	Concentration[a]
I	H_2N—NH_2 (unreacted Am)	$(1 - P_A)^2$ [Am]$_0$
II	H_2N—N with CH$_2$OH and H, CH$_2$—	$2(1 - P_A)(P_A - P_B)(1 - q)$ [Am]$_0$
III	H_2N—N with CH$_2$— and H	$2(1 - P_A)(P_A - P_B)q$ [Am]$_0$
IV	HOCH$_2$, CH$_2$OH on N—N, H, H	$(P_A - P_B)^2 (1 - q)^2$ [Am]$_0$
V	—CH$_2$, CH$_2$OH on N—N, H, H	$2(P_A - P_B)^2 (1 - q)q$ [Am]$_0$
VI	—CH$_2$, CH$_2$— on N—N, H, H	$(P_A - P_B)^2 q^2$ [Am]$_0$
VII	H_2N—N<{(CH$_2$OH)$_2$	$2(1 - P_A)P_B(1 - q)^2$ [Am]$_0$
VIII	H_2N—N< CH$_2$OH, CH$_2$—	$4(1 - P_A) P_B(1 - q)q$ [Am]$_0$
IX	H_2N—N<{(—CH$_2$—)$_2$	$2(1 - P_A)P_Bq^2$ [Am]$_0$
X	>N—N< (CH$_2$OH)$_3$, H	$2(P_A - P_B)P_B (1 - q)^3$ [Am]$_0$
XI	—CH$_2$, N—N< (CH$_2$OH)$_2$, H	$6(P_A - P_B)P_B(1 - q)^2q$ [Am]$_0$
XII	(—CH$_2$—)$_2$ N—N (CH$_2$OH), H	$6(P_A - P_B)P_B (1 - q)q^2$ [Am]$_0$
XIII	(—CH$_2$—)$_3$ N—N, H	$2(P_A - P_B)P_Bq^2$ [Am]$_0$
XIV	{>N—N<{ (CH$_2$OH)$_4$	$P_B^2 (1 - q)^4$ [Am]$_0$
XV	—CH$_2$, N—N (CH$_2$OH)$_3$	$4P_B^2 (1 - q)^3 q$ [Am]$_0$
XVI	(—CH$_2$—)$_2${>N—N<{(CH$_2$OH)$_2$	$6P_B^2 (1 - q)^2q^2$ [Am]$_0$
XVII	(—CH$_2$—)$_3${>N—N<{CH$_2$OH	$4P_B^2(1 - q)q^3$ [Am]$_0$
XVIII	(—CH$_2$—)$_4${>N—N<{	$P_B^2q^4$ [Am]$_0$

[a] Where, $q = \dfrac{2P_M}{(P_F + P_M)}$

On the other hand, an amino group may react with a methylol group to form $-NH-CH_2-$ with the probability

$$P_A \cdot P_M / (P_F + P_M)$$

Consequently, the probability for the formation of the structure $-NH-CH_2-$ through both pathways is:

$$P_A \cdot 2P_M / (P_F + P_M)$$

The probabilities of unreacted amino group, unreacted imino group, and free formaldehyde are $1 - P_A$, $P_A - P_B$, and $1 - P_F$, respectively. The probability for the existence of methylol groups is similarly given by

$$\frac{P_F}{P_F + P_M}\left(1 - \frac{P_M}{P_F}\right) = 1 - \frac{2P_M}{P_F + P_M}$$

Thus, the concentrations of various structures are represented as shown in Table I.

The possible structural units that constitute Am resin consist of the 18 species listed in Table I. Accordingly, the total concentration of the structures I–XVIII must be equal to $[Am]_0$:

$$[I] + ([II] + [III]) + ([IV] + [V] + [VI]) + ([VII] + [VIII] + [IX])$$
$$+ ([X] + \ldots + [XIII]) + ([XIV] + \ldots + [XVIII])$$
$$= [(1 - P_A)^2 + 2(1 - P_A)(P_A - P_B) + (P_A - P_B)^2 + 2(1 - P_A)P_B$$
$$+ 2(P_A - P_B)P_B + P_B^2][Am]_0 = [(1 - P_A)^2$$
$$+ 2(1 - P_A)P_A + P_A^2][Am]_0 = [Am]_0$$

Occurrence of Methylene Linkages in Soluble Species and Conditions for Gelation

For the purpose of determining the probability for the existence of soluble species containing methylene linkages, we consider first the probabilities for the formation of structures containing specifical combinations of methylene groups. Such structures and probabilities for their occurrence can be represented as follows:

$$\frac{2P_A}{2P_A + 2P_B} \cdot (1 - P_A)\left(1 - \frac{P_B}{P_A}\right) = (A)$$

$$\frac{2P_A}{2P_A + 2P_B} \cdot (1 - P_A) \cdot \frac{P_B}{P_A} = (B)$$

where

$$X = CH_2OH \qquad (B)(1-q)$$
$$X = CH_2 \qquad (B)q$$

$$\frac{2P_A}{2P_A + 2P_B} \cdot P_A \left(1 - \frac{P_B}{P_A}\right)^2 = (C)$$

where

$$X = CH_2OH \qquad (C)(1-q)$$
$$X = CH_2 \qquad (C)q$$

$$\frac{2P_A}{2P_A + 2P_B} \cdot P_A \cdot 2\left(1 - \frac{P_B}{P_A}\right)\left(\frac{P_B}{P_A}\right) = (D)$$

where

$$X = Y = CH_2OH \qquad (D)(1-q)^2$$
$$X = CH_2OH, Y = CH_2 \qquad (D)(1-q)q$$
$$X = CH_2, Y = CH_2OH \qquad (D)(1-q)q$$
$$X = Y = CH_2 \qquad (D)q^2$$

$$\frac{2P_A}{2P_A + 2P_B} \cdot P_A \left(\frac{P_B}{P_A}\right)^2 = (E)$$

where

$$X = Y = Z = CH_2OH \qquad (E)(1-q)^3$$
$$X = Y = CH_2OH, Z = CH_2 \qquad (E)(1-q)^2q$$
$$X = Z = CH_2OH, Y = CH_2 \qquad (E)(1-q)^2q$$
$$X = CH_2, Y = Z = CH_2OH \qquad (E)(1-q)^2q$$
$$X = CH_2OH, Y = Z = CH_2 \qquad (E)(1-q)q^2$$
$$X = Z = CH_2, Y = CH_2OH \qquad (E)(1-q)q^2$$
$$X = Y = CH_2, Z = CH_2OH \qquad (E)(1-q)q^2$$
$$X = Y = Z = CH_2 \qquad (E)q^3$$

$$\frac{2P_B}{2P_A + 2P_B} \cdot (1 - P_A) = (F)$$

where

$$X=CH_2OH \qquad (F_1)(1-q)$$
$$X=CH_2 \qquad (F_1)q$$

$$
\begin{array}{c}
-CH_2 \quad X \\
\diagdown \diagup \\
N \\
| \\
N \\
\diagup \diagdown \\
H \quad Y
\end{array}
\qquad :
$$

$$\frac{2P_B}{2P_A + 2P_B} \cdot P_A\left(1 - \frac{P_B}{P_A}\right) = (G)$$

where

$$X=Y=CH_2OH \qquad (G)(1-q)^2$$
$$X=CH_2OH,\ Y=CH_2 \qquad (G)(1-q)q$$
$$X=CH_2,\ Y=CH_2OH \qquad (G)(1-q)q$$
$$X=Y=CH_2 \qquad (G)q^2$$

$$
\begin{array}{c}
-CH_2 \quad X \\
\diagdown \diagup \\
N \\
| \\
N \\
\diagup \diagdown \\
Z \quad Y
\end{array}
\qquad :
$$

$$\frac{2P_B}{2P_A + 2P_B} \cdot P_A \cdot \frac{P_B}{P_A} = (H)$$

where

$$X=Y=Z=CH_2OH \qquad (H)(1-q)^3$$
$$X=Y=CH_2OH,\ Z=CH_2 \qquad (H)(1-q)^2 q$$
$$X=Z=CH_2OH,\ Y=CH_2 \qquad (H)(1-q)^2 q$$
$$X=CH_2,\ Y=Z=CH_2OH \qquad (H)(1-q)^2 q$$
$$X=CH_2OH,\ Y=Z=CH_2 \qquad (H)(1-q)q^2$$
$$X=Z=CH_2,\ Y=CH_2OH \qquad (H)(1-q)q^2$$
$$X=Y=CH_2,\ Z=CH_2OH \qquad (H)(1-q)q^2$$
$$X=Y=Z=CH_2 \qquad (H)q^3$$

Letting S be the fraction of methylene linkages in soluble species, we have

$$S = \frac{1}{P_A + P_B}\left\{ P_A + P_B - [(P_A + P_B)^2 + 2P_B](1-S)q \right.$$
$$\left. + 3P_B(P_A + P_B)(1-S)^2 q^2 - 2P_B(1-S)^3 q^3 \right\} \qquad (14)$$

By solving eq. (14), we obtain:

$$\left\{ 1 - \left[(P_A + P_B) + \frac{2P_B}{P_A + P_B}\right]q + 3P_B(1-S)q^2 \right.$$
$$\left. - \frac{2P_B^2}{P_A + P_B}(1-S)^2 q^3 \right\}(1-S) = 0 \qquad (15)$$

Obviously, when gelation has occurred, S is less than unity, and according to eq. (15) is expressed by

$$S = 1 - \left\{\frac{3q(P_A + P_B) + \sqrt{q^2(P_A + P_B)^2 + 8q(P_A + P_B) - 16P_B q^2}}{4P_B^2}\right. \qquad (16)$$

The gelation expression for the gel point of tetrafunctional amino resins is obtained from eq. (16) by setting S equal to unity:

$$\left[\frac{2P_{\text{P}}}{P_{\text{A}} + P_{\text{B}}} + (P_{\text{A}} + P_{\text{B}}) \right] q = 1 \tag{17}$$

This expression for the gel point can also be derived from of Case's gelation theory.[17] When a molecule with a specific methylene linkage forms a second methylene linkage, six structural species may arise. These species and their probabilities of formation are listed in Table II.

TABLE II

Structure	Probability of formation
	$q \cdot \dfrac{2P_{\text{A}}}{2P_{\text{A}} + 2P_{\text{B}}} \cdot \dfrac{P_{\text{B}}}{P_{\text{A}}}$
	$q \cdot \dfrac{2P_{\text{A}}}{2P_{\text{A}} + 2P_{\text{B}}} \cdot P_{\text{A}}$
	$q \cdot \dfrac{2P_{\text{A}}}{2P_{\text{A}} + 2P_{\text{B}}} \cdot P_{\text{A}} \cdot \dfrac{P_{\text{B}}}{P_{\text{A}}}$
	$q \cdot \dfrac{2P_{\text{B}}}{2P_{\text{A}} + 2P_{\text{B}}}$
	$q \cdot \dfrac{2P_{\text{B}}}{2P_{\text{A}} + 2P_{\text{B}}} \cdot P_{\text{A}}$
	$q \cdot \dfrac{2P_{\text{B}}}{2P_{\text{A}} + 2P_{\text{B}}} \cdot P_{\text{A}} \cdot \dfrac{P_{\text{B}}}{P_{\text{A}}}$

The sum of the six probabilities for the formation of these structures is identical with eq. (17) for the gel point determined by the treatment described in this paper.

The condition for gelation can be determined by using the kinetic eqs. (9)–(12), stoichiometric eq. (13), and eq. (17) for the gel point. For example, the result for $r = 1$, $K = 3$, is shown in Figure 2. In this figure curve a was obtained from eq. (17) for the gel point and the other curves
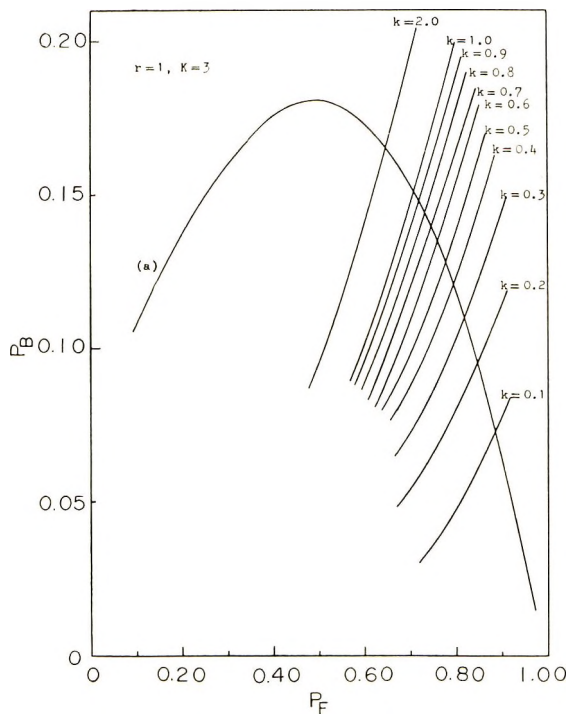
Fig. 2. Relation between extents of reaction of formaldehyde and the imino group for different values of k, where $r = 1$, $K = 3$.

were determined by using eqs. (9), (11), and (13). The points of intersection of the curve (a) and the other curves indicate the gel points for each value of k with $r = 1$, $K = 3$. In Figure 3 the relation between the extent of reaction of formaldehyde at the gel point and the value of k is plotted on the basis of the results in Figure 2. For other values of r and K, similar results are obtained.

Figure 3 permits comparison with experimental results, because it is possible to measure the values of P_F and P_M. The value of k can be determined by using the value of K determined above and the measured value of P_F.
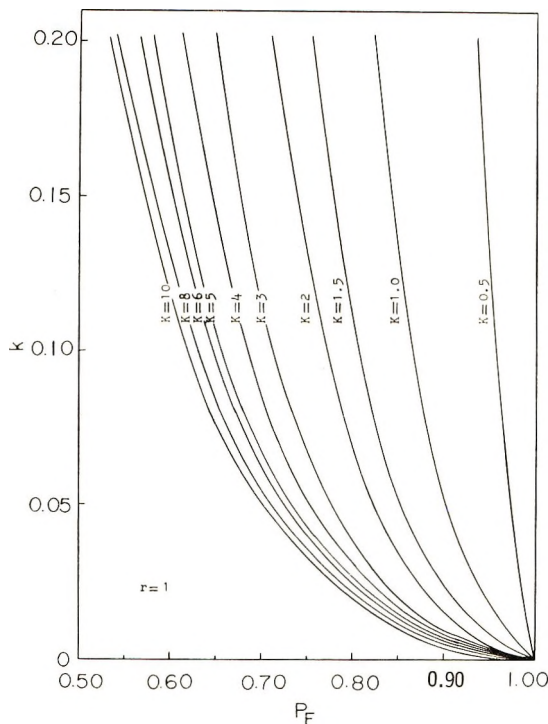
Fig. 3. Relation between the extent of reaction of formaldehyde at the gel point and the value of k for different values of K, where $r = 1$.

Sol and Gel Fractions

We will further calculate amounts of sol and gel fractions in the resin, and the average molecular weight of the sol fraction.

If the concentration of Am units in the sol fraction is represented by $[Am]_s$, the ratio $[Am]_s / [Am]_0$ is given by

$$[Am]_s/[Am]_0 = [I] + [II] + [III]S + [IV] + [V]S + [VI]S^2$$
$$+ [VII] + [VIII]S + [IX]S^2 + [X] + [XI]S$$
$$+ [XII]S^2 + [XIII]S^3 + [XIV] + [XV]S + [XVI]S^2$$
$$+ [XVII]S^3 + [XVIII]S^4$$
$$= 1 - 2(P_A + P_B)(1 - S)q + \{(P_A + P_B)^2 + 2P_B\}(1 - S)^2 q^2$$
$$- 2P_B(P_A + P_B)(1 - S)^3 q^3 + P_B{}^2 (1 - S)^4 q^4 \quad (18)$$

Similarly, if the concentrations of methylol groups and methylene linkages in the sol fraction are represented by $[M]_s$ and $[CH_2]_s$, respectively, we can write:

$$[M]_s/[Am]_0 = [II] + 2[IV] + [V]S + 2[VII] + [VIII]S$$
$$+ 3[X] + 6[XI]S + 3[XII]S^2 + 4[XIV] + 3[XV]S$$
$$+ 2[XVI]S^2 + [VII]S^3$$
$$= 2(1 - q)\left\{(P_A + P_B) - \left\{(P_A + P_B)^2 + 2P_B\right\}(1 - S)q\right.$$
$$+ 3P_B(P_A + P_B)(1 - S)^2q^2 - 2P_B^2(1 - S)^3q^3 \quad (19)$$

$$2[CH_2]_s/[Am]_0 = [III] + [V] + 2[VI]S + [VIII] + 2[IX]S$$
$$+ [XI] + 2[XII]S + 3[XII]S^2 + [XV]$$
$$+ 2[XVI]S + 3[XVII]S^2 + 4[XVIII]S^3$$
$$= 2q\left[(P_A + P_B) - \left\{(P_A + P_B)^2 + 2P_B\right\}(1 - S)q\right.$$
$$+ 3P_B(P_A + P_B)(1 - S)^2q^2 - 2P_B^2(1 - S)^3q^3] \quad (20)$$

By substituting eqs. (13) and (15) into eqs. (19) and (20), eqs. (19) and (20) are much simplified:

$$[M]_s/[F]_0 = (P_F - P_M)S \quad (21)$$

$$[CH_2]_s/[F]_0 = P_M S \quad (22)$$

Since the fraction of each unit in the sol can be found as mentioned above, the total yield W of resin and the yield W_s of sol can immediately be obtained from the following relations:

$$W = [Am]_0 + (P_F - P_M)(M_F/M_{Am})[F]_0 + P_M(M_M/M_{Am})[F]_0 \quad (23)$$

$$W_s = [Am]_s + (P_F - P_M)S(M_F/M_{Am})[F]_0 + P_M S^2(M_M/M_{Am})[F]_0 \quad (24)$$

where M_{Am} is the molecular weight of tetrafunctional amino monomer, and M_F and M_M are the increments of molecular weight due to the formation of methylol groups and methylene linkages, respectively.

The number-average molecular weight, $M_{n,s}$ of the sol fraction may be expressed as

$$M_{n,s} = \frac{M_{Am}W_s}{[Am]_s - P_M S^2[F]_0} \quad (25)$$

Conclusion

The value of K can be determined by plotting experimental measurements with the theoretical relation obtained from eqs. (11) and (12). The gelation condition for tetrafunctional amino resins can be determined by using the kinetic eqs. (9)–(12), the stoichiometric eq. (13), and eq. (17) for the gel point. Equation (17) is identical to the result obtained with Case's gelation theory.

The concentrations of Am skeletal units $[Am]_s$, of methylol groups $[M]_s$, and of methylene linkages $[CH_2]_s$, in the sol fraction are calculated from eqs. (18), (21), and (22), respectively. The total yield of resin W, yield

of sol W_s, and number-average molecular weight of the sol fraction $M_{n,s}$, are expressed by eqs. (23), (24), and (25), respectively.

Values of these quantities can be determined by combining experimental data with the theoretical relations.   This gelation theory will be applied to the gelation reaction of acetoguanamine-formaldehyde resin in the next paper.[18]

References

1. P. J. Flory, *J. Amer. Chem. Soc.*, **63**, 3083 (1941).
2. P. J. Flory, *J. Amer. Chem. Soc.*, **63**, 3091 (1941).
3. P. J. Flory, *J. Amer. Chem. Soc.*, **63**, 3039 (1941).
4. P. J. Flory, *J. Amer. Chem. Soc.*, **69**, 30 (1947).
5. W. H. Stockmayer, *J. Chem. Phys.*, **11**, 45 (1943).
6. W. H. Stockmayer, *J. Chem. Phys.*, **12**, 125 (1944).
7. E. Imoto, *Kobunshi Tenbo*, **2**, 226 (1950).
8. R. Inoue and M. Izumi, *Kobunshi Kagaku*, **9**, 191 (1952).
9. M. Gordon, B. M. Grieveson, and I. D. McMillan, *J. Polym. Sci.*, **18**, 497 (1955).
10. M. Oiwa, *Nippon Kagaku Zasshi*, **76**, 508 (1955).
11. T. Kakurai and T. Noguchi, *Kogyo Kagaku Zasshi*, **64**, 398 (1961).
12. Y. Tanaka and H. Kakiuchi, *J. Appl. Polym. Sci.*, **7**, 1951 (1963).
13. K. Ishii and H. Kakiuchi, *Kogyo Kagaku Zasshi*, **70**, 1235 (1967).
14. K. Ishii and H. Kakiuchi, *Kogyo Kagaku Zasshi*, **70**, 1238 (1967).
15. K. Ishii, R. Nakatsuka, and H. Kakiuchi, *Kogyo Kagaku Zasshi*, **70**, 2069 (1967).
16. K. Ishii, R. Nakatsuka, and H. Kakiuchi, *Kogyo Kagaku Zasshi*, **71**, 1096 (1968).
17. L. C. Case, *J. Polym. Sci.*, **26**, 333 (1957).
18. T. Uragami and M. Oiwa, *J. Polym. Sci. A-2*, **9**, 15 (1971).

Studies on Formaldehyde Condensation Resins.   XIII. Gelation of Acetoguanamine–Formaldehyde Resin

TADASHI URAGAMI and MASAYOSHI OIWA, *Department of Applied Chemistry, Faculty of Engineering, Kansai University, Osaka, Japan*

Synopsis

The gelation reaction of acetoguanamine with formaldehyde was investigated in the light of the gelation theory for tetrafunctional amino resins described in the previous paper.   The gel time and extents of reaction of formaldehyde, amino groups, and imino groups varied with the molar ratio in the feed, but values of K (the ratio of the rate constant for condensation to that for addition) and k (the ratio of the rate constant for addition of the imino group to that of the amino group) were nearly constant.   When the catalyst concentration was increased, the gel time, extents of reaction of each functional group, and the values of K and k varied; in particular K increased markedly.   From the results of varying the molar ratio and concentration of acidic catalyst, it was found that the number of methylol groups per molecule of acetoguanamine at the gel point was influenced by the reaction conditions but the number of methylene linkages per molecule of acetoguanamine was nearly constant at about 0.6, regardless of reaction conditions.   The number-average molecular weights up to the gel point varied with the reaction conditions, but at the gel point they were all nearly constant at about 385.

INTRODUCTION

In the previous paper,[1] the gelation of tetrafunctional amino resins was discussed theoretically in terms of addition-condensation reactions; the theoretical kinetic equations involving the relation between the extent of reaction of each functional group and the rate constant, or the extent of reaction of each functionality and the gelation condition, etc., were derived by considering the distribution of structural units.

In the present work, the gelation reaction of acetoguanamine with formaldehyde is studied by employing the gelation theory developed for tetrafunctional amino resins in the previous paper.[1]   The extent of reaction of each species of functional group and the ratio of rate constant are determined under different conditions.   Also, the variation of weight of the resin formed and of the molecular weight distribution are discussed in some detail.   Undefined symbols and equation numbers appearing in the following text are those of the preceding paper.[1]

15

EXPERIMENTAL

Materials

Nippon Gosei Co. best-grade acetoguanamine (AG) was recrystallized from water (mp 269–271°C) Formaldehyde (F) was obtained from Nippon Gas Co. as a 42.18% aqueous solution containing 1.40% methanol. Pure commercial dimethyl sulfoxide (DMSO) and N,N-dimethylformamide (DMF) were purified by the usual methods.[2,3]

Reaction Procedure

Measured amounts of acetoguanamine and formaldehyde were placed in glass ampoules, and the reaction mixture was diluted with hydrochloric acid to the desired concentration. The ampoule was then evacuated under reduced pressure, flushed with nitrogen, and then sealed under vacuum. It was then put into a thermostat regulated at 80°C.

Analyses

After the chosen reaction time, the ampoule was removed from the thermostat, and an aliquot of the solution was pipetted out and diluted with DMSO to the desired concentration. This sample solution was analyzed by the ammonium chloride[4] and iodometric[5] methods to determine respectively the conversion of free formaldehyde and the total amount of formaldehyde free and hydroxymethylated. The amount of hydroxymethylation was calculated from the difference between the two values obtained by the above methods. The amount of methylene linkages formed was calculated from the difference between the initial concentration of formaldehyde and the value obtained by the iodometric method.

The weight of resin formed was likewise measured after a definite reaction time, by precipitation with sodium hydroxide solution and centrifugation. The precipitate was washed with cold water and dried *in vacuo* to constant weight. The soluble fraction was extracted with DMSO from the resin so obtained and recrystallized from methanol. The molecular weight of the soluble resin was measured with a vapor-pressure osmometer, (Hewlett Packard, Model 302) and DMF as the solvent at 65°C.

RESULTS AND DISCUSSION

Effect of the Initial Molar Ratio $[F]_0/[AG]_0$ on Gelation.

For the purpose of investigating the effect of the molar ratio of gelation, reactions were carried out for $r = [F]_0/[AG]_0$ between 1 and 7 and $[F]_0$ from 0.98 to 4.75 mole/l. A measured amount of aqueous hydrochloric acid was used as the solvent and/or catalyst.

With $r = 4$, as shown in Figure 1, the concentration of methylene linkages becomes almost equal to that of methylol groups at 60 min and then increases with time. The gel fraction also begins to form at 60 min and

increases with an increase in concentration of methylene linkages.   For r between 4 and 7, similar results were obtained.   If we consider this result only, it might be thought that gelation depends upon the fraction of methylol groups and methylene linkages.   However, as is shown in Figure 2, in the case of a small molar ratio ($r = 2$), the concentration of methylene linkages is larger than that of methylol groups even in the early stage of the
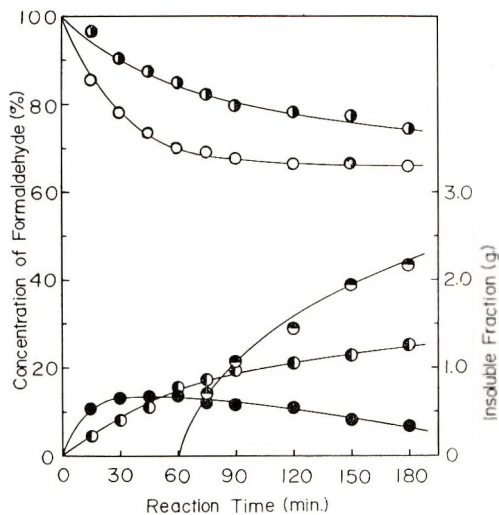
Fig. 1. Conversion of formaldehyde in the reaction of acetoguanamine with formaldehyde, at 80°C with $r = 4$:   (○) curve for hydroxymethylation; (◑) curve for methylene linkage formation; (●) concentration of methylol groups; (◐) concentration of methylene linkages; (◒) insoluble fraction.
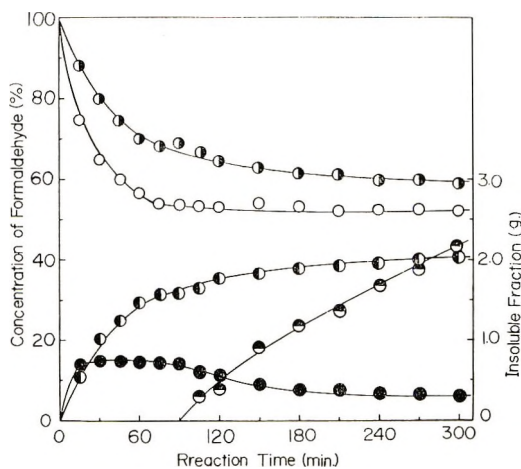
Fig. 2. Conversion of formaldehyde in the reaction of acetoguanamine with formaldehyde, at 80°C with $r = 2$:   (○) curve for hydroxymethylation; (◑) curve for methylene linkage formation; (●) concentration of methylol groups; (◐) concentration of methylene linkages; (◒) insoluble fraction.
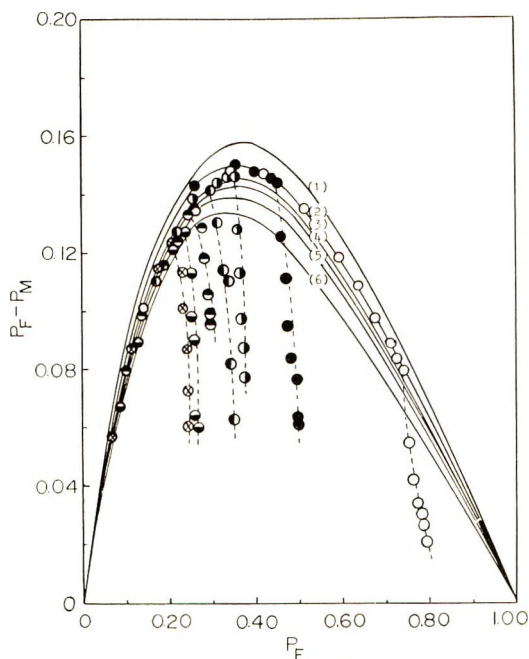
Fig. 3. Relation between P_F, the extent of the reaction of formaldehyde and the probability $P_F - P_M$, of occurrence of methylol groups. Theroretical curves: (1) $K = 4.0$, (2) $K = 4.3$, (3) $K = 4.4$, (4) $K = 4.5$, (5) $K = 4.7$, (6) $K = 5.0$; experimental results: (O) $r = 1$, (●) $r = 2$, (◑) $r = 3$, (◐) $r = 4$, (◒) $r = 5$, (◓) $r = 6$, (⊗) $r = 7$.

reaction, and the gel begins to form at 90 min, later than with $r = 4$. A similar tendency was found for r from 1 to 3. Thus, gelation does not always depend upon the fractions of methylol groups and methylene linkages in the soluble fraction. Perhpas, gelation depends upon the fractions of methylol groups and methylene linkages in the insoluble fraction and upon the molecular weight of the resin.

The ratio K can be determined by using the relation between the extent of reaction of formaldehyde P_F and the probability of occurrence of methylol groups, $P_F - P_M$, and the theoretical relation among P_F, P_M, and K given, by eq. (11) of the preceding paper.[1] This relation is plotted in Figure 3, where curves 1–5 represent the theoretical relation calculated by eq. (11) for K ranging from 4 to 5.

The amount of methylol groups in the insoluble fraction beyond the gel point could not be determined; therefore, the measured values of P_F and $P_F - P_M$ beyond the gel point are smaller than the true amounts reacted. However, even if this is considered, the concentration of methylol groups begins to drop rapidly, as is shown in Figure 3, at a value of P_F which just corresponds to the gel point. This seems to indicate that after the gel point condensation proceeds rapidly, while the addition reaction progresses very little.

For this reason the value of K beyond the gel point could not be obtained, but up to the gel point it could be determined by comparing the plots of experimental measurements with the theoretical curves.   The effect of the initial molar ratio $[F]_0/[AG]_0$ value of K thus obtained for r from 1 to 7 is shown in Table I.

TABLE I

Effect of the Molar Ratio $[F]_0/[AG]_0$ on the Gelation Reaction of Acetoguanamine (AG) with Formaldehyde (F) at 80°C

Expt. no.	$[AG]_0$, mole/l.	$[F]_0$, mole/l.	0.1N HCl, ml	Molar ratio, $[F]_0/[AG]_0$	Gel time, min.	Extent of reaction			K	k
						P_F	P_A	P_B		
1	0.98	0.98	15.2	1	110	0.724	0.553	0.129	4.3	0.60
2	0.92	1.84	15.2	2	90	0.460	0.602	0.176	4.3	0.67
3	0.85	2.55	15.2	3	75	0.355	0.631	0.211	4.4	0.73
4	0.80	3.20	15.2	4	60	0.297	0.661	0.241	4.5	0.75
5	0.76	3.77	15.2	5	55	0.265	0.698	0.281	4.5	0.75
6	0.71	4.29	15.2	6	55	0.237	0.716	0.309	4.7	0.76
7	0.68	4.75	15.2	7	55	0.223	0.756	0.353	4.5	0.75

The values of K do not vary appreciably with the molar ratio.   However, the gel time and the extents of reaction of formaldehyde, amino and imino groups, P_F, P_A, and P_B, vary considerably with $[F]_0/[AG]_0$.

In Table II are shown the numbers of methylol groups and methylene per molecule of acetoguanamine at the gel point.

TABLE II

Effect of the Molar Ratio $[F]_0/[AG]_0$ on the Number of Methylol Groups and Methylene Linkages per Molecule of Acetoguanamine at the Gel Point (80°C)[a]

Expt. no.	$[AG]_0$, mole/l.	$[M]$, mole/l.	$[CH_2]$, mole/l.	$[M]/[AG]$	$[CH_2]/[AG]$
1	0.98	0.08	0.63	0.08	0.64
2	0.92	0.26	0.58	0.29	0.63
3	0.85	0.38	0.53	0.44	0.62
4	0.80	0.46	0.49	0.58	0.61
5	0.76	0.52	0.48	0.69	0.64
6	0.71	0.56	0.46	0.78	0.64
7	0.68	0.61	0.45	0.90	0.66

[a] Methylol group and methylene linkage are abbreviated as M and CH_2, respectively.

As can be seen from Table II, the number of methylol groups $[M]/[AG]$ increases in the molar ratio, but that of methylene linkages $[CH_2]/[AG]$ is nearly constant at about 0.6, regardless of the molar ratio.   From these results, it appears that gelation does not depend upon the number of methylol groups but occurs when the number of methylene linkages increases to a critical value.
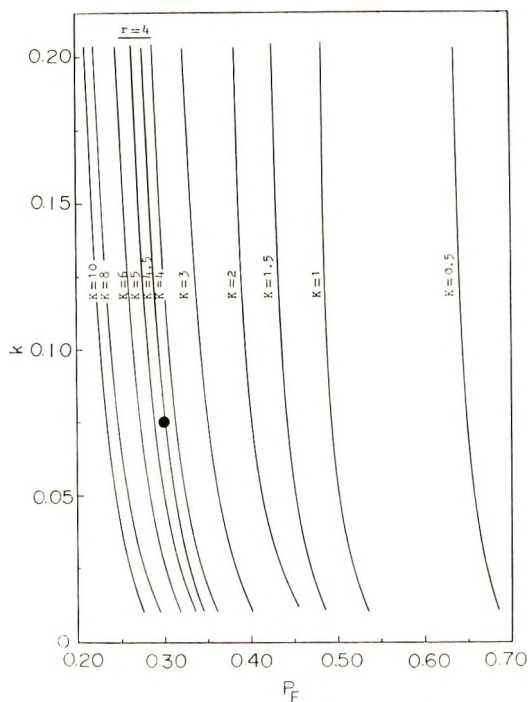
Fig. 4. Relation between the extent of reaction of formaldehyde and the value of k for $r = 4$. The curves represent theoretical relations; the point is an experimental result.

The relation among P_F, k, and K determined by using the kinetic relations, eqs. (9) through (12), the stoichiometric equation, eq. (13), and eq. (17) for the gel point, is shown in Figure 4, in which the curves indicate the theoretical relation between P_F and k for each value of K. From this figure, the value of k can be deduced if the experimental value of P_F corresponds to any point on the theoretical curve for the known value of K. Thus, for example, for $P_F = 0.297$, $K = 4.5$, and $r = 4$, (See Table I) k is estimated to be 0.7. The k values with $1 \leq r \leq 7$, determined in the same manner, are shown in Table I. It is evident that k is nearly constant over this range of r.

Since the values of K and k can be determined, the values of P_A and P_B can be computed, and are shown also in Table I. These results suggest that a correlation exists between the reactivity of the amino group and that of the imino group, regardless of the molar ratio r.

Effect of Catalyst

For the purpose of investigating the effect of catalyst concentration on gelation, the extent of reaction of each functionality at the gel point and the values of K and k were examined at a constant formaldehyde/acetoguanamine molar ratio of 4 and with concentrations of hydrochloric acid catalyst from 0.025 to 0.20N.
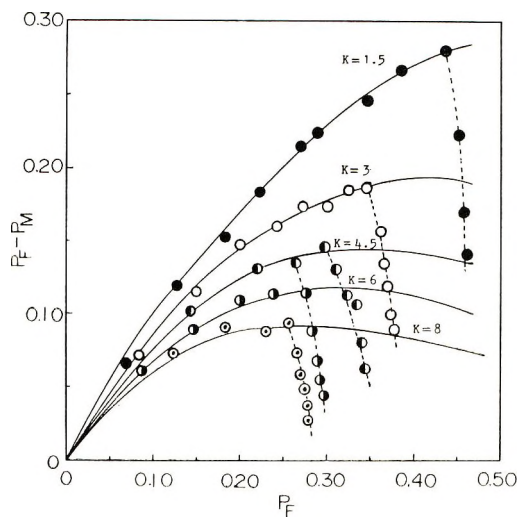
Fig. 5. Extent of reaction of formaldehyde P_F vs. the probability of occurrence of methylol groups, $P_F - P_M$, for $r = 4$. The curves represent theoretical relations. The points are experimental results: (●) 0.025N HCl; (○) 0.05N HCl; (◐) 0.10N HCl; (◑) 0.15N HCl, (⊙) 0.20N HCl.
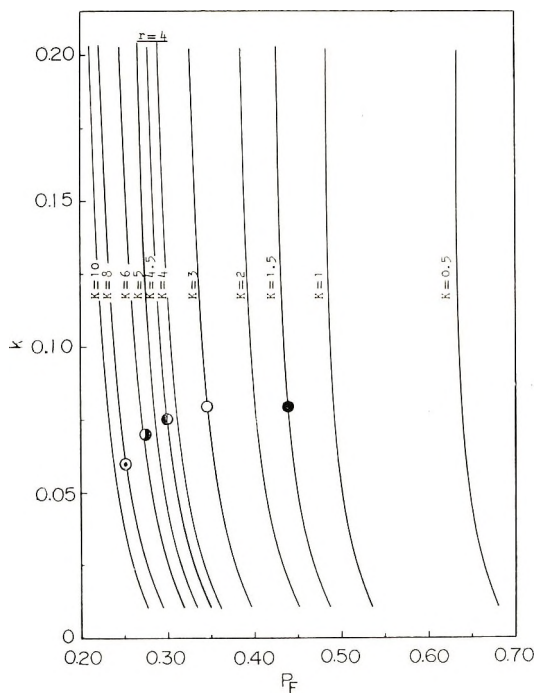
Fig. 6. Relation among values of P_F, k, and K at the gel point for $r = 4$, theoretical curves and experimental results: (●) 0.025N HCl; (○) 0.05N HCl; (◐) 0.10N HCl; (◑) 0.15N HCl; (⊙) 0.20N HCl.

TABLE III

Effect of the Concentration of HCl Catalyst on the Gelation Reaction of Acetoguanamine (AG) with Formaldehyde (F) at 80°C

Expt. no.	Molar ratio $[F]_0/$ $[AG]_0^a$	HCl concentration, N	Gel time, min.	Extent of reaction			K	k
				P_F	P_A	P_B		
8	4	0.025	210	0.434	0.786	0.403	1.5	0.8
9	4	0.05	120	0.344	0.704	0.297	3.0	0.8
4	4	0.10	60	0.297	0.661	0.241	4.5	0.75
10	4	0.15	50	0.275	0.647	0.213	6.0	0.7
11	4	0.20	35	0.253	0.640	0.183	8.0	0.6

a Initial concentrations of AG and F are 0.80 and 3.20 mole/l., respectively.

Values of K, as shown in Figure 5, varied with the concentration of catalyst. Beyond the gel point the condensation reaction proceeds very rapidly, and the addition reaction very little, as was also found when the molar ratio r was varied. This result may be understood as follows; the kinetic equations derived in the previous paper[1] can be applied only up to the gel point, i.e., to the homogeneous reaction.

Values of k with varying HCl catalyst concentration are shown in Figure 6. The values of k obtained from Figure 6 gradually decrease with an increase in the concentration of catalyst. The gelation conditions for various concentrations of catalyst are shown in Table III. The gel time gradually decreases and the extents of reaction of P_F, P_A, and P_B at the gel point also decrease with an increase in the concentration of catalyst.

Both K and k are linearly dependent on the concentration of catalyst, as is shown in Figure 7. The value of K increases markedly, and the value of k decreases slightly with an increase in catalyst concentration. The linear dependence of K on catalyst concentration agrees with the concept of acid-base catalysis in which reaction proceeds preferentially by addition in the presence of an acidic catalyst. To account for the behavior of k, it may be
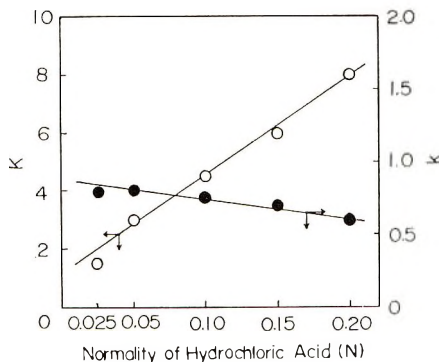
Fig. 7. Relation between the concentration of acid catalyst and (○) K and (●) k.

supposed that the reactivities of amino and imino groups vary with the concentration of acid catalyst, that is, that the imino group is activated more than the amino group by an increase in acid concentration.

In Table IV are given the numbers of methylol groups and methylene linkages per molecule of acetoguanamine at the gel point for different concentrations of catalyst. This result is similar to that for the variation of the molar ratio.

TABLE IV

Effect of the Concentration of Catalyst on the Number of Methylol Groups and Methylene Linkages per Molecule of Acetoguanamine at the Gel Point (at 80°C)

Expt. No.	$[AG]_0$, mole/l.	$[M]$, mole/l.	$[CH_2]$, mole/l.	$[M]/$ $[AG]$	$[CH_2]/$ $[AG]$
8	0.80	0.90	0.50	1.12	0.63
9	0.80	0.60	0.50	0.75	0.63
4	0.80	0.46	0.49	0.58	0.61
10	0.80	0.36	0.52	0.45	0.65
11	0.80	0.30	0.51	0.37	0.64

From the results of varying the molar ratio and the concentration of catalyst, it was found that the number of methylol groups in acetoguanamine at the gel point is influenced by the reaction conditions, but the number of methylene linkages is not, within the range studied.

In Table III, values of P_A and P_B are also shown. The correlation between the reactivity of the amino group and that of the imino group, which was recognized by varying the molar ratio, is not found when the catalyst concentration is varied. This result may be ascribed to a difference of the extent to which amino and imino groups taking part in a series of reactions are activated by the acid catalyst.

Molecular Weight Distribution

Since the gel point was influenced more by the catalyst concentration than by the molar ratio, the influence of catalyst concentration on the yield of resin and on the molecular weight distribution up to the gel point was investigated.

The total yield of resin W and the yield of soluble fraction W_s are given by eqs. (23) and (24). Since it is assumed that S, the fraction of methylene linkages in the soluble fraction, is equal to unity up to the gel point, eq. (23) of part XII is equivalent to eq. (24); i.e., $W = W_s$.

Figure 8 shows the theoretical relation between P_F and the total yield, the weight of the total resin per initial unit weight of acetoguanamine. In this figure, the three lower curves correspond to cases in which the unreacted acetoguanamine is considered in calculating the theoretical yield; in the three upper curves it is neglected. Since it is difficult to extract only
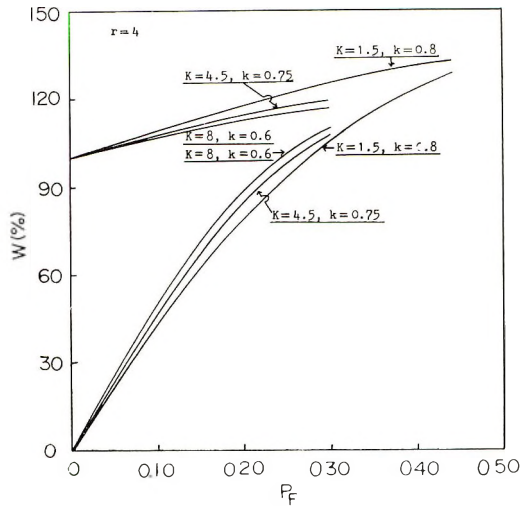
Fig. 8. Theoretical relation between P_F and the total yield of resin W.
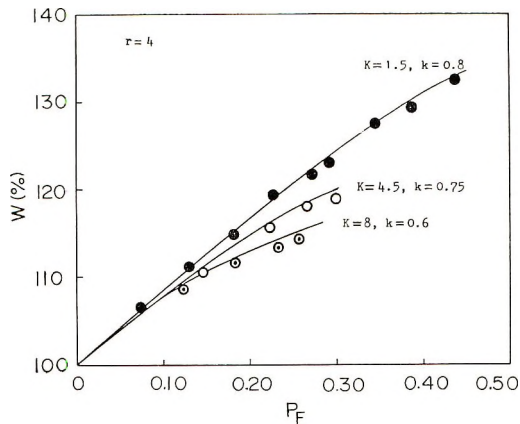
Fig. 9. Relation between P_F and the total yield of acetoguanamine–formaldehyde resin containing unreacted acetoguanamine; (———) theoretical curves and experimental results: (●) 0.025N HCl; (○) 0.10N HCl; (◎) 0.20N HCl.

the unreacted acetoguanamine, however, the upper curves can be used as the theoretical yield of resin.   In Figure 9 the relation between W and P_F is plotted; the measured values agree very closely with the theoretical values.

The relation between P_F and the number-average molecular weight is shown in Figure 10, in which the curves and the circle points indicate theoretical values calculated by combining eqs. (9), (11), (13), and (15) and values measured with a vapor-pressure osmometer, respectively.   The measured number-average molecular weight agrees very closely with the theoretical value.   The molecular weight up to the gel point increases with an increase in K.   However, at the gel point the molecular weight obtained

TABLE V

Relations between the Extent of Reaction of Formaldehyde, P_F, and Number-Average Molecular Weight with $r = 4$, $K = 1.5$, and $k = 0.8$

P_F	$M_{n,s}$		
	Theoretical	Calculated[a]	Measured
0.070	136	133	137
0.128	147	144	144
0.179	161	160	158
0.224	178	179	180
0.268	199	194	193
0.289	212	210	201
0.345	258	261	247
0.385	317	309	303
0.438	383	397	384

[a] From P_F, P_M, and total yield.

for the resin is about 385, regardless of the K value. This agrees with the fact that the number of methylene linkages per molecule of acetoguanamine at the gel point is nearly constant regardless of reaction conditions.

A number-average molecular weight can be determined in another way, i.e., by substituting the measured values of P_F and P_M and the measured total yields into eq. (25). We denote this molecular weight as the "calculated value" in Table V, which also includes theoretical and measured values. It can be seen that there is close agreement among the three molecular weights.
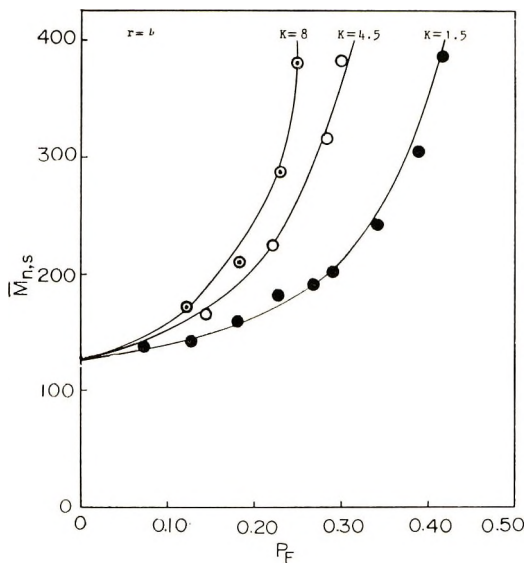
Fig. 10. Plots of number-average molecular weight versus P_F: (——) theoretical relations and measured values: (●) 0.025N HCl; (○) 0.10N HCl; (◉) 0.20N HCl.

References

1. T. Uragami and M. Oiwa, *J. Polym. Sci. A-2*, **9**, 1 (1971).
2. C. A. Kingsbury, *J. Org. Chem.*, **29**, 3262 (1964).
3. E. Pirot, *Chem. Abstr.*, **50**, 1683 (1956).
4. J. Büchi, *Pharm. Acta Helv.*, **6**, 1 (1931).
5. A. Takahashi and I. Yamazaki, *Kobunshi Kagaku*, **15**, 232 (1958).

Orientation in Nylon 6 Films as Determined by the Three-Dimensional Polarized Infrared Technique

JOHN P. SIBILIA, *Corporate Chemical Research Laboratories, Allied Chemical Corporation, Morristown, New Jersey 07960*

Synopsis

A three-dimensional polarized infrared technique was used to obtain information about molecular orientation in both uniaxially and biaxially drawn nylon 6 films. The 835 and 930 cm^{-1} bands were used to describe the orientation of the A (extended chain) conformation while absorptions at 1175 cm^{-1}, 1120 cm^{-1} and 1075 cm^{-1} were used to give some information about orientation of the B (twisted chain) conformation. On the basis of the 835 and 930 cm^{-1} bands, it was shown that the hydrogen-bonded sheets made up of chains in the A conformation are parallel to the film surface in the biaxially drawn film. Uniaxially drawn films obtained by drawing both at 100 and 150°C showed a high degree of chain alignment in the draw direction for the A conformation at draw ratios greater than 2.5. Some planar orientation was also observed in these uniaxially drawn films for both the A and B conformations at high draw ratios.

INTRODUCTION

When a polymer film is drawn, some preferred alignment of the molecular chains normally occurs. Polarized infrared spectroscopy has proved to be a useful technique in describing such molecular orientation through measurement of the dichroic ratio R. The dichroic ratio can be defined as $R = A_{\parallel}/A_{\perp}$, where $A_{\parallel}$ is the absorbance parallel to the draw direction in the film and $A_{\perp}$ is the absorbance perpendicular to the draw direction. Although R has proved to be a useful parameter, it has provided in most cases information only about two-dimensional orientation effects.

However for a more meaningful understanding of the structure–property relationships in oriented materials, it is important to determine the three-dimensional orientation characteristics of the molecular system.

Recently, an infrared technique has been developed[1-3] which allows one to obtain information about the orientation of molecular chains in three dimensions. This approach has previously been applied to poly(ethylene terephthalate)[2,4,5] and polyethylene.[3] The present work shows how it can be applied to obtain useful information about oriented nylon 6.

27

THEORETICAL

Mathematical Treatment

Details of the theoretical treatment for the technique have already been reported.[1,2] However a brief description will serve to clarify the present results.

Film coordinates are defined as y, the draw direction; x, the transverse direction (perpendicular to y); and z, the direction normal to the film surface. For a particular absorption mode, a quantity A_0 can be defined as:

$$A_0 = (A_x + A_y + A_z)/3 \qquad (1)$$

where A_x, A_y, and A_z are the absorbances in the respective film coordinate directions and A_0 is described as the structurally dependent term.[2] A_0 is related to the amount of the particular absorbing group present in the material and is independent of the orientation of the group. If the absorption being examined can be assigned to a specific vibrational mode of a particular molecular group and if the direction of its transition moment with respect to the chain direction can be ascertained, then a knowledge of the parameters A_x, A_y, and A_z will serve to describe the orientation of the chain as well as the orientation of the group with respect to the film coordinates. The values of A_x and A_y, which are respectively $A_\perp$ and $A_\parallel$ in conventional notation, can be readily obtained. However, A_z, the component of the absorbance in the direction normal to the film surface, is difficult to obtain.

The main features of the three-dimensional infrared orientation technique are concerned with measuring the parameter A_z. Basically the technique involves rotating the film around the x axis so that the electric vector of polarized radiation is at a tilt angle α_t with respect to the y direction. A value for A_z can then be determined from A_t, the absorbance at α_t, from the expression:[2]

$$A_z = \frac{A_t[1 - (1/n_{yz}^2) \sin^2 \alpha_t]^{1/2} - A_y}{(1/n_{yz})^2 \sin \alpha_t} \qquad (2)$$

The parameters A_t, α_t, and A_y can be readily obtained, while the value of n_{yz}, the index of refraction in the yz plane at the α_t angle, poses more of a problem. The actual values used in the calculations will be discussed in the experimental section.

Infrared Spectrum of Nylon 6

A considerable amount of infrared spectroscopic work has been done on nylon 6 (polycaprolactam). A paper by Schneider, Schmidt and Wichterle[6] describes the spectra of nylon 6 in terms of two conformers, A and B. The A conformer is the extended-chain form, the form that exists in the α-crystalline state.[7] The B conformer represents a twisted or pleated-chain conformation and is the form that exists in γ-crystalline,[8,9] amorphous, and

smectic-hexagonal nylon 6.   Although the extent of twist in the B form may be different in the γ, amorphous, and smectic-hexagonal states, the infrared spectra of these phases are very similar.

Two weak bands which occur in the A conformation at 835 and 930 cm^{-1}, have been assigned by Sandeman and Keller[10] to a CH_2 rocking and a $CONH$ in-plane vibration, respectively.   Both absorptions are highly dichroic in oriented specimens, the 835 cm^{-1} band showing perpendicular dichroism and the 930 cm^{-1} band showing parallel dichroism.

We would like to suggest further that these two bands are mutually perpendicular, with the transition moment of the 930 cm^{-1} band along the molecular axis of the extended chain conformation, and the transition moment of the 835 cm^{-1} band perpendicular to the molecular axis and normal to the plane of the hydrogen bonded sheets formed by the extended-chain conformation.   This can be illustrated by the structure I:

I
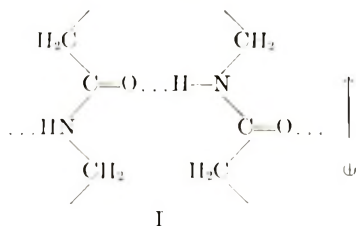
where the arrow denotes the transition moment direction of the 930 cm^{-1} band and the transition moment direction of the 835 cm^{-1} band is out of the plane of the paper (indicated by $\oplus$).

Therefore if we can accurately describe the dichroism of these mutually perpendicular bands with respect to the three film coordinates, then some information about the three-dimensional orientation of the extended molecular chain can likewise be obtained with respect to the film coordinates.

EXPERIMENTAL

Description of the Apparatus

In Figure 1 is a photograph of the apparatus used to tilt the film samples at any desired angle up to 55°.   This is equivalent to a rotation about the x axis.   The apparatus also has a means of rotating the sample about the direction of the incident radiation by a known amount.   In practice, all spectra were obtained with the films rotated +45° from the incident ray so that the y direction of the film (draw direction for uniaxially drawn films) was likewise rotated +45°.   The purpose of doing this was to minimize the polarization effects of the spectrometer.

Polarization of the infrared radiation was accomplished by means of a Perkin-Elmer AgBr disk polarizer mounted in the common beam of a Beckman IR-12 spectrometer, just before the exit slits.   Since the sample was
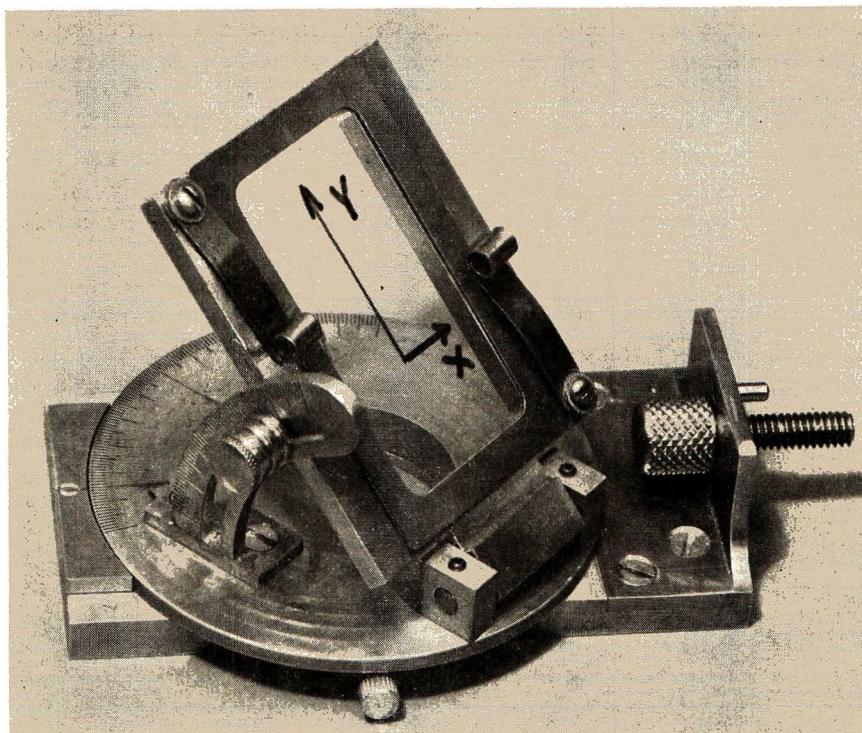
Fig. 1. Film mount used to study three-dimensional orientation in thin films.

always rotated $+45°$, a $+45°$ rotation of the polarizer resulted in examination of light with the electric vector parallel to the y direction. A rotation of the polarizer to the $-45°$ position resulted in the electric vector being perpendicular to the y direction (or parallel to the x direction of the film).

All films were examined on a Beckman IR-12 spectrometer at speeds of 20 cm^{-1}/min and slower.

Description of Samples

Two types of film samples were examined. One sample was prepared by simultaneously stretching a film in both the transverse and machine directions. The final film was about 1 mil thick.

A second set of films, which were highly amorphous to begin with, were drawn uniaxially at about 100%/min and at temperatures of $100°$C and $150°$C. The draw ratios were determined from "bench marks" on the films and varied up to about 3.6. The original film was 2.0 mils thick and quite uniform (thickness variation was less than ± 0.1 mil).

Determination of n_y

Since the index of refraction is a function of wavelength, it should be determined at the wavelength of the absorption band being examined. Schmidt[2] describes a procedure, based on a rotation about the y axis, for

measuring the n_y, the index in the y direction. The appropriate relation is:

$$n_y = \left[\frac{\sin^2 \alpha_t}{1 - (A_y/A_t)^2} \right]^{1/2} \tag{3}$$

Results obtained for films drawn at both 3.5/1 and 1.8/1 and at tilt angles of 30 and 50° were $n_y = 1.7 \pm 0.2$ for absorptions measured at 930, 1075, and 1120 cm^{-1}.

Since the results for n_y were not very precise and since the values for the three bands measured were the same within experimental error, it was decided to obtain an overall value of n_y for nylon 6 by another method. The interference fringe method was used whereby $n = (dN/d\nu)/4t$; where n is the index of refraction, $dN/d\nu$ is the slope of the plot of N (fringe number) versus ν, the wave number in reciprocal centimeters, and t is the film thickness in centimeters.

An average value $n = 1.62 \pm 0.03$ was obtained from twelve different films covering the ranges 1900–2500 cm^{-1} and 3500–4000 cm^{-1}. Amorphous unoriented as well as highly α-crystalline unoriented films were used. Values of n were also obtained on crystalline films highly drawn uniaxially. These were found to be 1.62 for fringes obtained with light parallel (n_y) and 1.62 for fringes obtained with light perpendicular ($f[n_x, n_z]$) to the draw direction. These data are consistent with birefringence data obtained with light in the visible region of the spectrum, which indicate a difference between n_y and ($f[n_x', n_z]$) of the order of only 0.06 for highly oriented fibers.[11]

It may be possible to obtain values of n_{yz} as a function of n_y, and n_z by a consideration of the index of refraction ellipse. However, for the present work, calculations of A_z were made from eq. (2) by assuming $n_y \approx n_{yz}$, where $n_y = 1.62$. All values of A_z were obtained at a tilt angle of 45° about the x axis.

Base Lines

Base lines were drawn for each band at or near the points of maximum transmission on the spectrum from the high wavelength side to the low wavelength side of the band.

The approximate high and low wavenumber values used to define the base lines were as follows for the various bands: for the 1175 cm^{-1} band, from 1185 to 1135 cm^{-1}; for the 1120 cm^{-1} band, from 1135 to 1090 cm^{-1}; for the 1075 cm^{-1} band, from 1090 to 1040 cm^{-1}; for the 930 cm^{-1} band, from 940 to 900 cm^{-1}; for the 835 cm^{-1} band, from 850 to 820 cm^{-1}.

DISCUSSION

Biaxially Drawn Film

In Figure 2 are given the spectra obtained on film simultaneously stretched in the transverse and machine directions. The x-ray diffraction

J. P. SIBILIA
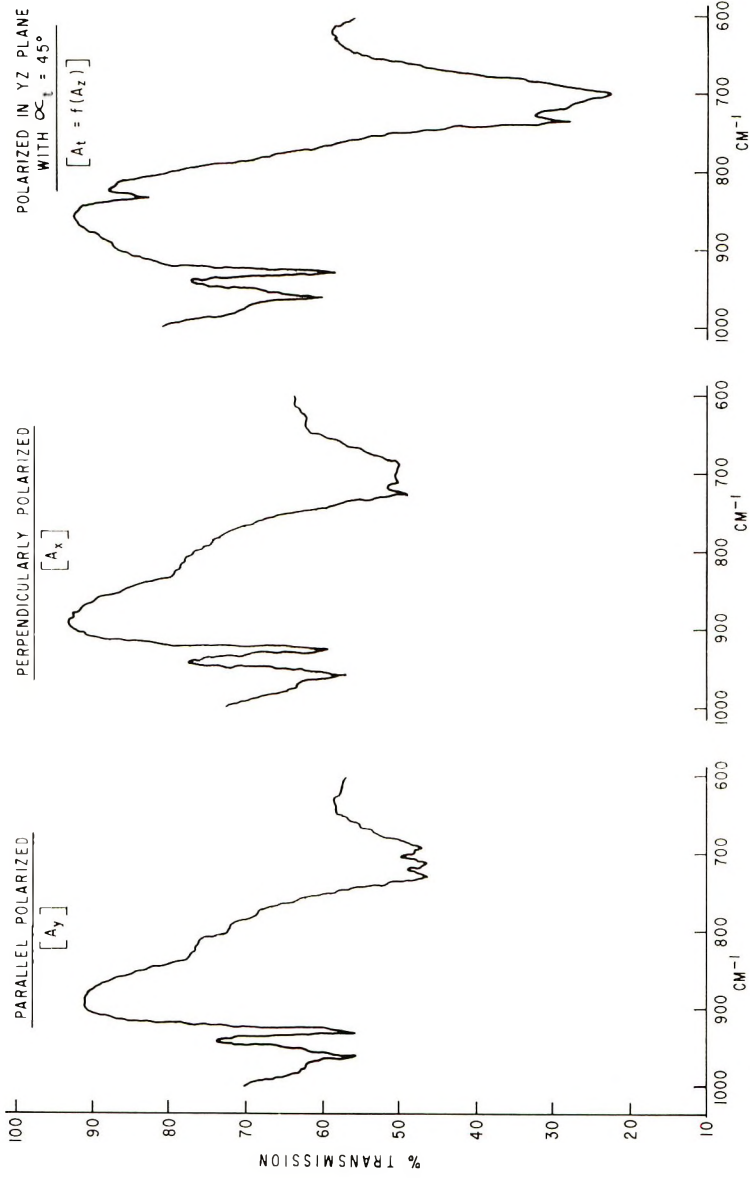
Fig. 2. Polarized infrared spectra of a biaxially drawn nylon 6 film.
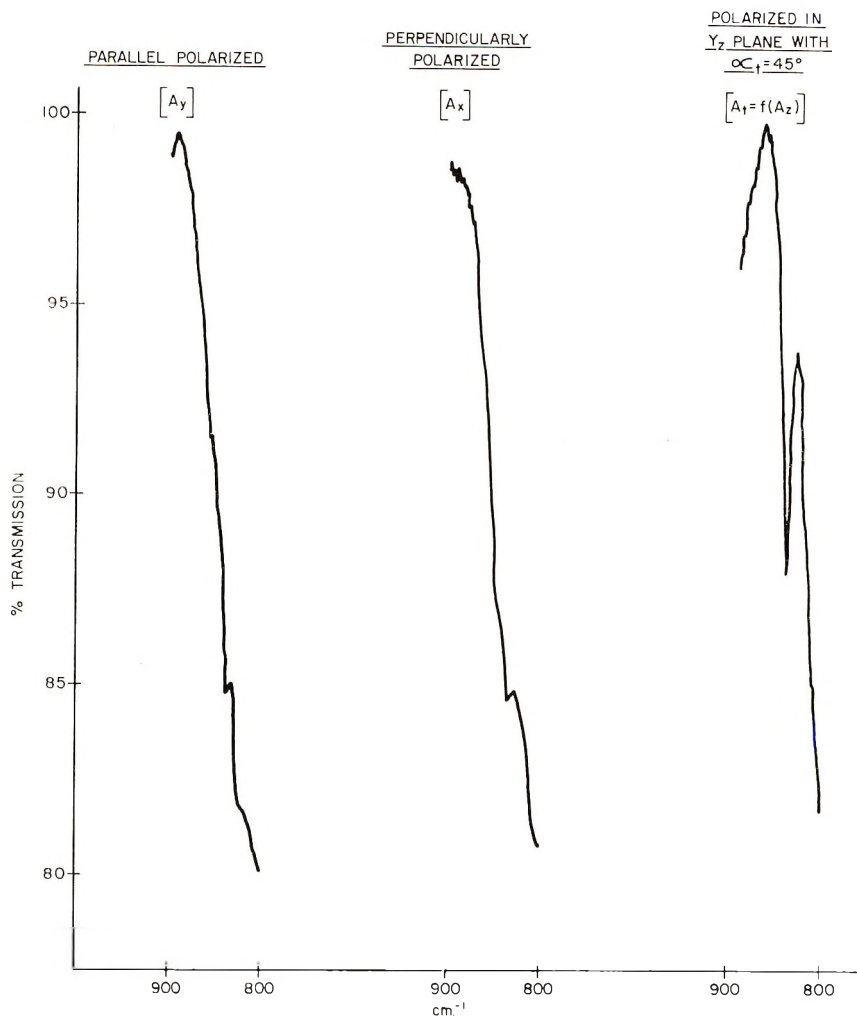
Fig. 3. Scale-expanded polarized infrared spectra of a biaxially drawn nylon 6 film.

data obtained on this film indicated that it contained about 45% of the α polymorph and was highly oriented in the xy plane with a relatively small amount (ca. 13%) of chain orientation in the y direction. The fact that only slight differences are observed in the 930 cm^{-1} band, confirm the relatively low degree of chain orientation with respect to either the x or y film direction. On the other hand, the lack of absorption at 835 cm^{-1} in both the y and x directions and the relatively strong amount of absorption appearing as the film is tilted indicates the high degree of planar orientation. This is shown more clearly in the expanded curves of Figure 3. Therefore, it can be concluded that the hydrogen-bonded planes made by the A conformation in the α polymorph are parallel to the film surface in the planar-oriented film.

This is in agreement with both the x-ray data and with infrared data obtained by Arimoto[12] on similarly prepared film. His infrared technique however, involved the use of polarized light and an infrared microscope with direct observation of the z direction on microtomed films.

It can also be seen in Figure 2 that the NH out-of-plane deformation mode (amide V) of the A conformation at 692 cm^{-1} has an extremely large A_z (A_t) component relative to the A_x and A_y components.[6] Since its transition moment direction is also out of the plane of the hydrogen-bonded sheets made by the A conformation, this band would be expected to behave as the 835 cm^{-1} band. It is also important to note that the 711 cm^{-1} band, attributed to the amide V of the B conformation,[6] does not have the same degree of polarization as the amide V of the A conformation, as is indicated from the different relative intensities of the two bands in the three spectra presented. This suggests that the chain orientation and/or the amide group orientation is different for the A and B conformations. The A conformation appears to have a much higher degree of planar orientation.

Uniaxially Drawn Film: The A Conformation

In Figure 4 are given plots of the structure-dependent factor A_0, as a function of draw ratio at 100°C for both the 835 and 930 cm^{-1} bands for
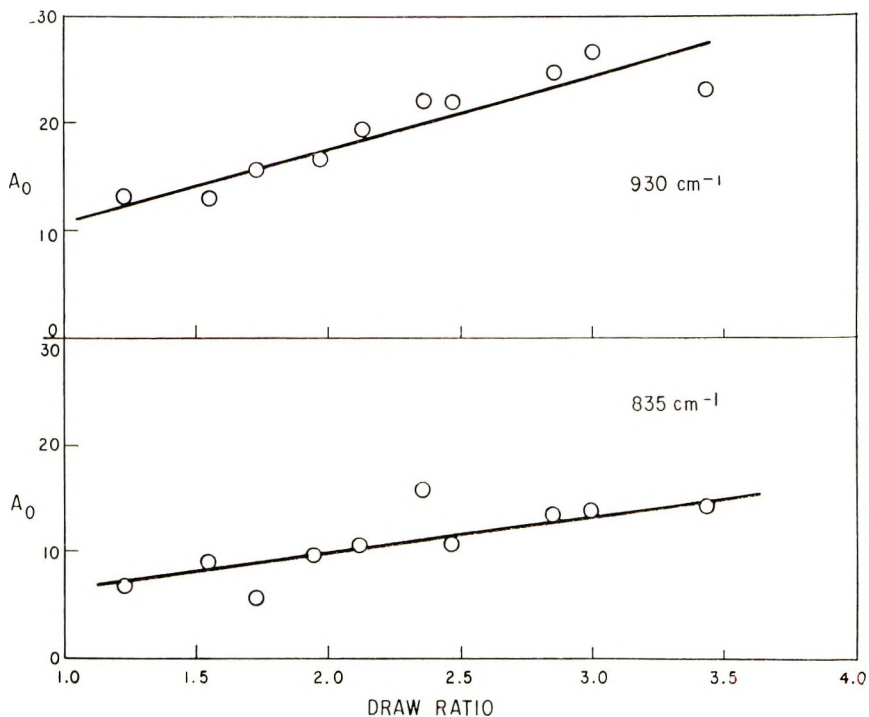
Fig. 4. Structure-dependent parameters (A_0) as a function of draw ratio for both the 930 cm^{-1} and 835 cm^{-1} bands of nylon 6 for film drawn at 100°C.
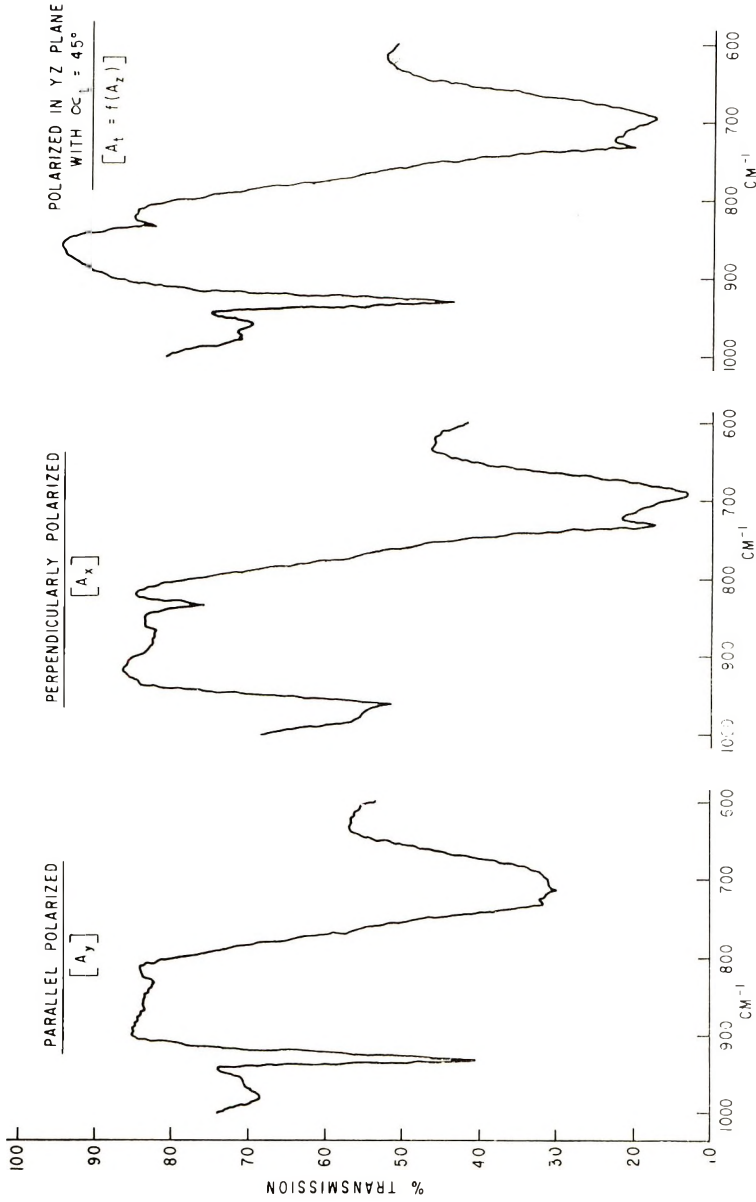
Fig. 5. Polarized infrared spectra of a uniaxially drawn nylon 6 film (draw ratio 3.5 at 150°C).
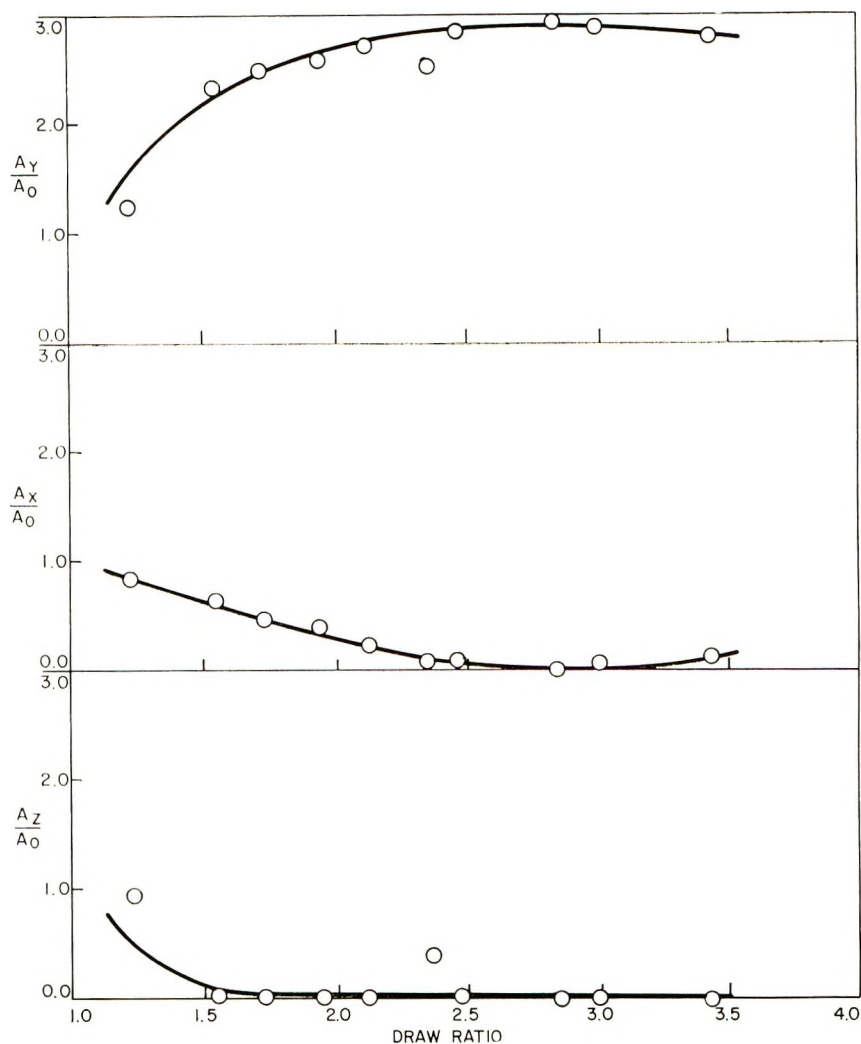
Fig. 6. Orientation parameters for the 930 cm^{-1} band of nylon 6 as a function of draw ratio for films drawn at 100°C.

films which were originally highly amorphous. These data indicate that some increase in the A conformation occurs for materials drawn under these conditions.

In Figure 5 are given spectra of a film drawn uniaxially to a draw ratio of 3.5 at 150°C. The highly dichroic nature of the 930 cm^{-1} band is clearly evident. The band is present in the A_y and A_t spectra but missing in the spectrum (A_x) obtained with perpendicularly polarized light. This suggests that the chains in the A conformation in this particular sample are all highly oriented in the direction of drawing.

In Figure 6 are given plots of A_y/A_0, A_x/A_0, and A_z/A_0 for the 930 cm^{-1} band as a function of draw ratio for films uniaxially drawn at 100°C. It
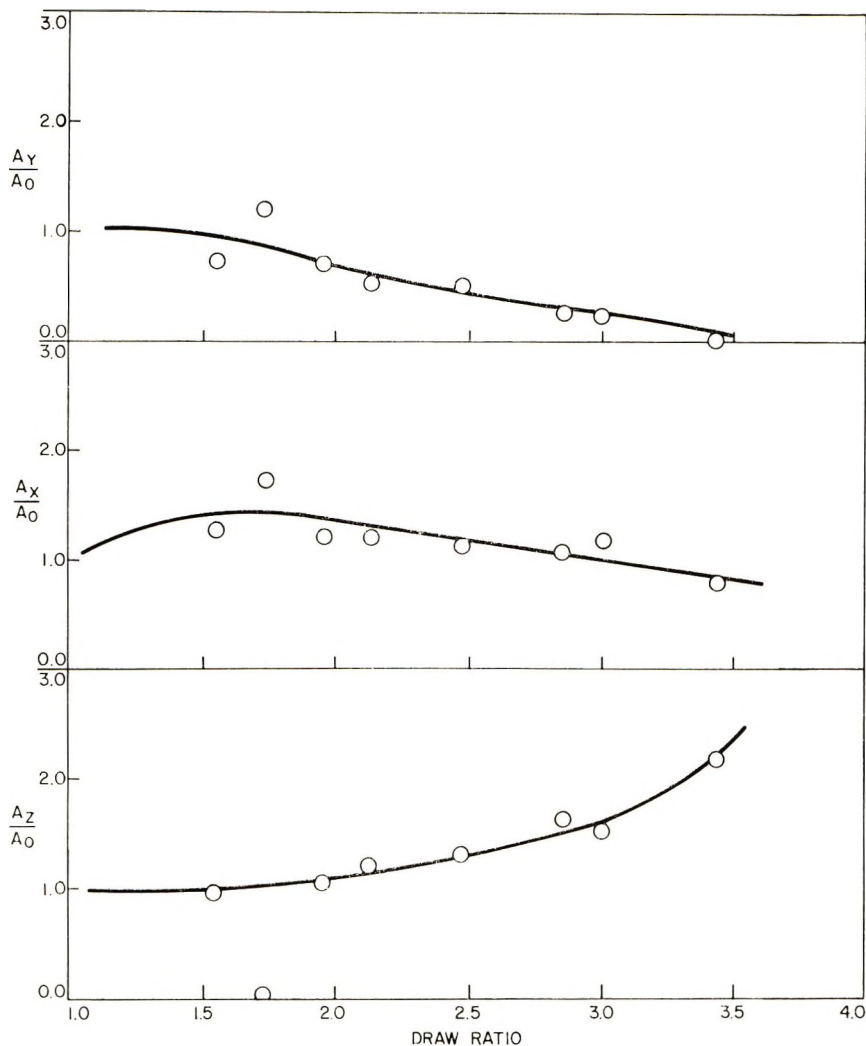
Fig. 7. Orientation parameters for the 835 cm^{-1} band of nylon 6 as a function of draw ratio for films drawn at 100°C.

can be seen that a very high degree of alignment of the chains in the A conformation occurs along the draw direction at draw ratios greater than about 2.5. This is the point where the value of A_y/A_0 is close to the value of 3.0 which represent 100% alignment.

Since the A conformation is the one that exists in the α polymorph, it can be said that the α phase is also highly aligned with the polymer chains in the direction of draw.

Although both A_x/A_0 and A_z/A_0 approach zero, the values are different at early stages of drawing. This suggests that some preferential orientation of the chains also occurs with respect to the film surface.
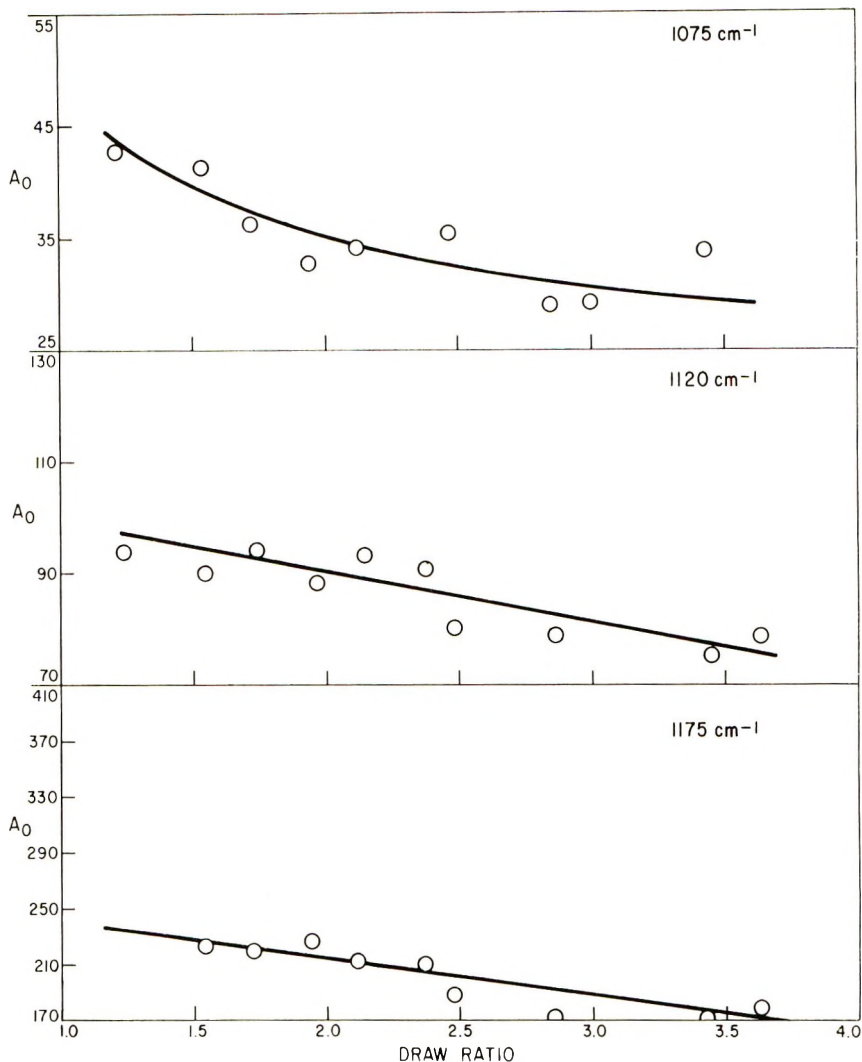
Fig. 8. Structure-dependent parameters (A_0) as a function of draw ratio for the 1075, 1120, and 1175 cm^{-1} bands of nylon 6 for film drawn at 100°C.

In Figure 7 are given the plots of A_y/A_0, A_x/A_0, and A_z/Z_0, for the 835 cm^{-1} band for the same films. The perpendicular nature of this band is evident since the A_y/A_0 term approaches zero at high draw ratios while A_x/A_0 and A_z/A_0 remain finite. Furthermore, the higher values of A_z/A_0 relative to A_x/A_0 suggest that some planar orientation exists, even in these uniaxially drawn films. Since the transition moment of the 835 cm^{-1} band is normal to the plane of the hydrogen bonded sheets made by the A conformation in the α phase, then the higher value of A_z/A_0 suggests that the hydrogen-bonded sheets in this phase tend to lie parallel to the surface of the film.
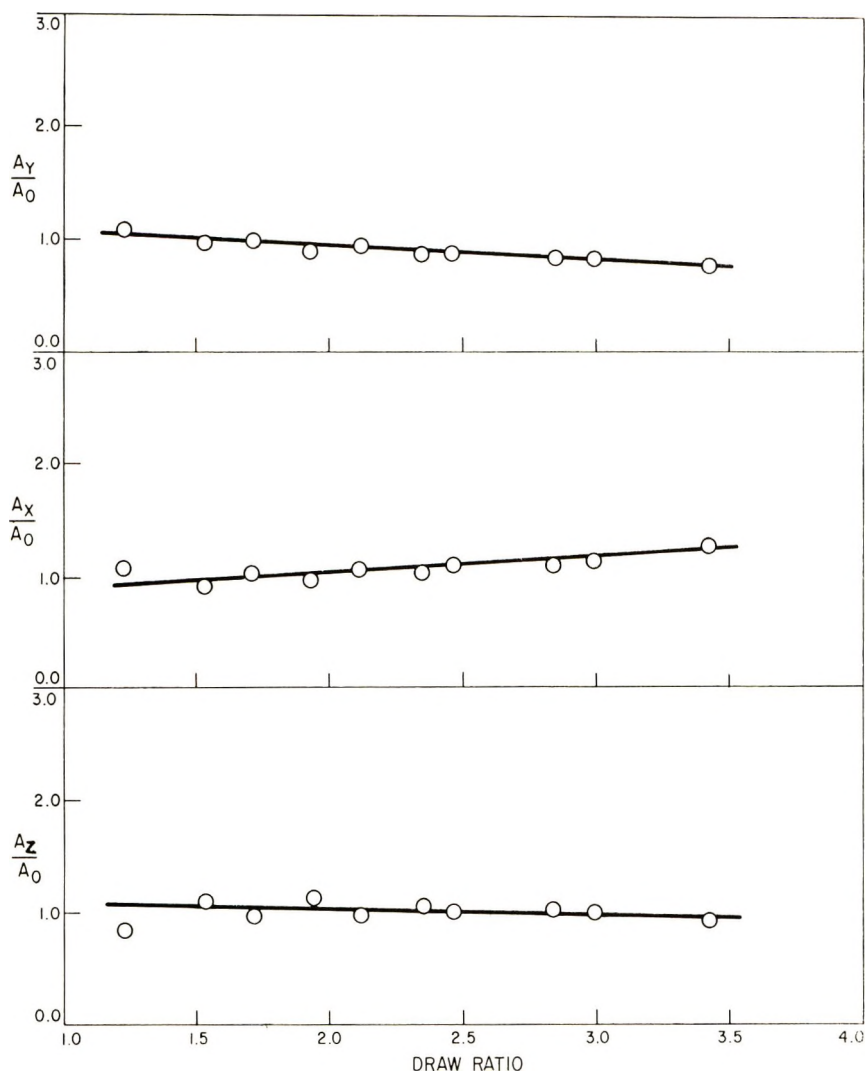
Fig. 9. Orientation parameters for the 1175 cm^{-1} band of nylon 6 as a function of draw ratio for films drawn at 100°C.

Uniaxially Drawn Film: The B Conformation

A number of absorptions related at least in part to the B conformation were also examined by the three-dimensional infrared technique on uniaxially drawn films. The A_0 values for bands at 1175, 1120, and 1075 cm^{-1} are given in Figure 8. All the values tend to decrease with increasing draw ratio at 100°C. Since the results on the 835 and 930 cm^{-1} bands indicated that the A conformation content was increasing under these conditions, the B conformation content must be decreasing. Therefore, the 1175, 1120, and 1075 cm^{-1} bands must be at least partially associated with the B
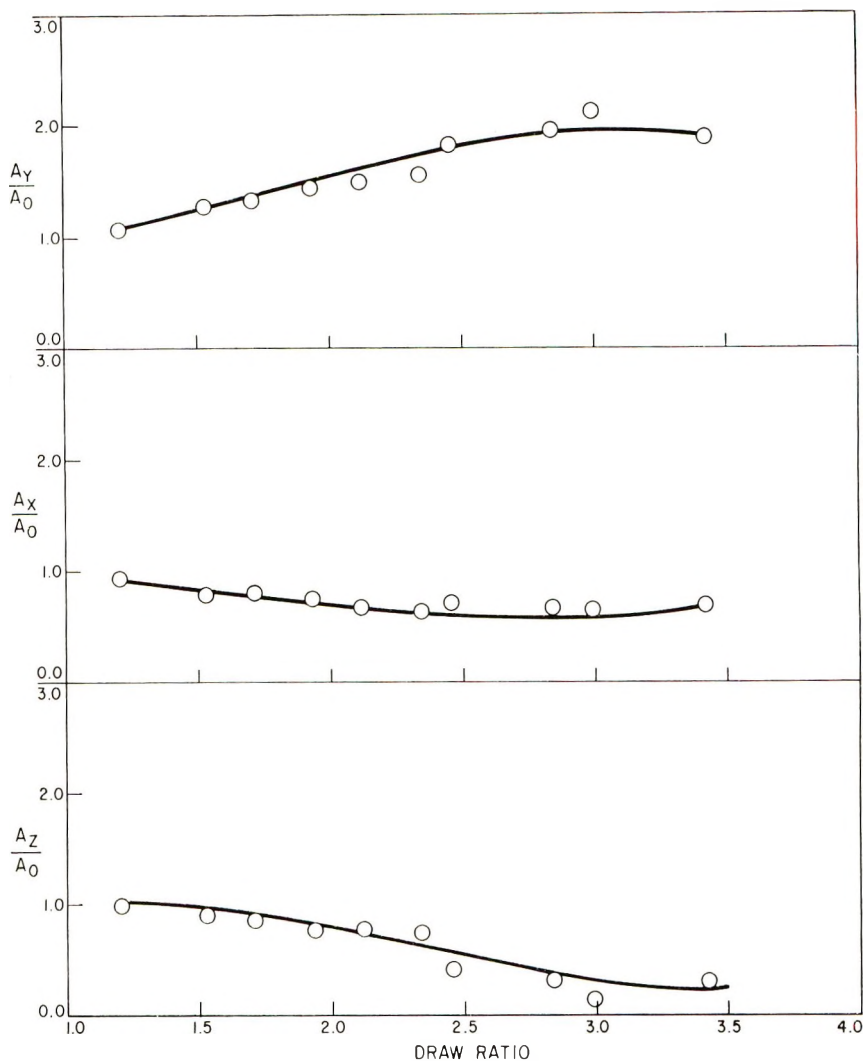
Fig. 10. Orientation parameters for 1120 cm^{-1} band of nylon 6 as a function of draw ratio for films drawn at 100°C.

conformation, as has already been suggested.[6]   The scatter in the plots in Figure 8 may be due in part to the fact that the twisted B conformation is not a well-defined conformer, as in the A form; but rather, a mixture of conformers such as those that might exist in the γ state, or in amorphous polymer.   Therefore, although the absorbances occur at the same frequencies for all the known twisted forms, the band shapes and/or intensities of particular twisted conformers may be different.

In Figures 9, 10, and 11 are given the orientation parameters A_y/A_0, A_x/A_0, and A_z/A_0 for the three absorptions as a function of draw ratio for films drawn at 100°C.   Since the assignments of these bands are not clear
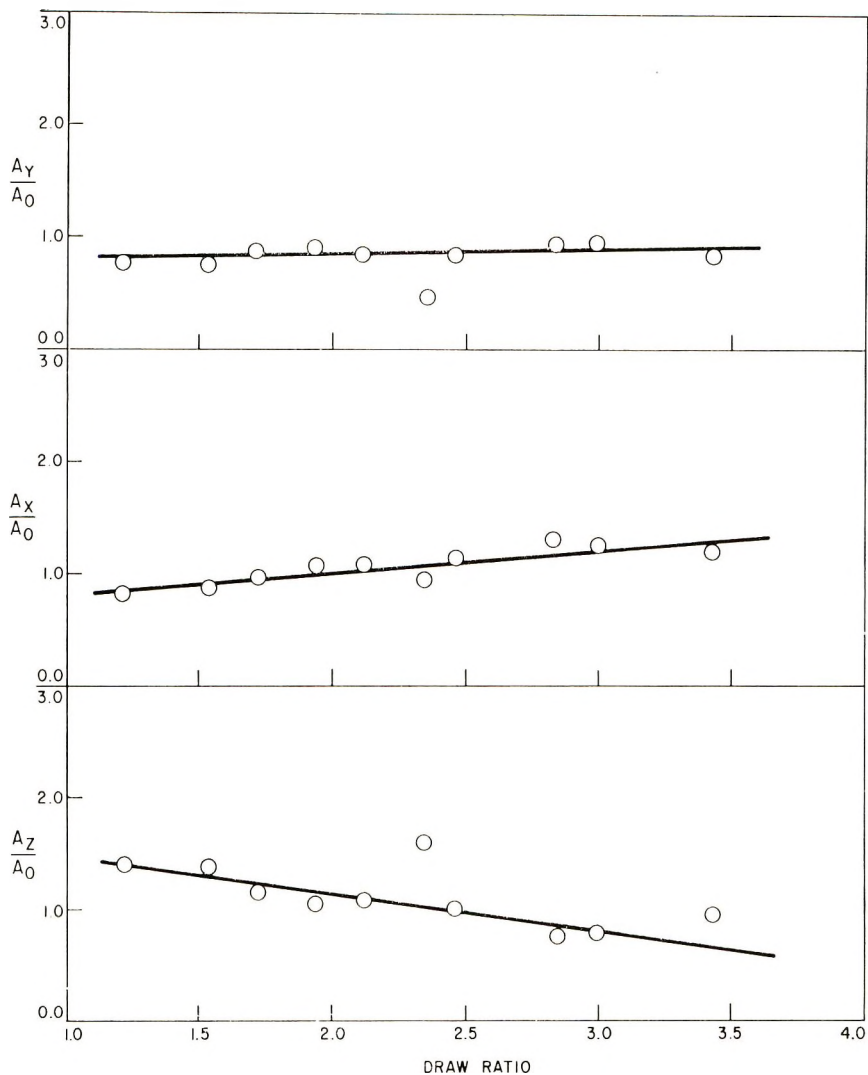
Fig. 11. Orientation parameters for the 1075 cm^{-1} band of nylon 6 as a function of draw ratio for films drawn at 100°C.

at the present time it is not possible to relate the orientation parameter of these bands to the orientation of groups in the B form. However some orientation trends for these bands are noted which can be used at least in a general way to compare B conformation changes in materials treated in different ways.

Both the 1075 and 1175 cm^{-1} bands appear to show increases in the A_x component relative to both the A_y and A_z component. This suggests some preferred planar orientation occurs in the B conformation. The 1120 cm^{-1} band is essentially a parallel band, again with the A_x component slightly greater than A_z.

Considerably more information will be realized as the assignments and transition-moment directions of these bands become known.

Results obtained for films drawn uniaxially at 150°C were similar to those for film drawn at 100°C, for both the A and B conformations.

References

1. R. Zbinden, *Infrared Spectroscopy of High Polymers*, Academic Press, New York; 1964, pp. 180–189.

2. P. G. Schmidt, *J. Polym. Sci. A*, **1**, 1271 (1963).

3. J. L. Koenig, S. W. Cornell, and D. E. Witenhafer, *J. Polym. Sci. A-2*, **5**, 301 (1967).

4. J. L. Koenig and S. W. Cornell, in *Macromolecular Chemistry, Brussels–Louvain 1967 (J. Polym. Sci. C*, **22**), G. Smets, Ed., Interscience, New York, 1969, p. 1019.

5. J. L. Koenig and S. W. Cornell, *J. Macromol. Sci. (Phys.)*, **B1**, 279 (1967).

6. B. Schneider, P. Schmidt, and O. Wichterle, *Coll. Czechoslov. Chem. Commun.*, **27**, 1749 (1962).

7. D. R. Holmes, W. Bunn, and D. J. Smith, *J. Polym. Sci.*, **17**, 159 (1955).

8. Y. Kinoshita, *Makromol. Chem.*, **33**, 1 (1959).

9. A. Miyake, *J. Polym. Sci.*, **44**, 223 (1960).

10. I. Sandeman and A. Keller, *J. Polym. Sci.*, **19**, 401 (1956).

11. E. R. Kaswell, *Textile Fibers, Yarns and Fabrics*, Reinhold, New York, 1953, pp. 476–477.

12. H. Arimoto, *J. Polym. Sci. A*, **2**, 2283 (1964).

Characterization of Diene Polymers.   I.
Infrared and NMR Studies: Nonadditive Behavior
of Characteristic Infrared Bands

YASUYUKI TANAKA and YASUMASA TAKEUCHI, *Central Research Laboratory, Japan Synthetic Rubber Co. Ltd., Ikuta, Kawasaki, Japan* and MASAMICHI KOBAYASHI and HIROYUKI TADOKORO, *Department of Polymer Science, Faculty of Science, Osaka University, Toyonaka, Osaka, Japan*

Synopsis

Extinction coefficients of the characteristic infrared bands due to isomeric structural units were measured for polybutadiene and polyisoprene in CS_2 or CCl_4 solutions and were compared with the isomer composition determined by NMR. The NMR signal assignments were made on the basis of the spectra of deutero derivatives of the polymers. In the case of polyisoprene, linear relations were obtained between the extinction coefficients and the isomer contents determined by NMR for the absorption bands at 1385 cm^{-1} (characteristic of *trans*-1,4 units), 1376 cm^{-1} (*cis*-1,4 units), and 889 cm^{-1} (3,4 units). However, for the absorption bands at 840 cm^{-1} (characteristic of *cis*-1,4 and *trans*-1,4 units), isomerized polyisoprenes did not give such a linear relationship. In polybutadiene, the extinction coefficient for the atactic 1,2 units was found to be lower than that of the syndiotactic 1,2 unit. These experimental facts lead to the conclusion that additivity of the extinction coefficients does not always hold for diene polymers. The deviation from the linear relation may be associated with regular sequences of one isomeric conformation in the chain.

INTRODUCTION

Diene monomers polymerize to give several types of addition, i.e., *trans*-1,4, *cis*-1,4, 3,4, and 1,2 units in the case of isoprene and *trans*-1,4, *cis*-1,4, and 1,2 units in the case of butadiene. Since the thermal and mechanical properties of diene polymers are affected by the distribution of the isomeric structural units along the polymer chain as well as the overall contents of these units, it is very important to characterize the microstructures of these polymers. At the present stage, the overall contents of the isomeric structural units in polybutadiene and polyisoprene have been determined by infrared spectroscopy, while a method of determining the distribution of these units has not yet been reported, as far as we know.

The infrared methods are based on the assumption that the extinction coefficient of a structural unit is always constant independently of the neighboring units. For accurate quantitative analysis of copolymers, how-

ever, we have to take into account the case in which the simple assumption
of additivity may not be applicable because of the influence of the neigh-
boring units upon the vibrations of the component unit in question.   In
fact, there are experimental data showing that infrared spectra of 1,4-
polyisoprene obtained by isomerization of either natural rubber or gutta
percha are somewhat different from the superposition of the spectra of the
starting polymers.[1]   These facts indicate that additivity does not always
hold for some characteristic absorption bands of diene polymers.   The
deviation from the simple additivity approximation suggests that the dis-
tribution of the isomeric structural units is reflected in the infrared spec-
trum.

NMR spectroscopy has been applied recently for determination of the
isomeric structure of polyisoprene[2-5] and butadiene–styrene copolymer.[6]
In some copolymers, ethylene–vinyl chloride,[7] styrene–methyl methac-
rylate,[8] etc., the NMR signals appear with fine structure characteristic of
dyads or triads of monomeric units, and give information concerning the
distribution of monomeric units.   In the case of diene polymers, such sig-
nal splitting due to dyads or triads of the isomeric structural units have not
yet been found.

In the present paper, the NMR spectra of polybutadiene and polyiso-
prene including deutero derivatives are studied.   On the basis of the NMR
measurements the additivity of the extinction coefficients of the infrared
absorption bands is examined.

EXPERIMENTAL

Samples

Polyisoprene.   A *cis*-1,4-polyisoprene was prepared with $TiCl_4$–Al-
$(C_2H_5)_3$ catalyst and *trans*-1,4-polyisoprene was prepared with VCl_3–Al-
$(C_2H_5)_3$ catalyst.[9]   Polyisoprene containing a relatively large amount of
3,4 units was prepared with $Ti(OC_4H_9)_4$–$Al(C_2H_5)_3$[10] or with n-C_4H_9Li–
$O(C_2H_5)_2$ catalyst.   For these samples the content of 1,2 units was con-
firmed to be negligibly small by the absence of the characteristic infrared
band at 909 cm^{-1}.

Polybutadiene.   Syndiotactic 1,2-polybutadiene and atactic 1,2-poly-
butadiene were prepared with $CoBr_2(PR_3)_2$–Al(alkyl)$_3$–H_2O catalyst.[11]
Atactic 1,2-polybutadiene was prepared with $Co_2(CO)_8$–$MoCl_5$ catalyst.[12]
Polybutadienes composed of *cis*-1,4 and 1,2 units and of *cis*-1,4, *trans*-1,4,
and 1,2 units were prepared with $CoBr_2(PR_3)_2$–$Al(C_2H_5)_3$–$(CH_3)_2S_2$–H_2O
catalyst[13] and n-C_4H_9Li–$O(C_2H_5)_2$ catalyst, respectively.

Isomerized Polymers.   Isomerization of polyisoprene and polybutadiene
was carried out according to the method developed by Cunneen.[14]   The
starting *cis*-1,4 or *trans*-1,4-polyisoprene was dissolved in benzene so as to
make a 2% polymer solution and thiobenzoic acid (2.5–10% of the weight of
polymer) was added.   The solution was irradiated with a low-pressure

mercury lamp for 1–24 hr in a nitrogen atmosphere. Then, the polymer was precipitated in methanol and dried under reduced pressure. The polymer was purified by repeated reprecipitation from a benzene solution with acetone. In the case of polybutadiene, phenyl disulfide was used as an initiator, and the polymer solution was irradiated with a high-pressure mercury lamp.

Deuterated Polymers. Butadiene sulfone, $CH_2CH=CHCH_2SO_2$, or isoprene sulfone, $CH_2C(CH_3)=CHCH_2SO_2$, was treated with D_2O in the presence of K_2CO_3 at 55°C for 14 hr followed by drying under reduced pressure. This procedure was repeated four times.[15] Then the deuterated sulfones were recrystallized twice from methanol. The decomposition of the deuterated sulfone was carried out in nitrogen at 120°C. Butadiene-1,1,4,4-d_4, $CD_2=CHCH=CD_2$, or isoprene-1,1,4,4-d_4, $CD_2=C(CH_3)-CH=CD_2$, was polymerized with the catalysts described above.

NMR and Infrared Measurements

High resolution NMR spectra were measured with a Japan Electron Optics Laboratory 4H-100 (100 MHz) NMR spectrometer. Solutions of the polymer samples (3.5 to 7% by weight) were prepared in deuterochloroform for polybutadiene or in benzene for polyisoprene. Measurements were made at 60°C by using tetramethylsilane as internal standard.

Infrared spectra were measured with a Japan Spectroscopic Co. DS-402G double beam grating spectrophotometer. Compensation for the solvent, CS_2 or CCl_4, was made by placing a cell of appropriate thickness filled with the same solvent in the reference beam.

RESULTS

Determination of Isomeric Structural Units by NMR

The NMR spectra of cis-1,4 and trans-1,4-polybutadiene exhibit little difference in the chemical shifts of corresponding signals, as is shown in Figures 1A and 1B. Any signal splitting due to cis-1,4 and trans-1,4 units is not detected in the spectra of the mixture of cis-1,4 and trans-1,4-polybutadiene homopolymers or in the isomerized polybutadiene samples (Fig. 1C). The NMR signals of both syndiotactic and atactic 1,2-polybutadienes (Fig. 2) are divided into four groups. The integrated intensity ratio of these four groups varies with variation of the content of 1,2 units. With decreasing the content of 1,2 units, the signals become broader, but no additional signal appears. The same is the case for the mixtures of 1,2 and 1,4-polybutadiene homopolymers. This shows that the observed signals around 5.40 and 2.10 ppm (δ) are both due to overlapping signals for 1,2 and 1,4 units.

The assignments of the NMR signals were made by taking account of the data of polybutadiene-1,1,4,4-d_4. The signal at 2.0–2.1 ppm in cis-1,4 and

trans-1,4-polybutadienes vanishes in deutero derivatives. As for deutero 1,2-polybutadiene, the signals at 1.2 ppm and at 4.9–5.4 ppm vanish (Fig. 2*C*). From these data, the assignments of the signals are obtained as given in Table I.
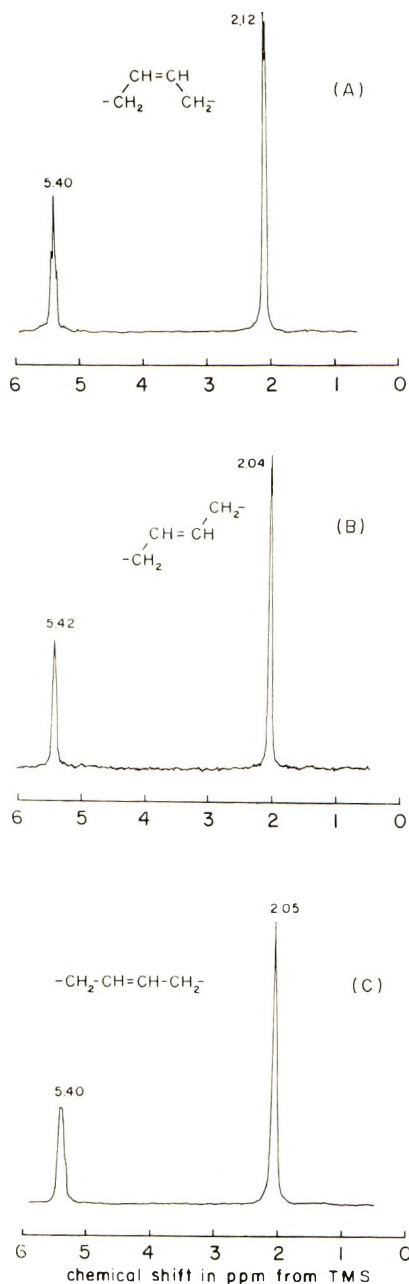
Fig. 1. NMR spectra of 1,4-polybutadiene measured on CDCl₃ solutions at 50°C: (A) *cis*-1,4-polybutadiene; (B) *trans*-1,4-polybutadiene; (C) isomerized polybutadiene.

On the basis of the assignments, the contents of 1,2 and 1,4 units can be calculated by the following equation.

$$\frac{I(1.20)}{I(2.10)} = \frac{2[1,2]}{[1,2] + 4[1,4]} \Bigg\}$$

$$[1,2] + [1,4] = 1 \Bigg)$$

(1)
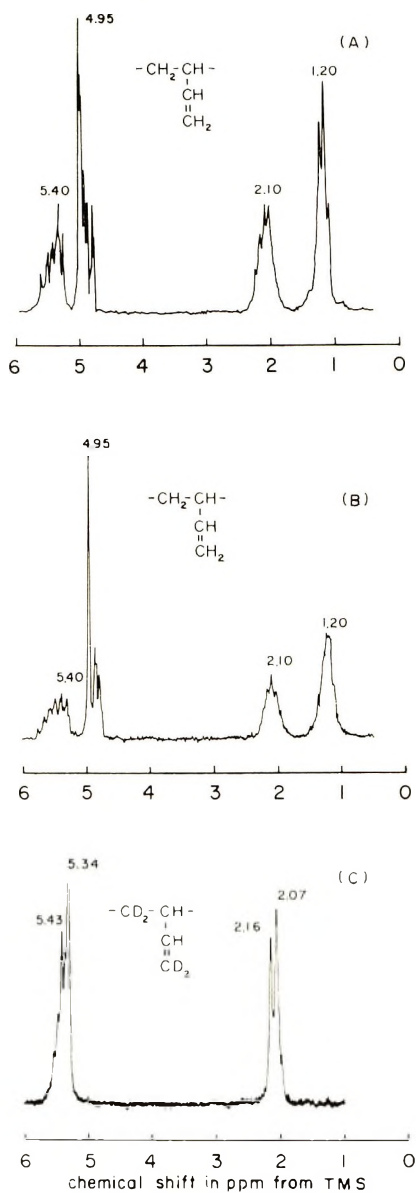
Fig. 2. NMR spectra of 1,2-polybutadiene measured on CDCl₃ solutions at 50°C: (A) syndiotactic 1,2-polybutadiene; (B) atactic 1,2-polybutadiene; (C) syndiotactic 1,2-polybutadiene-1,1,4,4-d₄.

TABLE I
NMR Signal Assignments for Polybutadiene
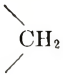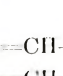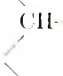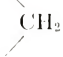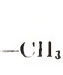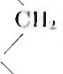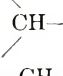
Unit	Type of proton	δ, ppm
1,4	=CH—	5.40
	$\diagdown$ CH$_2$ $\diagup$	$\{2.12\ (cis\text{-}1,4)$ $\{2.04\ (trans\text{-}1,4)$
1,2	=CH—	5.04
	=CH$_2$	4.80–5.01
	$\diagdown$ CH— $\diagup$	2.10
	$\diagdown$ CH$_2$ $\diagup$	1.20

TABLE II
NMR Signal Assignments for Polyisoprene

Unit	Type of proton	δ, ppm
1,4	=CH—	5.24
	$\diagdown$ CH$_2$ $\diagup$	$\{2.19\ (cis\text{-}1,4)$ $\{2.14\ (trans\text{-}1,4)$
	—CH$_3$	$\{1.74\ (cis\text{-}1,4)$ $\{1.65\ (trans\text{-}1,4)$
3,4	=CH$_2$	4.81
	$\diagdown$ CH$_2$ $\diagup$	1.50
	$\diagdown$ CH— $\diagup$	2.21
	—CH$_3$	1.69

Here, as well as in the following equations, the bracket denotes the mole fraction of the respective structural unit indicated and $I(\delta)$ represents the relative integrated intensity of the signal with chemical shift δ.

The NMR spectra of cis-1,4 and trans-1,4-polyisoprene are shown in Figure 3. The signals at 1.65 and 1.74 ppm in the isomerized polyisoprene (Fig. 3C) are due to trans-1,4 and cis-1,4 units, respectively, and this splitting pattern is identical with that of the mixtures containing cis-1,4 and trans-1,4-polyisoprene homopolymers. The signal at 2.1–2.2 ppm in cis-1,4 and trans-1,4-polyisoprenes vanishes in the case of cis-1,4 and trans-1,4-polyiso-prene-1,1,4,4-d_4. In Figure 4 the NMR spectra of polyisoprene containing 65% of 3,4 units is compared with that of deutero-polyisoprene prepared with the same catalyst. In the case of deutero-polyisoprene, the signals at
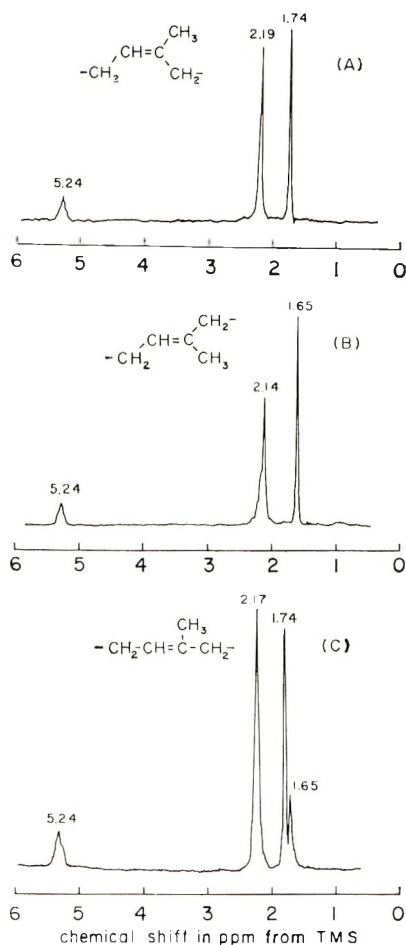
Fig. 3. NMR spectra of 1,4-polyisoprene measured on C_6H_6 solutions at 60°C: (A) cis-1,4-polyisoprene; (B) trans-1,4-polyisoprene; (C) isomerized polyisoprene.

4.81 ppm and 1.50 ppm vanish and the signal at 2.2 ppm appears clearly owing to disappearance of the overlapping signal from 1,4 unit. On the basis of these data, the assignments are obtained as given in Table II. These assignments are in accord with those obtained by using low molecular weight olefins as model compounds.[3-5]

On the basis of the assignments, the contents of cis-1,4, trans-1,4, and 3,4 units can be calculated by eq. (2):

$$\frac{I(4.81)}{I(5.24)} = \frac{2[3,4]}{[cis\text{-}1,4] + [trans\text{-}1,4]}$$

$$\frac{I(1.70)}{I(1.65\text{-}1.69)} = \frac{[cis\text{-}1,4]}{[trans\text{-}1,4] + [3,4]} \qquad (2)$$

$$[cis\text{-}1,4] + [trans\text{-}1,4] + [3,4] = 1$$
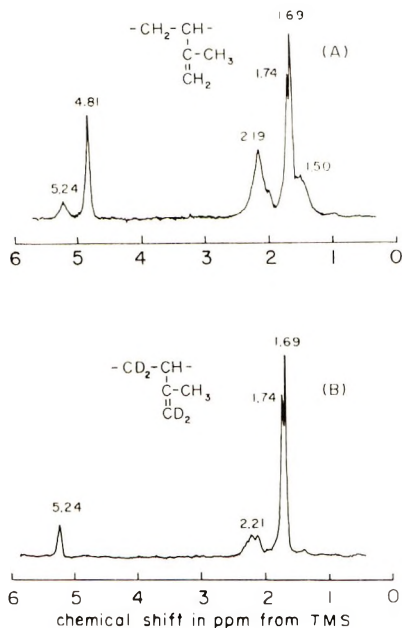
Fig. 4. NMR spectra of polyisoprene containing 65% 3,4 units, measured on C_6H_6 solutions at 60°C: (A) 3,4-polyisoprene; (B) 3,4-polyisoprene-1,1,4,4-d_4.

The content of 1,2 units is negligibly small in these polymers, as was indicated in the preceding section.

Extinction Coefficients of the Isomeric Structural Units

Polyisoprene shows absorption bands at 889 and 840 cm^{-1} characteristic of 3,4 and 1,4 units, respectively (Fig. 5).   The absorption bands at 1376 and 1385 cm^{-1} have been used for the determination of the content of cis-1,4 and trans-1,4 units, respectively.[16]   For these absorption bands the peak intensities are measured by the use of the baseline method as shown in Figures 5 and 6.

Polybutadiene exhibits the absorption band at 909 cm^{-1} characteristic of 1,2 unit (Fig. 7).   In the case of this band, the baseline method was not used because of very weak background absorption.

Extinction Coefficient of 3,4 Unit at 889 cm^{-1} in Polyisoprene.   The extinction coefficient at 889 cm^{-1} per monomeric unit is given by the equation

$$\epsilon_{889} = \epsilon_{3,4}\cdot[3,4] + \epsilon_{cis-1,4}\cdot[cis-1,4] + \epsilon_{trans-1,4}\cdot[trans-1,4] \qquad (3)$$

The plot of the extinction coefficient of the monomeric unit at 889 cm^{-1} versus the content of 3,4 units gives a straight line passing through the origin, as shown in Figure 8.   From this figure the absorption of cis-1,4 and trans-1,4 units at 889 cm^{-1} was found to be very small compared with that
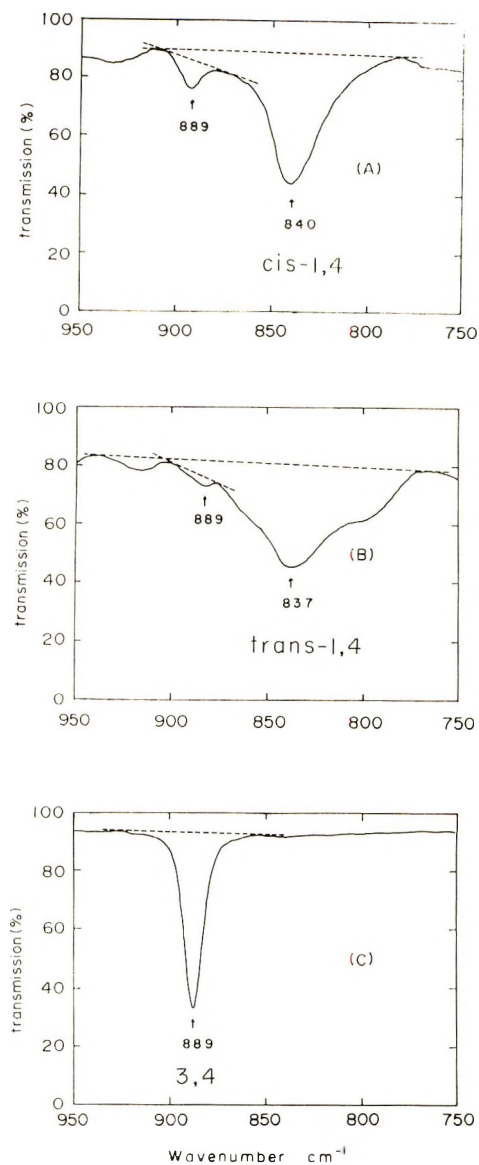
Fig. 5. Infrared spectra of CS₂ solutions of polyisoprene at room temperature: (A) *cis*-1,4-polyisoprene; (B) *trans*-1,4-polyisoprene; (C) polyisoprene containing 65% 3,4 units.

of 3,4 unit, which was estimated to be 177 l./mole-cm. The peak extinction coefficients at 889 cm^{-1} of the lower molecular weight olefins as model compounds for 3,4 unit are measured to be 175, 176, and 190 l./mole-cm for 2-methyl-1-butene, 3-methyl-1-pentene, and 2,3-dimethyl-1-butene, respectively. These results suggest that the extinction coefficient for 3,4 unit at 889 cm^{-1} is independent of the neighboring units in the polymer chain.
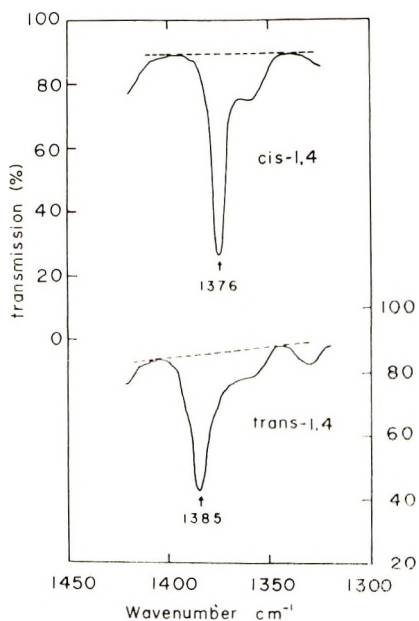
Fig. 6. Infrared spectra of CCl₄ solutions of 1,4-polyisoprene at room temperature: (A)
cis-1,4-polyisoprene;   (B) trans-1,4-polyisoprene.
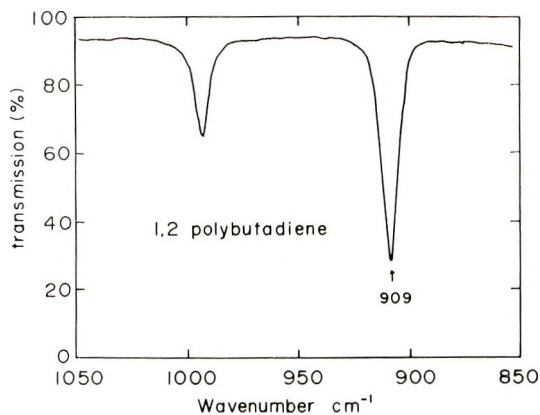
Fig. 7. Infrared spectrum of CS₂ solution of 1,2-polybutadiene at room temperature.

**Extinction Coefficients of 1,4 Unit at 1376 and 1385 cm⁻¹ in Poly-
isoprene.**   In the case of mixtures of cis-1,4 and trans-1,4-polyisoprene
homopolymers, the absorption peaks at 1376 and 1385 cm⁻¹ are separated,
and the peak intensities of both bands can be measured.   On the other
hand, the separation of the two peaks is not clear in the case of the isomer-
ized polyisoprenes, and the weaker band appears as a shoulder.   Accord-
ingly, only the intensity of the stronger band was measured; 1385 cm⁻¹
band for the high-trans-1,4 sample and 1376 cm⁻¹ band for the low-trans-1,4
sample.
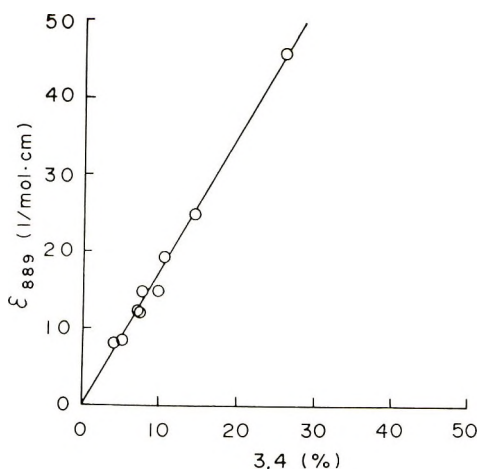
Fig. 8. Correlation between the extinction coefficient per monomeric unit at 889 cm^{-1} in polyisoprene and content of 3,4 units determined by NMR.
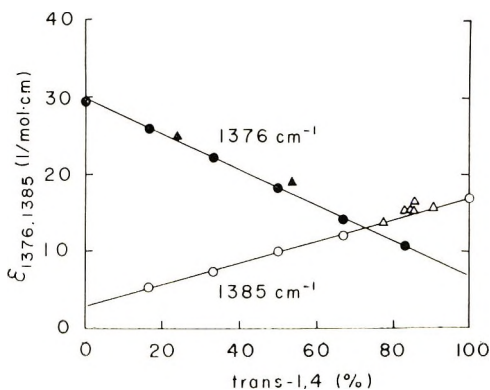
Fig. 9. Extinction coefficients per monomeric unit at 1385 cm^{-1} and 1376 cm^{-1} in polyisoprene vs. trans-1,4 content determined by NMR: (○●) for mixtures of cis-1,4 and trans-1,4 homopolymers, (△▲) for isomerized polyisoprenes.

In Figure 9, the extinction coefficients of 1385 and 1376 cm^{-1} bands per monomeric unit are plotted against the content of trans-1,4 units determined by the NMR method. The linear relations for both the mixtures and the isomerized samples indicate additivity of the extinction coefficients of the absorption bands at 1385 and 1376 cm^{-1} for cis-1,4 and trans-1,4 units.

Extinction Coefficient of 1,4 Unit at 840 cm^{-1} in Polyisoprene.   The absorption band characteristic of 1,4 unit shows a peak at 840 cm^{-1} for cis-1,4-polyisoprene and at 837 cm^{-1} for trans-1,4-polyisoprene. However, both the mixtures of cis-1,4 and trans-1,4-polyisoprene homopolymers and the isomerized polyisoprenes show only one peak at 840 cm^{-1}. In Figure 10, the extinction coefficients at 840 cm^{-1} per monomeric unit are plotted
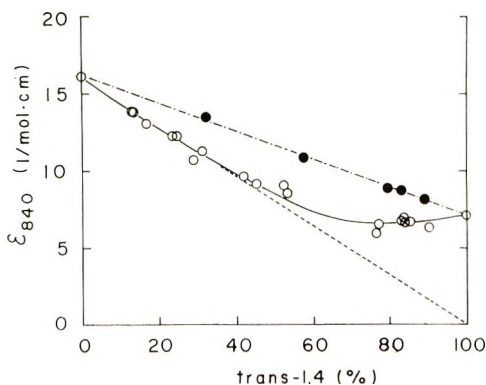
Fig. 10. Correlation between the extinction coefficient per monomeric unit at 840 cm^{-1} in polyisoprene and the *trans*-1,4 content determined by NMR: (O) for isomerized polyisoprenes; (●) for mixtures of *cis*-1,4 and *trans*-1,4 homopolymers.
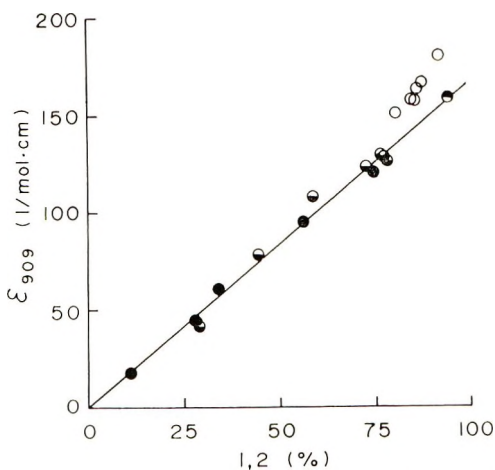
Fig. 11. Correlation between the extinction coefficient per monomeric unit at 909 cm^{-1} in polybutadiene and content of 1,2 units determined by NMR: (O) syndiotactic 1,2-polybutadiene; (◓) atactic 1,2-polybutadiene; (◒) polybutadiene containing *cis*-1,4 and 1,2 units; (●) polybutadiene containing *cis*-1,4, *trans*-1,4, and 1,2 units.

against the content of *trans*-1,4 units determined by NMR. A linear relation is obtained only for mixtures of *trans*-1,4 and *cis*-1,4 polyisoprene homopolymers. The isomerized samples, on the other hand, give a curve with the minimum at about 80% *trans*-1,4 units. The extinction coefficient at 840 cm^{-1} per monomeric unit is given by eq. (4), since the absorption of 3,4 unit at 840 cm^{-1} is negligibly small, as is shown in Figure 5C.

$$\epsilon_{840} = \epsilon_{trans\text{-}1,4} \cdot [trans\text{-}1,4] + \epsilon_{cis\text{-}1,4} \cdot [cis\text{-}1,4]$$

$$= \epsilon_{trans\text{-}1,4} \cdot [trans\text{-}1,4] + \epsilon_{cis\text{-}1,4} \cdot (1 - [trans\text{-}1,4]) \qquad (4)$$

If $\epsilon_{trans\text{-}1,4}$ and $\epsilon_{cis\text{-}1,4}$ are constant, as is the case for mixtures of homopolymers, the correlation between ϵ_{840} and the content of $trans$-1,4 units should be linear. On the other hand, it is clear that the extinction coefficient for cis-1,4 or $trans$-1,4 units at 840 cm^{-1} varies with the overall content of $trans$-1,4 units in the isomerized polyisoprene.

Extinction Coefficient of 1,2 Unit at 909 cm^{-1} in Polybutadiene.   In Figure 11 the extinction coefficient of polybutadiene is plotted against the content of 1,2 units.   A linear relation is obtained only for atactic samples. For syndiotactic samples, the extinction coefficient is always higher than the corresponding value for atactic 1,2-polybutadiene.   These facts indicate that the extinction coefficient for 1,2 unit is affected by the configuration of the polymer chain.

DISCUSSION

The deviation from simple additivity of the infrared extinction coefficients for the 840 cm^{-1} band of 1,4-polyisoprene suggests that the distribution of cis-1,4 and $trans$-1,4 units in the polymer chain has some effect on the absorption intensity of the infrared band.   The nonadditivity of the extinction coefficients at 840 cm^{-1} in polyisoprene was previously suggested by Golub and Heller[17] on the basis of an experimental result obtained by a different method: a nonlinear decrease in the absorbance of the 840 cm^{-1} band for hevea and balata with consumption of 1,4 double bonds by progressive hydrochlorination.   These facts should be taken into account, when this band is used as a measure of cis-1,4 and $trans$-1,4 content in quantitative analysis.

The $trans$-1,4-polyisoprene homopolymer is highly crystalline at room temperature.   The crystallinity of the isomerized samples obtained from $trans$-1,4-polyisoprene decreases drastically with decrease in $trans$-1,4 content.   It was confirmed by x-ray diffraction that isomerized polyisoprene samples containing less than 80% $trans$-1,4 units do not crystallize at room temperature.   This suggests that the isomerization gives copolymer in which cis-1,4 and $trans$-1,4 units are distributed randomly along the chain. In the case of polybutadiene, similar random isomerization has been reported by Berger and Buckley.[18]

According to the results of the NMR study of the photochemical reaction of polyisoprene in the solid state by Golub and Stephens,[19] an appreciable loss of 1,4-double bonds was deduced from the appearance of the signals due to the vinylidene or cyclopropyl groups.   In the present case, however, no signal due to these groups is detectable in the NMR spectrum of the isomerized samples as shown in Figure 3C; and so it may not be necessary to consider the possibility of loss of 1,4 units.

In general, the absorption intensity of the so-called crystalline band is closely related to the length of sequences of the same units.   Thus some crystalline bands of isotactic polymers observed in the spectra of dilute solution at low temperatures have been ascribed to the regular helical conformations of short length present in solution.[20,21]
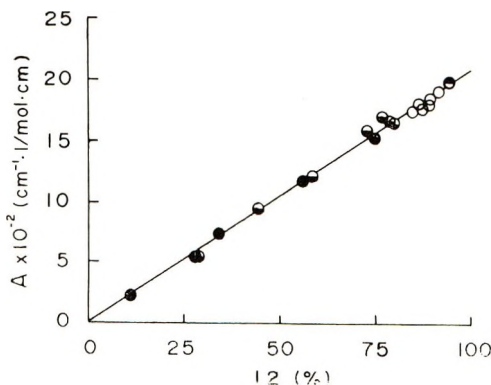
Fig. 12. Plot of integrated extinction coefficient versus content of 1,2 units determined by NMR.   Samples are the same as in Fig. 11.

For the isomerized samples, a plot of the extinction coefficient against *trans*-1,4 content falls on a straight line for *trans*-1,4 content less than 50%, and the line gives zero for the extrapolated value at 100% *trans*-1,4 units, as shown by the dashed line in Figure 10.   This means that we may regard the extinction coefficient at 840 cm^{-1} as zero for *trans*-1,4 units in very short sequences.

It should be noted that there are no notable differences in the shape and the half-intensity width of the absorption near 840 cm^{-1} in mixtures of *cis*-1,4 and *trans*-1,4-polyisoprene homopolymers and the isomerized polymers. Therefore, the discussion described above should also be applicable to integrated absorption intensities as well as peak intensities.

The absorption band at 909 cm^{-1} in polybutadiene is another example in which the additivity of the extinction coefficient does not hold.   The syndiotactic and atactic samples give different plots of ϵ versus percent of 1,2 units, as is shown in Figure 11.   The extinction coefficient for 1,2 unit at 909 cm^{-1} is estimated to be 167 l./mole-cm for atactic 1,2 samples and 192 l./mole-cm for syndiotactic 1,2 samples.   The half-intensity width $\Delta_{1/2}$ of this 909 cm^{-1} band is evaluated as 8.0 cm^{-1} for atactic 1,2 samples and 6.9 cm^{-1} for syndiotactic 1,2 samples.   If we assume a Lorentz function for the absorption curve, the integrated extinction coefficient A is given by

$$A = 1/2\epsilon\Delta_{1/2} \qquad (5)$$

where ϵ is the extinction coefficient at the peak.[22]   By the use of this equation, the integrated extinction coefficient per monomeric unit at 909 cm^{-1} has been calculated for these samples.   The points fall on a common straight line for the syndiotactic 1,2 and atactic 1,2 samples, as is shown in Figure 12.   Consequently, the integrated extinction coefficient for 1,2 unit is constant regardless of the tacticity of the chain.

From the above results, the nonadditive behavior of the extinction coefficient was clarified for some characteristic absorption bands.   These

findings indicate that great care must be taken in determining isomeric structural units by the infrared method.

References

1. M. A. Golub, *J. Polym. Sci.*, **36**, 523 (1959).

2. M. A. Golub, S. A. Fuqua, and N. S. Bhacca, *J. Amer. Chem. Soc.*, **84**, 4981 (1962).

3. H. Yu. Chen, *Anal. Chem.*, **34**, 1134 (1962).

4. F. Schué and J-P. Dole-Robbe, *Bull. Soc. Chim. France*, **1963**, 975.

5. J-P. Kistler, G. Friedmann, and B. Kaemp, *Bull. Soc. Chim. France*, **1967**, 4759.

6. W. L. Senn, Jr., *Anal. Chim. Acta*, **29**, 505 (1963).

7. J. Schaefer, *J. Phys. Chem.*, **70**, 1975 (1966).

8. K. Ito and Y. Yamashita, *J. Polym. Sci. B*, **3**, 625 (1965).

9. G. Natta, L. Porri, P. Corradini, and D. Morero, *Chim. Ind. (Milan)*, **40**, 362 (1958).

10. G. Natta, L. Porri, and A. Carbonaro, *Makromol. Chem.*, **77**, 126 (1964).

11. Y. Takeuchi, M. Ichikawa, and K. Mori, paper presented at the 15th Polymer Symposium, Osaka, Japan, 1965.

12. S. Otsuka, K. Mori, and M. Kawakami, *Kogyo Kagaku Zasshi*, **67**, 1952 (1964).

13. Y. Takeuchi and M. Ichikawa, paper presented at the 21th Annual Meeting, the Chemical Society of Japan, Tokyo, Japan, 1969.

14. J. I. Cunneen, G. M. C. Higgins, and W. S. Watson, *J. Polym. Sci.*, **40**, 1 (1959).

15. S. Ikeda, M. Yogo, and K. Morifuji, paper presented at the 13th Annual Meeting of the Society of Polymer Science, Japan, Kyoto, 1964.

16. F. Ciampelli, D. Morero, and M. Cambini, *Makromol. Chem.*, **61**, 250 (1963).

17. M. A. Golub and J. Heller, *J. Polym. Sci. B*, **2**, 723 (1964).

18. M. Berger and D. J. Buckley, *J. Polym. Sci. A*, **1**, 2945 (1963).

19. M. A. Golub and C. L. Stephens, *J. Polym. Sci. A-1*, **6**, 763 (1968).

20. M. Takeda, K. Iimura, and S. Ochiai, *J. Polym. Sci. B*, **4**, 155 (1966).

21. F. A. Bovey, F. P. Hood, III, E. W. Anderson, and L. C. Synder, *J. Chem. Phys.*, **42**, 3900 (1965).

22. D. A. Ramsay, *J. Amer. Chem. Soc.*, **74**, 72 (1952).

Chain Folding in Poly-*Trans*-1,4-Butadiene Crystals Grown From Various Solvents

J. M. STELLMAN and A. E. WOODWARD,

Department of Chemistry, The City College of The City University of New York, New York 10031

Synopsis

Crystals of poly-*trans*-1,4-butadiene of uniform size have been grown from three solvents (*n*-heptane, methyl isobutyl ketone, and toluene) by using a minimum dissolution temperature technique. The percentage of double bonds available for reaction in the crystals was determined by epoxidation in suspension; crystal thicknesses were measured by electron microscopy. These values were used to calculate the number of monomer units per fold. The number of available double bonds was found to increase with decreasing molecular weight, evidence for the presence of non-reentrant chains (cilia) at the crystal surfaces. The nature of the chain fold in poly-*trans*-1,4-butadiene crystals is discussed.

Introduction

In a previous publication[1] the results of a quantitative investigation of chain folding in poly-*trans*-1,4-butadiene (PTBD) crystals, obtained by precipitation from dilute *n*-heptane solution, were presented and briefly discussed. In that study it was reported that 14% of the double bonds in the crystals when suspended in benzene were available for an epoxidation reaction. This led to the conclusion that, in general, the chain folds at the surfaces of the crystals are regularly reentrant. However, there was a question as to the effect of cilia (loose chain ends at the surface of the crystal) on the epoxidation results. Further work has now been carried out to clarify that point.

Hexagonal-shaped crystals of PTBD can be obtained from various solvents in addition to *n*-heptane, and it has been shown that the dynamic mechanical behavior of mats of these crystals depends on the solvent used.[2] In order to obtain information concerning the effect of solvent on the fold structure of PTBD crystals, the number of available double bonds was determined for crystals grown from *n*-heptane, methyl isobutyl ketone (MIBK), and toluene.

Experimental

Samples of PTBD supplied by Ube Kosan Co., Ltd. of Japan (PTBD-K) and by Uniroyal Inc. (PTBD-U) were found by infrared analysis to have

59

>95% *trans* content. For the PTBD-K, as received, a number-average molecular weight $\bar{M}_n$ of 8670 ($\pm 10\%$) was reported by DeBell and Richardson Co., Inc. by using a Hitachi Perkin-Elmer vapor pressure osmometer. The intrinsic viscosity in chloroform at 30°C was found to be 1.53 dl/g, which leads[3] to a viscosity-average molecular weight $\bar{M}_v$ of 92,000. For a sample of PTBD-K crystals recovered from *n*-heptane solution, as described below, $\bar{M}_n$ was found to be 36,900 ($\pm 10\%$). The intrinsic viscosity of PTBD-U in chloroform at 30°C was 0.32, yielding an $\bar{M}_v$ of 11,000.

Crystals were prepared in the following manner. The polymer was dissolved at the minimum dissolution temperature for that particular system, the solution (0.02% by weight) filtered, the resulting mixture reheated to the original dissolution temperature, and the solution then placed in a constant temperature bath set low enough to produce a large quantity of crystals of uniform size. Then, the crystals were separated from the growth liquid by hot filtration, resuspended in benzene, placed in a cold box at 0°C, and *m*-chloroperbenzoic acid (MCPBA) was added. The amount of MCPBA used was varied from run to run but was at least enough to react with 18–26% of the total double bonds in the polymer sample; however, for the one run on crystals of PTBD-U the amount of MCPBA added was 135% of the amount of double bonds present and for one PTBD-K–heptane run and one PTBD-K–MIBK run it was 41–42%. The epoxidation reaction was followed by iodometric titration of the unreacted peracid, and in each run a control solution was also titrated. The reaction was followed for at least 48 hr after no further disappearance of acid was noted. The amount of polymer originally present was determined for the PTBD-K–heptane runs by difference after finding the amount of polymer remaining in the mother liquor following the hot filtration. For the other crystal samples, weighing of the crystal mats after washing, filtering, and drying the reaction mixture was employed.

Small samples were removed from the reaction mixture at various time intervals for electron microscope investigation. Both selected-area electron diffraction and transmission micrographs were obtained with a Phillips EM 300 instrument. Crystal thicknesses were estimated from shadow castings, at least six crystals from each preparation being measured.

Results

Crystals were prepared from PTBD-K by using three solvents and of PTBD-U from one solvent, as noted in Table I. Essentially the same dissolution temperature–precipitation temperature regimes were used for the PTBD-K–*n*-heptane (78°C/63.5°C) and PTBD-K–MIBK (92°C/73°C) crystal preparations as were employed previously by Tatsumi et al.[2] The minimum dissolution temperature in *n*-heptane for PTBU-U was 9°C below that for PTBD-K, an effect believed to be due to the lower molecular weight of the former.

TABLE I

Determination of Available Double Bonds on PTBD Crystals

Sample	Solvent	(Minimum) dissolution temperature, °C	Precipitation temperature, °C	Precipitate, %	Crystal thickness, Å	No. of epoxidation determinations	Double bonds reacted, %	No. monomer units/fold	
								Uncorr.	Corr.[a]
PTBD-K	Heptane	78	63.5	78	140 ± 10	3	14	$4\frac{1}{2}$	$3\frac{1}{2}$
PTBD-K	MIBK	92	73	68	130 ± 15	4	22	6	5
PTBD-K	Toluene	50	23	76	105 ± 10	2	18	4	$3\frac{1}{2}$
PTBD-U	Heptane	69	53	13	95 ± 10	1	28	$5\frac{1}{2}$	$3\frac{1}{2}$

[a] Value corrected for double bonds in chain ends (see text).
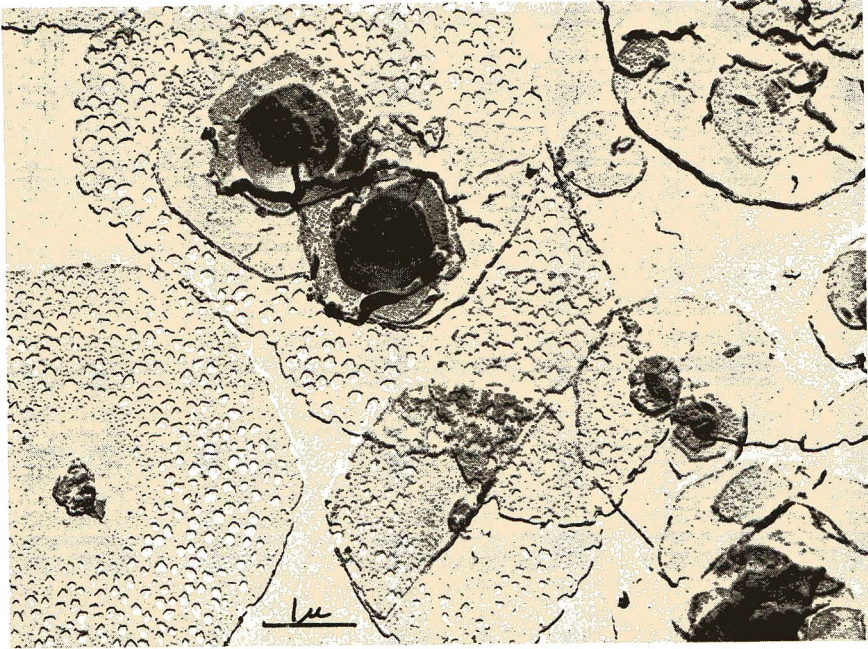
Fig. 1. PTBD-K crystals from MIBK; dissolved at 92°C and precipitated at 73°C.
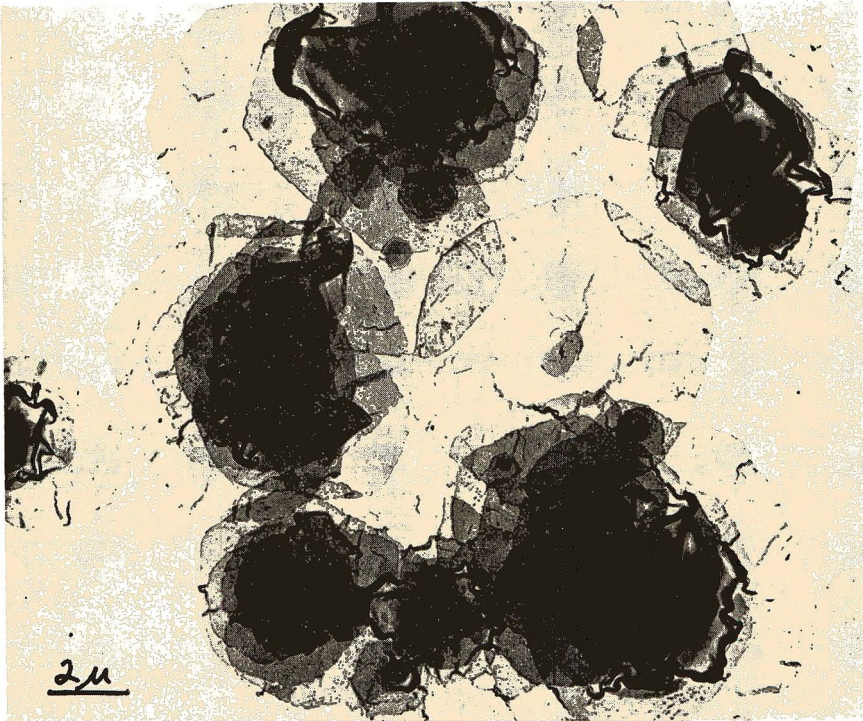
Fig. 2. Same as Fig. 1; different preparation.
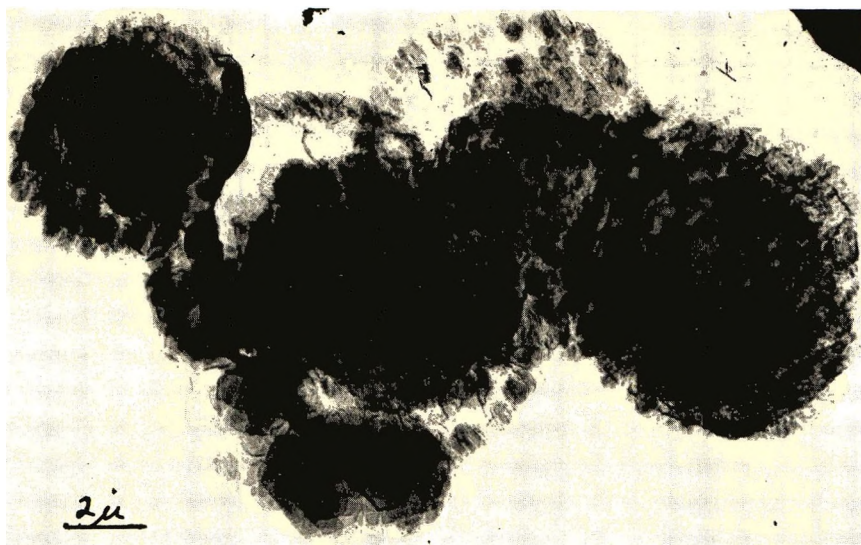
Fig. 3. PTBD-U crystals from *n*-heptane; dissolved at 69°C, precipitated at 53°C.

The percentage of polymer precipitated during the single-crystal prepara-
tion from a solution of the bulk material is similar for PTBD-K from the
three different solvents but is much lower for the PTBD-U–heptane sys-
tem (Table I, column 5). The crystallization process for PTBD-K does
lead to a fractionation of the bulk material as is evident from the change
in $\bar{M}_n$. The bulk PTBD-U is believed to be less polydisperse than the
bulk PTBD-K, but it also has a lower $\bar{M}_v$, which may account for its
higher solubility in *n*-heptane at the precipitation temperature employed.

Electron micrographs of PTBD crystals obtained from MIBK and
heptane are given in Figures 1–3 herein and Figures 1 and 2 of a previous
communication.[1] Due to the poor contrast electron micrographs of the
toluene grown crystals are not shown. It was found in this study that a
large number of the PTBD-K crystals from MIBK have holes and/or
rough surfaces. A representative field showing this is given in Figure 1.
These effects were incurred during the crystal preparation and/or isola-
tion and are not due to subsequent thermal treatments known to yield
thicker hole-ridden crystals.[4] It was also found that the PTBD-K crys-
tals from toluene were consistently smaller by a factor of about 2 than
those from *n*-heptane and MIBK.

Additional experiments in which the dissolution temperature was varied
were carried out for PTBD-K crystals from *n*-heptane and MIBK. It
was found that an increase in dissolution temperature in the 92–103°C
range for MIBK-grown crystals at 73°C resulted in an increase in crystal
size, average diameters of 3, 8 and 48 μ being observed when dissolution
temperatures of 92, 97, and 103°C, respectively, were used. For PTBD-K
crystals from heptane, a change in dissolution temperature from 78 to
88°C resulted in a change of crystal diameter from 4 to 20 μ when the

precipitation temperature was 63.5°C. The same effect was reported[5] previously for polyethylene crystals, although it was the temperature at which the precipitate was redissolved which was found to be critical.

An apparent change in crystal thickness with crystallization conditions is seen on comparing the values in Table I. However, the values given for the PTBD-K crystals from n-heptane and MIBK may be too high because of curling at the edges of the n-heptane crystals and variations in thickness due to surface roughness for the MIBK crystals, although attempts were made to avoid such effects in carrying out the thickness measurements. A crystal thickness value for PTBD-K crystals from n-heptane was given earlier as 100 Å. The higher value given here was obtained after further thickness determinations.

Selected-area electron diffraction patterns were obtained for all preparations before and after reaction and in all cases the pattern reported earlier[2] for the low temperature form of PTBD was found.

The results of three separate epoxidation runs in which the number of available double bonds was determined by reaction with m-chloroperbenzoic acid (MCPBA) for crystals grown from n-heptane solutions of PTBD-K were given previously.[1] It was found that although there were differences in the rates of double bond disappearance at times below 100 hr, a leveling off at 14% double bonds reacted occurred at later times. This same type of leveling-off behavior was generally observed for runs on the other crystal preparations. The number of runs and the mean values of the percentage of double bonds available for reaction are given in Table I for the four systems studied.

Discussion

The crystal structure of PTBD has been reported[6] as monoclinic with a chain repeat distance of 4.83 Å. Division of the crystal thickness by this repeat distance gives the number of monomer units in one traverse of a chain between the two fold surfaces of the crystal. Multiplication of this number of monomer units by the fraction of double bonds available yields the number of monomer units at all the surfaces per chain between the fold surfaces. Assuming that these reactive monomer units reside in folds (i.e., the amount in chain ends, tie molecules and on the sides of the crystals is considered negligible) values of 4–6 monomer units per fold are obtained from the experimental results (Table I). (The difference between the value given in Table I for PTBD-K crystals from n-heptane and that given earlier[1] is due to the difference in crystal thickness.)

A calculation of the surface area of a hexagonal crystal 100 Å thick and 2 μ on a side shows that the total area of six sides is only 0.05% of that of of the two large faces and indicates that the double bonds exposed on the crystal sides are negligible as compared to those at the two surfaces. Therefore, for the n-heptane-grown crystals, and even for the smaller toluene-grown crystals, this effect is negligible. For crystals with holes

a larger number of double bonds would be exposed, the amount depending on the number and size of the holes.

An estimate of the number of monomer units in non-reentrant chains (cilia) is obtained by dividing an average number of total monomer units in two cilia by the number-average degree of polymerization. The average length of cilia is taken as one-half the length of the chains in the body of the crystal between fold surfaces.[7] For $\overline{M}_n \leq 11{,}000$, the number of monomer units in cilia is thereby calculated to be $\geq 10\%$ and for $\overline{M}_n = 37{,}000$ it is calculated to be 3%. Using the first value to correct the number of monomer units per fold for the PTBD-U crystals and the second to correct those for the PTBD-K crystals yields the values for the corrected number of monomer units per fold is given in Table I. In making these corrections, in addition to the assumptions above, it is further assumed (1) that $\overline{M}_n$ of the PTBD-U chains in the crystals is equal to $\overline{M}_v$ of the bulk material and (2) that $\overline{M}_n$ of PTBD-K in crystals grown from toluene and MIBK is the same as that for crystals from n-heptane.

It is apparent from the experimental results that PTBD-K crystals from MIBK have a greater number of available double bonds than those grown from either n-heptane or toluene. This greater number can be directly linked with the presence of holes in these crystals and the observed surface roughness which suggests a prevailing surface disorder (see Fig. 1).

There has been considerable discussion concerning the tightness and the reentry character of chain folds in polymer crystals.[8-13] For this reason it is of interest to compare the values of the number of monomer units per chain fold given in Table I with the minimum number necessary to connect two adjacent chains in a crystal with the structure given for the low temperature form of PTBD. The unit cell for the low-temperature form of PTBD is believed[6] to contain four repeat units, with the distance between units I and IV being larger than the other interchain distances by at least 50%. Excluding the distance between units I and IV, the distance between units at the same elevation in the cell ranges from 4.3 to 5.0 Å, which at the lower extreme is shorter than and at the upper extreme is longer than the length of a repeat unit. Also, a given atom in the repeat unit is not necessarily coplanar with the same atom in an adjacent chain. Of the twenty possible connections between adjacent chains (ruling out I–IV) seven are found to include only one double bond and 13 to include two double bonds. It is therefore concluded that the average number of double bonds necessary for the tightest reentrant fold will be between 1.5 and 2. Comparison of these values with those in Table I leads us to the conclusion that reentrant folding is highly probable, although some fold looseness does occur.

In an earlier study of the dynamic mechanical behavior of crystal mats[2] it was postulated that crystals from a "good" solvent, such as benzene, should have looser folds than crystals from "poor" solvents, such as n-peptane, a "good" solvent being defined as one in which the particular polymer material dissolves at a relatively low temperature. However,

in that investigation[2] and in the present work the temperature of dissolution and the precipitation temperature were varied according to the solvent used, being lower the better the solvent. Since the dissolution temperatures employed were close to or at the minimum dissolution temperature for the particular solvent, the solvent–polymer interactions in the various solutions should be approximately the same. Furthermore, at any temperature at which precipitation takes place all the liquids used are "poor" solvents and therefore the effects of solvation are minimal. In light of the above, differences in fold structure for crystals grown from the various single liquid systems are not expected to be large under the conditions used in this or the previous investigation.[2]

References

1. J. M. Stellman and A. E. Woodward, *J. Polym. Sci. B*, **7**, 755 (1969).

2. T. Tatsumi, T. Fukushima, K. Imada, and M. Takayanagi, *J. Macromol. Sci. (Phys.)*, **B1**, 459 (1967).

3. R. Endo, *Nippon Gomu Kyokaishi*, **34**, 527 (1961).

4. P. H. Geil, *Polymer Single Crystals*, Interscience, New York, 1963.

5. P. J. Blundell and A. Keller, *J. Macromol. Sci.-(Phys.)*, **B2**, 301 (1968).

6. S. Iwayanagi, I. Sakurai, T. Sakurai, and T. Seto, *J. Macromol. Sci. (Phys.)*, **B2**, 163 (1968).

7. A. Keller and D. J. Priest, *J. Macromol. Sci. (Phys.)*, **B2**, 479 (1968).

8. P. H. Lindenmeyer, *Science*, **147**, 1256 (1965).

9. J. D. Hoffman, *SPE Trans.*, **4**, 315 (1964).

10. A. Keller, *Phil. Mag.*, **2**, 1171 (1957); *Makromol. Chem.*, **34**, 1 (1959).

11. P. H. Geil, *J. Polym. Sci.*, **44**, 449 (1960); *ibid.*, **47**, 65 (1960).

12. E. W. Fischer and G. Schmidt, *Angew. Chem.*, **74**, 551 (1962).

13. P. J. Flory, *J. Amer. Chem. Soc.*, **84**, 2857 (1962).

Plastic Deformation of Polyethylene II. Change of Mechanical Properties during Drawing

G. MEINEL* and A. PETERLIN, *Camille Dreyfus Laboratory, Research Triangle Institute, Research Triangle Park, North Carolina 27709*

Synopsis

The crystallinity, elastic modulus, and tensile strength of samples of various draw ratios together with the true stress–strain curves of high-density polyethylene were determined to establish correlations with morphological changes occurring during deformation. Changes of crystallinity at draw ratios below 5, i.e., constancy during drawing of quenched film and a decrease during drawing of annealed film, are explained by the formation of microfibrils with crystallinity independent of the thermal history of the film. The microfibrils slide past each other at higher draw ratios, generating an increasing number of interfibrillar tie molecules, which is reflected in the increase of crystallinity, elastic modulus, and tensile strength. From the true stress–strain curves, the differential work density for the deformation of the volume element was calculated as a function of the draw ratio. It contains two components which reflect two different mechanisms of deformation. The first component, decreasing with increasing draw ratio, can be associated with the destruction of the original microspherulitic structure; the second one, increasing with increasing draw ratio, can be associated with the deformation of the new fiber structure, i.e., with the sliding motion of the microfibrils formed during the first deformation step.

INTRODUCTION

The first paper of this series[1] was concerned with morphological changes in polyethylene (PE) during drawing. The main emphasis was on orientation and crystal size. During drawing, the original crystal lamellae of the more or less spherulitic polymer film are destroyed, and a new fiber structure is developed, which is independent of the thermal history of the original film. This change should be reflected also in the properties of the drawn sample. In this paper an attempt is made to correlate the mechanical properties and the crystallinity with morphological changes. The true stress–strain curves are of special interest, since comparison with morphological data should give some insight into the state of the drawn material, particularly with respect to the tie molecules. The crystallinity data should be an additional indicator of how far the transformation from film to the fiber is independent of the thermal history of the film. As in the first paper, the investigations involve a quenched and an annealed PE sample.

67

EXPERIMENTAL

The linear Fortiflex (trademark of Celanese Corporation) of medium molecular weight used for the investigation was described previously.[1] The densities of the samples were investigated in a density-gradient column prepared with a mixture of butyl cellulose and methyl carbitol at 20°C. The density distribution in the column was determined by use of calibrated glass beads. The heats of fusion were obtained by a Perkin-Elmer Differential Scanning Calorimeter.

The elastic modulus and the tensile strength were measured with an Instron TM-M tester at different specified temperatures. Test specimens of 2.5 cm gauge length were extended at 0.1, 0.5, 1.0, and 5 cm/min for the measurement of the elastic modulus and the ultimate tensile strength. The stress-strain curves in Figure 1 and other true stress–strain plots were taken with specimens of a gauge length of 1 cm at specified drawing rates. Equidistant ink marks were made on the sample before deformation. Photographs of marked samples taken simultaneously at short intervals during the drawing process were used for calculations of true stress–strain curves. For this calculation the density was assumed to be constant. The method with ink marks is sufficiently precise for high draw ratios but yields less satisfactory results in the neck where the draw ratio varies rapidly with location.
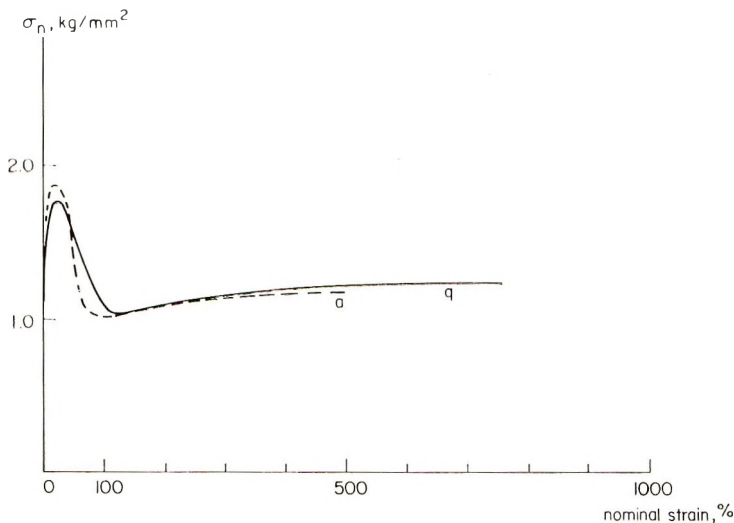
Fig. 1. Nominal stress–strain curve of quenched (——) and annealed (- -) Fortiflex samples at 24°C (v_d = 0.1 cm/min).

RESULTS

Influence of Crystallinity on Drawing

The drawing behavior of PE depends strongly on the crystallinity of the sample. When the yield point is reached, which is around a nominal yield

TABLE I
Changes of the Ratio $(\sigma_y/\sigma_d)_n$ with Temperature of Drawing

T_d, °C	$(\sigma_y/\sigma_d)_n$
0	1.6
24	1.9
60	1.6
90	1.4

stress σ_{yn} of 1.9 kg/mm² for annealed Fortiflex and around 1.7 kg/mm² for quenched Fortiflex (FF) samples at room temperature (Fig. 1), the nominal stress decreases rapidly to a minimum drawing stress σ_{dn} of about 1 kg/mm² (draw rate $v_d = 0.1$ cm/min). This minimum occurs at a nominal strain of about 80% in the annealed sample and at a higher strain, i.e., in 120% in the quenched sample. With further overall extension, the nominal stress increases slightly to about 1.2 kg/mm² until fracture occurs. The ratio of nominal yield stress to drawing stress, $(\sigma_y/\sigma_d)_n$ increases from 1.6 to 1.9 between 0 and 24°C but drops to 1.6 and 1.4 when the temperature increases to 60 and 90°C (Table I).

Despite the constant crosshead speed, the extension rate of an individual section of the sample is not uniform, as can be seen from Figure 2. The draw ratio $\lambda = l/l_0$ of the section where necking began is indicated by solid line as a function of the nominal strain $\epsilon_n = \lambda_n - 1$. Before the neck appears, the draw ratio increases nearly linearly with the nominal strain. With neck formation it increases quite rapidly up to $\lambda \approx 8$. From here on, as a consequence of the transformation into the new fiber structure, the draw ratio increases less rapidly up to the final fracture. The steepness
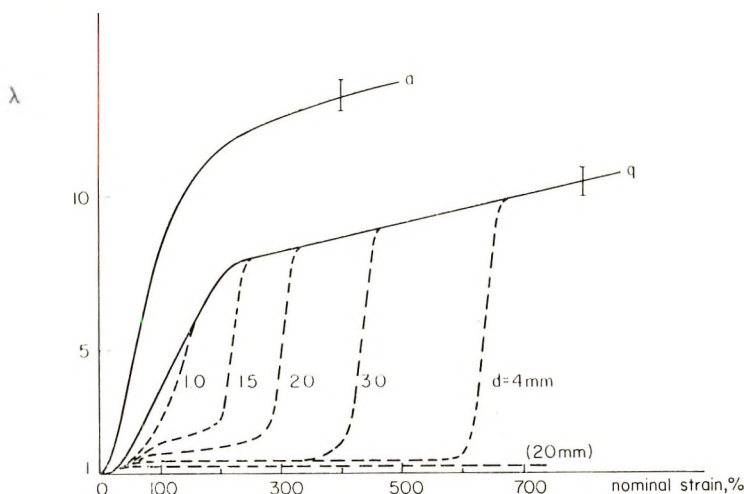
Fig. 2. Draw ratio λ (——) at the cross section where necking began and (– –) at cross sections which were originally a distance d from the beginning of the constriction as function of nominal strain: (a) annealed film; (q) quenched film ($v_d = 0.1$ cm/min).

of the initial increase in draw ratio depends on the thermal history of the sample: it is much higher in the annealed sample than in the quenched sample. The transition from the original rapid rate to the lower rate of extension takes place at about $\lambda = 8$ in quenched Fortiflex and around $\lambda = 12$ in the annealed Fortiflex; the final slope is nearly the same in all
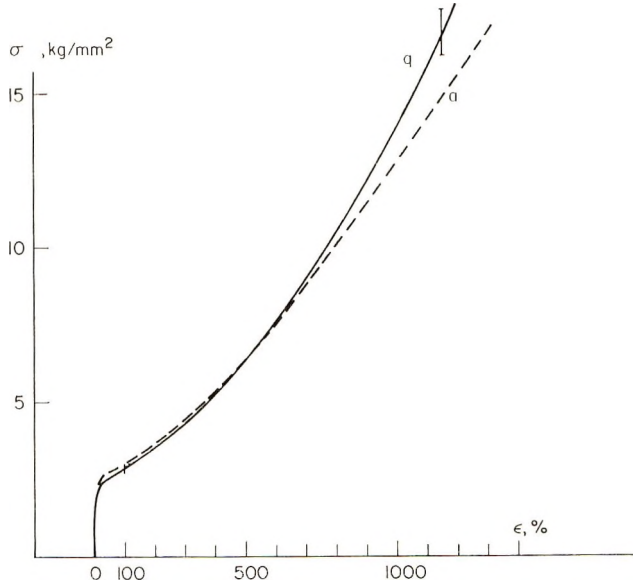
Fig. 3. True stress–strain curve of (——) quenched and (– –) annealed Fortiflex samples ($T_d = 20°C$, $v_d = 0.1$ cm/min).
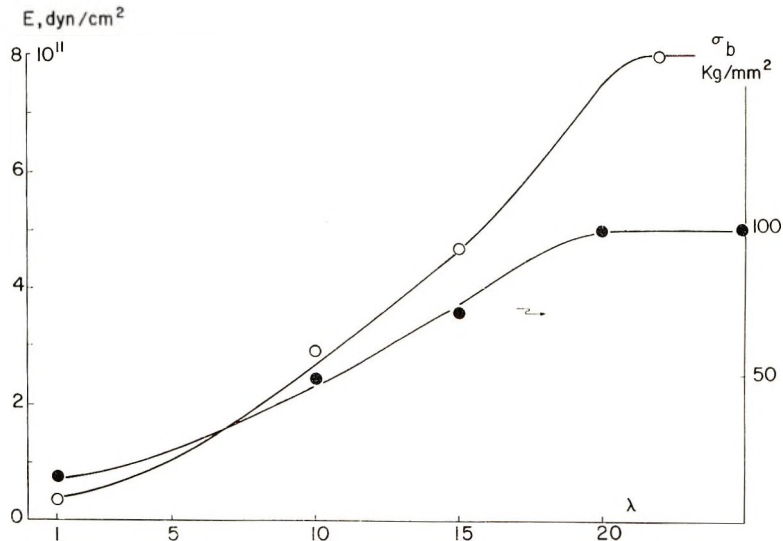
Fig. 4. Plots of (O) elastic modulus E and (●) tensile strength σ_b, measured at $-196°C$ as functions of the true draw ratio λ of the sample ($T_d = 60°C$).
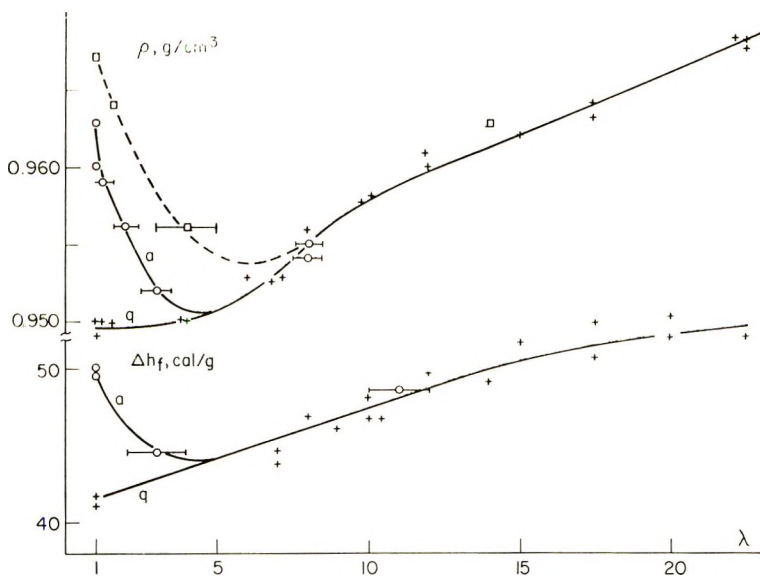
Fig. 5. Density ρ and heat of fusion Δh_f of drawn samples ($T_d = 60°C$) as functions of the true draw ratio. Film used for drawing was either quenched ($+$), annealed ($\bigcirc$), or slowly cooled from the melt ($\square$).

samples. The broken lines in Figure 2 show the behavior of neighboring sections of the quenched Fortiflex which were a distance d in the undeformed sample from the section where the neck started. In the beginning these neighboring sections are the more extended, the smaller d is, i.e., the closer they are to the initial constriction from which the neck develops. After the stabilization of the neck, the two shoulders of the quenched sample travel (in this particular sample) at a constant rate in opposite directions. When the neck approaches a given section, a slow increase in draw ratio up to $\lambda = 2$ or $\lambda = 2.4$ precedes the following sharp increase of the local draw ratio. This later increase is faster and reaches a higher draw ratio than that in the sections where the neck originated.

From the nominal stress σ_n and the knowledge of the true draw ratio λ at the section where the constriction started, the true stress $\sigma = \sigma_n \lambda$ for this section can be obtained. A plot of the true stress versus strain $\epsilon = \lambda - 1$ is rather similar in all samples investigated (Fig. 3). The true stress exhibits an extremely steep linear increase up to the yield point at $\lambda \approx 1.2$, which is followed by a sharp inflection. The subsequent gradual increase in stress, initially small, gets larger at higher draw ratios. The true stress-strain curve of the annealed sample lies nearly within the error limit of that of the quenched sample. The error of a single measurement is indicated in the drawing. The small differences in the two curves, however, seem to be real, since the reproducibility of the curves was within the indicated error limits of a single measurement. Such differences are seen below a strain of 100%, where the true stress is slightly higher in the an-

nealed than in the quenched sample. At higher strain, this is reversed; the stress in the annealed sample falls below the values obtained in the quenched material.

The mechanical properties, i.e., elastic modulus and the tensile strength, of drawn PE depend on the draw ratio, as is shown in Figure 4. The data were obtained on quenched samples drawn at 60°C to the specified draw ratio. The elastic modulus of Fortiflex measured at $-196°C$ increases with higher draw ratio from 4.8×10^{10} dyne/cm² at $\lambda = 1$ to a value of 80 $\times 10^{10}$ dyne/cm² at $\lambda = 20$. The ultimate tensile strength σ_b also measured at $-196°C$ increases from 14 kg/mm² to 100 kg/mm² between $\lambda = 1$ and $\lambda = 20$. The low temperature was chosen for the measurement in order to prevent plastic flow and the ensuing structure transformation before the final break.

During drawing, the density of the material changes (Fig. 5). The density of annealed Fortiflex drops from $\rho = 0.963$ g/cm³ and approaches 0.951 g/cm³, the density of the quenched and drawn material, at a draw ratio near 4. The density of the quenched material does not change initially during drawing; it increases for $\lambda > 5$. The additional points in Figure 5 were obtained from a very slowly cooled sample, which was drawn at 60°C. Behavior similar to that of the density is found in the heat of fusion (Fig. 5). The heat of fusion of the quenched sample increases steadily from 42 cal/g at $\lambda = 1$ to 52 cal/g at $\lambda = 20$. The heat of fusion of the annealed sample, however, decreases until it reaches the value of the quenched sample around a draw ratio of $\lambda \approx 5$. With increased draw ratio, the values become independent of the thermal history of the film used for drawing.

Influence of the Temperature of Drawing

The local draw ratio at the section where the neck formed is plotted as a function of the nominal strain in Figure 6 for two different temperatures of drawing, 24 and 90°C. With lower temperature of drawing T_d, the changes of draw ratio in the neck are larger and faster, indicating that the neck sharpens. The change to a smaller rate of deformation occurs at higher draw ratios; at $\lambda = 7$ at 90°C and at $\lambda = 9$ at 24°C. The plastic deformability of the fiber structure decreases with lower temperature.

Figure 7 shows the true stress-strain curves at different draw temperatures. As the draw temperature increases, the yield point falls to a lower yield stress and the following stress increase gets progressively smaller.

The density and heat of fusion of a sample with a draw ratio of 8 are somewhat affected by the drawing temperature, as is shown in Figure 8. The density increases slightly from 0.950 g/cm³ to 0.959 g/cm³ as the drawing temperature goes from 9 to 110°C, the increase being greater at low drawing temperature and leveling off completely above 80°C. The data were all obtained on translucent, drawn samples, either as-drawn (open circles) or after slight pressing (filled circles). The pressing did not affect the crystallinity, as indicated by density data. Parallel to this

behavior is that of the heat of fusion which also increases from 43 to 49 cal/g between 9 and 110°C. Other properties, elastic modulus and ultimate tensile strength, both measured at room temperature are scarcely influenced by the temperature of drawing, as is indicated in Figure 8.
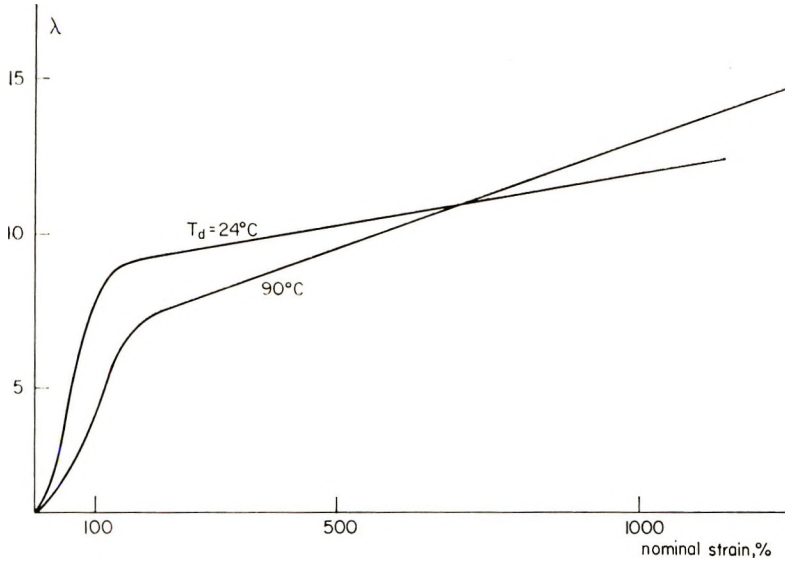
Fig. 6. Draw ratio λ at the cross section where constriction started as function of the nominal strain for two different temperatures of drawing ($v_d = 1$ cm/min).
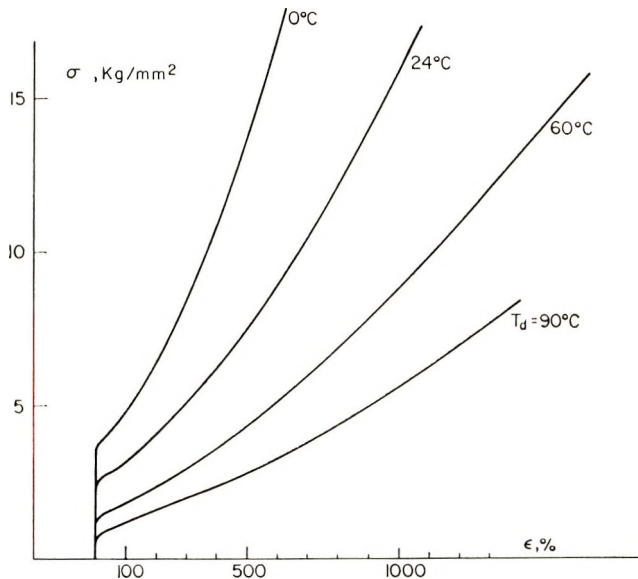
Fig. 7. True stress–strain curve obtained after drawing at different temperatures ($v_d = 1$ cm/min).
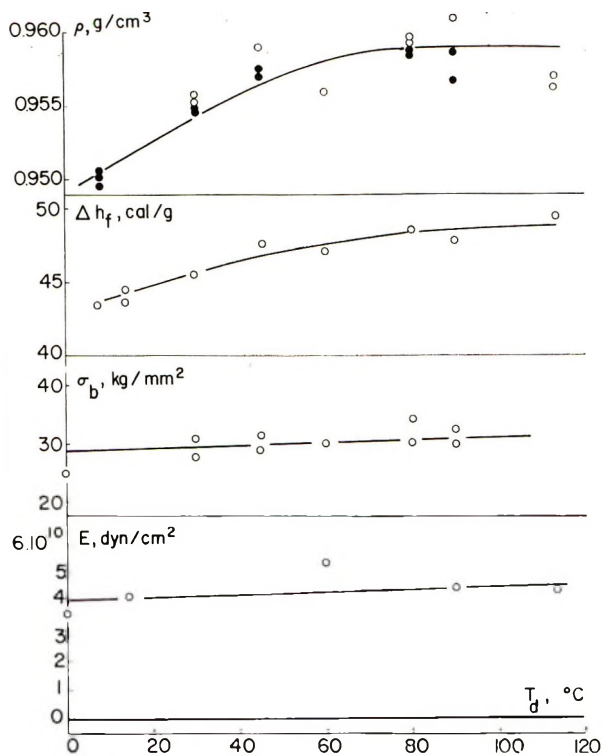
Fig. 8. Density ρ, heat of fusion Δh_f, tensile strength σ_b and elastic modulus E of drawn samples at 20°C ($\lambda = 8$) as functions of the temperature of drawing T_d; (O) as drawn; (●) pressed samples (see text).
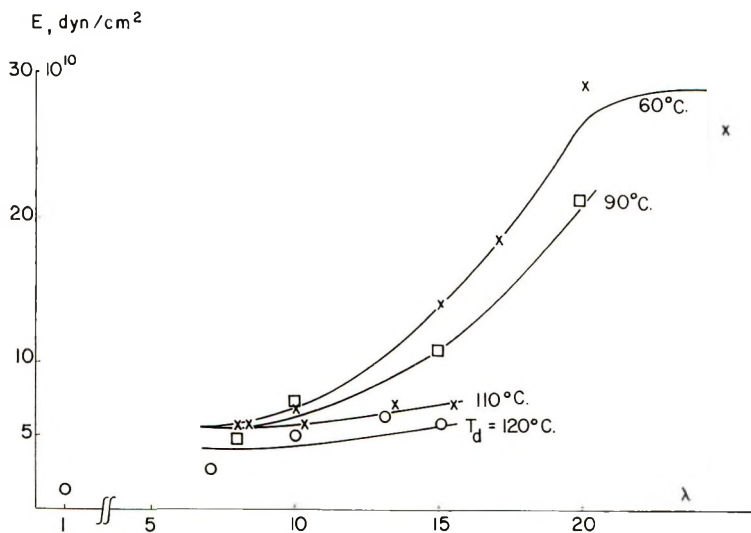
Fig. 9. Elastic modulus E at 20°C as function of true draw ratio λ for the values of drawing temperature indicated.

An influence of the draw temperature on the elastic modulus is observed, however, at higher draw ratios, as shown in Figure 9 where the elastic modulus is plotted versus draw ratio with drawing temperature T_d as parameter. The elastic modulus, being practically independent of the drawing temperature below a draw ratio of 10, shows a strong temperature dependence above that draw ratio; the lower the drawing temperature, the higher the elastic modulus is.
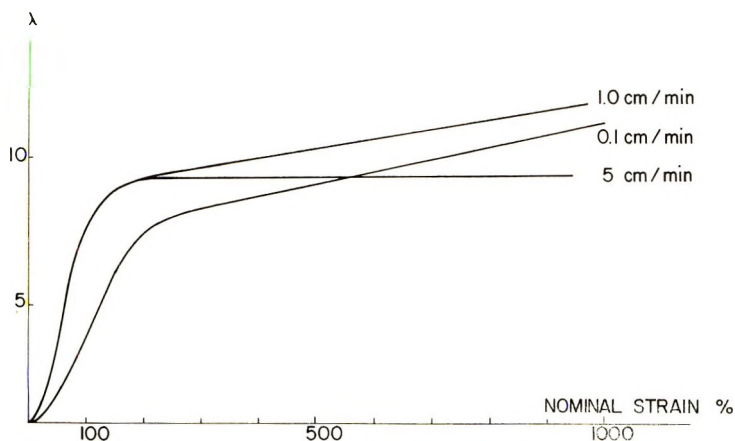
Fig. 10. Draw ratio λ at the cross section where constriction began as a function of the nominal strain for three values of v_d.
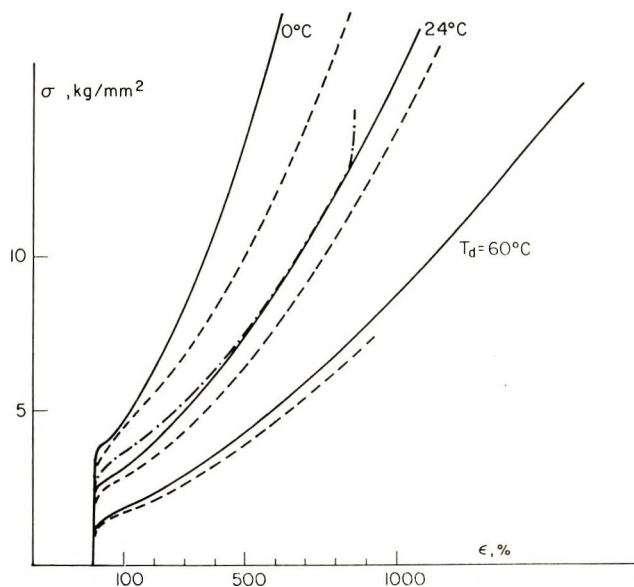
Fig. 11. True stress–strain curves obtained after drawing at different temperatures and drawing rates: $(- -) v_d = 0.1$ cm/min; $(——) v_d = 1$ cm/min; $(- \cdot -) v_d = 5$ cm/min.

Influence of the Draw Rate

The draw rate influences the drawing behavior to some degree within the range of overall elongation rates investigated, 0.1 and 5 cm/min. As can be seen from the plot of the local draw ratio versus time (Fig. 10) at 24°C, the initial changes in draw ratio (up to $\lambda \approx 10$) are relatively faster at high draw rates, indicating a sharpening of the neck with increasing draw rate. The change to the smaller local extension rate takes place around $\lambda = 7.5$ at a crosshead speed of 0.1 cm/min and at $\lambda = 9$ at 1 or 5 cm/min. The subsequent extension rate of the fiber structure decreases with increasing crosshead speed and is practically zero at 5 cm/min.

The corresponding true stress–strain curves are plotted in Figure 11. When the elongation rate is increased from 0.1 to 1 cm/min, the true stress is always higher. This effect is enhanced at lower drawing temperatures. At the higher rate of 5 cm/min, the yield stress increases still further. At higher strain, however, the curve approaches that of a sample drawn at 1 cm/min. At a strain of 860%, the ultimate strain at 5 cm/min, a sudden stress increase followed by fracture is observed.

DISCUSSION

A goal of the investigation of the drawing process is the correlation of morphology with the properties of drawn samples. The main morphological changes during deformation are initially tilt and slip of lamellae. With higher draw ratio, the original lamellae are destroyed and microfibrils are formed. These microfibrils may undergo further changes during the subsequent drawing. The whole transformation occurs gradually in the neck and hence extends over a finite length of the sample, in spite of the fact that the transformation of single lamellae into microfibrils occurs in micronecks located at the crystal cracks with negligible extension in draw direction. The elementary act is discontinuous, but it occurs in nearly randomly distributed places in the neck and thus produces a gradual transition from the microspherulitic to the fiber structure. This gradual transition was observed by investigation of the debris after etching, wide-angle x-ray measurements, and small-angle x-ray scattering (SAXS).[1] Other properties of the samples, e.g., crystallinity and the true stress–strain curves, are therefore not expected to show a sharp transition in agreement with the results obtained here.

Crystallinity

The crystallinity measurements show a few features which may be related to the morphology. Above a draw ratio of $\lambda = 5$, the crystallinity as derived from density or heat of fusion is independent of the thermal history of the film used for drawing (Fig. 5). This observation supports the previous claims derived from electron microscopy,[2] SAXS,[3] and crystal-size determination[1] that microfibrils are newly formed morphological units independent of the history of the film.[4-7]

The initial decrease of the crystallinity as seen at low draw ratios of the annealed samples can be the consequence of spherulite destruction, and formation, at very low draw ratios, of microfibrils of lower density. The existence of microfibrils can indeed be observed by SAXS already at λ = 1.1 for highly branched PE, and at λ = 1.3 for linear PE.[8] Since a finite concentration is needed for detection by SAXS, one might conclude that microfibrils are formed quite early in the drawing process. Most probably, they have a lower density than the original annealed film for two reasons: first, the crystals of a fiber structure exhibit larger paracrystalline disorder;[9] and second, the decrease of long period from 300 to 170 Å increases the surface-to-volume ratio and hence reduces the density. With drawing at room temperature, the density of microfibrils must be similar to that of the quenched sample since no changes in density are observed during drawing of quenched PE.

As is indicated in Figure 8, the crystallinity depends on the drawing temperature. It is lower at lower temperature. Since long periods do not change appreciably in this temperature range, one has to assume that more imperfections are incorporated in the microfibrils during their formation at lower temperatures.

A surprising fact is the steady increase in crystallinity between λ = 10 and λ = 20 (Fig. 5). An explanation for this might be the increasing number of tie molecules which is required for the explanation of the discrepancy in crystal size as measured by SAXS and WAXS[1] or in the elastic modulus[10] (as described in the following discussion of mechanical properties).

Mechanical Properties

The true stress–strain curves do not seem amenable to a detailed discussion in terms of the individual deformation steps. This is, as mentioned before, a consequence of the deformation processes which extend over a large range in draw ratios. The curves are also very insensitive to a change in crystallinity of the sample used for drawing (Fig. 3). This might be interpreted by the similarity of the number of tie molecules connecting the newly formed crystallites within the microfibrils.

A second feature of the true stress–strain curves, which has to be related to the deformation process, is their large temperature dependence (Fig. 7). It shows that the single deformation steps are very temperature-dependent. This could be expected for processes like chain tilting or slipping, as long as the number of tie molecules is not too large. The slipping seems to go on up to very high draw ratios, allowing high extension of the sample.

Additional information on these temperature dependent processes can be obtained, when properties of samples drawn at different temperatures are compared at the same temperature. The mechanical properties, i.e., the elastic modulus E and the tensile strength σ_b measured at room temperature are independent of the temperature of drawing in the temperature range of 0 and 110°C up to a draw ratio of 8 (Fig. 8); at higher draw ratios, however, they show a strong dependence on the temperature of drawing.
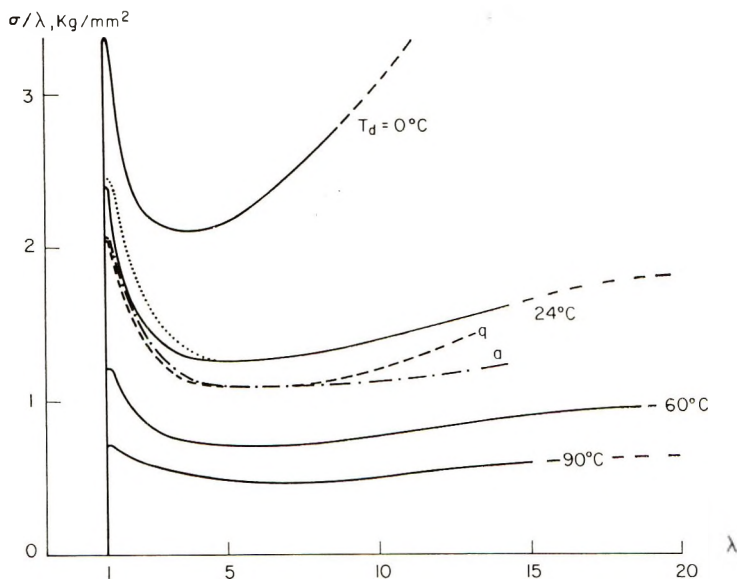
Fig. 12. Differential work density σ/λ as function of draw ratio at various draw temperatures and draw rates: (———) 1 cm/min; ($\cdots$) 0.1 cm/min; (–·–) 5 cm/min; (— —) quenched samples.

This indicates that with higher draw ratio a second process occurs, which is probably a relaxation. The presence of this process can be seen also in other measurements, for example, the dependence of the true stress–strain curves on the draw rate (Fig. 11). The stress decreases at lower draw rate and this decrease gets smaller with increasing draw temperature, which indicates the expected behavior of a relaxation process.

With the knowledge of the true stress-strain curves, one can calculate the work W necessary for the plastic deformation of the sample. One has for every volume element

$$dW = Fdl = A\sigma l_0 d\lambda = (V_0/\lambda)\sigma d\lambda \tag{1}$$

which yields the differential work per unit volume

$$(1/V_0)\,dW/d\lambda = \sigma/\lambda \tag{2}$$

In this derivation the sample is assumed incompressible, i.e., $V = Al = V_0 = A_0 l_0$. The differential work density σ/λ is plotted in Figure 12 as function of λ for different drawing temperatures. As in Figures 3, 6, 7, 10, and 11, the data apply to the volume element where necking begins. The differential work density increases extremely fast at the beginning of the drawing experiment as a consequence of high elastic energy storage at relatively small strain. The following plastic deformation with conspicuously higher compliance causes the ratio σ/λ to decrease to minimum with a subsequent nearly linear rise up to the final fracture of the sample.

The shape of the differential work versus strain curves as shown in Figure 12 was not detectably influenced by heating effects, since drawing at 0.1 or 1 cm/min provides practically isothermal drawing.[11] It should therefore reflect specific morphological changes. The existence of the minimum is an unmistakable indication of two different deformation mechanisms, one operating predominantly during and the other after actual necking of the volume element. This is in agreement with the morphological changes of the sample and with the course of deformation as shown in Figure 2. During the deformation in the neck, the original microspherulitic structure is discontinuously destroyed in more or less randomly scattered micronecking zones so that the macroscopic transformation into the fiber structure appears gradual: the microspherulitic component decreases and the fiber component increases continuously. If the destruction rate is proportional to the volume fraction of the remaining original structure, one expects an exponential decrease of differential work density as function of time or strain during necking, as is indeed observed in the decreasing portion of the σ/λ curve.

The new fiber structure exhibits a smaller plastic compliance than the original microspherulitic structure as may be deduced from the slopes of λ and λ_n curves after and before necking (Fig. 2). The significant reduction of cross section by a factor λ means a λ-fold larger true stress on the fiber structure. As a consequence the maximum at the yield point and the subsequent decrease in the load elongation curve disappear in the true stress-strain curve.

The plastic deformation of the fiber structure cannot proceed by further rotation and destruction of lamellae because it is composed of more or less perfectly aligned microfibrils. The microfibrils are extremely strong and stable as a consequence of the great many tie molecules connecting the folded chain blocks. But the lateral cohesion between adjacent microfibrils is rather modest because it is based on the relatively weak van der Waals forces between slightly mismatched crystalline blocks separated by a layer of highly concentrated lattice defects (the quasiamorphous boundary between adjacent mosaic blocks) and on the few tie molecules going from one microfibril to an adjacent one. Such tie molecules may eventually be formed during drawing by exchange of folded-chain blocks between adjacent microfibrils. More likely they originate from tie molecules interconnecting different lamellae in the original sample.[12]

The high tensile strength of microfibrils and the relatively weak lateral cohesive forces among them favor longitudinal sliding motion as the mechanisms for plastic deformation of the fiber structure. During sample elongation, the microfibrils slide past each other. The interfibrillar tie molecules cause partial unfolding at the blocks where they are affixed. As a consequence, the length of such a tie molecule increases with λ, and so does the distance between the two blocks it connects. The mass fraction of interfibrillar tie molecules increases with drawing and hence
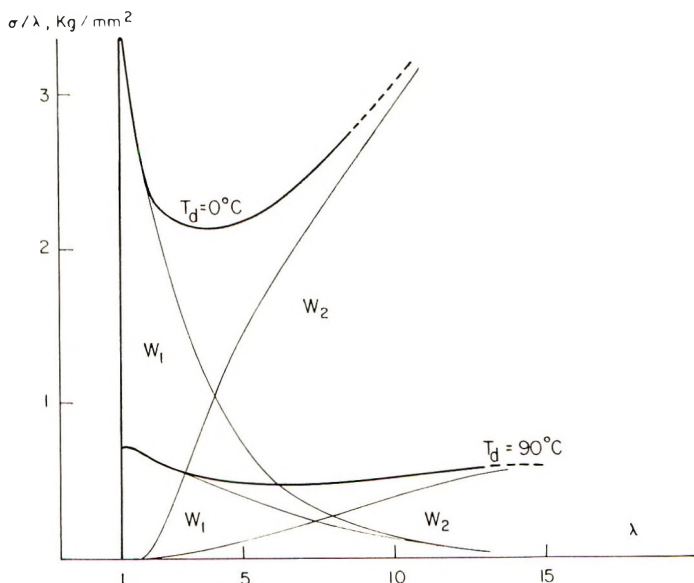
Fig. 13. Separation of the differential work density σ/λ into the two components W_1 and W_2 (see text).

the resistance to further deformation increases as is shown by the increase of true stress with strain (Figs. 3 and 11).

The differential work density for such a deformation of the fiber structure does not contribute to σ/λ before neck formation because there is as yet no fiber component. This is gradually formed in the neck, and is fully developed after the neck has passed the volume element in question. Hence the corresponding contribution to the differential work density starts from zero in the neck, reaches nearly its full value at the end of the neck, and later increases as a consequence of stiffening of the fiber structure by the increasing volume fraction of interfibrillar tie molecules.

The superposition of the two contributions, the destruction of spherulites in the neck and secondly the microfibrillar sliding in the fiber structure, explains the curves in Figure 12. A reasonable separation is attempted, as shown in Figure 13, by assuming an exponential decrease of the first component.

The minimum is located at the λ value where the negative slope of the destruction mechanism equals the positive slope of the fiber stretching mechanism. Consequently it is located at a draw ratio prevailing somewhere between the center and the end of the neck. It moves to higher λ with increasing temperature of drawing T_d. Since the magnitude of drawing in the neck decreases with increasing T_d, one has to conclude that the ratio of specific contributors of both mechanisms changes with temperature. At higher T_d the transformation from the spherulitic to the fiber structure by lamella destruction extends over a range of draw ratios beyond that
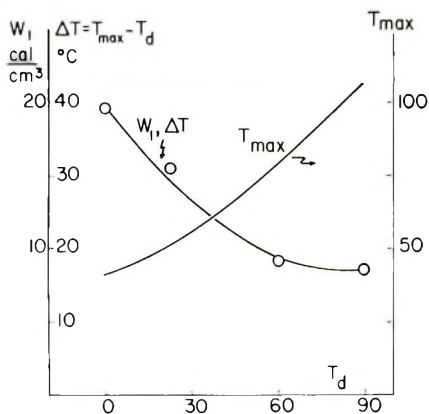
Fig. 14. Total work of spherulitic destruction W_1 and maximum temperature, T_{max}, in adiabatic deformation (see text) as functions of drawing temperature.

achieved in the neck.   Evidence for the latter behavior is found indeed by SAXS in PE[13] and in polypropylene.[14,15]

The area under the curve representing the contribution of the destruction mechanism in the neck gives the work W_1 of applied forces during elastic deformation, subsequent lamellar slipping, chain tilting and slipping, and the final lamellar fracture.   It is plotted in Figure 14 as a function of T_d.   Although the absolute values depend on the rather arbitrary separation into two components of the differential work density curves, one sees that the total work of destruction W_1 rapidly decreases with increasing temperature of drawing.   If no heat were transferred to the environment, the maximum increase of temperature calculated under the assumption of a constant specific heat of 0.5 cal/g is simply obtained by a proper change of the scale of the ordinate.   By adding the temperature of drawing, one obtains the maximum temperature T_{max}, which may occur in the neck during drawing.   Both values are plotted in Figure 14.

The deformational work W_2 of the fiber structure is of the same order of magnitude or even larger than W_1, but it is uniformly produced over all the fibrous volume elements, in contrast with W_1 which is to a large extent concentrated in the extremely thin destruction zones.   As a consequence, the local heating caused by W_2 is small at low draw rate and identical with the macroscopic heating of the drawn sample after necking.

A further source of information on the morphology is the elastic modulus of the drawn sample.   In the microfibril model given before, the crystalline blocks are in series and held together by intrafibrillar tie molecules.   With this assumption, one can calculate from the elastic modulus of a sample the fraction β_E of nonfolding or tie molecules in a sample of crystallinity α according to

$$\frac{1}{E} = \frac{\alpha}{E_c} + \frac{(1 - \alpha)}{(1-\beta) E_a + \beta_E E_{ak}} \tag{3}$$

MEINEL AND PETERLIN

TABLE II

λ	β_{HNO_3}, $\%$[a]	β_E, $-196°C$, $\%$[b]	β_σ, $-196°C$, $\%$[c]
1	5	—	—
7	5	3	3
10	20	4	4
20	30	13	7
25	30	13	7

[a] Results taken from Peterlin and Sakaoku.[2]

[b] β_E calculated from eq. (3): $E_{ak} = 2.4 \times 10^{12}$ dyne/cm^2.

[c] β_σ calculated from $\sigma_{b-196°C}/\sigma_{id}$; $\sigma_{id} = 1400$ kg/mm^2. Data of Mark.[16]

Here E_c and E_a are the elastic moduli of the crystalline and amorphous components. Assuming that the modulus of the tie molecules E_{ak} equals that of an extended chain E_k, one obtains the values given in Table II together with the results previously obtained by the fuming nitric acid treatment.[1,2] This number increases with increasing draw ratio (slightly smaller numbers have been obtained before by using elastic moduli measured at room temperature). The agreement between the results of the two methods could be improved if one assumes a statistically varying number of tie molecules along a fibril instead of the constant number assumed in the calculation. In the third column finally, a number of tie molecules was calculated from the ultimate strength according to $\beta_\sigma = \sigma_b/\sigma_{id}$. This number is always less than values obtained by fuming nitric acid treatment and partly below values obtained from the elastic modulus. This discrepancy is probably due to inhomogeneities of the sample or to the fact that a great many chains break before the final fracture of the material.[17]

Apart from the exact number, one finds by all methods of investigation an increasing number of tie molecules with increasing draw ratio. This might also explain the density increase at higher draw ratio as already mentioned in the discussion of the crystallinity. On the basis of our deformation model, one must conclude that the increase of tie molecules with draw ratio is mainly the consequence of sliding motion of adjacent microfibrils, which extends the interfibrillar tie molecules by partial unfolding and hence increases their volume fraction. Such a deformation model does not provide a mechanism for a substantial increase of intrafibrillar tie molecules.

CONCLUSIONS

The true stress–strain curve and the differential work density curve derived from it definitely point to the existence of two simultaneous deformation mechanisms during drawing of PE: destruction of the original microspherulitic structure and deformation of the new fiber structure. The first mechanism starts before necking by tilting and slipping of lamellae into the position of maximum plastic compliance for chain tilt and slip, which finally leads to the break up of lamellae into folded-chain blocks.

The destruction is nearly completed at a draw ratio of about 10. Concurrently, the new fiber structure appears as the torn-off blocks are incorporated in well-aligned microfibrils. The deformation of the new fiber structure can hardly proceed by further deformation of the single microfibril which is firmly held together in the fiber direction by many intrafibrillar tie molecules generated by partial chain unfolding during fracture of the original lamellae and connecting the folded-chain blocks. But there is much less resistance to longitudinal slip of microfibrils which are connected by a much smaller number of tie molecules. These interfibrillar tie molecules most likely originate from tie molecules connecting adjacent lamellae in the undeformed, microspherulitic material. During longitudinal slip of microfibrils, the interfibrillar tie molecules extend as a consequence of partial unfolding of their ends fixed in the blocks of adjacent microfibrils. Such an increase of their volume fraction with increased draw ratio is reflected in the increased elastic modulus, tensile strength, and number of tie molecules.

References

1. G. Meinel, N. Morosoff, and A. Peterlin, *J. Polym. Sci. A-2*, **8**, 1723 (1970).

2. A. Peterlin and K. Sakaoku, *J. Appl. Phys.*, **38**, 4152 (1967).

3. A. Peterlin and R. Corneliussen, *J. Polymer Sci. A-2*, **6**, 1273 (1968).

4. A. Peterlin, *Kolloid-Z. Z. Polym.*, **216**, 129 (1967).

5. A. Peterlin in *Structure and Properties of Polymers* (*J. Polym. Sci. C*, **9**), A. V. Tobolsky, Ed., Interscience, New York, 1965, p. 61.

6. A. Peterlin, in *U.S.–Japan Seminar in Polymer Physics* (*J. Polym. Sci. C*, **15**), R. S. Stein and S. Onogi, Eds., Interscience, New York, 1967, p. 427.

7. A. Peterlin, in The Meaning of Crystallinity in Polymers (*J. Polym. Sci. C*, **18**), F. P. Price, Ed., Interscience, New York, 1967, p. 123.

8. A. Peterlin and F. J. Baltá-Calleja, *Kolloid-Z. Z. Polym.*, in press.

9. N. W. Wyckoff, *J. Polym. Sci.*, **62**, 83 (1962).

10. G. Meinel, A. Peterlin, and K. Sakaoku, in *Analytical Calorimetry*, R. S. Porter and Y. F. Johnson, Eds., New York, 1968, p. 15.

11. P. Vincent, *Polymer*, **1**, 7 (1960).

12. F. J. Baltá-Calleja and A. Peterlin, *J. Macromol. Sci. (Phys.)*, **B4**, 519 (1970).

13. G. Meinel, unpublished data.

14. F. J. Baltá-Calleja and A. Peterlin, *J. Mat. Sci.*, **4**, 722 (1969).

15. A. Peterlin and F. J. Baltá-Calleja, *J. Appl. Phys.*, **40**, 4238 (1969).

16. H. Mark, *Cellulose and Cellulose Derivatives*, Interscience, New York, 1943.

17. D. Campbell and A. Peterlin, *J. Polym. Sci. B*, **6**, 481 (1968).

Lamellar and Interlamellar Structure in Melt-Crystallized Polyethylene. II. Lamellar Spacing, Interlamellar Thickness, Interlamellar Density, and Stacking Disorder

S. KAVESH* and J. M. SCHULTZ, *University of Delaware, Newark, Delaware 19711*

Synopsis

Measurements of the small-angle scattering power and the degree of crystallinity in melt-crystallized high-density polyethylene have been used to evaluate the "amorphous" density *in situ* by the relation,

$$(2\pi/V) \int_0^\infty S\tilde{g}(S)dS = (\rho_c - \rho_a)^2 v_{cr}(1 - v_{cr})$$

where V is the irradiated volume and $\tilde{g}(S)$ is the "slit-smeared" absolute intensity.   The amorphous density is a function of sample history and is always higher than the extrapolated melt density.   After slit-height correction, and within the experimental error, the ratio of the two observed long periods is 2:1 at all temperatures (25–126°C).   The lamellar thickness and the average interlamellar spacing are obtained from the degree of crystallinity and the first corrected long period.   At increasing temperatures between 25°C and 110°C, the lamellae become thinner while the interlamellar zone expands by almost half.   Over this range the changes are reversible with temperature.   Above 110°C, both the lamellae and the interlamellar region expand with temperature.   The thickening is partially reversible upon recooling.   Other results obtained include measurements of stacking disorder and of microstructural changes with crystallization temperature and with time at ambient temperature.

INTRODUCTION

Context of the Present Work

The work reported in this paper is the result of the application of a special x-ray instrument—a combination high-angle and low-angle diffractometer[1]—to the study of the intimate substructure of spherulitic polyethylene.   The specific capabilities of the instrument are (a) to record in direct sequence low-angle and high-angle x-ray data, (b) to do so for varying ambient conditions, and (c) to provide data amenable to absolute intensity analysis.   As we shall see, these diffraction capabilities enable a number of

* Present address: Materials Research Center, Allied Chemical Corporation, Morristown, New Jersey 07960.

substructural characteristics to be evaluated in the same experimental sequence, the principal such characteristics being the degree of crystallinity, the density of the amorphous phase, and (using a specific model) the thickness of the crystalline lamellae and the intervening amorphous layer. The method for obtaining degree of crystallinity and interpretation have been dealt with in the preceding paper in this series[2] and will be mentioned again here only insofar as necessary to define the conditions of the present analysis. The remainder of the introductory remarks are therefore aimed at reviewing the background into which the present structural results should fit.

Interlamellar Density

It appears that opinion is divided as to the density of the amorphous regions in spherulitic polyethylene *vis a vis* the density of a supercooled melt. Several investigators have correlated room temperature specimen density with degree of crystallinity as determined by x-ray diffraction,[3-5] infrared absorption,[3,6] and thermal[7-9] methods. By extrapolating density data to zero crystallinity, values of amorphous density are found. These values converge on 0.85 gm/cm^3, nearly the value which would be obtained by extrapolation of melt densities to room temperature. The convergence has been implicitly taken as strong evidence that the amorphous density in a spherulitic aggregate is the same as that of a supercooled melt.[10]

There is, however, a body of evidence which conflicts with the above. Mandelkern et al. found[11] that enthalpy of fusion data yielded an amorphous density of 0.90 g/cm^3 when extrapolated linearly to zero density. Further, in a subsequent publication, Mandelkern et al. showed[12] that the slope of a curve relating specific volume to enthalpy of fusion is not constant, but rather depends on the crystallite size and the interfacial free energy (different, in general, for each sample). The work of Okada and Mandelkern has placed the results of infrared studies in some doubt also, since only one of the "crystalline" bands yielded an amorphous density value as low as 0.85.[6] Lastly, Swan[13] extrapolated density and unit cell data so as to set the amorphous density equal to the melt density at the melting point of polyethylene. Using this procedure, he found the amorphous density to be greater than the extrapolated melt density at all temperatures below the melting point. All these data suggest that one must look with some skepticism at the conclusion that the properties of the amorphous phase may be easily extrapolated from those of the melt.

Further information on the structure of the amorphous regions in partially crystalline polyethylene has been obtained from the position of a diffuse band appearing in x-ray diffraction photographs. The angular position of maximum intensity in the diffuse band is related to the relative interchain distance in the amorphous material through Bragg's equation. (The actual interchain distance must be obtained by Fourier transformation of the x-ray intensities. For the normal paraffins through pentadecane, the actual interchain spacing, rigorously determined, is about 20% greater
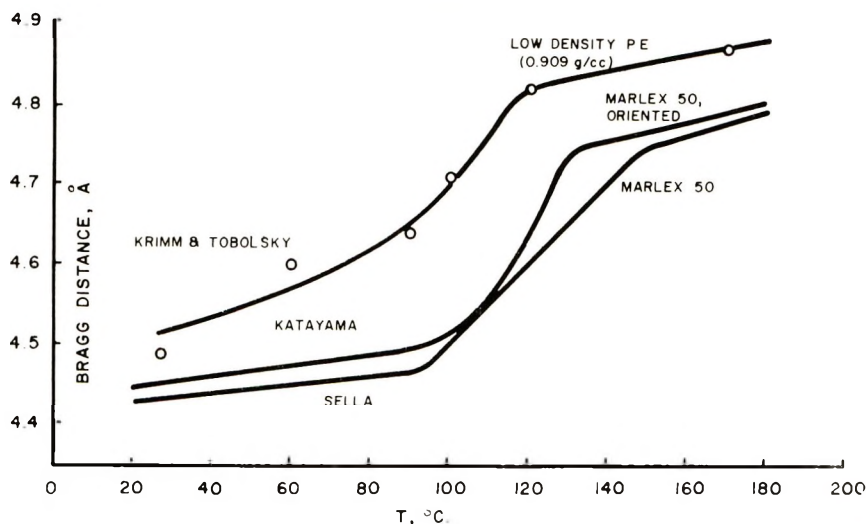
Fig. 1. Amorphous interchain spacing in polyethylene.

than that calculated from Bragg's equation.[14])   Figure 1 shows the relative amorphous interchain spacing observed by several authors[4,15,16] for linear polyethylenes.   In each case, it is seen that the amorphous spacing increases markedly with increasing temperature near the melting point. Extrapolation of the liquid portions of the curves to room temperature would yield an interchain spacing 3–5% higher than is actually experienced. This is the same size discrepancy as was observed in the "anomalous" amorphous densities mentioned in the preceding paragraph.

Hermans and Weidinger[17] suggested a direct method of measurement of the density of the amorphous regions based on a principle of conservation of scattered intensity formulated by Guinier and Fournet,[18] Porod,[19] and Stern.[20]   In a macroscopically isotropic two-phase system (a condition fulfilled by a fine spherulitic aggregate) the conservation principle can be written,

$$4\pi \int_0^\infty S^2 I(S)dS = V(\rho_1 - \rho_2)^2 v_1(1 - v_1) \tag{1}$$

where S is related to the scattering angle 2θ and the incident wavelength λ by $S = 2 \sin \theta/\lambda$, $I(S)$ is the intensity at a particular value of S, V is the irradiated volume, ρ_1 and ρ_2 are the electron densities of the two phases present, and v_1 is the volume fraction of one of the phases.   The validity of eq. (1) is independent of the size and shape of the constituent particles and requires only that they be large compared to atomic dimensions.   As noted, the small-angle scattering power is an experimentally available quantity. Thus, if the crystalline density is known and absolute measurements of the degree of crystallinity can be made, the amorphous density may then be calculated.

Fischer et al.[21] have utilized eq (1) to assess the density of the interlamellar layer in polyethylene single crystals and in highly stretched linear and branched polyethylenes. A relative crystallinity index[22] (by heat of fusion) was used in determination of the amorphous densities. On this basis the amorphous density of single crystals and of stretched branched polyethylene agreed with an extrapolated melt density. The amorphous density of stretched linear polyethylene was substantially higher than the extrapolated melt density.

A principal objective of the present work has been the measurement of the density of the amorphous regions in melt-crystallized, unstretched, linear polyethylene from absolute measurements of the small-angle scattering power and the degree of crystallinity.

Relationship between Lamellar Periodicity and Small-Angle Long Period

The x-ray small-angle diffraction patterns from melt-crystallized polymers show, in general, one to three broad intensity maxima. It is conventionally accepted that these maxima relate in some manner to the lamellar microstructure observed by electron microscopy. More specifically, it is usually assumed that the small-angle maxima should be described by the periodicity of stacking of the lamellae. Both general[23] and specific[24,25] theories of the scattering by lamellar stacks predict such intensity peaks. The angular positions of the peaks should depend on the mean spacing of lamellae according, approximately, to Bragg's law. In this case the spacings calculated from the angular position of the peaks, by using Braggs law, should be integral multiples of each other, if they arise from the same periodic structural source. The "approximate" nature of the application of Bragg's law is due to irregularities in the stacking[23,24] or to the effect of refraction.[26]

Proof of the nature of the specific relationship between the x-ray small-angle maxima and the lamellar microstructure of melt-crystallized polymers has, however, been elusive. When three small angle maxima have been seen,[25,27,28] it has been the position of the second peak which agrees well with the electron-microscope measurements of the thickness of the lamellae.[25,28] In general, the second peak is not a second order of the first. The position of the first peak is invariant with thermal conditioning, where as the second peak is responsive to sample history. The intensity of the second maximum is comparable to or greater than the intensity of the first. It was concluded in each study that the second of the three small-angle diffraction peaks corresponded to the lamellar periodicity. No conclusions have as yet been reached as to the origin of the first (lowest-angle) small angle peak. With regard to the third (highest-angle) of the three observed peaks, its position corresponded to somewhat less than one-half the long period of the second peak. It should be noted that all the data cited above were obtained with slit-collimated radiation. The effects of slit-height "smearing"[18] would be directionally satisfactory to explain the discrepancy from a 2:1 long-period ratio if the second and third peaks are in

a first- and second-order relationship. Another possibility is that both peaks arise from the same structural periodicity but are not related exactly according to Bragg's law because of structural irregularities. A third possibility is, of course, that these peaks manifest different structural elements. However, since the data were in fact not corrected for slit smearing, the source of the third scattering maximum has remained conjectural.

Conclusions regarding the correspondence between diffraction maxima and structural features for the studies in which only two small-angle maxima were seen are even more tenuous. Geil has reported that for polyethylene as crystallized, the second peak relates to the lamellar thickness if the crystallization took place at atmospheric pressure,[29] whereas the correlation was with the first peak for material crystallized under pressure[30] or for annealed material.[29] Brown and Eby have reported the lamellar thickness of six melt-crystallized polyethylene specimens to lie between the two long periods, but to agree best with the second.[31] Both long periods were observed to increase with crystallization temperature. For all the above, slit collimation was used; and the ratios of long periods always exceeded 2:1. On the basis of the several observations, it has not been possible to define the sources of the two small-angle peaks.

Interlamellar Thickness

Direct microscopic measurements of the thickness of the interlamellar layer have also been elusive. Osmium staining procedures developed by Andrews[32,33] to enhance the contrast of the interlamellar region have been used to observe the microstructure of several polymers.[32-37] While uncertainties have prevented quantitative analyses of interlamellar thickness, all observations have shown an interlamellar thickness which is a substantial fraction of the crystallite thickness.

The hope of quantitative measurements more probably lies primarily with small-angle x-ray scattering (SAXS) techniques, which are quite sensitive to periodic changes in electron density. Fischer and Schmidt were the first to detect changes in interlamellar thickness by using a SAXS procedure in polyethylene quenched to room temperature after annealing.[38] They found that during the initial stages of the annealing process the crystallinity decreased while the SAXS long period increased. They thus concluded that partial melting of the lamellae and expansion of the interlamellar region had occurred. Lower initial crystallinity and greater increases in long period occurred at higher temperatures, indicating that the interlamellar spacing had also increased with temperature. Unfortunately, the data are ambiguous for the later stages of annealing, when both crystallinity and long period were increasing. It could not be determined if only the lamellae thickened or if both lamellar and interlamellar thicknesses had increased. In another type of experiment, the intensity of the SAXS peaks is monitored during heating or cooling of the material. This measurement is useful, since it can be related to lamellar structure. It can be shown that,

for a very regular stacking of lamellae, the intensity I of the nth order small-angle peak must follow the law,

$$I_n \propto (\rho_c - \rho_a)^2 \sin^2(\pi n t / P) \tag{2}$$

where ρ_c and ρ_a are the densities of the crystalline and interlamellar (amorphous) regions, respectively; P is the periodicity of lamellar stacking, and t is the thickness of the interlamellar zone. Thus variations in I_n must be related either to the density difference $\rho_c - \rho_a$ or to the interlamellar thickness t. Nukushina et al.,[39] using polyethylene single-crystal mats, and Schultz et al.,[25] using bulk polyethylene, have noted reversible peak-height intensity changes up to fourfold. In the temperature regime below the critical temperature for onset of annealing phenomena (associated with the crystallization temperature in bulk polymers), any changes in long period P were found to be very small. This intensity effect was assumed to be much larger than that which would arise from density changes alone, hence to point toward a reversible change in t, the interlamellar thickness. In order to explain the data, a theory was presented for the reversible loosening of surface defects (chain folds, tie chains, or chain-end cilia) at the expense of the crystals, i.e., "surface melting" of the lamellae.

O'Leary and Geil, investigating polyoxymethylene, stretched nylon and poly(ethylene terephthalate),[40] found significant degrees of reversibility in both SAXS intensity and long period following annealing at temperatures far above the original crystallization temperature. The reversibility in long period was much greater than has been observed to date in polyethylene.[39,41] The data again did not permit separation of the effects of dimensional changes in the lamellae and interlamellar regions, nor could the contribution of density changes be assessed. The observations are intriguing because they imply one of the following.

1. The lamellae undergo reversible changes in dimension above the crystallization temperature. This would be in conflict with crystallization theories and observations which hold that the extended-chain configuration is thermodynamically favored and that folded-chain crystals form only at high supercooling where folded-chain nucleation is more rapid. According to this view, annealing above the crystallization temperature should permit the lamellae to thicken, but cooling should have no effect.

2. The small-angle long period is not related to the lamellar spacing.

3. The interlamellar region is subject to greater dimensional change and has more influence on lamellar periodicity than has generally been realized.

Need for Further Research

In general, the SAXS measurements have indicated in a qualitative way that the interlamellar zone in polyethylene thickens with increasing temperature. However, the crystallinity measurements referred to have not been quantitative, nor have the SAXS intensity measurements been unambiguous. Unfortunately, it has not been possible to say just how much

the interlamellar distance changes nor what its value is at some particular
condition. As for the lamellae, below the crystallization temperature the
evidence indicates that they "melt" to some extent with increasing tem-
perature. Above the crystallization temperature, it is known for certain
only that the periodicity of the stacked lamellar structure increases dramati-
cally. However, data are lacking which can show what this signifies. It
is not clear whether the lamellar thickness increases or whether the inter-
lamellar zone thickens, or both. Quantitative measurements of crystal-
linity, long period, and lamellar and interlamellar densities are all needed
to define the changes which occur simultaneously in the lamellae and in the
interlamellar zones. It was to these measurements that this study was
directed. Specifically, its objectives were: to determine the thickness and
density of the interlamellar regions in bulk polyethylene: to characterize
the lamellae as to thickness, mosaic block dimensions, density, volume
fraction, and intralamellar disorder of the first and second kinds; to deter-
mine how the above structural features depend on the temperature at which
the material is crystallized and the temperature at which it may be found,
and thus to define in large degree the morphology of the polymer.

THEORETICAL

Degree of Crystallinity and Intralamellar Disorder

The meaning and measurement of the degree of crystallinity of polymers
in the context of conflicting views of polymer structure have been discussed
in detail elsewhere.[2,22] In brief, if a measurement of degree of crystallinity
is to be meaningful, the method of measurement must distinguish between a
one-phase homogeneously disordered structure and a two-phase structure
consisting of relatively ordered and relatively disordered regions. Further,
if a two-phase structure exists, small intracrystalline defects of atomic di-
mensions should be included in the measurement of the crystalline content.

Part I of this study[2] described in detail the x-ray diffraction method de-
veloped for the simultaneous determination of crystallinity (including
intracrystalline defects) and effective Debye-Waller factors. It was found
that Marlex 6002 polyethylene unambiguously constituted a two-phase
system under the conditions of the investigation. Measurements of the
degree of crystallinity were based on the following relation, believed to be
rigorous:

$$I_{ABS} = v_{cr} \left| F_{hkl} \right|^2 D_{hkl} \tag{3}$$

where I_{ABS} is the observed absolute intensity of the (hkl) Bragg reflection
(electrons)^2/unit cell, v_{cr} is the volume-fraction crystallinity, including
intracrystalline defects, F_{hkl} is the structure factor of the unit cell for the
(hkl) reflection, and D_{hkl} is an effective Debye-Waller function, i.e., a dis-
order function which must be found appropriate to the polymer.

Interlamellar Density

Following the suggestion of Hermans and Weidinger,[17] measurement of the density of the amorphous region of semicrystalline polyethylene was based on the principle of conservation of scattered intensity. Guinier and Fournet[18] show that when the x-ray beam is slit-collimated and effectively infinitely high, as was the case here, the appropriate form of the conservation principle is as follows:

$$2\pi/V \int_0^\infty S\tilde{g}(S)dS = (\rho_c - \rho_a)^2 v_c(1 - v_c) \tag{4}$$

where $\tilde{g}(S)$ is the "slit-smeared" absolute intensity and v_c is now the volume fraction crystallinity.

The units of eq. (4) are (electrons)^2/Å^6. When expressed in terms of the experimental quantities and for ρ_c and ρ_a expressed in units of g/cc, eq. (4) becomes (see the Appendix):

$$(\rho_c - \rho_a)^2 v_c(1 - v_c) = \left(\frac{m}{ZN}\right)^2 \frac{2\pi V_c \times 10^{24}}{r_e^2 E_0 \bar{w} h t^2 \exp\{-\mu t\}} \int_0^\infty S\tilde{g}_{exp}dS \tag{5}$$

where m is the molecular weight of the polymer repeat unit (14 for —CH$_2$—); Z is the number of electrons per repeat unit (8 for —CH$_2$—); N is Avogadro's number; r_e is the classical radius of an electron ($r_e^2 = 7.83 \times 10^{-26}$ cm^2); V_c is the unit cell volume (Å^3); $\bar{w}$ is the average breadth of the beam at the sample position (cm); h is the height of the beam at the sample position (cm); t is the sample thickness (cm); μ is the absorptivity of the sample for the x-radiation; S is the magnitude of the scattering vector $S = 2\sin\theta/\lambda$; E_0 is the primary beam intensity at the sample position in arbitrary units. The experimental scattered intensity $\tilde{g}_{exp}$ is corrected for background scattering (in the same units as E_0). Thus, we have

$$\tilde{g}_{exp} = \tilde{g}_{sample} - \tilde{g}_B \exp\{-\mu t\}$$

where $\tilde{g}$ sample is the measured intensity with the sample in position and $\tilde{g}_B$ is the background intensity without a sample in the x-ray beam.

Small-Angle Long Period

If the x-ray beam has a finite height, although it be infinitely narrow, there is nevertheless a range of incident angles to the sample. Thus, scattering is produced over a range of angles and the resulting data are said to be "slit smeared." The result of the slit smearing is to shift the small angle maxima toward longer angles in a manner related to the beam geometry and the positions of the maxima. Guinier and Fournet[18] show the following relation to hold between the measured intensity distribution $\tilde{g}(S)$ and the true scattered intensity $I(S)$:

$$\tilde{g}(S) = \int_0^\infty W(y) I(\sqrt{S^2 + y^2})dy \tag{6}$$

where y is the ordinate of a point in the beam and $W(y)$ is a weighting function describing the fraction of the total beam power at y.   If the height of the beam is at least equal to the diameters of the scattering rings, the beam is effectively infinitely high.   In this case, and for a Gaussian weighting function, a solution to eq. (6) is:

$$I(S) = - \frac{\exp\{k^2 S^2\}}{k\sqrt{\pi}} \int_0^\infty \frac{\tilde{g}'(\sqrt{S^2 + u^2})}{\sqrt{S^2 + u^2}}\, du \qquad (7)$$

where k is a constant and

$$\tilde{g}'(\sqrt{S^2 + u^2}) = \frac{d\tilde{g}(\sqrt{S^2 + u^2})}{d(\sqrt{S^2 + u^2})} \qquad (8)$$

Schmidt[42] has devised a fast numerical solution to eq. (7) and programmed it for a digital computer. Schmidt's program (modified in its input requirements by F. Wilson) was checked for correctness and used in this work.   In the apparatus employed here, the weighting factor was constant (constant beam intensity).

Lamellar and Interlamellar Thickness

The lamellar and interlamellar thicknesses measured in this study were based on identification of the first SAXS long period P_1 (after slit-height correction) with the average periodicity of a stacked lamellar model (Fig. 2).   The lamellae were considered to be of constant thickness, but variably spaced, reflecting paracrystalline disorder in the stacking arrangement. From the geometry, the lamellar thickness l and the average interlamellar spacing $\bar{l}$ are related to the degree of crystallinity as follows:

$$l = v_{cr} P_1$$
$$\bar{l} = (1 - v_{cr}) P_1 \qquad (9)$$

where v_{cr} is the volume fraction crystallinity.

Stacking Disorder

In general, the intensity scattered by an object is [43]

$$I(\mathbf{S}) = \frac{F^2(\mathbf{S})}{V} \bar{z}(\mathbf{S}) * |\bar{\sigma}(\mathbf{S})|^2 \qquad (10)$$

where F is the structure factor of the average scattering unit; $Z(\mathbf{S})$ is the Fourier transform of $Z(\mathbf{x})$; $Z(\mathbf{x})$ is the probability density of finding a scattering unit within the volume dv_x at the extremity of vector $\mathbf{x}$, one scattering unit being at the origin of coordinates; and V is the volume of the object. The quantity $\sigma(\mathbf{S})$ is the Fourier transform of $\sigma(\mathbf{x})$, the "form function" of the object; $\sigma(\mathbf{x})$ is unity when the terminus of the vector $\mathbf{x}$ is inside the object and zero otherwise.   The asterisk denotes the convolution integral.

The disordered stacked lamellar structure under consideration may be considered a one-dimensional paracrystal of N scattering groups. For such a structure Guinier[43] evaluated eq. (10) at the Bragg condition ($S = n/P$):

$$I(S = n/P) = \frac{F^2(S)}{V} N^2 \left[\frac{1 - H^2}{1 + H^2 - 2H} \right] \equiv \frac{F^2(S)}{V} N^2 \bar{Z}(S = n/P) \quad (11)$$
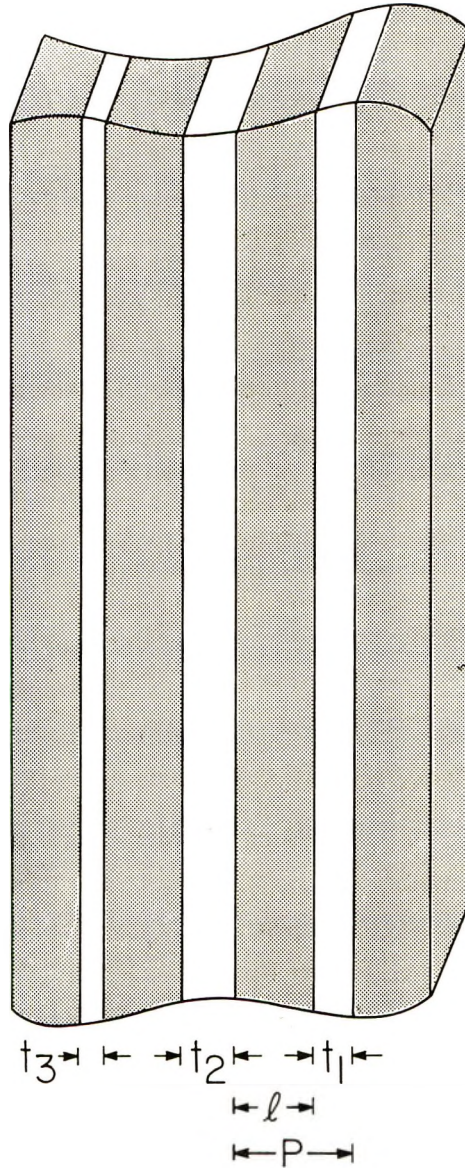
Fig. 2. Stacked lamellar model of Reinhold et al.[24] Constant lamellar thickness. Randomly distributed interlamellar spacing l.

where $H = \exp\{-2\pi S^2 g_p{}^2\}$, g_p is a constant characteristic of the extent of paracrystalline disorder, P is the average periodicity of the structure, and the quantity is $\bar{Z}(S = n/P)$ is defined.

The particle factor for the disordered stacked lamellar structure has been given by Reinhold, et al.:[24]

$$F^2(S) = H^2 \frac{\sin^2(\pi Sl)}{(\pi S)^2} \tag{12}$$

where l is the lamellar thickness. Thus, the intensity scattered by a stacked lamellar paracrystal at the Bragg condition $(S = n/P)$ is

$$I = \frac{N^2}{\pi^2 V} \frac{P^2}{n^2} H^2 \sin^2\left(\frac{n\pi l}{P}\right) \bar{Z}(S = n/P)$$

If first-order and second-order reflections of the same periodicity are seen, the ratio of their intensities is as follows:

$$\frac{I_1}{I_2} = 4 \frac{\sin^2(\pi l/P)}{\sin^2(2\pi l/P)} \frac{\bar{Z}(S = 1/P)}{\bar{Z}(S = 2/P)} \tag{13}$$

Rearranging, we have

$$\bar{Z}(S = 1/P) - \left[\frac{1}{4}\frac{I_1}{I_2}\frac{\sin^2(2\pi l/P)}{\sin^2(\pi l/P)}\right]\bar{Z}(S = 2/P) = 0 \tag{14}$$

This is an equation in only one unknown, the paracrystalline stacking parameter g_p.

EXPERIMENTAL

Apparatus

The apparatus has been described in detail elsewhere.[45] In order to achieve the objectives of this investigation, both small-angle and wide-angle x-ray scattering measurements were needed closely spaced in time on the same specimens, maintained at controlled temperatures. Both sets of measurements on a sample were made without having to alter the sample environment and within a period of four hours.

The x-ray diffractometer employed a ground and bent focusing monochromator and Johansson-Guinier[44] optics. An x-ray beam was produced whose width at half-intensity was 4×10^{-4} radians and whose height in relation to the SAXS maxima was effectively infinite.[18] Beam intensity was constant along its length. The SAXS limit of resolution of the diffractometer was between 800 and 1000 Å, depending on the magnitude of the scattered intensity. The wide-angle limit of resolution was $0.05°(2\theta)$ as measured by the half breadth of the (110) reflection from quartz. The spectral purity of the CuKα_1 radiation used was very high[2] and enabled use of calibrated brass attenuators to weaken and measure the primary beam and thus to evaluate the absolute intensities.

Specimens were maintained at elevated temperatures during x-ray studies by means of closed-loop circulation of heated helium through a sample cell fabricated of a glass-reinforced plastic with low thermal conductivity. Specimen temperature control was ±0.14°C.

Material

The material studied was Marlex 6002 high density polyethylene. Properties reported by Phillips Petroleum Company for this material are listed in Table IV of Part I.[2] The x-ray specimens were sheets, 1 mm thick, compression-molded at 170°C to eliminate influence of prior history. After molding and relaxation at 170°C the hot-molding platens were transferred to a constant temperature bath for crystallization. Crystallization times permitted were 1 day at 110°C, 118°C, and 123°C, three days at 126°C, and one week at 129°C. Pinhole powder diagrams of the specimens showed no preferred orientation of the crystallites.

Procedure

The experimental program was in two parts. In the first part, samples crystallized at 110°C were studied at temperatures ranging from 25°C to 129°C at time intervals of 3 hr, 1 day, and 3 days. Between x-ray runs, samples were immersed in mercury and maintained at temperature regulated to ±0.1°C. After 3 days at temperature the samples were reexamined at 25°C. In the second series of runs, samples crystallized in a constant temperature bath at temperatures from 110 to 129°C were characterized at 25°C. The densities of the x-ray specimens were determined at 25°C by the density-gradient method. Densities at elevated temperatures were determined dilatometrically according to the method of Bekkedahl,[45] with specimens subjected to the same time and temperature schedule as the x-ray specimens.

The wide-angle x-ray measurements have been described previously.[2] SAXS measurements were usually made over the angular range $-0.10°$ $\leq 4\theta \leq 1.40°$, by stepping the detector and counting scintillations at each position. At each step the x-ray intensity was measured with and without the sample in the x-ray beam in order to determine background scattering. Over the range $0 \leq 4\theta \leq 0.4°$, the scattered intensity was measured at least twice at each angular position for the dual purposes of measuring and reducing experimental errors. At least 1000 pulses were counted at each position. Up to $4\theta = 0.8°$ the number of pulses was usually at least 10,000.

Figure 3 is a plot of small-angle x-ray scattering at 25°C for a sample crystallized at 110°C. This may be considered a typical run. Plots of all experimental data are given elsewhere.[46] Two curves are shown in the figure. One is drawn through the experimental points. The second was calculated from the first by the slit-height correction procedure of Schmidt.[42] Both curves show two broad scattering bands. The desmeared curve also shows a small sharp maximum at $4\theta = 0.90°$, corresponding to the inflection
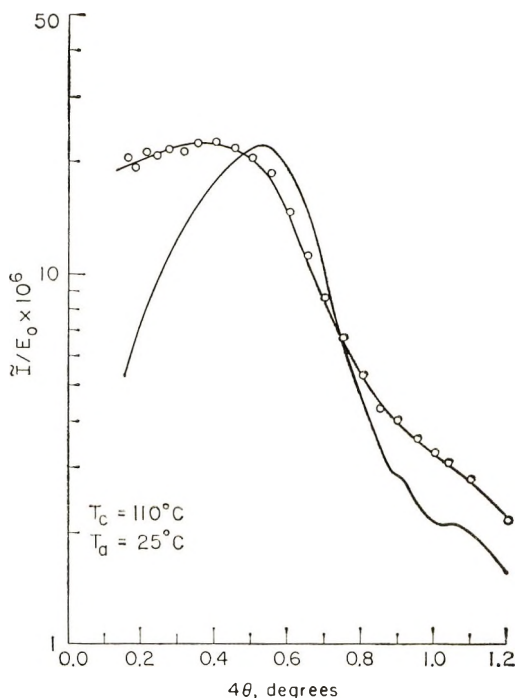
Fig. 3. Example of small-angle x-ray data: (O) experimental data: (——) after slit height correction.

region of the experimental data. This sharp peak is a spurious detail resulting from sensitivity of the desmearing procedure to random errors in the experimental data. It can be suppressed by appropriate smoothing of the data. The magnitudes and positions of the broad peaks are, however, insensitive to data fluctuations. The positions of all peaks (including spurious ones) are given in reference 46. Only the positions of the broad peaks are treated here.

The integration of eq. (4) was carried out by fitting a linear equation in S to $\tilde{g}_{exp}$ between successive points, then multiplying by S and analytically evaluating the integral of the resulting quadratic.

The data were extrapolated to zero angle by extending at constant intensity the lowest angle reliable point to $4\theta = 0°$. Because of the multiplication by S, this interval contributed only about 5% of the total integral. The extrapolation of the data to infinity was based on fitting to the last data point an equation of the form

$$\tilde{g}_{exp} = c/S^2$$

where c is a constant. This is the theoretical asymptotic form of the small angle scattering valid for particles of any shape.[18] The extrapolation to infinity contributed roughly 25% of the total integral.

RESULTS

The principal results of this portion of the investigation are measurements for Marlex 6002 polyethylene of long period, interlamellar spacing, overall density, interlamellar density, and the relationships among these quantities, temperature and time.

Density Relationships

Overall Density.   Figure 4 presents the results of a dilatometric density study of Marlex 6002 crystallized at 110°C and exposed to temperatures of 23–110°C for periods up to 3 days.   Density was independent of time over this range and reversible with temperature.   No change in the density of
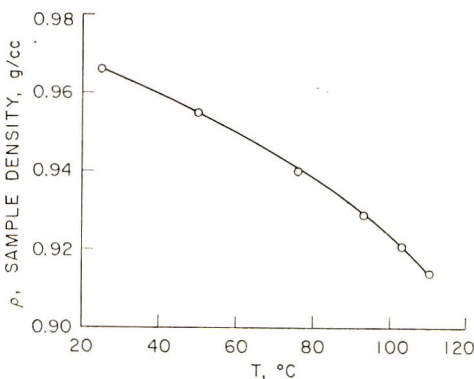
Fig. 4. Density of sample crystallized at 110°C at temperatures between 23°C and 110°C.
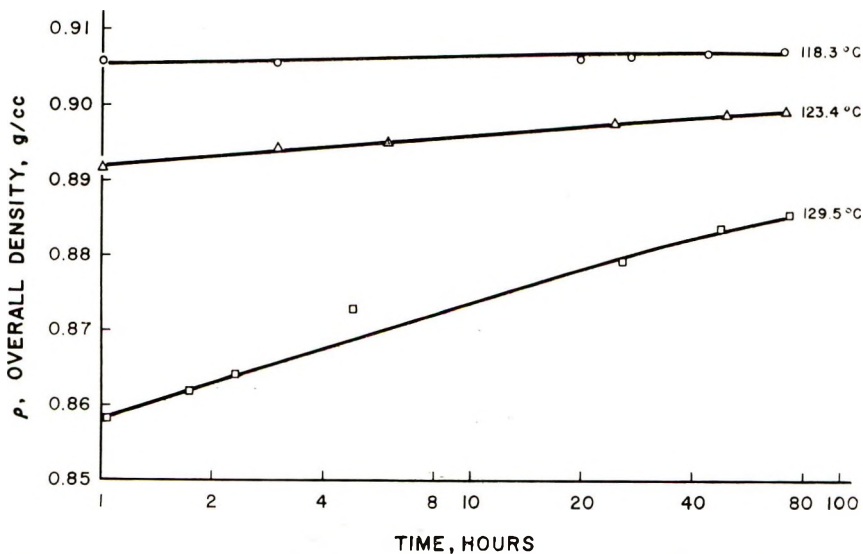
Fig. 5. Density of sample crystallized at 110°C after annealing at temperatures above 110°C.
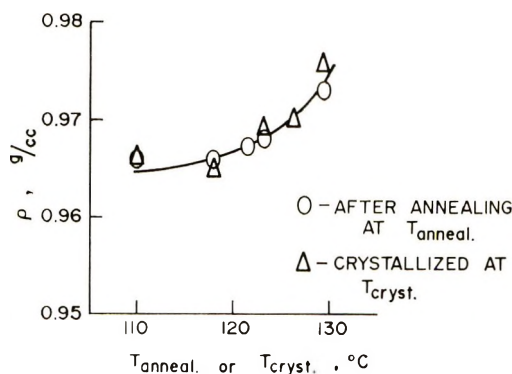
Fig. 6. Density of annealed samples upon return to 25°C. Density at 25°C of samples crystallized at 110–129°C.
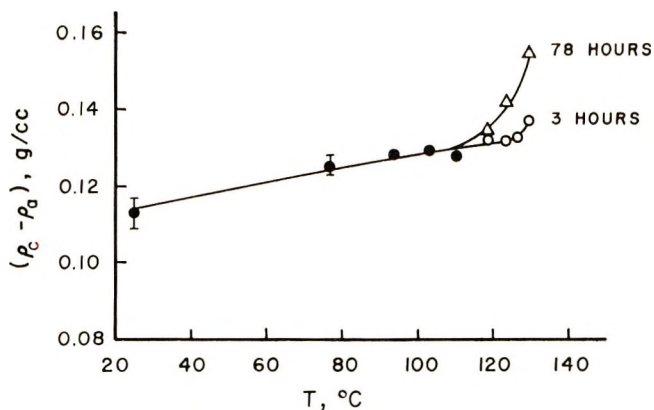
Fig. 7. Density difference between phases.

the sample was seen upon return to 23°C after exposure to the elevated temperature for the three day period.

At temperatures above 110°C, sample density was time-dependent, and an annealing effect was observed.   Figure 5 presents data obtained at 118.3, 123.4, and 129°C for a sample crystallized at 110°C.   After initial thermal equilibration, sample densities decreased slightly over a period of about 15 min (not shown).   Thereafter, sample densities increased approximately logarithmically with time.   The rate of density increase was more rapid at the higher temperatures.   The densities of these samples upon their return to 25°C are presented in Figure 6.   Also shown are the densities at 25°C of samples crystallized isothermally at the same temperatures.   The overall density increased both with increased annealing temperature above the crystallization temperature and increased crystallization temperature. A single curve can reasonably be drawn through both sets of data.

Lamellar–Interlamellar Density Differences.   Lamellar–interlamellar density differences were obtained from measurements of the small-angle
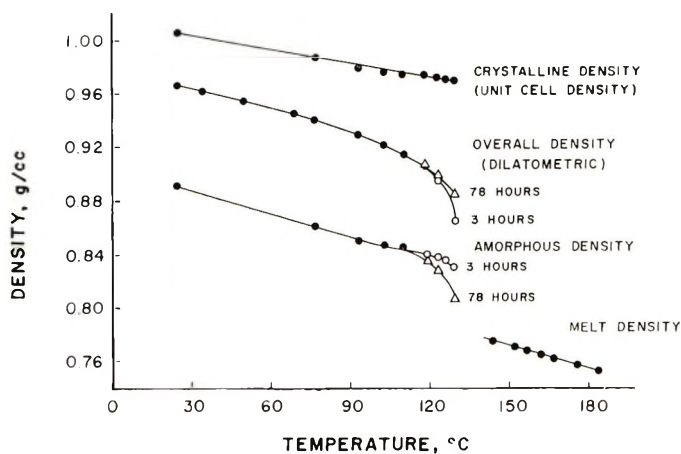
Fig. 8. Density–time–temperature relationships for crystalline, amorphous, partially crystalline, and liquid states of Marlex 6002.

scattering power and the volume-fraction crystallinity as related to eq. (4). Data on degree of crystallinity are reported in Part I of this study.[2] Figure 7 presents the measured density differences between the crystalline and amorphous phases. Below the crystallization temperature of the sample, $(\rho_c - \rho_a)$ increased reversibly from 0.113 g/cc at 25°C to 0.128 g/cc at 110°C. Above the crystallization temperature, $\Delta\rho$ increased more rapidly and changes were no longer reversible upon cooling. The effect of annealing at these higher temperatures was to increase $\Delta\rho$ with time. At 129°C, $\Delta\rho$ increased from 0.128 g/cc after 3 hr at temperature to 0.155 g/cc after 3 days at temperature.

Density–Time–Temperature Relationships for Marlex 6002. Figure 8 presents density–time–temperature relationships for crystalline, amorphous, partially crystalline, and liquid states of Marlex 6002. The crystalline densities shown are the unit cell densities obtained from measurement of wide-angle x-ray positions.[2] The amorphous density was obtained by subtracting the density differences $\Delta\rho$ of Figure 7 from the unit cell densities. The overall densities of the partially crystalline material determined dilatometrically are from Figures 4 and 5. The melt densities were also obtained dilatometrically. It is noted that the density of the amorphous phase was higher than an extrapolated melt density at all temperatures in the range 25–129°C. The amorphous density at 25°C was 0.89 g/cc or almost 6% higher than an extrapolated melt density of 0.84 g/cc. Above 120°C, both overall density and amorphous density decreased sharply with temperature. In contrast to the increase of overall density with time above 110°C, the amorphous density decreased with time.

The unit-cell density[2] and melt density were well fitted over the range of the data by linear correlations with temperature. Least-squares regression equations and 95% confidence limits are presented in Table I. In addition,
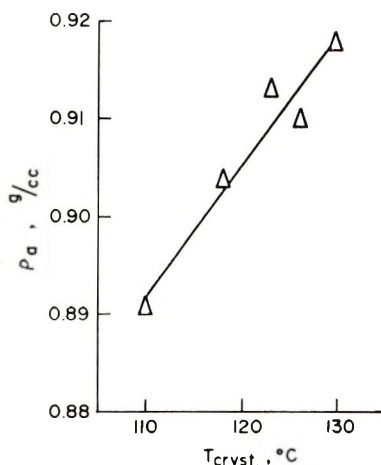
Fig. 9. Effect of crystallization temperature on amorphous density at 25°C.

Table I presents a least-squares straight line fit to the measured amorphous densities in the temperature range 25–110°C. Confidence limits for the amorphous density were not obtained from the regression analysis but were calculated instead from a Monte Carlo analysis of propagation of error.[46] Trends in the values for the amorphous density following crystallization at various temperatures were clearly defined. Upon increase of crystallization temperature from 110°C to 129°C, the amorphous density at 25°C increased from 0.89 g/cc to almost 0.92 g/cc (Fig. 9).

The effect of annealing on final amorphous density at 25°C was highly variable. The room-temperature value of the amorphous density was higher after annealing at 123 and 126°C but lower after annealing at 118 and 129°C. These differences may have resulted from uncontrolled quench rates after annealing.

TABLE I

Least-Squares Density Correlations and 95% Confidence Limits

	T, °C	Density, g/cc	Specific volume, cc/g
Unit cell properties	25–129	$\rho_c = 1.01_4 - 3.55 \times 10^{-4}T \pm 0.004$	$V_c = 0.98_0 + 3.63 \times 10^{-4}T \pm 0.004$
Melt properties	142–180	$\rho_{melt} = 0.85_7 - 5.62 \times 10^{-4}T \pm 0.003$	$V_{melt} = 1.15_0 + 9.61 \times 10^{-4}T \pm 0.004$
Amorphous phase properties	25–110	$\rho_a = 0.90_5 - 5.72 \times 10^{-4}T \pm 0.007$	$V_a = 1.10_5 + 7.40 \times 10^{-4}T \pm 0.007$

Molecular Scale Structure

Long Period at Elevated Temperatures. It is useful to note first the effects of slit-smearing on the small-angle results. SAXS long periods observed at sample temperatures of 25–126°C for Marlex 6002 crystallized at 110°C are shown in Figure 10, uncorrected for slit height effects. No data
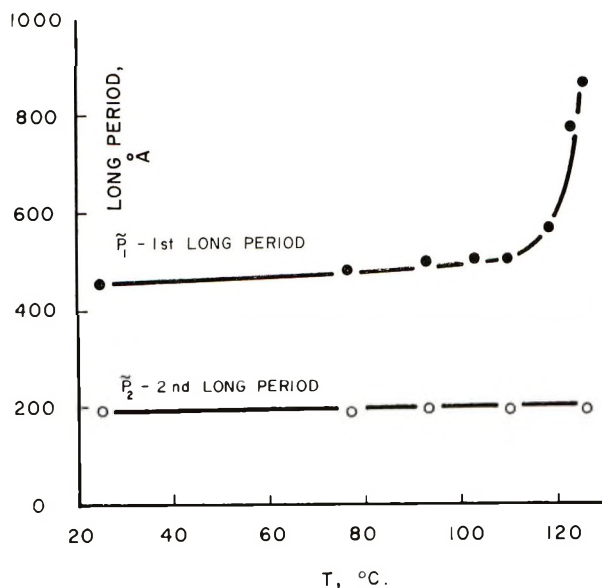
Fig. 10. Uncorrected small-angle long period.

point is shown at 129°C, as the position of the first scattering maximum was obscured by the primary beam. Figure 11 shows the corresponding relationship after correction of the data for the effects of slit height smearing. The ratio of first and second long periods, obtained from Figures 10 and 11, is plotted in Figure 12. After correction for slit height effects, the two small-angle long periods observed were in a ratio of 2:1.

The corrected long period P_1 at 25°C for Marlex 6002 crystallized at 110°C was 335 Å. It increased slightly (approximately 5%) between 25 and 110°C. Above 110°C, the long period increased at an accelerating pace, and at 126°C it was 515 Å.

No effect of annealing time on the long period was evident over the range 3 hr to 3 days. The long periods observed upon return to room temperature are listed in Table II. The increases in long period observed at the

TABLE II
Changes in Long Period Upon Annealing and Recooling of
Marlex 6002 (T_c = 110°C)

Annealing temp, °C	Long period, Å			Reversibility $\dfrac{P_1^T - P^{25}}{P_1^T - P_1^0} \times 100, \%$	Permanent change on annealing, %
	P_1^0 Initially at 25°C	P_1^T at temp T	P_1^{25}, on return to 25°C		
118	335	368	350	55	4
123	335	417	400	21	19
126	335	515	425	50	27
129	335	—	500	—	76

annealing temperatures were 20–50% recovered upon returning to room temperature; but permanent increases in long period of 4–76% occurred, the higher figure applying to the highest temperature.
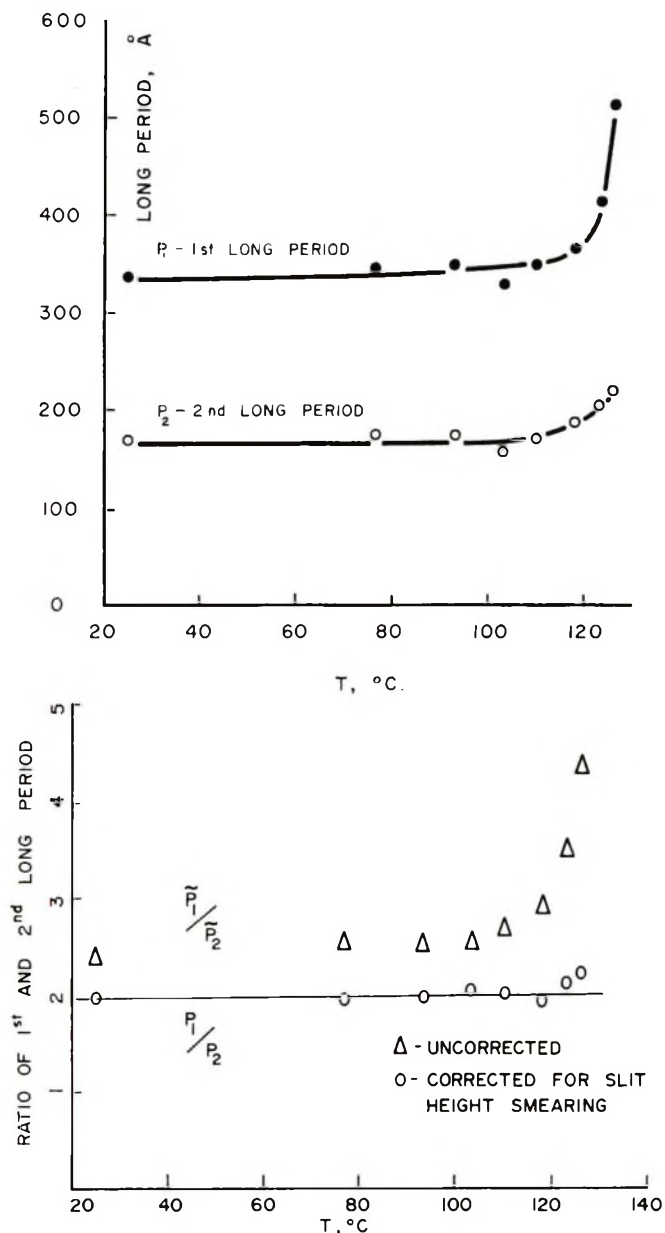
Fig. 11. Small-angle long period after slit-height correction.

Fig. 12. Ratio of first and second long periods.

Figure 13 shows the effect of crystallization temperature ranging from 110°C to 129°C on the first SAXS long period P_1, measured at 25°C. This long period increased from 335 Å to approximately 795 Å upon increasing the crystallization temperature. In comparison, a sample air quenched
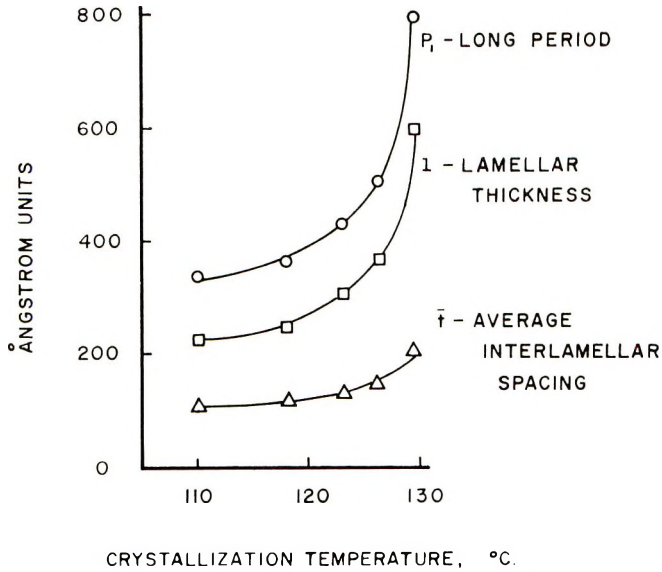
Fig. 13. Long period, lamellar thickness, and average interlamellar spacing as related to crystallization temperature.
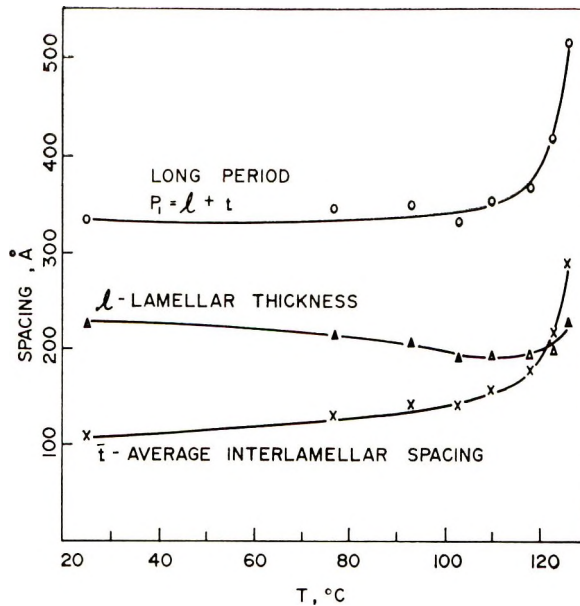
Fig. 14. Effect of temperature on long period, lamellar thickness, and average interlamellar spacing for sample crystallized at 110°C.

from 170°C to room temperature over a period of a few minutes showed a long period of 208 Å.

Lamellar and Interlamellar Thickness.   As previously noted, the results presented in this section are based on identification of the smallest-angle long period P_1 with the average periodicity of a stacked lamellar model containing paracrystalline disorder in the stacking arrangement.   The lamellar thickness l and the average interlamellar spacing $\bar{l}$ are related to the degree of crystallinity and to the average periodicity according to eq. (9). The lamellar thicknesses and average interlamellar spacings obtained from the combined small-angle and wide-angle x-ray measurements of long period and degree of crystallinity are presented for the range of ambient temperatures in Figure 14.   It should be emphasized that both the small-angle and wide-angle x-ray data used in computing one point according to eq. (9) were obtained on the same sample in the same apparatus, without change of temperature and within a short time interval.   The lamellar thickness decreased 31 Å, from 225 Å to 196 Å, over the temperature range 25–110°C.   Over the same temperature range the interlamellar thickness increased 49 Å, from 110 Å to 159 Å.   Over this temperature range, the overall periodicity expanded slightly (about 5%).

Above the crystallization temperature both lamellar and interlamellar thickness increased, but the interlamellar thickness increased more markedly.   The lamellar thickness, initially 225 Å at 25°C, increased from its minimum value of 196 Å back to 226 Å over the range 110–126°C.   In comparison, the interlamellar spacing was initially 110 Å at 25°C, and nearly tripled to 290 Å at 126°C.

The effect of annealing time on lamellar and interlamellar thickness at the annealing temperature is presented in Table III.   The SAXS long period at the annealing temperature did not measurably increase with time between 3 hr and 3 days, but over this time the lamellar thickness increased 10–18% while interlamellar spacing decreased 8–15%.   The greatest changes with time occurred at the highest annealing temperature.

The spacings observed upon returning the polymer to 25°C are recorded in Table IV.   The lamellar thickness increased by a factor of about one-fourth on cooling.   In contrast, the interlamellar spacing shrank by half.

TABLE III
Effect of Annealing Time on Lamellar and Interlamellar Thickness Marlex 6002 (T_c = 110°C); Measurements Made at Annealing Temperature

| Annealing temp, °C | Lamellar thickness l, Å | | | Average interlamellar spacing, $\bar{l}$, Å | | |
| | Annealing time | | Change, % | Annealing time | | Change, % |
	3 hr	3 days		3 hr	3 days	
118	191	210	+10	177	158	−11
123	200	229	+14	217	200	−8
126	226	268	+18	289	247	−15

TABLE IV

Changes in Lamellar and Interlamellar Spacings upon Annealing and Recooling of Marlex 6002 (T_c = 110°C), Annealed Three Days

	Annealing temperature		
	118°C	123°C	126°C
Lamellar thickness			
Initial at 25°C, Å	225	225	225
At annealing temperature, Å	210	229	268
On return to 25°C, Å	245	300	320
Change on cooling, %	+16	+31	+19
Change from initial thickness, %	+9	+33	+42
Interlamellar spacing			
Initial at 25°C, Å	110	110	110
At annealing temperature, Å	158	200	247
On return to 25°C, Å	105	100	105
Change on cooling, %	−33	−50	−57
Change from initial thickness, %	−5	−10	−5

The lamellar thickness was increased 9–42% from its original dimensions by the annealing process, higher figures applying to higher temperatures. The interlamellar spacing was reduced approximately 5%, independent of the annealing temperature. Overall, the long period was permanently increased by 4–27% over the same temperature range (Table I).

Figure 13 shows the lamellar and interlamellar thickness measured at 25°C for samples crystallized at temperatures ranging from 110 to 129°C. The lamellar thickness and interlamellar spacing both increased with crystallization temperature, but the lamellar thickness tripled over this range while interlamellar spacing only doubled.

Stacking Disorder. By using the ratio of the first-order and second-order small-angle maxima, eq. (14) was solved iteratively to yield values of the paracrystalline stacking parameter g_p. Values of g_p were computed only for runs in which l/P exceeded 0.67; solutions of eq. (14) become increasingly imprecise as l/P approaches one-half. It was found that the paracrystalline stacking disorder was 12–18% of the average periodicity, independent of crystallization temperature, as is indicated in Table V.

TABLE V

Effect of Crystallization Temperature on Stacking Disorder

T_c, °C	Lamellar thickness, Å	Long period, Å	I_1/I_2	Paracrystalline parameter g_p
110	225	335	11.4	0.12
118	247	363	9.3	0.18
123	301	430	9.6	0.14
126	363	504	8.5	0.16
129	596	795	7.3	0.12

DISCUSSION

Lamellar and Interlamellar Zones

The previous section has presented data on the degree of crystallinity, long period, lamellar thickness, interlamellar spacing, and the phase densities. The degree of crystallinity was determined by an absolute procedure[2] simultaneously with the SAXS measurements, so that changes in the lamellar and interlamellar regions could be distinguished. To bring all of the results into sharper focus, we consider the simultaneous changes which occurred in Marlex 6002 polyethylene, crystallized at 110°C, upon holding at temperatures between 25 and 129°C and then recooling.

These changes are illustrated in Figure 15. First of all, (Fig. 15A) at 25°C the long period was 335 Å and the degree of crystallinity was 67% by volume. In view of the stacked lamellar structure of the material, this must mean that the average thickness of the zone in which the atoms were sufficiently well ordered to diffract x-rays sharply was 225 Å (0.67 × 335 Å). This well ordered zone (which does not include disordered surface layers) has been referred to as the lamellar thickness. It is similarly to be concluded that the average space between the well ordered zones was 33% of 335 Å or 110 Å. This relatively disordered region, referred to here as the interlamellar zone, includes the fold surfaces of the lamellae, interlamellar tie molecules, chain end cilia, and molecules trapped during crystallization between the lamellae but not connected to them. The interlamellar density at 25°C was 0.89 g/cc as compared to 0.84 g/cc for an extrapolated melt density. Thus, the interlamellar zone in the semicrystalline polymer, though it gave a diffuse x-ray scattering pattern, was evidently more ordered than a liquid phase.
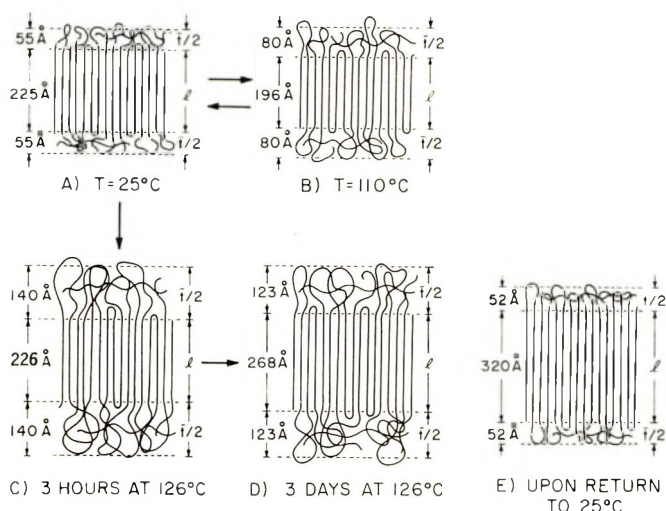
Fig. 15. Microstructural effects of temperature and time.

Upon heating of the polymer to 110°C, the long period increased about 14 Å to 349 Å, while the degree of crystallinity decreased to 55% by volume. Thus, the lamellae apparently became thinner on the average, their thickness dropping to 196 Å (Fig. 15B). The interlamellar spacing increased to 155 Å, picking up the roughly 30 Å lost by the lamellae and causing the 14 Å increase in long period. Temperature-induced changes of this type were observed up to the original crystallization temperature of 110°C and were reversible on recooling to 25°C. The observation of reversibility is evidence for the existence of an equilibrium between the well-ordered regions and the surface layers of the lamellae.[47]

Upon continuing the heating of the polymer above the crystallization temperature, the interlamellar zone continued to thicken but the lamellae reversed the decreasing trend shown below 110°C and thickened also. At 126°C the long period increased to 515 Å and the degree of crystallinity decreased to 44%. Thus the lamellar thickness had increased to 226 Å and the interlamellar zone had increased to 289 Å (Fig. 15C). The change in the interlamellar zone accounted for the largest part of the increase in the long period.

Comparison of the changes in the small-angle long period and the specific volume provides evidence of possible changes in the number of lamellae in the sample upon increasing the temperature from 25 to 110°C. In this temperature range the SAXS long period increased 4% while specific volume increased 5.7%. Thus the number of lamellae seems to have remained approximately constant between 25 and 110°C. In contrast to the indication of an approximately constant number of lamellae below 110°C, the number of lamellae must have decreased between 110°C and 126°C. This was evidenced by an increase in specific volume between 110°C and 126°C of only 3% as compared to a long period increase of 46%. The increased long period is possible within approximately the same volume only if the number of lamellae decreased. Thus, above the original crystallization temperature a process of melting and recrystallization appears to have occurred.

Upon continuation of the heating of the polymer above the crystallization temperature of 110°C, several of the properties measured became time-dependent. These were: degree of crystallinity, thickness of the lamellar and interlamellar zones, and interlamellar density. The long period did not change noticeably with time.

Annealing for 3 days caused small (ca. 10%) increases in the degree of crystallinity and the lamellar thickness and small (ca. 10%) decreases in the interlamellar spacing and the interlamellar density (Fig. 15D). This last effect is interesting in conjunction with the increase in crystallinity. It suggests possible depletion of the interlamellar zone by incorporation of chains into adjoining lamellae. Possibly the effect was caused by tie molecules and molecules attached to one or the other lamellae being "reeled in" during annealing. Formation of new lamellae between existing lamellae is not indicated, for this would have caused a decrease in long period

and such was not observed.   The formation of voids during annealing is not believed to have occurred in most specimens, since good agreement was obtained in cross-checks of density and x-ray determinations of degree of crystallinity (see below).

Upon returning the polymer to room temperature after annealing, the long period decreased 4–17%, maintaining 20–55% of its previous increase at the annealing temperature.   The decrease in long period on cooling resulted entirely from a decrease in the interlamellar thickness (Fig. 15E). The interlamellar spacing at 25°C was about half of its value at 126°C and 5–10% less than in the polymer as-crystallized.   The lamellar thickness was 9–42% greater than the original value after annealing and recooling.

Nukushina et al. had previously noted a 10% decrease in long period upon cooling polyethylene single crystals from 120°C.[39]   Zubov and Tsvankin[48] found a 9% decrease in long period upon cooling oriented polyethylene fibers from 113°C.   O'Leary and Geil[40] had also noted decrease in both small-angle scattered intensity and long period upon cooling from annealing temperatures.   The simultaneous measurements of degree of crystallinity and long period of this study have shown that the most influential cause of both intensity and long-period changes occurring upon cooling are associated with the contraction of the interlamellar zone.

Crystallizing the polymer at temperatures above 110°C had the effects of increasing long period, crystallinity, lamellar thickness, interlamellar spacing, interlamellar density, and lamellar mosaic-block size.   Not surprisingly, the overall effect of crystallization at higher temperatures, at which the rate of crystallization was reduced, was to enhance the general level of order.

Identification of the First Long Period with Lamellar Periodicity

The identification in this study of the first SAXS long period with the periodicity of the stacked lamellar structure of the polymer requires comment.   In the few studies of polyethylene in which both electron microscopy and SAXS measurements have been made and in which two, rather than three, SAXS long periods have been seen,[29–31] the evidence has been conflicting as to whether the first or second long period corresponded to the structural periodicity of the stacked lamellae.   Both long periods changed in response to sample history, but they were in a ratio exceeding 2:1 and seemed not to be different orders of reflection by the same periodic structural feature.   However, in each of the studies referred to, the SAXS data were obtained with slit-collimated beams but were not corrected for the effects of slit-height smearing.

The data of this study were also obtained with a slit-collimated beam but were corrected for the effects of slit-height smearing.   In this study, also, the uncorrected data showed a ratio of long periods in excess of 2:1.   However, the significant point of departure is that after correction, the long periods were in a ratio of almost precisely 2:1.   This fact is an indication

of the importance of the slit-height correction, and, most significantly, it suggests that the two small-angle reflections are indeed produced by the same structural feature.

Interlamellar Density

That the density of the amorphous regions of partially crystalline linear polyethylene is greater than that of the supercooled melt had previously been reported by Fischer et al.[21] from measurements of the small-angle scattering power of highly stretched linear polyethylenes, by Swan[13] on the basis of calculations from overall and unit cell densities, and by Sella[15] from measurements of average chain spacings in the amorphous regions. Other data which fall into alignment with this finding are presented in the work of Mandelkern et al.,[11] Okada and Mandelkern,[6] and Hendus and Schnell.[3]

The density of the amorphous phase as it exists in the partially crystalline polymer was obtained in this study from measurements of the total small-angle scattering power, the volume-fraction crystallinity, and the density of the crystalline phase. The relation between these quantities, eq. (4), is based on the following premises:[19] (1) scattering particles are small compared to the irradiated sample volume but large compared to atomic dimensions; (2) there prevails random orientation (or spherical symmetry) of scattering particles; (3) particle densities are constant in a given sample, and interparticle densities are also constant in a given sample; (4) only two phases are present.

The first and second premises are justified by the small size and spherical symmetry of the stacked lamellae within the spherulites. The third premise is a statement that density differences among particles are small as compared to density differences between the phases. This seems to be a valid assumption. As for the last premise, if voids were present in the solid of the order of size of the scattering particles, the form of eq. (4) for the scattering power would no longer be valid. The total scattering power would be increased by the presence of the voids and the measurements of the interlamellar density would be too low. On the other hand, if voids of a size much larger than particle dimensions were present, scattering would be increased at such small angles that the increase would not be observed. Thus, measurements of interlamellar density at worst represent a lower limit on the actual interlamellar density.

Evidence on the presence of voids comes from comparison of x-ray and density determinations of volume-fraction crystallinity from measured values of lamellar (unit cell) density, interlamellar density, and overall density. Data obtained under all experimental conditions are plotted in Figure 16. With the notable exception of five points on the figure (six experimental conditions) the correspondence between x-ray and density determinations of crystallinity was excellent. Interestingly, the six runs in question had two factors in common. First, all but one of the samples had been quenched after annealing or after crystallization at an elevated temperature. The last sample had been quenched directly from the melt at
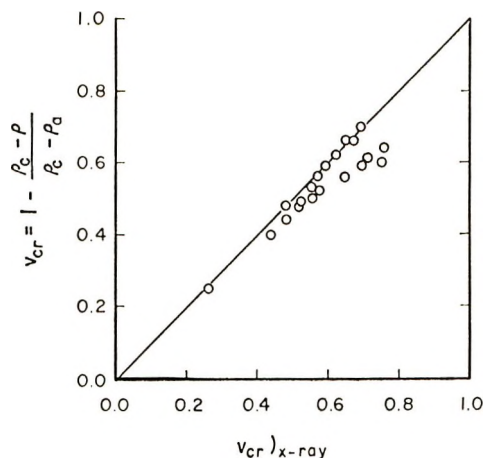
Fig. 16. Degree of crystallinity. Consistency of measurements of lamellar, interlamellar, and overall density with wide-angle x-ray determination.

170°C. Secondly, all of the deviations were toward lower crystallinity by the density measure. Thus, it is indicated that voids were present in these six specimens, the voids probably being produced as a result of shrinkage during quenching. However, since the measured interlamellar densities were not smaller than those found in other runs, it would seem that the voids were large as compared with particle dimensions and did not contribute to the measured small-angle scattering power.

CONCLUSIONS

The following conclusions have been reached regarding the structure, properties, and behavior of a melt-crystallized linear polyethylene.

1. A two-phase structure exists in the polymer. The more ordered phase scatters x-rays sharply and for material crystallized at 110°C is identified with lamellar crystals 225 Å thick at 25°C and stacked on a repeat distance of 334 Å. Disorder of the second kind of about 15% exists in the repeat distance.

2. The less ordered phase gives a diffuse x-ray pattern and is identified with the 110 Å space between the crystals at 25°C.

3. Between 25°C and the crystallization temperature T_c of 110°C an equilibrium exists between lamellar and interlamellar regions. Upon increasing the temperature, the lamellae become thinner while the interlamellar spacing increases. Over this temperature range the changes are reversible with temperature.

4. Above T_c, changes in the morphological variables become time dependent and increasingly irreversible with increasing temperature. Above T_c both the lamellar and interlamellar regions increase in thickness with temperature, but the lamellae thicken with time, whereas the interlamellar regions become thinner with time.

5. The density of the interlamellar region is a function of sample history and is always higher than the density of a melt extrapolated to the same temperature.

APPENDIX

Evaluation of the Small-Angle Scattering Power From Experimental Quantities

The appropriate form of the conservation principle for a slit collimated x-ray beam of effectively infinite height has been given by Guinier and Fournet.[18]

$$(2\pi/V)\int_0^\infty S\tilde{g}(S)dS = (\rho_v - \rho_a)^2 v_c(1 - v_c) \tag{A-1}$$

By definition the absolute intensity is[43]

$$\tilde{g}(S) = \tilde{g}_{exp}/NI_e \tag{A-2}$$

where N is the effective number of unit cells and I_e is the Thomson scattering of a free electron. The Thomson scattering is

$$I_e = r_e^2(E_0/2A)[1 + \cos^2(2\theta)] \tag{A-3}$$

where r_e is the classical radius of the electron ($r_e^2 = 7.83 \times 10^{-26}$ cm^2); A is the irradiated cross-sectional area (cm^2); and E_0 is the energy in the primary beam. At small angles, the Thomson expression becomes

$$I_e = r_e^2 E_0/A \tag{A-4}$$

The effective number of unit cells in the sample volume V is

$$N = 10^{24} V_{eff}/V_c \tag{A-5}$$

where V_{eff} is the effective sample volume (cm^3) and V_c is the average unit-cell volume (expressed in Å^3). The effective sample volume is less than the irradiated sample volume because of absorption of energy from both the primary and secondary beams on traversing the sample. Guinier[43] shows the effective sample volume for a sheet sample with faces perpendicular to the incident beam to be

$$V_{eff} = \frac{A \exp(-\mu t)}{\mu(1 - 1/\cos 2\theta)}\{\exp[\mu t(1 - 1/\cos 2\theta)] - 1\} \tag{A-6}$$

where μ is the linear absorption coefficient; t is the sample thickness; and A is the irradiated cross-sectional area. The limit of V_{eff} at small angles is:

$$V_{eff} = At \exp\{-\mu t\} \tag{A-7}$$

Combining eqs. (A-1) to (A-7) gives

$$\tilde{g}(S) = (\tilde{g}_{exp}V_c)/0.0783 E_0 t \exp\{-\mu t\}$$

The primary beam intensity is variable at the sample position. It is convenient to express the irradiated sample volume in eq. (A-1) as

$$V = \bar{w}ht \tag{A-8}$$

where h and $\bar{w}$ are the height and integral breadth of the beam at the sample position:

$$\bar{w} = \int_{-\infty}^{\infty} I dx / E_0 \tag{A-9}$$

It follows that

$$2\pi/V \int_0^{\infty} S\tilde{g}(S)dS = \frac{2\pi V_c}{0.0783 E_0 \bar{w}ht^2 \exp\{-\mu t\}} \int_0^{\infty} S\tilde{g}_{exp}dS \tag{A-10}$$

The integral intensity of the primary beam $E_0\bar{w}$ is measured by removing the detector slit and counting with the detector opened wide. The height of the primary beam at the sample position is obtained by exposing an x-ray film mounted in the sample position.

The units of eq. (A-1) and (A-10) are (electrons)^2/Å^6. Thus for ρ_c and $_a$ expressed in g/cm^3 we have

$$(\rho_c - \rho_a)^2 v_c(1 - V_c) = \left(\frac{m}{ZN}\right)^2 \frac{2\pi V_c}{0.0783 E_0 \bar{w}ht^2 \exp\{-\mu t\}} \int_0^{\infty} S\tilde{g}_{exp}dS$$

$$\tag{A-11}$$

where m is the molecular weight of the scattering unit (14 for —CH$_2$—); Z is the number of electrons per scattering unit (8 for —CH$_2$—); and N is Avogadro's number.

The experimental intensity was corrected for background scattering by

$$\tilde{g}_{exp} = \tilde{g}_{sample} - \tilde{g}_B \exp(-\mu t) \tag{A-12}$$

where $\tilde{g}_{sample}$ is the measured intensity with the sample in position and B is the background intensity without a sample in the x-ray beam.

References

1. S. Kavesh and J. M. Schultz, *Rev. Sci. Instr.*, **40**, 98 (1969).
2. S. Kavesh and J. M. Schultz, *J. Polym. Sci. A-2*, **8**, 243 (1970).
3. H. Hendus and G. Schnell, *Kunststoffe*, **51**, 69 (1961).
4. S. Krimm and A. V. Tobolsky, *J. Polym. Sci.*, **7**, 57 (1951).
5. J. L. Matthews, H. S. Peiser, and R. B. Richards, *Acta Cryst.*, **2**, 85 (1949).
6. T. Okada and L. Mandelkern, *J. Polym. Sci. A-2*, **5**, 239 (1967).
7. M. R. Gopalan and L. Mandelkern, *J. Phys. Chem.*, **71**, 3833 (1967).
8. H. Hendus and K. H. Illers, *Kunststoffe*, **57**, 193 (1967).
9. E. W. Fischer and G. Hinrichsen, *Kolloid-Z.*, **213**, 93 (1966).
10. L. Mandelkern, *Polym. Eng. Sci.*, **7**, 232 (1967).
11. L. Mandelkern, J. G. Fatou, R. Denison, and J. Justin, *J. Polym. Sci. B*, **3**, 803 (1965).
12. L. Mandelkern, A. L. Allou, and M. R. Gopalan, *J. Phys. Chem.*, **72**, 309 (1968).
13. P. R. Swan, *J. Polym. Sci.*, **42**, 525 (1960).

14. B. E. Warren, *Phys. Rev.*, **44**, 969 (1933).

15. C. Sella, *C. R. Acad. Sci.* (Paris), **248**, 2348 (1958).

16. K. Katayama, *J. Phys. Soc. Japan*, **16**, 462 (1961).

17. P. H. Hermans and A. Weidinger, *Makromol. Chem.*, **39**, 67 (1960).

18. A. Guinier and G. Fournet, *Small-Angle Scattering of X-Rays*, Wiley, New York, 1955.

19. G. Porod, *Kolloid-Z.*, **124**, 83 (1951).

20. F. Stern, *Trans. Faraday Soc.*, **51**, 430 (1955).

21. E. W. Fischer, H. Goddar, and G. F. Schmidt, *Makromol. Chem.*, **118**, 144 (1968).

22. S. Kavesh and J. M. Schultz, *Polym. Eng. Sci.*, **9**, 452 (1969).

23. R. Hosemann and S. N. Bagchi, *Direct Analysis of Diffraction By Matter*, North Holland, Amsterdam, 1962.

24. C. Reinhold, E. W. Fischer, and A. Peterlin, *J. Appl. Phys.*, **35**, 71 (1964).

25. J. M. Schultz, W. H. Robinson, and G. M. Pound, *J. Polym. Sci. A-2*, **5**, 511 (1967).

26. J. M. Schultz, *Acta Cryst.*, in press.

27. J. D. Hoffmann and J. J. Weeks, *J. Chem. Phys.*, **42**, 4301 (1965).

28. J. J. P. Blais and R. St. J. Manley, *J. Macromol. Sci. (Phys.)*, **B1**, 525 (1967).

29. P. H. Geil, *Bull. Am. Phys. Soc.*, **7**, 206 (1962).

30. P. H. Geil, in *Small Angle Scattering from Fibrous and Partially Ordered Systems* (*J. Polym. Sci. C*, **13**), R. H. Marchessault, Ed., Interscience, New York, 1966, p. 149.

31. R. G. Brown and R. K. Eby, *J. Appl. Phys.*, **35**, 1156 (1964).

32. E. H. Andrews, *Proc. Roy. Soc.* (London), **A270**, 232 (1962).

33. E. H. Andrews, *Proc. Roy. Soc.* (London), **A271**, 562 (1963).

34. E. H. Andrews, *J. Polym. Sci. B*, **3**, 353 (1965).

35. J. A. Rusnock and D. Hansen, *J. Polym. Sci. A*, **3**, 647 (1965).

36. C. W. Hock, *J. Polym. Sci. A-2*, **5**, 471 (1967).

37. E. H. Andrews, M. W. Bennett, and A. Markham, *J. Polym. Sci. A-2*, **5**, 1235 (1967).

38. E. W. Fischer and G. F. Schmidt, *Angew. Chem., Int. Ed.*, **1**, 448 (1962).

39. Y. Nukushina, Y. Itoh, and E. W. Fischer, *J. Polym. Sci. B*, **3**, 383 (1965).

40. K. O'Leary and P. H. Geil, *J. Macromol. Sci. (Phys.)*, **B1**, 147 (1967).

41. J. V. Dawkins, P. J. Holdsworth, and A. Keller, *Makromol. Chem.*, **118**, 361 (1968).

42. P. Schmidt, *Acta Cryst.*, **19**, 938 (1965).

43. A. Guinier, *X-Ray Diffraction in Crystals, Imperfect Crystals and Amorphous Bodies*, W. H. Freeman, San Francisco, 1963.

44. A. Guinier, *Ann. Phys.*, **12**, 161 (1939); *Theorie et Technique de la Radiocristallographie*, Dunod, Paris, 1956.

45. N. Bekkedahl, *J. Res. Nat. Bur. Stand.*, **42**, 145 (1949).

46. S. Kavesh, Ph.D. Dissertation, University of Delaware, Newark, Delaware, 1968.

47. E. W. Fischer, *Kolloid-Z.*, **218**, 97 (1967).

48. Yu. A. Zubov and D. Ya. Tsvankin, *Polym. Sci. USSR*, **7**, 2028 (1965).

Correlation between the Temperature Dependence of Apparent Specific Volume and the Conformation of Oligomeric Propylene Glycols in Aqueous Solution

L. S. SANDELL and D. A. I. GORING, *Physical Chemistry Section, Pulp and Paper Research Institute of Canada, Point Claire, Quebec, and Chemistry Department, McGill University, Montreal, Quebec, Canada*

Synopsis

The apparent specific volumes, ϕ_2, of a series of poly(propylene glycol) and poly(ethylene glycol) oligomers in aqueous solution were determined as a function of temperature from 4 to 25°C. The slope, $d\phi_2/dT$, was taken as a measure of the extent of interaction between the hydrophobic portions of the oligomer and water, higher values of $d\phi_2/dT$ representing diminished hydrophobic interaction. It is suggested that the observed increase in $d\phi_2/dT$ with chain length for the poly(propylene glycol) oligomers can be attributed to the previously proposed disk coiled conformation of the chain which reduces the degree of contact between the side-chain methyl groups and water as the chain length increases. This interpretation is supported by (1) the direct relationship between the difference in the thermal expansion behavior of the two oligomer series and the accessibility of the methyl groups in the poly(propylene glycol) disk-coil, and (2) the agreement between the calculated volume changes on mixing for the methyl groups and the values predicted for the disk-coil model from the Némethy and Scheraga theory.

INTRODUCTION

In a recent investigation, Neal and Goring were able to show that the derivative of the apparent specific volume of the solute with respect to temperature, $d\phi_2/dT$, is a sensitive measure of the effect of a solute molecule on the structure of water.[1] For a variety of small, nonionic solutes, correlations were established between $d\phi_2/dT$ and other properties which are commonly considered to be indexes of structural interactions (e.g., the heat of mixing). The main conclusion of this work was that hydrophobic compounds, which promote water structure, have lower values of $d\phi_2/dT$ than hydrophilic compounds.

In the present analysis, the thermal expansion behaviour of a series of polypropylene glycol (PPG) oligomers in water is examined. The parameter, $d\phi_2/dT$, is then utilized as a measure of the "hydrophobic character" of these compounds in aqueous solution.

In a chain molecule, the extent of the hydrophobic interaction with water will be governed by the conformation of the chain in solution. Recently, it was shown that the viscometric behavior of the oligomeric poly-

115
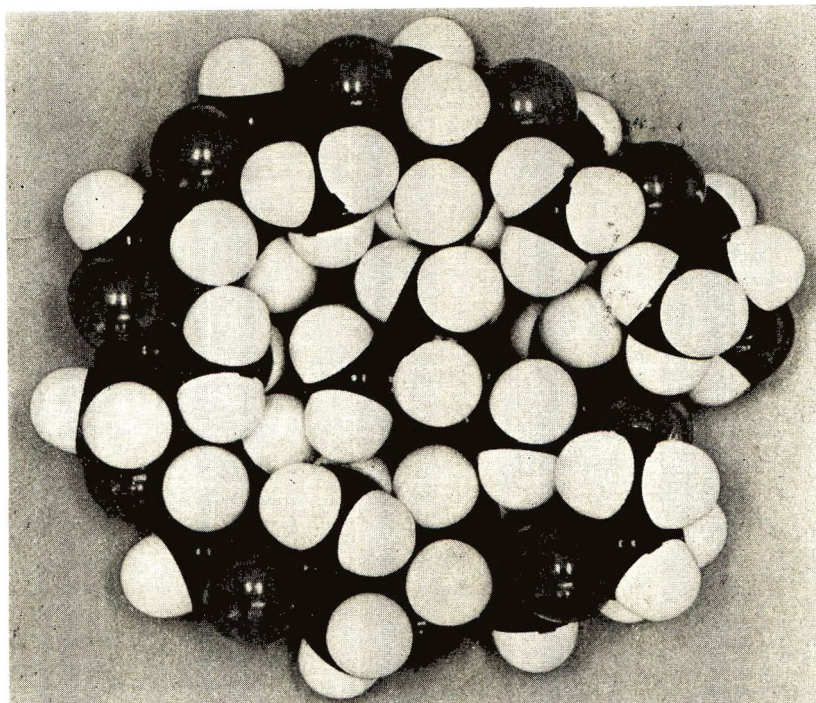
Fig. 1. Photograph of the polypropylene glycol disk-coil model of DP 12.

(propylene glycols) in water could be interpreted in terms of a particular conformational model of the chain, i.e., a solvent-impermeable, disk-shaped hypercoil (Fig. 1).[2] It was postulated that this conformation was stabilized by hydrophobic interactions among the side-chain methyl groups which form the core of the structure.   The purpose of the present work is to show that the observed variation of $d\phi_2/dT$ with the degree of polymerization (DP) can be attributed to the disk-coiled conformation of the chain, which reduces the degree of contact between the hydrophobic portions of the oligomer and the surrounding water.

As a basis for comparison, thermal expansion measurements have also been conducted on a series of poly(ethylene glycol) (PEG) oligomers which have the same backbone structure as poly(propylene glycol) but lack the pendant methyl groups. Since the poly(ethylene glycol) oligomers are less hydrophobic than PPG,[3] differences are expected in the thermal expansion behavior of the two series which can be ascribed to the side-chain methyl groups on PPG.

ESTIMATION OF THE HYDROPHOBIC CHARACTER OF THE DISK-COIL MODEL

In order to relate the trend in $d\phi_2/dT$ to the disk-coil model, a theoretical estimate must be made of the "hydrophobic character" of each oligomer in
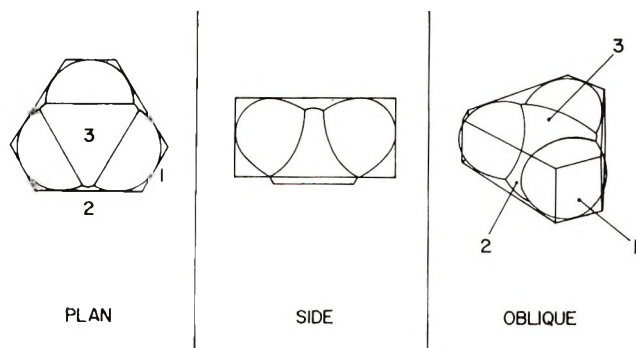
Fig. 2. Designation of the methyl group area factors.

the disk-coil configuration. This may be done by calculating the hydrophobic area of the disk-coil which is accessible to water.

In the disk-coil, a large proportion of the methyl groups are close-packed in the interior of the structure and are thus removed from the aqueous environment. By observation of the Stuart-Briegleb models, it was possible to estimate the loss of accessibility of the methyl groups, relative to the fully accessible groups on the extended chain. The loss of methyl group accessibility due to hypercoiling was calculated as a reduction in the hydrophobic surface area of the chain.

The computational method involved the assignment of an area factor to each methyl group. The CH_3 group was approximated by a polyhedron as shown in Figure 2. The end-on face of a single hydrogen atom was designated an area factor of unity. The upper surface of the polyhedron corresponding to a side view of the three hydrogen atoms of the methyl group was assigned a value of three units, while each of the three polyhedron edges was given a value of two units. The fully accessible methyl group therefore had an exposed surface area of twelve units. If, in the disk-coil, part of a methyl group was buried in the interior, then its exposed surface area was reduced accordingly to some fraction of the value 12. When the exposed surface area was summed for all of the methyl groups in a disk-coil, then a figure was arrived at which represented the "hydrophobic area" of the disk-coil. This number divided by the theoretical maximum methyl group area for the equivalent extended chain gave the fraction of the total methyl group area in the disk-coil which was exposed to the aqueous medium. This fraction expressed as a percentage was designated as the exposed methyl group factor, $Me_{(exposed)}$. As an example, an extended chain of DP 10 would have a total hydrophobic surface area of 120 units. By visual inspection of the disk-coil it is estimated that 65 units are buried in the interior of the structure leaving only 55 units exposed. Thus the exposed methyl group factor is $55/120 = 46\%$.

A complicating feature of this treatment was the fact that, because of the nonspecific nature of methyl group hydrophobic interactions, it was not possible to reproduce by model building the exact internal structure of a

DP	$Me_{exposed}$, %
2	83 ± 0[a]
3	71 ± 2
5	63 ± 2
7	54 ± 2
10	49 ± 3
12	49 ± 2
15	47 ± 3
17	46 ± 4

[a] Mean deviation.

particular disk-coil. However, after dismantling the structure and reassembling it several times for each degree of polymerization, average values of $Me_{(exposed)}$ could be determined. These are given in Table I with the mean deviations taken over six trials.

In a later section of the paper the $Me_{(exposed)}$ values in Table I derived from a study of the molecular models will be correlated with the volume behavior of the aqueous solutions of the oligomers.

EXPERIMENTAL

Materials

All except one of the poly(propylene glycol) samples have been described fully in a previous paper.[2] Tetrapropylene glycol, tetraethylene glycol, and pentaethylene glycol were prepared and fractionated by Dr. B. Weibull of Mo Do Aktiebolag (Sweden), to whom we are indebted for the samples. The samples of diethylene glycol, triethylene glycol, and the Carbowaxes 300, 600 and 1000 were obtained from the J. T. Baker Chemical Company.

Number-average molecular weights $\bar{M}_n$ were determined by vapor-pressure osmometry (Mechrolab 301A) in isopropanol at 37°C. The calibration standard was propionamide.[4]

Two per cent solutions of the glycols were made up by weight using freshly boiled, distilled water. Prior to an experimental run the glycol solutions were heated to ca. 90°C to expel any dissolved air, and were then allowed to cool to room temperature in a stoppered flask.

The higher polyglycols show inverse solubility–temperature behavior in aqueous solution.[5] In particular, the PPG 1025 and PPG 425 samples had lower critical solution temperatures at about 25°C and 70°C, respectively. Therefore, to ensure redissolution, these samples were stirred while being cooled slowly to about 4°C.

Dilatometry

The change in solution volume with temperature was measured between 4 and 25°C with a capillary dilatometer which was capable of detecting

volume changes of $1 \times 10^{-4}\%$. The details of the dilatometer design and the dilatometry techniques and computational methods are given elsewhere.[4] Readings were generally taken at 3°C intervals for the solutions and at 8°C intervals for the pure solutes. To convert the relative dilatometer volumes to densities, an independent density measurement of the appropriate liquid was made pycnometrically at one temperature. This "calibrating" density was then combined with the volume reading of the liquid in the dilatometer at that same temperature to give the weight of the liquid in the dilatometer.

The apparent specific volume of the solute was obtained from the density of the solution by using the equation

$$\phi_2 = \frac{1}{w_2}\left(\frac{1}{\rho} - \frac{1 - w_2}{\rho_0}\right) \tag{1}$$

where ρ is the density of the solution, ρ_0 is the density of water, and w_2 is the weight fraction of the solute.

Trial runs with water revealed that the reproducibility in density was about 2×10^{-5} g/ml, which, for a 2% solution, would result in an uncertainty of ± 0.001 ml/g in ϕ_2. This estimate of the absolute precision in ϕ_2 was confirmed by comparing the results of trial runs on 2% sucrose solutions with ϕ_2 values calculated from the literature.[6] The corresponding error in the slope, $d\phi_2/dT$, is less than 0.3×10^{-4} ml/g-°C.

RESULTS

Number-average molecular weights and degrees of polymerization of the pure glycols are listed together with their densities in Table II.

TABLE II

Molecular Weights, Degrees of Polymerization, and Densities of the Pure Polyglycols

Glycol	$\overline{M}_n$	Average DP	Density at 9°C, g/ml
Dipropylene	130	1.93	1.0309
Tripropylene	175	2.7	1.0267
Tetrapropylene	229	3.6	1.0201
Pentapropylene	291	4.7	1.0210
PPG P400	313	5.1	1.0196
PPG 425	410	6.8	1.0193
PPG 1025	940	15.9	1.0138
Diethylene	102	1.90	1.1244
Triethylene	141	2.8	1.1325
Tetraethylene	180	3.7	1.1336
Pentaethylene	198	4.1	1.1341
PEG 300	284	6.1	1.1352
PEG 600	533	11.7	1.1223 (25°C)
PEG 1000	802	17.8	1.1069 (45°C)
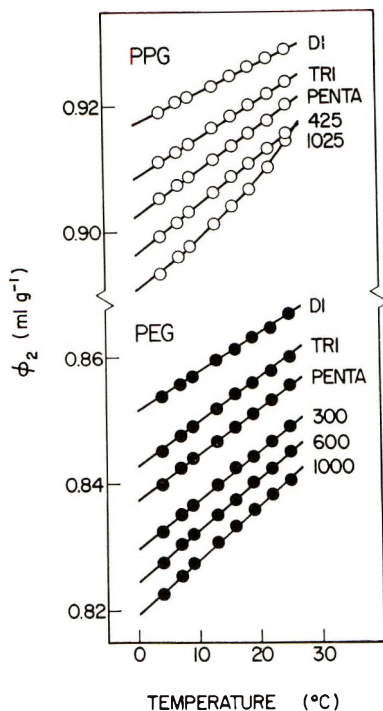
Fig. 3. Plots of apparent specific volume vs. temperature for some of the oligomers.

Table III contains the apparent specific volumes ϕ_2, expressed as least-square polynomial functions of temperature. Examples of ϕ_2 versus temperature plots in both oligomer series are shown in Figure 3.* With the exception of PPG 1025, the expansion data for all of the glycols in solution were fitted by straight lines within experimental error. The thermal expansion behavior for the two PPG 1025 solutions was best expressed by higher-order equations in temperature. This was due to the upward curvature in the ϕ_2 versus T plots at higher temperatures, and is probably a reflection of the inverse solubility–temperature relationship in this system. The coefficients for the PPG 1025 equations are listed in Table IIIB.

Plots of $d\phi_2/dT$ as a function of degree of polymerization of the oligomer are shown in Figure 4. In both series the values of $d\phi_2/dT$ increase with chain length. However, it is evident that this trend is more pronounced for the poly(propylene glycol) oligomers. It should be noted that the datum point for PPG 1025 is unreliable, since it represents an average value of $d\phi_2/dT$ determined at one temperature only, i.e., 10°C. Values of $d\phi_2/dT$ for this system varied from 0.8×10^{-3} to over 1.0×10^{-3} ml/g-°C in the temperature range 4–25°C. Consequently, the intersection of the two curves in Figure 4 may be an artifact, since the $d\phi_2/dT$ values interpolated from the PPG curve above a DP of 7 are only approximate.

* Thermal expansion measurements were actually carried out over the range 4–60°C. The more extensive data and polynomials for this temperature range are available.[4]

Table IV lists empirical equations for the temperature dependence of the specific volumes v_2 of the pure polyglycols. These equations were obtained by combining the independently measured densities in Table II with the average value of dv_2/dT for each oligomer series, as determined from thermal expansion measurements on representative polyglycols. Average values of dv_2/dT for the PPG and PEG oligomers were 0.810×10^{-3} and 0.697×10^{-3} ml/g-°C, respectively.

TABLE IIIA

Fitting of Empirical Equations for ϕ_2 from 4 to 25°C $\phi_2 = A + (B \times 10^{-3})T$

Glycol	Concentration (weight fraction)	A, ml/g	B, ml/g-°C	SD, ml/g $\times 10^{3a}$
Dipropylene	0.0206	0.9171	0.4736	0.1
Tripropylene	0.0212	0.9085	0.6102	0.1
Tetrapropylene	0.0200	0.9084	0.6318	0.2
Pentapropylene	0.0198	0.9025	0.6995	0.1
PPG P400	0.0198	0.9010	0.6984	0.1
PPG 425	0.0199	0.8964	0.7635	0.2
PPG 1025(1)	0.0192	—	0.877[b]	—
PPG 1025(2)	0.0202	—	0.933[b]	—
Diethylene	0.0197	0.8516	0.6107	0.1
Triethylene	0.0204	0.8428	0.7020	0.2
Tetraethylene	0.0191	0.8386	0.7191	0.2
Pentaethylene	0.0212	0.8374	0.7229	0.2
PEG 300	0.0193	0.8297	0.7798	0.2
PEG 600	0.0195	0.8245	0.8252	0.1
PEG 1000	0.0202	0.8195	0.8620	0.2

[a] Standard deviation of ϕ_2.

[b] $d\phi_2/dT \times 10^3$ at 10°C.

TABLE IIIB

Fitting of Empirical Equations for ϕ_2 from 4 to 25°C

$\phi_2 = A + (B \times 10^{-3})T + (C \times 10^{-5})T^2 + (D \times 10^{-7})T^3$

Glycol	A, ml/g	B, ml/g-°C	C, ml/g-°C²	D, ml/g-°C³	SD, ml/g $\times 10^{3a}$
PPG 1025(1)	0.8908	0.6512	1.1291	—	0.3
PPG 1025(2)	0.8862	1.6067	−5.6550	15.2458	0.1

[a] Standard deviation of ϕ_2.

The densities of the pure glycols determined from the empirical equations may be compared with values from the literature. For diethylene glycol, triethylene glycol, tetraethylene glycol, and PEG 300 (DP = 6.1), the densities calculated from Table IV were within 0.001 g/ml of literature values reported at 15,[7] 20,[8,9] and 25°C.[10] Literature values at 20 and 25°C for dipropylene glycol,[8,10] PPG 425,[8] and PPG 1025[8] are within 0.001 g/ml
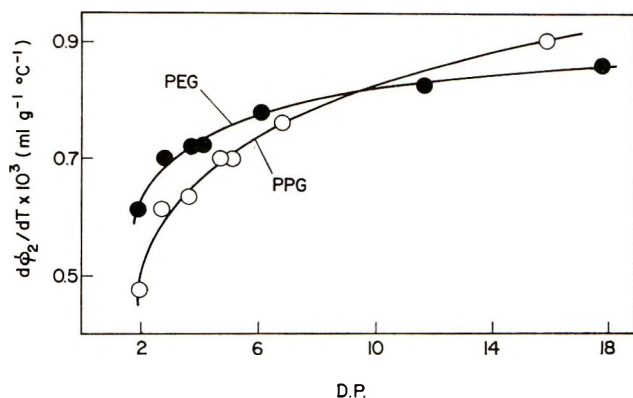
Fig. 4. DP dependence of $d\phi_2/dT$.

of the densities calculated for these compounds from our empirical equations.

Only one value could be found for the partial specific volume of a polyglycol in dilute aqueous solution. A PEG oligomer of molecular weight 240 was reported to have a partial specific volume in water of 0.846 ml/g at 23°C.[11] This is in excellent agreement with our own value of ϕ_2 for PEG 300 ($\overline{M}_n = 284$) at 22°C; viz, 0.847 ml/g.

TABLE IV

Empirical Equations for v_2 of the Pure Polyglycols from 4 to 25°C

$$v_2 = A + (B \times 10^{-3})T$$

Glycol	A, ml/g	B, ml/g-°C
Dipropylene	0.9628	0.810
Tripropylene	0.9667	"
Tetrapropylene	0.9730	"
Pentapropylene	0.9722	"
PPG P400	0.9735	"
PPG 425	0.9738	"
PPG 1025	0.9791	"
Diethylene	0.8831	0.697
Triethylene	0.8767	"
Tetraethylene	0.8759	"
Pentaethylene	0.8755	"
PEG 300	0.8746	"
PEG 600	0.8736	"
PEG 1000	0.8720	"

DISCUSSION

Thermal Expansion Coefficients

According to Neal and Goring,[1] the increasing values of $d\phi_2/dT$ in Figure 4 correspond to a reduction in the hydrophobic character of the solute.
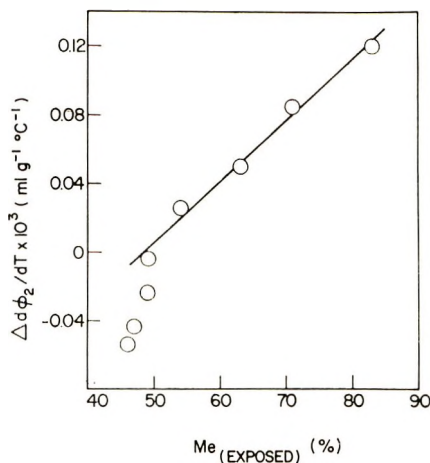
Fig. 5. The difference between $d\phi_2/dT$ of PEG and PPG vs. the exposed methyl group factor of the disk-coil.

The fact that both oligomer series exhibit the same trend for the dependence of $d\phi_2/dT$ on chain length suggests that the mechanism for the reduction of hydrophobicity is similar in both instances.

Such an effect may be due to intramolecular hydrophobic bonding in the oligomers. In PEG, these interactions could take place between backbone (—CH_2CH_2—) groups, since the chain is extremely flexible.[12,13] The overlapping of hydrophobic regions in PEG must result in a reduction of the (—CH_2CH_2—) area which is accessible to water. The loss of available hydrophobic area in the chain due to such interactions corresponds to a reduction in the hydrophobic character of the oligomer when compared to an equivalent, fully extended PEG chain. Examination of molecular models of PEG oligomers indicates that the ease of forming (—CH_2CH_2—) (—CH_2CH_2—) hydrophobic contacts greatly increases with increasing chain length, especially in the low DP range. Consequently, the relative decrease in hydrophobic character should be more pronounced for longer chain lengths, which accounts for the trend observed in Figure 4.

The $d\phi_2/dT$–DP behavior of the PPG series can be interpreted in terms of the disk-coil model. In the disk-coil configuration some of the backbone (—CH_2CH_2—) groups can participate in hydrophobic bonding and consequently are partially removed from the aqueous environment. An additional contribution to the loss of hydrophobic area arises from the reduction in the methyl group accessibility due to hypercoiling (cf. Table I). These combined effects are more pronounced at higher degree of polymerization; thus, compared to the equivalent, extended PPG chain the disk-coil becomes relatively less hydrophobic as the chain length increases.

The difference in the thermal expansion behavior of the two oligomer series probably arises from the structure-forming tendencies of the PPG methyl groups which are exposed to water. This effect is more pronounced

at low degrees of polymerization, where the methyl groups are more accessible. In fact, as shown in Figure 5, $\Delta d\phi_2/dT \equiv (d\phi_2/dT)_{PEG} - (d\phi_2 dT)_{PPG}$ is a linear function of $Me_{(exposed)}$ for DP between 2 and 10. The negative $\Delta d\phi_2/dT$ values for oligomers of DP > 10 result from the intersection of the two curves in Figure 4. As noted previously, the thermal expansion behavior in this region is indeterminate, and consequently, little can be inferred from the trend in Figure 5 in this DP range.

Volume Changes on Mixing

The trends observed in the present work show that for the PPG and PEG oligomers there is a correlation between $d\phi_2/dT$ and the volume contraction on mixing, with $(\phi_2 - v_2)$ decreasing as $d\phi_2/dT$ and the oligomer chain length increase. The question then arises as to whether the volume changes on mixing can be related to the configuration of the polypropylene glycols in aqueous solution.

Némethy and Scheraga have made theoretical estimates of the volume changes accompanying the transfer of aliphatic hydrocarbons from the nonpolar medium to water.[14] Friedman and Scheraga showed that the theory was reasonably successful in predicting the volume of mixing of a homologous series of alcohols.[15] They assumed that the effect of the polar group was common to all the members of the series and it could therefore be subtracted to give the volume contribution of the hydrocarbon moieties. In the present study, the volume contribution of the methyl group side chains in PPG may similarly be obtained by subtracting the effect of the PEG backbone. These values may then be compared with two sets of theoretical estimates for the methyl group volume changes. One of these sets corresponds to the Némethy and Scheraga values for the fully accessible methyl groups of the extended chain and the other corresponds to the values determined for the partially accessible methyl groups in the disk-coil configuration.

At a given temperature the decrease in volume accompanying the transfer of one mole of a glycol oligomer into water was determined from the equation

$$\Delta V = (\phi_2 - v_2)\bar{M}_n \tag{2}$$

where ΔV is the volume decrease on mixing (in ml/mole) for an oligomer of number-average molecular weight $\bar{M}_n$ at a concentration of 2% by weight (ca. 4×10^{-3}–4×10^{-4} mole fraction).

The volume contribution of the methyl groups was then obtained from the equation

$$\Delta V_{CH_3} = \Delta V_{PPG} - \Delta V_{PEG} \tag{3}$$

where ΔV_{CH_3} is the volume decrease due to the methyl groups on a PPG oligomer of given DP and ΔV_{PPG} and ΔV_{PEG} are the experimental volume changes of PPG and PEG oligomers of the same DP as determined from eq. (2). The error in ΔV_{CH_3} was approximately $\pm 10\%$.

Theoretical values of the volume shrinkage of the methyl groups were
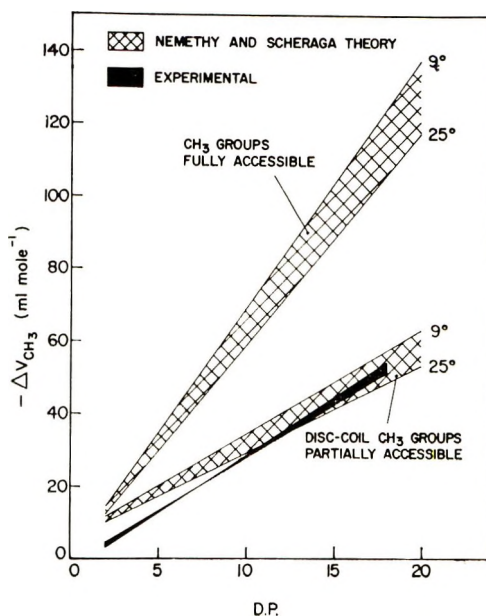
Fig. 6. Experimental and theoretical volume changes on mixing for the PPG methyl groups vs. DP.

calculated from a modified version of the Némethy and Scheraga equation,[14] as follows,

$$\Delta V_{CH_3} = -(43/24)nY^c X_4^c \tag{4}$$

where n is the degree of polymerization of the oligomer, Y^c is the number of water molecules in the first layer around the hydrocarbon solute molecule ($Y^c = 8$ for methyl groups) and X_4^c is the mole fraction of water in the first layer that is tetra-hydrogen bonded. Values of X_4^c are tabulated as a function of temperature.[14]

Values of ΔV_{CH_3} as determined from eq. (4) correspond to the volume shrinkage when all the methyl groups on the oligomer are assumed to be fully accessible to the solvent. To obtain estimates of the volume decrease for the methyl groups accessible in the disk-coils, the values of ΔV_{CH} obtained from eq. (4) were multiplied by the exposed methyl group factors in Table I.

The results are shown in Figure 6 for the temperature range 9–25°C. The values of ΔV_{CH_3} as predicted for the fully accessible methyl groups are in the order of 100% greater than the experimental values. However, the agreement between the experimental values and the values calculated for the disk-coil model is fairly good, particularly in the range of higher degree of polymerization. One notable discrepancy is that the theoretical values of ΔV_{CH_3} are temperature-dependent, while the experimental values are relatively insensitive to temperature between 4 and 25°C. Friedman and Scheraga noted this shortcoming in their volume study on alcohols, and attributed it to limitations in the original statistical thermodynamic treatment of volume changes.[15]

CONCLUDING REMARKS

The main conclusion to be drawn from the present work is that the differences between the volume behavior of PEG and PPG oligomers in aqueous solution can be attributed to water structural effects. In addition, it has been possible to interpret the results semiquantitatively in terms of the disk-coil model proposed previously to explain the viscometric behavior of PPG oligomers in aqueous solution.[2]

It should be pointed out that there are several uncertainties in the treatment given. In the first place, the correlations in Figures 5 and 6 do not constitute proof of the disk-coil model. A tightly coiled conformation, having spherical symmetry, with the methyl groups buried within the coil would probably have given similar trends. However, a spherical model would not have explained the viscometric data.[2] A second point concerns the correctness of ascribing the parameters $\Delta d\phi_2/dT$ and ΔV_{CH_3} solely to the effect of the exposed methyl groups. Such an assumption is valid only if the conformations of the two types of oligomer are such that their backbone hydrophobic interactions are equivalent. One may also question the application of the Némethy and Scheraga theory for assessing the volume of mixing, particularly in view of its failure to predict the temperature dependence correctly.

In the light of the above reservations, the correlations obtained are surprisingly good and lend support to the general validity of the concepts presented, including that of the disk-coil model. Further elucidation of the problem will probably come from different types of experimental observations on similar systems.

References

1. J. L. Neal and D. A. I. Goring, *J. Phys. Chem.*, **74**, 658 (1970).
2. L. S. Sandell and D. A. I. Goring, *Macromolecules*, **3**, 50 (1970).
3. F. E. Bailey, Jr. and R. W. Callard, *J. Appl. Polym. Sci.*, **1**, 56 (1959).
4. L. S. Sandell, Ph.D. Thesis, McGill University, Montreal, P.Q., Canada, 1970.
5. G. N. Malcolm and J. S. Rowlinson, *Trans. Faraday Soc.*, **53**, 921 (1957).
6. F. Schneider, D. Schliephake, and A. Klimmek, *Zucker*, **16**, 1 (1963).
7. T. Ishiguro, S. Kato, Y. Sakata, and Y. Akazawa, *J. Pharm. Soc. Japan*, **73**, 1167 (1953).
8. G. O. Curme, Jr., Glycols, Reinhold, New York, 1952.
9. P. Rempp, *J. Chim. Phys.*, **54**, 421 (1957).
10. S. S. Kurtz, Jr., D. L. Camin, and A. R. Thompson, *J. Chem. Eng. Data*, **10**, 335 (1965).
11. G. R. Andersson, *Arkiv. Kemi*, **20**, 513 (1963).
12. L. S. Sandell and D. A. I. Goring, *Macromolecules*, **3**, 54 (1970).
13. G. G. Hammes and P. R. Schimmel, *J. Amer. Chem. Soc.*, **89**, 442 (1967).
14. G. Némethy and H. A. Scheraga, *J. Chem. Phys.*, **36**, 3401 (1962).
15. M. E. Friedman and H. A. Scheraga, *J. Phys. Chem.*, **69**, 3795 (1965).

Ethylene-Propylene Copolymers: Degree of Crystallinity and Composition *

G. VER STRATE and Z. W. WILCHINSKY, *Enjay Polymer Laboratories, Linden, New Jersey 07036*

Synopsis

X-ray, differential scanning calorimeter, and density measurements of the degree of crystallinity have been made on ethylene–propylene copolymers which range in composition from 60 to 100 mole-% ethylene.   At 23°C the degree of crystallinity was found to vary from zero to approximately 75 wt-% in a regular manner with composition.   A systematic difference exists between the x-ray and heat of fusion measurements if a simple two-phase model is assumed in order to calculate the per cent crystallinity from heats of fusion.   The apparent heat of fusion of the crystalline fraction detected by the x-ray method is as low as 30 cal/g.   This discrepancy increases with comonomer content.   It is suggested that large surface or defect energies are present.   The broad melting behavior of the samples is also consistent with such a description of the system.

INTRODUCTION

Certain studies in the literature have concerned themselves with crystallinity in ethylene–propylene copolymers[1-10] while others have discussed the dependence of the degree of crystallinity measured on the means of measurement and have correlated this dependence to support a particular model for bulk and solution crystallized polymers.[11,12]

Data are presented here for the degree of crystallinity (23°C) of ethylene–propylene copolymers over a range of compositions from polyethylene to approximately 60 mole-% ethylene and thus from ca. 75% crystallinity to 0%.

Density, differential scanning calorimetry (DSC), and x-ray techniques are used on samples with identical thermal history, and thus the study has generated a novel set of data for ethylene propylene copolymers.

EXPERIMENTAL

The ethylene to propylene ratio in all of the polymers studied was determined by infrared spectroscopy (Beckman IR 5A).   The ratios of peaks at 4400, 1160, and 720 cm⁻¹ were used.   This method was calibrated by using ¹⁴C-tagged polymers prepared by the same catalyst system which was used to prepare the copolymers discussed here.

* Taken in part from a paper presented at the 1969 Gordon Conference on Elastomers, Colby College, New London, New Hampshire, July 28–August 1, 1969.

TABLE I

Sample	$[\eta]^a$	Ethylene, mole-%	Annealed at room temperature, days	From x-ray data		From DSC		$\dfrac{\Delta H_f}{f_c}$	Density, (23°C), g/cc	Crystallinity by density, %
				K	Crystallinity, %	ΔH_f, cal/g^b	Crystallinity from ΔH_f, %			
Copolymers										
379-1	2.5	89	1	0.695	40	22.2	32.4	55	0.9153	45.5
379-4	2.0	88 ± 3^d	11	0.645	30	18.0	26.4	60	0.9084	40.5
379-3	2.0	87	8	0.58	27	14.7	22.3	55	0.8910	28.0
379-2	2.5	85	8	0.645	23	12.8	19.4	55	—	—
1249A	4.0	73	20	—	22	11.4	17.8	52	0.8847	23.0
1354F	4.4	74	20	—	20	8.5	13.3	42	0.8808	20.0
1354D	4.0	72	20	—	17	7.3	11.4	43	0.8773	17.5
1354E	4.0	71	20	—	16	6.5	10.1	40	0.8758	16.0
1193A	4.1	69	20	—	15	5.1	8.0	34	0.8725	14.0
774B	4.5	73	9	0.62	14	4.7	7.3	33	0.8720	13.5
1223B	4.0	67	20	—	11	4.0	6.1	36	0.8682	10.5
1354C	3.9	69	20	—	10	3.8	5.9	38	0.8690	11.0
1354B	3.6	66	20	—	5	1.5	2.4	30	0.8612	4.5
768D	3.9	66	13	—	1	0.6	0.9	—	—	—

Sample									
660F[e]	—	74	14	0.55	11	5.9	9.2	54	0.8810	20[f]
709B[e]	—	73	6	0.64	12	6.1	9.5	50	0.8809	20[f]
770B[e]	—	65	7	—	1	0.9	1.5	—	0.8651	8
344D	—	86	—	0.63	27	—	—	—	—	—
477A[e]	—	74	—	0.55	17	—	—	—	—	—
3708[e]	—	71	—	0.58	11	—	—	—	—	—
820G	4.0	60	7	—	0	0	0	0	0.853	0
Linear Polyethylenes										
393-15	11		1[g]	—	52	35	51	66	—	—
Marlex 6001	2.3		1[g]	—	70	45	66	64	0.9587	74.0
Marlex 6002	—		1[g]	—	(63)	44	64	69	0.9556	72.0
Marlex 6009	2.1		1[g]	—	72	47	69	65	0.9594	75.0
Marlex 6035	1.7		1[g]	0.925	72	48	70	66	0.9680	80.5
Branched Polyethylene										
109NA	1.1		4	0.778	44	29.8	43	67	0.9257	53.0

[a] Intrinsic viscosity in Decalin at 135°C.
[b] Average of two scans.
[c] Based on polyethylene data as expressed by eq. (6).
[d] Contaminated by trace of silicone grease 88 ± 3%.
[e] These samples contained ca. 3 wt-% of nonconjugated diene ethylidene norbornene.
[f] High due to diene effect on density.
[g] Unimportant changes at times >60 min.

NMR data on the polymers gave results which depended on the resolution obtained. Data obtained at 100 MHE and 160°C generally gave higher ethylene contents (especially at low $C_2^=$ levels) than data at 60 MHE and 100°C. The latter data agreed with the ^{14}C values. Symmetrical peak resolution was used.

Other independent methods, including use of the 1380 cm^{-1} methyl band, gave unsatisfactory results, these being due to variation of the extinction coefficient among polypropylene samples. This band could be used if the ^{14}C polymers were used for calibration.

Samples which were used for heat of fusion, x-ray, and density measurements were prepared by pressing pads of the polymer between Mylar in a Carver press at ca. 160°C for 30 min. Pads were 0.030–0.125 in. thick. Crystalline samples prepared in this way showed birefringence, as measured in an Abbé refractometer. The "amorphous" samples had to be stressed to produce birefringence.

For samples in which preferred orientation of the crystallites was present, the diffracted x-ray intensity was randomized by a procedure described elsewhere.[13] Interpretation of the oriented patterns was thus reduced to the method described below for isotropic specimens.

The samples were either bulk ethylene–propylene copolymers, terpolymers, or polyethylenes as noted in Table I. The polyethylenes used were "as received" commercial samples with the exception of sample 393–15 which was prepared in our laboratory with the catalyst described below; whereas the copolymers were laboratory preparations synthesized in heptane (solution or slurry depending on solubility) at ca. 25°C in a continuous stirred tank reactor with a Ziegler-Natta type homogeneous catalyst. For this catalyst the reactivity ratio product (ethylene + propylene, terminal model) was ca. 0.5.

The copolymers were heterogeneous in both composition and molecular weight. This in part was due to the presence of more than one active catalyst species. However, 98% of the polymer was within ±10 wt-% ethylene of the stated average value.

These statements are based on column elution fractionation data and on studies of the kinetics of the polymerization process. The stated reactivity ratio product thus represents an average value. The functional form of the copolymerization reactivity ratio equation is unaltered in the presence of multiple catalyst species; the meaning of the reactivity ratio product changes.

After cooling to room temperature at 10°C/min, the samples were annealed at room temperature for at least one day (see Table I for actual times); x-ray and DSC measurements were then made on different sections of the sample simultaneously. As a result of the thermal and aging history described, the change in crystallinity during the elapsed time of the analyses was negligible.

Since the measured crystallinity in a polymer sample depends upon experimental procedures and interpretation of the data, we detail how the density, x-ray, and calorimetric measurements were made.

X-Ray Crystallinity Determinations

The fraction of the polymer in the crystalline state was determined by an adaption of the procedures reported by Weidinger and Hermans.[14,15]

In a selected range of diffraction angles (7–32°), the diffraction pattern was resolved into an area A_a attributable to the amorphous phase and an area A_c attributable to the crystalline phase. The weight fraction f_c of the polymer in the crystalline phase is proportional to A_c, and the fraction f_a in the amorphous phase is proportional to A_a. These relations may be written:

$$f_c = K_c A_c \tag{1}$$

and

$$f_a = (1 - f_c) = K_a A_a \tag{2}$$

where K_c and K_a are the respective proportionality factors. By combining these equations, one may write:

$$1 = K_c A_c + K_a A_a \tag{3}$$

Dividing eq. (1) by eq. (3), one obtains

$$f_c = 1/[1 + K(A_a/A_c)] \tag{4}$$

where $K = K_a/K_c$, a constant independent of the intensity scale factor used. The evaluation of K through the solution of eq. (3) for K_a and K_c requires at least two diffraction patterns representing different degrees of crystallinity. In the present work, the two levels of crystallinity were obtained for a given polymer by the method of Hermans and Weidinger[15] in which the polymer was examined at room temperature and just above its melting point. Except for the temperature differences, the diffraction patterns were obtained under identical experimental conditions. From these two patterns it was possible to evaluate K_a and K_c in eq. (3) for an individual polymer. The validity of the method depends on K_a being independent of temperature in the range considered. A test of this condition was made by measuring values of A_a for an amorphous polymer at 25°C intervals between 25 and 150°C. The values were all within $\pm 1\%$ of the mean. In considering these results, intensity corrections for the thermal expansion of the sample can be neglected for two reasons. First, the thickness of the sample was close to the optimum for maximum intensity in transmission diffraction. Under these conditions the intensity is rather insensitive to small changes in thickness or mass of sample per unit surface area. Secondly, when the sample is in a state of low plasticity at elevated temperatures, the thermal expansion is restricted almost entirely to changing the sample thickness, because of the sample holder construction. Thus, the mass of sample intercepted by the incident x-ray beam is almost constant.

The diffraction patterns were obtained by a transmission method[16] with samples $1/8$ in. thick. For the calibration experiments involving molten

samples, a furnace containing a stainless steel cell with beryllium windows was used.   The procedure for measuring A_a and A_c will be described with reference to Figure 1.   A straight base line ab is drawn from $2\theta = 7°$ to $2\theta = 32°$.   The area above this base line may now be considered consisting
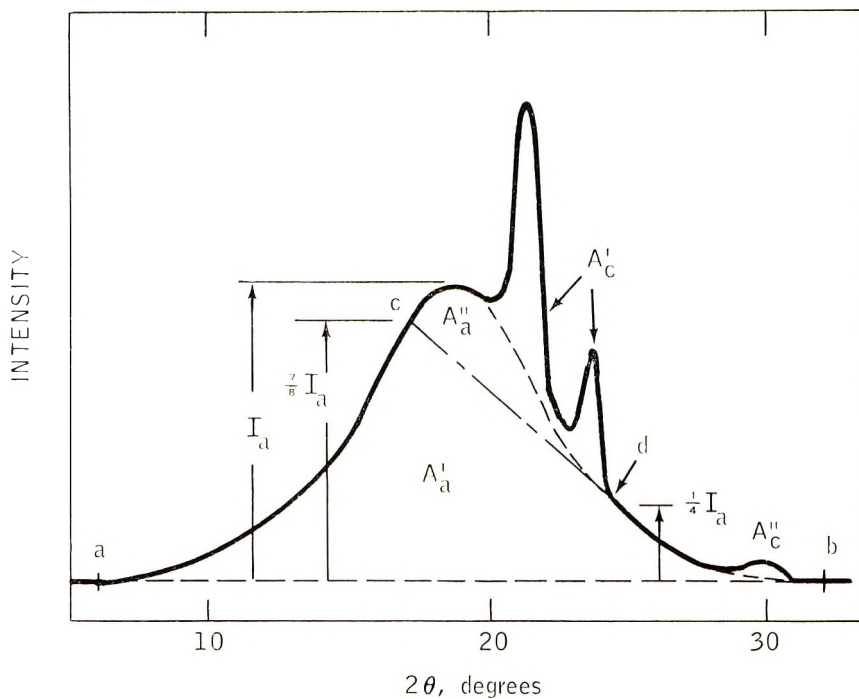
Fig. 1. Resolution of x-ray diffraction pattern.
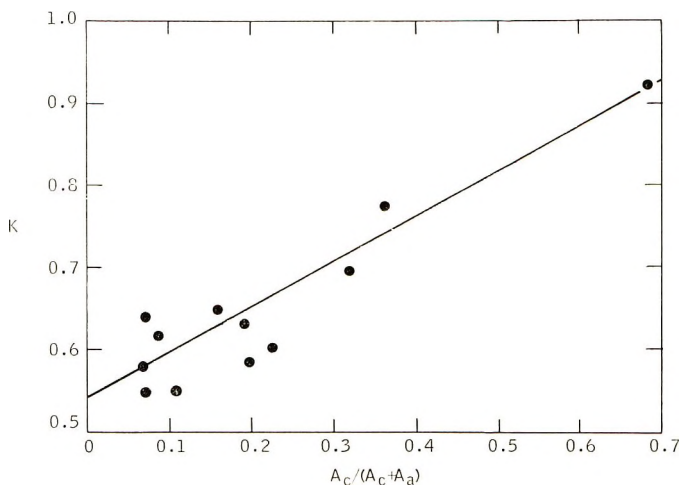
Fig. 2. Correlation of calibration constant in x-ray crystallinity equation with crystalline area.   Data in Table I.

of $A_c = A_c' + A_c''$ and $A_a = A_a' + A_a''$. However, because of the nature of the superposition of the crystalline reflections on the amorphous halo, the dashed line separating A_c' from A_a'' may be difficult to establish with the desired accuracy. To circumvent this difficulty, the following construction was used. The height I_a of the amorphous halo above the base line is determined, and the points c and d on the diffraction trace at $(^7/_8)I_a$ and $(^1/_4)I_a$ are marked to establish the line cd. From measurements of over 50 amorphous patterns, at various temperatures ranging from 25 to 150°C, the average value of A_a''/A_a' was found to be 0.119, the standard deviation being 0.006. Thus, from measurements of A_a' and $A_a'' + A_c'$, one can determine A_a and A_c. Although A_a can also be estimated by multiplying I_a by an empirical constant, the value thus obtained can be shown to be less precise than that obtained by the procedure described.

Values of K determined separately for the samples indicated in Table I decrease with a decrease in ethylene content, room temperature crystallinity, or the area ratio $A_c/(A_c + A_a)$ as shown in Figure 2. For convenience in carrying out crystallinity determinations, the correlation of K with $A_c/(A_c + A_a)$ is preferred. This relation, can be expressed by the equation

$$K = 0.55A_c/(A_c + A_a) + 0.54 \tag{5}$$

where A_c and A_a are the room temperature values.

Since the determination of K by the present procedure depends on measuring two levels of crystallinity, the precision of K increases as the difference between the crystallinity values increases. A greater scatter of the points at low values of $A_c/(A_c + A_a)$ is thus expected. In evaluating the degree of crystallinity for the polymers, the value of K was that of eq. (5). The computed uncertainty in the value of K from the correlation (95% confidence limit) is 0.08 (for $A_a/(A_a + A_c)$ in the range 0 to 0.4) leading to an associated uncertainty of about 0.02 in f_c. Having selected the correlation line for K, we find the precision of f_c measurements determined by the method described is within ± 0.02 (95% confidence limit).

Detection of Crystallinity by the Heat of Fusion

Heats of fusion ΔH_f of the polymer samples were determined with a Du Pont DTA 900 DSC cell. This instrument measures differences between the temperature of an inert reference and that of a sample containing holder as the reference material is heated at a constant rate through the transition region. It may be shown[17] that the excursions from a linear baseline are related to heats associated with first order transitions while heat capacity changes lead to changes in the position or slope of this baseline. To relate the area of the excursion to the ΔH_f one must calibrate the instrument. For the Du Pont instrument the calibration constant is a function of the temperature of transition. Thus indium, mercury, and benzophenone (criterio-quality, Matheson Coleman Bell, for the latter) were used to cali-

TABLE II
Constants Used in DSC Calibration

	T_m, °C	ΔH_f, cal/g	T_m^*, °C[a]
Hg[b]	−38.9	2.7	−33
Benzophenone	48.2	23.5	51
Indium[b]	156.2	6.79	164

[a] T_m^* recorded at peak on our instrument at 10°C/min heating rate.
[b] Data of Krigbaum.[25]

brate the instrument; see Table II for the physical constants used. An external recorder (Honeywell) was used in the calibration runs. The areas of the instrument XY recorder and the external time base recorder were compared by running samples with broad enough melting regions to give good precision for integration on both instruments, and simultaneously recording the peak.

It was found that the calibration constant changed linearly with temperature over the range of interest (−40 to +165°C) and the total change amounted to approximately 3.0%. The calibration constant is known to better than 1% at any given temperature. All of the polymer samples exhibited broad melting and the calibration constant was chosen that cor-
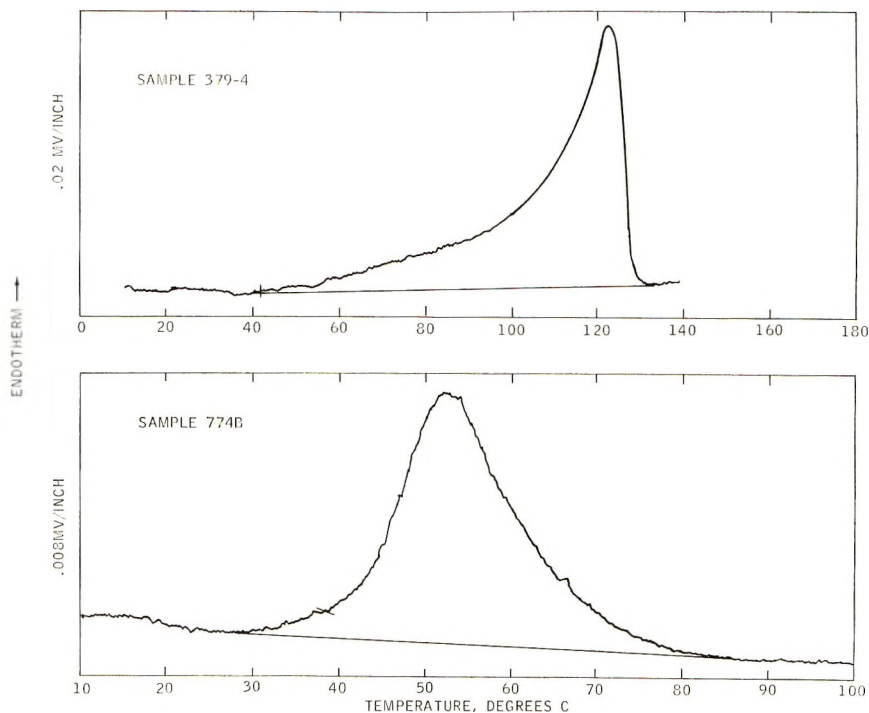
Fig. 3. Differential scanning calorimeter traces.

responded to the median point in the scan area. (The same was done for the standards.) The same scanning speed of 10°C/min was used throughout, and the sample size was chosen to give approximately the same total heat of transition for all the runs. This varied from ca. 2 mg for the standards and polyethylene to ca. 12 mg for some of the low crystallinity copolymers.

The ratio of heat given off to the total heat capacity of the sample becomes a systematically changing variable for such samples. It is not anticipated that the magnitude of this change could cause the "low" heats of fusion reported herein (see below). In addition, the change in heat capacity of the sample in the transition region was not accounted for (i.e., no baseline shift correlation made). In all cases an unambiguous baseline was drawn tangent to the trace before and after the transition, however. Typical traces appear in Figure 3.

We have used 69 cal/g[18] for $\Delta H_f{}^*$, the heat of fusion for perfectly crystalline polyethylene at $T_m = 145°C$[19] (a difference of a few degrees here will not make much difference), and the relation

$$\text{Per cent crystallinity} = (\Delta H_f / \Delta H_f{}^*) \times 100. \qquad (6)$$

Some comment on the recent publication of Atkinson and Richardson[20] is appropriate here. These authors give $T_m = 141 \pm 1°C$ and $\Delta H_f = 73.5 \pm 5\%$. As has been stated, the difference in T_m does not make much difference in the correction to the heat of fusion, however, the 73.5 cal/g value is some 6.5% higher than the value we use. Atkinson and Richardson[20] ascribe the difference between their value and the lower values of others using calorimetric techniques to the fact the broad melting samples give ΔH adiabatic $- \Delta H_{DSC}$ as approximately $+5\%$ due to baseline uncertainty. Lacking data, we are unable to comment on this, however; since both the polyethylene value, 69 cal/g, and our results are ΔH_{DSC}, errors if they exist should be somewhat compensatory.

Another consideration with our data regarding baselines is that the samples may crystallize further upon cooling for the DSC run to be made. Thus, the "apparent" heat capacity of the samples at temperatures below the melting region would be too high due to melting below room temperature and the baseline shift (e.g., Fig. 3, Sample 774B) would lead to too low a ΔH_f. This is a problem inherent in the DSC study of materials which crystallize down to T_g.

Since the addition of the comonomer causes major melting point depressions to occur and also since a significant number of methyl groups may enter the lattice, a question arises as to the proper $\Delta H_f{}^*$ to use for samples other than the polyethylenes that melt at 145°C. As a first estimate, we have corrected $\Delta H_f{}^*$ for temperature by using the data of Wunderlich and Dole.[21] No correction is made for the copolymer units. Thus, we write

$$C_{p,\text{crystal}} = 0.3513 + 1.98 \times 10^{-3}\, T \text{ cal/g-°C} \qquad (7)$$

$$C_{p,\text{liquid}} = 0.5455 + 5.38 \times 10^{-4}\, T \text{ cal/g-°C} \qquad (8)$$

$$\Delta H_f{}^* \,=\, \Delta H_f{}^{**} \,-\, \int_{145}^{T} (C_{p,\mathrm{crystal}} \,-\, C_{p,\mathrm{liquid}})dT \qquad (9)$$

$$=\, 55.9 \,+\, 0.1942T \,-\, 7.2 \times 10^{-4}T^2 \qquad (10)$$

where $\Delta H_f{}^{**}$ denotes the value of $\Delta H_f{}^*$ for a sample melting at 145°C. At $T = 50°C$, eq. (10) represents a 7% correction on ΔH_f.

Crystallinity From Density Determinations

All density determinations were made in gradient columns (ethanol–H_2O) at 23°C. Samples (ca. 10 mg) were cut from the pads described above. In order to convert the density values to degrees of crystallinity it is assumed that a two phase system exists and that the contributions to the specific volume from the amorphous and crystalline phases are additive. The following equation was used:

$$\text{per cent crystallinity} \,=\, (v - v_\mathrm{a})/(v_\mathrm{c} - v_\mathrm{a}) \times 100 \qquad (11)$$

$$=\, 6.882 \,-\, 5.992v$$

where v is the specific volume of the sample, v_a is the specific volume of the amorphous phase (1.170 cm^3/g)[2], and v_c is the specific volume of the crystalline phase (1.000 cm^3/g)[22].

It should be pointed out that the volume of the unit cell increases with increasing number of methyl sidegroups of the copolymer.[4] However, as the methyl sidegroups are assumed to be incorporated into the unit cell to produce the expansion, the cell increases in weight. These effects are in opposite directions and very nearly cancel, as discussed in Appendix I. Although the cancellation may not be complete, no correction for the residual was carried out because of the uncertainty in the cell expansion data.

DISCUSSION

The crystallinity data given in Table I and Figures 4 and 5 will be discussed first.

There are systematic deviations among the degrees of crystallinity obtained by the different methods. Calorimetry gives the lowest values. The difference between crystallinities from the heat of fusion and from x-ray data far exceeds experimental error. As shown in Figure 5, for all but the lowest crystallinity samples the discrepancy increases as the degree of crystallinity diminishes. A comparison of crystallinity values from x-ray and density measurements shows good agreement for the copolymers below 30% crystallinity and for two of the high-density polyethylenes. However, significant discrepancies can be noted for several of the samples, including two of the high density polyethylenes. A satisfactory explanation for the occasional discrepancies has not been found. These results are not in complete accord with at least one previous study[11] in which the
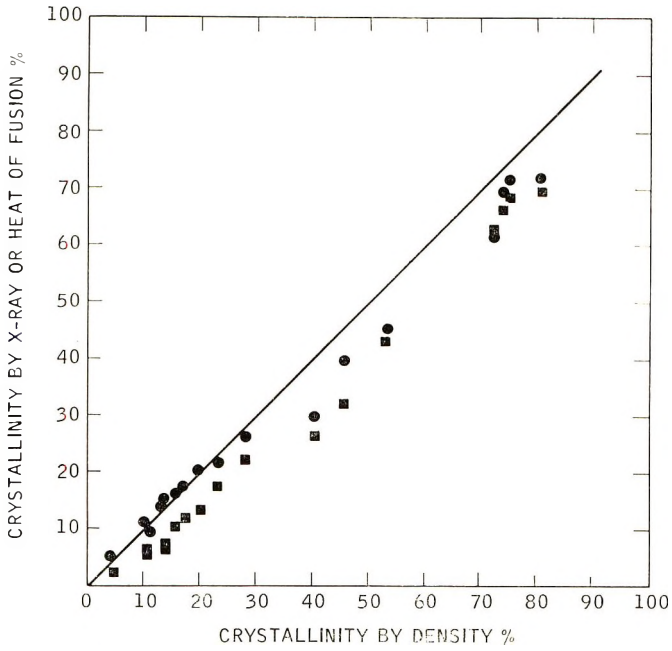
Fig. 4. Comparison of degree of crystallinity obtained by the three methods used: (■) DSC, (●) x-ray.
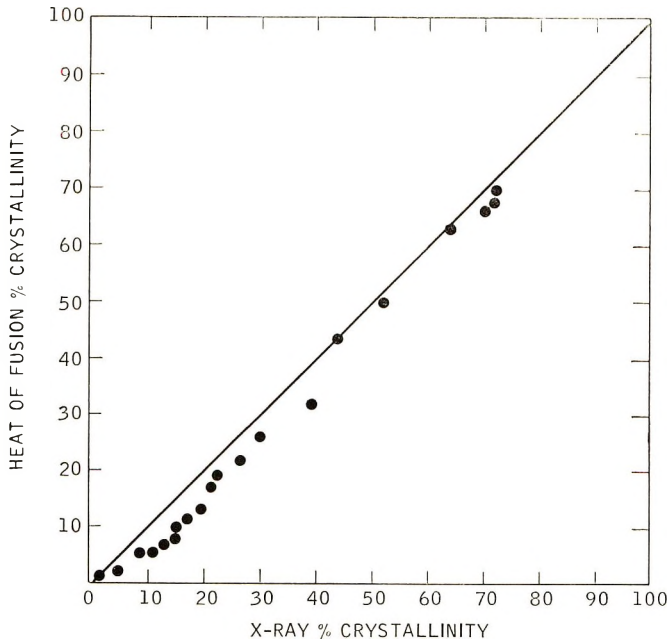
Fig. 5. Correlation of x-ray crystallinity with heat of fusion crystallinity.

x-ray and density crystallinities were found to be in agreement. As the x-ray method measures the crystallinity in a direct manner and requires no independent calibrations, we regard the x-ray values of crystallinity as being valid within the stated precision limits, and will use these values as standards of reference in the remainder of this discussion.

In Figure 5 it can be noted that the data should follow the solid line for agreement between the methods involving use of eqs. (4) and (6). The validity of the assumption of additivity of contributions from amorphous and crystalline phases has been discussed at length,[11,12] as have the defect characteristics of the crystallites formed[4,5,6,10] and unit cell variation with annealing conditions.[22] There is sufficient evidence to suggest that there is some contribution from a variety of ordered structures, especially in rapidly cooled samples. The divergence of our ΔH_f, density, and x-ray
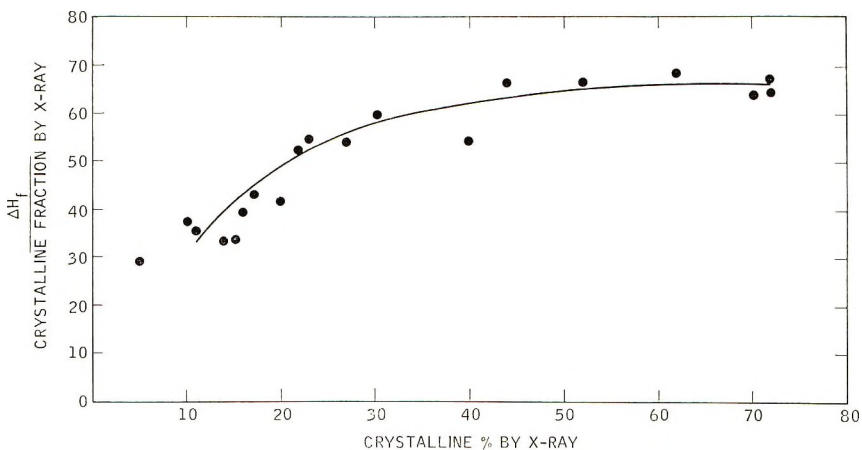
Fig. 6. Dependence of apparent heat of fusion of crystalline material on degree of crystallinity.

data is consistent with the presence of defect or surface energies. Our data are thus in qualitative agreement with Mandelkern et al.[11] and Hamada et al.,[12] for example, with regard to the effects of morphology on the heat of fusion of the crystalline material.

The "range of crystallite sizes and a diversity of interfacial structures and properties" which were studied by Mandelkern et al.[11] lead to enthalpies of fusion which became smaller fractions of the values expected from density measurements as molecular weight and undercooling increased. The small-size crystallites which resulted in that study apparently arise from kinetic restrictions due to the chain connectivity, which increase with molecular weight. In our case, small crystallites result not only from this effect (for which we have presented no data here) but from the disruptive nature of the methyl groups. This effect is the important one in our case. We can change the distribution of crystalline size and presumably the interfacial or defect energy contribution by altering annealing procedures and

sample molecular weight; however, both our data and those of Baker and Mandelkern[4] indicate these effects to be of secondary importance, once the molecular weight is high enough to permit neglect of endgroups. The presence of the comonomer units produces enthalpies of fusion which are much below those expected from the x-ray (or density) measurements even for the samples for which the undercooling is small.

These effects can be noted in the behavior of the heat of fusion. In Figure 6, the ratio of ΔH_f to f_c (from x-ray data) is plotted as a function of the per cent crystallinity (x-ray). This quantity represents the apparent heat of fusion of the crystalline material itself and it is seen that this quantity consistently decreases as the degree of crystallinity decreases. That the samples of highest crystallinity do not attain the value 69 cal/g is consistent with the data of Mandelkern et al.[11] since our data were taken at large undercoolings.

Further insight into the nature of the crystallinity in these samples can be gained by describing the regions in which melting occurs. (All data are uncorrected for instrument lag.) For the linear polyethylene of lowest molecular weight melting is not observed until the sample is heated to at least 80°C. For the branched samples melting begins at a lower temperature; similarly, for a high molecular weight linear sample, melting occurs over a broad range which starts almost immediately above room temperature. The melting terminates sooner for the branched sample, i.e., at 125°C compared with about 140°C for the linear polymers. For the copolymer samples the melting begins at some temperature slightly above room temperature and continues to a temperature which decreases as ethylene content decreases. (For our copolymer data ΔH_f is related to the temperature of maximum excursion from the baseline by $\Delta H_f \approx 0.45T - 18.0$.) This behavior is different from that of the broad-melting linear samples and is consistent with the existence of a maximum melting temperature[23] determined by copolymer content.[2,4] Thermodynamic considerations[23] lead to the conclusion that the copolymers are being annealed (room temperature) at progressively smaller undercoolings as the propylene content increases. This annealing at smaller undercoolings is not expected to produce measurable amounts of more perfect crystalline material in the context of the model of Flory,[23] however.

It can be shown (see Appendix II) that on the basis of the Flory model the reduced undercooling produced by additional comonomer, at a given temperature, does not lead to increased values of ΔH_f/(fraction crystalline). This quantity is predicted to decrease at a given temperature, with increasing comonomer content. It also decreases with increased undercooling at constant composition. The magnitude of the decrease in ΔH_f/(fraction crystalline) is of the order of that observed in Figure 6. That model is wrong for our system (comonomer units rejected from lattice, only surface energy term); however that result indicates that even in the "perfect copolymer crystal," which probably underestimates the surface effects, a large decrease in the observed enthalpy of fusion is expected.
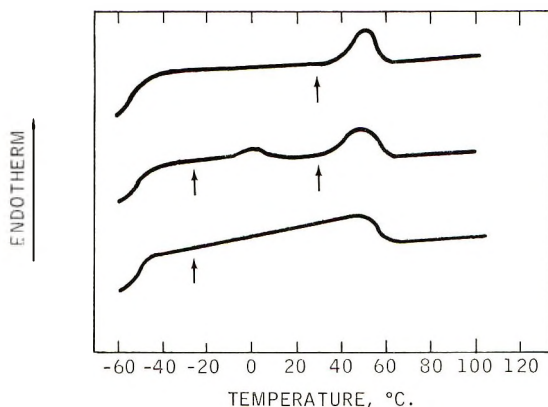
Fig. 7. Effect of annealing on DSC Traces. Arrows indicate annealing temperatures. See text for discussion.

Thus copolymers of the same molecular weight and viscosity as the lower molecular weight linear polymers (Marlex) always exhibited melting immediately above room temperature. In fact, melting that starts just above the annealing temperature can be induced by annealing at temperatures down to T_g (ca. $-60°C$) (see Fig. 7). The point of Figure 7 is that annealing of the copolymers at any temperature below the maximum melting point leads to the formation of crystalline material, some of which melts immediately above that annealing temperature. Depending on the length of the annealing period, the temperature, the polymer composition and molecular weight, one can produce multiple regions of enhanced melting by annealing at several different temperatures. This is shown by the middle scan. Complete melting of that sample and annealing only at the lower temperature produces only one broad melting region, as shown in the bottom scan. This latter behavior is important, since it indicates that "amorphous" ethylene–propylene copolymers are not usually amorphous down to T_g. The recent paper by Johnson et al.[24] discusses these effects in ethylene-vinyl acetate copolymer.

This behavior can be interpreted as copolymer units causing crystallites to form (defect containing folded structure, small folded structures, fringed micelles, or whatever) which change or are affected in a regular manner as the composition or degree of crystalinity of the polymer changes. The broad melting is indicative of crystalline material with a spectrum of stability (due to defects or size).

It is interesting, therefore, to note that these data are in agreement with the qualitative prediction of Flory's model.[23] This model is based on the concept that copolymer units are rejected from the lattice and that a surface energy results as the chain exiting from a crystalline region continues its course through the polymer (either to fold back or not).

It is known that the methyl group[5,10] can enter the lattice and also that folded lamellae can be formed with copolymers at least at low comonomer

content; however, a reasonable approach to a semi-quantitative model for the system appear to be an extension of the Flory[23] model to include these effects and with appropriate concern for the changes in the amorphous regions as discussed by Krigbaum.[25]

APPENDIX I

The unit cell volume and weight can be readily estimated from published data of interplanar spacings and copolymer composition. For example, for a composition corresponding to 7 methyl sidegroups per 100 chain carbon atoms, plotted data of Baker and Mandelkern[4] give the value $d_{200} = \frac{1}{2} a = 3.920$ Å and $d_{110} = 4.225$ Å; and for zero methyl content values of $d_{200} = 3.695$ and $d_{110} = 4.105$. From these, the calculated values for b are 5.02 Å for the former composition and 4.94 for the latter. The c dimension remains constant, within the accuracy of measurement.[5] From this information it can be easily shown that the unit cell for 7 methyl groups per 100 carbon atoms is larger by a factor of 1.076. Assuming that the chain segments contained in the crystal have the average composition (as indicated by Baker and Mandelkern[4]), the unit cell for this methyl content is heavier. Hence, we have

$$\frac{v_c(7 \text{ CH}_3/100 \text{ C})}{v_c(0 \text{ CH}_3/100 \text{ C})} = 1.006 \tag{A-1}$$

Within the accuracy of the estimate, the specific volume of the crystalline phase can be considered independent of the methyl side group concentration. However, if more accurate data for the volume of the unit cell as a function of methyl content were available, a corrected value of v_c might be justified.

APPENDIX II

The heat of fusion of a copolymer (in cal/g), corrected for surface energy effects given by:

$$\Delta H_{\text{corrected}} = \sum_{\delta = \delta^*} (W^0{}_\delta - W^e{}_\delta)(\Delta H_u - 2\sigma_e/\delta)\frac{1}{X_1 M_1 + X_2 M_2} \tag{A2}$$

where M_1, M_2 denote molecular weight of crystallizable monomer and non-crystallizable monomer, respectively; ΔH_u is the heat of fusion of the monomer (cal per mole of units); σ_e is the surface energy (in cal/mole) of emerging chains; δ^* is the minimum sequence length crystallizable; $W\delta^0$, $W\delta^e$ are the actual and equilibrium concentrations of crystallizable units, respectively; X_1, X_2 are mole fractions of monomers in the polymer.

By using eqs (9) and (12) of reference 23 in eq (A-2) we obtain:

$$\Delta H_{\text{corrected}} = \frac{1}{X_1 M_1 + X_2 M_2}[W_c \Delta H_u$$
$$- 2\sigma_e[X_1(1-p)p^{\delta^*-1} - D^{-1}(1-e^{-\theta})e^{-\theta(\delta^*)}]] \tag{A3}$$

where $D = \exp\{-2\sigma_e/RT\}$

$$\theta = \Delta H_u/R[(1/T)-(1/T_m{}^0)\,]$$

R is the gas constant, $T_m{}^0$ is the melting temperature of perfect crystalline homopolymer, p is the propagation probability of a crystallizable unit, and w, is the mole-fraction crystallinity.

Using[2] the values, $\sigma_e = 4600$ cal/mole, $T_m{}^0 = 145°C$, $\Delta H_u = 980$ cal/mole, $p = X_1$, $M_1 = 14$, $M_2 = 14$, one finds that in the composition range $0.8 < X_1 < 0.9$, with T ca. $300°K$, the surface energy lowers the heat of fusion by as much as 25%. At lower temperatures the effect is greater due to the shorter sequences crystallizing. The effects of a composition change on the melting temperature (i.e., degree of undercooling at a given temperature) are less than those on the average length of sequences involved in crystallites however, and the polymers less rich in crystallizable monomer always have the greater percentage surface energy contribution.

References

1. L. Michajlov, P. Zugenmaier, and H. J. Cantow, *Polymer*, **9**, 6, 325 (1968).
2. M. J. Richardson, P. J. Flory, and J. B. Jackson, *Polymer*, **4**, 221 (1963).
3. P. J. Holdsworth and A. Keller, *J. Polym. Sci. B*, **5**, 605 (1967).
4. C. H. Baker and L. Mandelkern, *Polymer*, **9**, 7, 71 (1966).
5. P. R. Swan, *J. Polym. Sci.*, **56**, 409 (1962).
6. D. Bodily and B. Wunderlich, *J. Polym. Sci. A-2*, **4**, 25 (1966).
7. F. J. Linnig et al., *J. Appl. Polymer Sci.*, **8**, 2645 (1964).
8. J. F. Jackson, *J. Polym. Sci. A*, **1**, 2119 (1963).
9. T. A. Veerkamp and A. Veermans, *Makromol. Chem.*, **58**, 147 (1961).
10. P. J. Holdsworth et al., *Makromol. Chem.*, **125**, 70 (1969).
11. L. Mandelkern, A. L. Allou, Jr., and M. Gopalan, *J. Phys. Chem.*, **72**, 1,309 (1968).
12. F. Hamada et al., *J. Phys. Chem.*, **72**, 1, 178 (1968).
13. Z. W. Wilchinsky, *Rev. Sci. Instr.*, **4**, 592 (1969).
14. A. Weidinger and P. H. Hermans, *Makromol. Chem.*, **50**, 98 (1961).
15. P. H. Hermans and A. Weidinger, *Makromol. Chem.*, **44–46**, 24 (1961).
16. Z. W. Wilchinsky, *Advances in X-Ray Analysis*, W. M. Mueller, G. R. Mallett, and M. J. Fay, Eds., Plenum Press, New York, 1965, Vol. 8, p. 151.
17. T. Ozawa, *Proc. Phys. Soc. Japan*, **39**, 2071 (1966).
18. B. Wunderlich, *J. Polym. Sci. A-2*, **5**, 987 (1967).
19. P. J. Flory and A. Vrij, *J. Amer. Chem. Soc.*, **85**, 3548 (1963).
20. C. M. L. Atkinson and M. J. Richardson, *Trans. Faraday Soc.*, **65**, 1794 (1969).
21. M. Dole, in *The Meaning of Crystallinity in Polymers* (*J. Polym. Sci. C*, **18**), F. P. Price, Ed., Interscience, New York, 1967, p. 57.
22. G. T. Davis et al., *J. Appl. Phys.*, **39**, 4973 (1968).
23. P. J. Flory, *Trans. Faraday Soc.*, **51**, 848 (1955).
24. V. Johnsen and A. Nachtrab, *Angew. Makromol. Chem.*, **7**, 134 (1969).
25. W. R. Krigbaum, in *U.S.–Japan Seminar on Polymer Physics* (*J. Polym. Sci. C*, **15**), R. S. Stein and S. Onugi, Eds., Interscience, New York, 1966, p. 251.
26. *American Institute of Physics Handbook*, McGraw-Hill, New York, 1957.

Planar Organosilicon Polymers

JOHN P. LINSKY, THOMAS R. PAUL, and MALCOLM E. KENNEY,
*Department of Chemistry, Case Western Reserve University,
Cleveland, Ohio 44106*

Synopsis

Work on two sheet organosilicon polymers, one derived from the mineral chrysotile and the other from the mineral apophyllite, is described. This work provides direct evidence that both these polymers are composed of sheets. In addition, it shows that in the chrysotile-derived polymer the sheets curl into scrolls, and that in the apophyllite-derived polymer the sheets are essentially flat.

INTRODUCTION

Covalently bound sheet polymers, although little known as either natural or synthetic species, appear to be of some interest. For one thing, they can be expected to be flexible on a molecular scale and pliable on a macroscopic scale (given suitably flexible connecting linkages and suitably weak intersheet attractive forces). Further, since the separation of substantial fragments from sheet frameworks requires the breaking of a large number of bonds in a concerted fashion, organic sheet polymers can be expected to show high resistance to drastic molecular weight changes upon slight framework degradation.

The opportunity for morphological control through architectural control is also to be expected of organic sheet polymers. This comes about because sheet polymers based on sheets with no strain or with balanced strain can be expected to yield powders or coherent solids, while sheet polymers based on sheets having a suitable combination of size, shape, and strain can be expected to yield fibrous products. Strong support for this view is found in the behavior of sheet silicates.[1a-e] Further support comes from what little is known about organic sheet polymers.[2-6]

While these and other features make sheet organic polymers attractive for investigation, the synthesis of such polymers presents very large hurdles. These arise because planar polymers require repeating units of functionality of three or greater[7] and such units can equally well, in general, participate in the formation of three-dimensional polymers.

One way that these preparative difficulties can be met is to synthesize in an initial step the essence of the framework desired and then in subsequent steps to convert this to the final polymer, e.g., to synthesize a crystalline material having as an inherent part of its structure the essence of the de-

sired framework and then to convert this to the final polymer by extraction, grafting, addition, substitution, etc. Of course, if a naturally occurring material containing the desired framework is available, the difficult first step can then be avoided.

The practicality of this general approach has been already established. For example, graphite has been converted to a graphite fluoride polymer by a fluorine addition process.[5,6] Similarly, the sheet silicate ion in the mineral chrysotile [common asbestos, approximately $Mg_3(OH)_4Si_2O_5$] has been converted to an organosilicon polymer by an extraction-grafting process[2−4] patterned on that developed by Lentz for the conversion of simple silicate ions to organosilicon compounds.[8]

The work that follows gives further consideration to the preparation and properties of organosilicon sheet polymers derived from silicates by extraction and grafting. Two polymers have been investigated, one being the just mentioned, but only partially characterized, polymer derived from chrysotile. The other is a similar, briefly described,[2] polymer derived from the mineral apophyllite (approximately $KFCa_4Si_8O_{20} \cdot 8H_2O$).

EXPERIMENTAL

Five similarly prepared samples of the chrysotile-derived polymer and two similarly prepared samples of the apophyllite derived polymer were used in making the micrographs shown in this paper. The new preparations of the chrysotile polymer were patterned on the earlier work of Frazier et al.[3] The preparations of the apophyllite polymer were also patterned on earlier work.[2] The Arizona chrysotile used to prepare sample 1 was a gift of the Jacquays Asbestos Corp. and came from its Eldorado Mine, 30 miles north of Globe, Arizona. It was obtained through the courtesy of Mr. D. W. Jacquays. The Quebec chrysotile used in preparation of samples 3 and 4 was from the Province of Quebec and was obtained from Ward's Natural Science Establishment, Rochester, N. Y. The synthetic chrysotile used to prepare sample 5 was a gift of the Johns Manville Corporation and was obtained through the courtesy of Dr. Julie Chi-Sun Yang. The apophyllite (samples 6 and 7) was from India and secured from Ward's Natural Science Establishment.

Chrysotile Polymer from Natural Mineral

Sample 1. This synthesis was carried out under conditions designed to disturb the fiber bundles as little as possible. A mixture of Arizona chrysotile in the form of fiber bundles about 1–2 mm in diameter and 10–20 mm in length (3.3 g), 2-propanol (150 ml), chlorotrimethylsilane (50 ml), and concentrated hydrochloric acid (30 ml) was heated gently for a few minutes, additional chlorotrimethylsilane was added (15 ml), and the mixture refluxed for 1 day. The resultant was cooled, further chlorosilane added (30 ml), and the refluxing continued for 9 more days. The product was recovered, washed, and dried (2.0 g) and then refluxed with a mixture of ben-

zene (180 ml), chlorotrimethylsilane (20 ml), and pyridine (2.4 ml) for 2 days. Since the material still contained a little unreacted mineral after being washed and dried, it and a previously refluxed (30 min) mixture of chlorotrimethylsilane (95 ml) concentrated hydrochloric acid (30 ml), and 2-propanol (150 ml) were refluxed for 3.5 days. The product, after washing and drying (2.0 g), was identified as the desired polymer by its infrared spectrum. Its spectrum also showed that it was free of mineral. Parts of the product were spotted yellow-brown, but only fiber bundles free from this discoloration were selected for use. (These discolorations were introduced in the pyridine step and were probably attributable to a decomposition product from the pyridine mixture.)

Sample 2. This sample was prepared in the manner described earlier.[3]

Sample 3. A mixture of chlorotrimethylsilane (50 ml), Quebec chrysotile dispersed in a blender in 2-propanol (2.5 g and 150 ml), additional propanol (50 ml), and concentrated hydrochloric acid (25 ml) was heated with stirring for 1 day. The mixture was then cooled, additional chlorosilane added (25 ml), and the refluxing continued for 7 days. After recovery the product was washed and dried (1.5 g) and a portion of it (1.2 g) refluxed with stirring with benzene (100 ml), chlorotrimethylsilane (15 ml), and pyridine (2.0 ml) for 3 days. The resultant, after washing and drying (1.2 g), was identified as the desired product by infrared spectra.

Sample 4. Quebec chrysotile that had previously been dispersed in distilled water, freed of impurities, and air-dried (3.1 g) was mixed with 2-propanol (156 ml), chlorotrimethylsilane (65 ml), and concentrated hydrochloric acid (30 ml) and refluxed with stirring for 1 day and cooled. Additional chlorosilane was added (30 ml) and the refluxing continued for 9 days. The product was recovered, washed, and dried (1.9 g). It was identified as the polymer by its infrared spectrum. (Experience showed that the second step of the procedure described for samples 1–3 generally added little substitution and so analogous, the step was omitted here and for sample 5.)

Chrysotile Polymer from Synthetic Mineral

Sample 5. The synthetic chrysotiles used were found to give products with low degrees of substitution with reaction mixtures of the type described above (presumably because the effective particle size of the mineral was smaller, thus leading to unsatisfactory balance between the rates of leaching and substitution). However, reaction of a stirred mixture of the synthetic mineral with a modified reaction mixture did yield a good product. In this procedure, 2-propanol (25 ml), chlorotrimethylsilane (15 ml), and concentrated hydrochloric acid (5 ml) were refluxed for 1 day, cooled, and synthetic chrysotile (0.50 g) added. The resultant slurry was refluxed for 9 days and the product recovered and washed by centrifugation (0.30 g). This product was a white hydrophobic powder that apparently swelled only slightly in solvents known to swell the natural mineral derived polymer. It gave a broad, weak x-ray diffraction maximum at about 15 Å

and an infrared spectrum similar to that of the other samples. The differences in the diffraction pattern and the swelling characteristics of this product were attributed to differences in the shape and size of the polymer particles.

Apophyllite Polymer

Sample 6. A mixture of apophyllite ground to pass 100 mesh (1.3 g), malonic acid (2.0 g), acetone (50 ml), diethyl ether (2.0 ml), distilled water (1.0 ml), and chlorotrimethylsilane (25.0 ml) was allowed to stand in a stoppered flask for 13 days. The resultant was recovered, washed, and dried (1.3 g) and a mixture of it (0.20 g), pyridine (10 ml), and N,O-bis(trimethylsilyl)acetamide (10 ml) was refluxed for 5 days. The product, after being recovered, washed, and dried, was a white hydrophobic powder which gave only one x-ray diffraction peak. This peak was fairly sharp (considerably sharper than that of the chrysotile polymer, presumably because the sheets in this polymer lie essentially flat (see below) and corresponded to a Bragg spacing of about 16 Å. The infrared spectrum was similar to that of the chrysotile polymer,[3] except that the bands associated with the organosilicon groups were relatively more intense.

Sample 7. To prepare this sample, apophyllite (100 mesh, 10.0 g) was treated with a mixture of acetone (500 ml), distilled water (4.0 ml), and chlorotrimethylsilane (200 ml) in a stoppered flask for 1 day. The resultant was recovered, washed, dried, and treated with an identical mixture for 11 more days. Again the resultant was recovered, washed and dried (10.1 g). A mixture of this (2.0 g), pyridine (50 ml), and N,O-bis(trimethylsilyl)-acetamide (50 ml) was refluxed for 3 days. The final product, after being washed and dried, had the same infrared spectrum as sample 6.

Elemental analyses of the apophyllite polymer gave erratic results, particularly for silicon, in spite of considerable effort spent on technique. As a whole, they indicated that half or somewhat more of the available sheet sites were occupied by trimethylsilyl groups. In earlier work the chrysotile also seemed to present difficulties in analysis though they were less severe.

Microscopy

Japan Electron Optics Laboratory JEM-6A and Hitchi Limited HU-11A electron microscopes equipped with hairpin filaments were used in this work. Embedding was carried out with Araldite 6005 resin and sectioning with a Reichert Om-U2 ultramicrotome equipped with a diamond knife. The unembedded samples were supported on carbon coated copper and tungsten grids while the embedded samples were supported on uncoated grids. Sample 1 was used for the micrographs shown in Figures 3–6, sample 2 for Figure 7, sample 3 for Figure 8, sample 4 for Figures 9 and 10, sample 5 for Figure 11, sample 6 for Figure 13, and sample 7 for Figure 14.

RESULTS AND DISCUSSION

Previous work[3] has shown that the treatment of chrysotile with a mixture of isopropanol, hydrochloric acid, and chlorotrimethylsilane leads to a complex reaction in which the composite brucite–silicate sheets making up the mineral (Figure 1)[1d] are converted into trimethylsilyl-substituted sheets. On the basis of the available data and what is known of the general chemistry of silicon it has been concluded that the stripping and grafting steps involved in this reaction take place simultaneously on a given
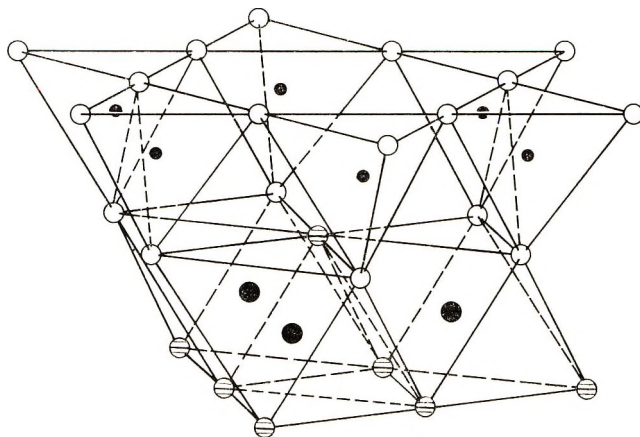
Fig. 1. Composite sheet of chrysotile (•Si, ●Mg, ⊖OH, ○ o).
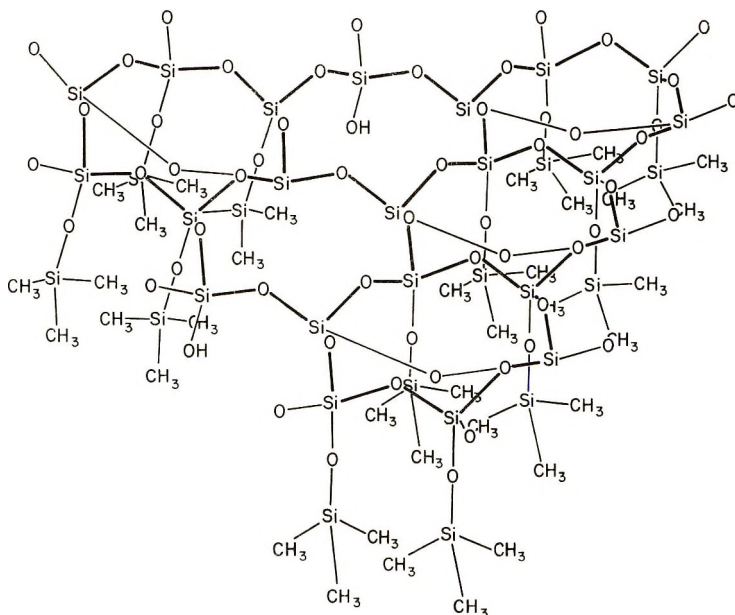
Fig. 2. Chrysotile-derived polymer sheet as proposed by Frazier et al.[3]
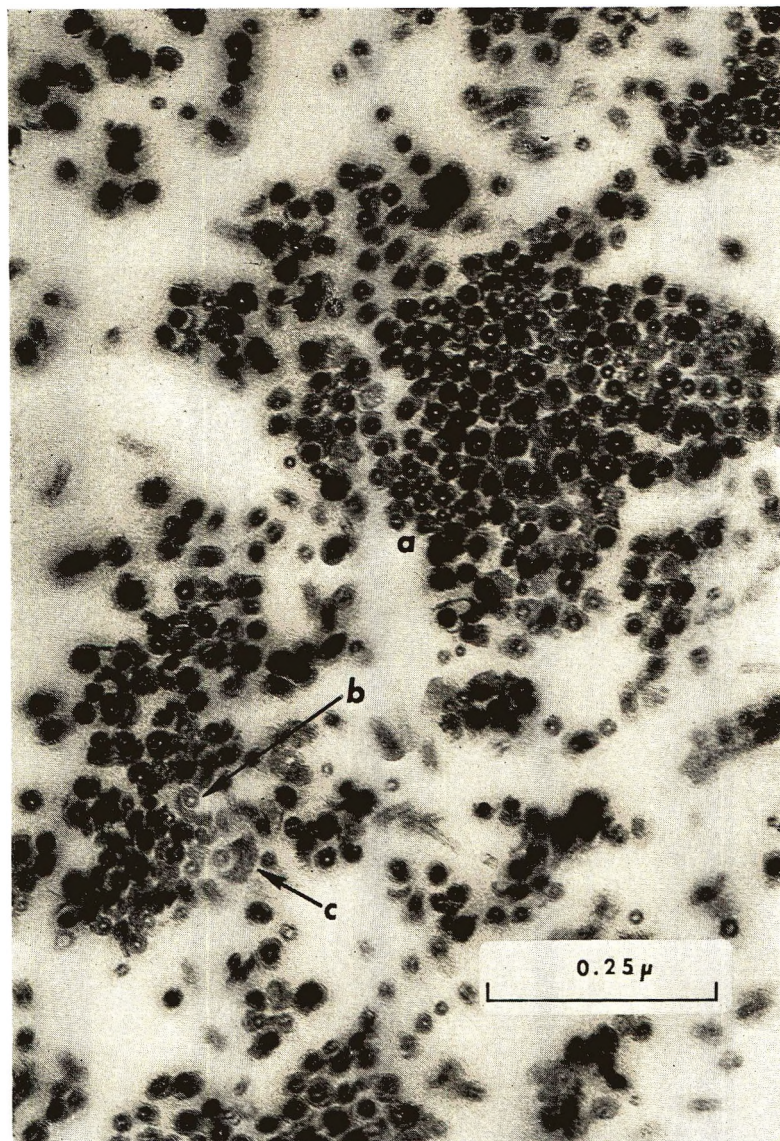
Fig. 3. Cross sections of the chrysotile polymer fibers embedded in Araldite resin showing
(a) ring, (b) spiral, and (c) semiring outlines.

sheet. It has also been concluded that about half the sites available
on a given sheet are occupied by trimethylsilyl groups and that the rest are
occupied by OH groups or are linked together by oxygen bridges. A
schematic representation of this postulated structural arrangement is
shown in Figure 2.

To account for the observed fibrous morphology of the polymer, it has
been postulated that the individual polymer sheets have internal strains and
that these cause the sheets to curl into tubelike fibers. The observed
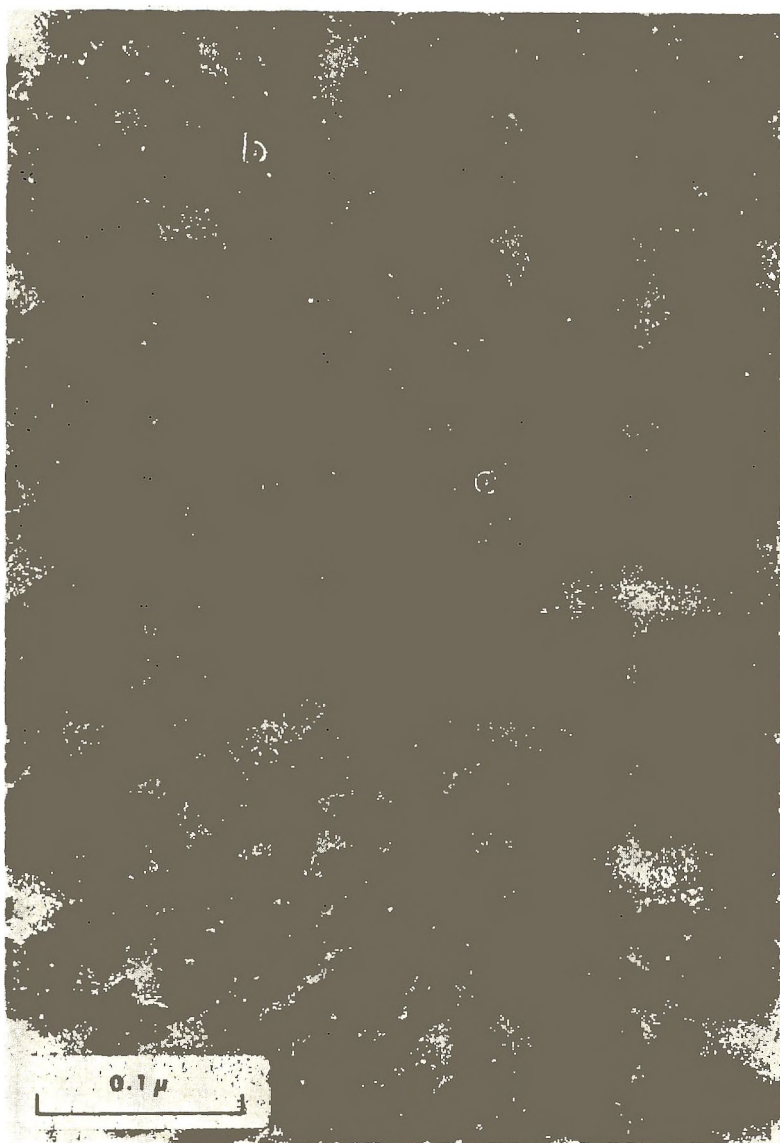
Fig. 4. Cross sections of the chrysotile polymer fibers embedded in Araldite resin having unusual double cores, (a) and (b).

swelling of the polymer in ordinary organic solvents has been attributed to an uncoiling of the polymer sheets.

The present work supports these conclusions and provides a basis for their elaboration and extension. Figures 3 and 4 present micrographs of cross sections of the fibers embedded in Araldite resin. Most of the fibers in these micrographs appear as rings although a few appear as spirals or partial rings. In accord with earlier conclusions, the rings are thought to be associated with unswelled scrolls, the spirals with swelled scrolls, and the
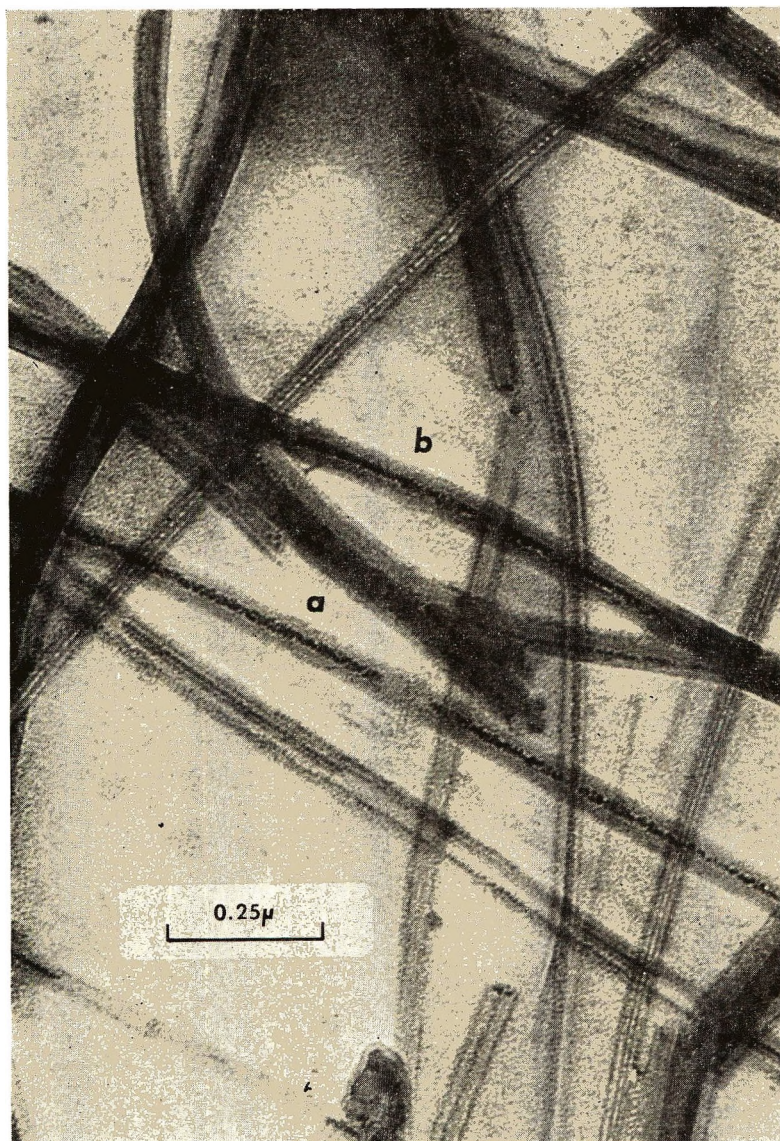
Fig. 5. Chrysotile polymer fibers with lead filled cores, (a) and (b).

semirings with pieces of scrolls. (In the earlier similar micrographs most
of the fibers are swollen and have spiral cross sections. This difference is
attributed to differences in the synthetic and embedding procedures used.)
The fact that the cores of the rings of Figures 3 and 4 are quite transparent
to the electron beam is of interest and suggests that these fibers are essen-
tially empty.

Further evidence on the nature of the cores is provided by the results of a
lead-staining experiment. In this experiment some fibers on a carbon-
coated grid were wetted with a drop of a dilute lead acetate–dimethylform-

Fig. 6. Lattice images of the chrysotile polymer fibers embedded in Araldite resin showing the layerlike nature of polymer. Note the incomplete layers of fibers around (a).

amide solution and allowed to dry in air. The dark cores of some of the fibers (Fig. 5) give unmistakable evidence of trapped lead and hence of the hollow character of these fibers. That only some of the fibers trapped lead is not surprising, even assuming, as is reasonable, that most of them were hollow,* since the trapping of lead during the evaporation of the solvent

* Whether or not the chrysotile fibers are sometimes partially filled has been a subject of debate.[9]

Fig. 7. Lattice image of a chrysotile polymer fiber embedded in Araldite resin giving
clear indications of a spiral structure, (*a*).

and the accompanying recurling of the fibers is clearly a chance process. (It should be pointed out that it is now believed that the uncoiling of the fiber scrolls in solvents is probably only partial and not complete. This does not, however, alter the essence of the argument presented.) Pertinent to these results is the fact that Clifton, Huggins and Shell earlier achieved a similar result with chrysotile fibers by a somewhat different means.[9]

Direct confirmation of the previously proposed layerlike nature of the fibers is provided by the lattice images of the fiber cross sections shown in
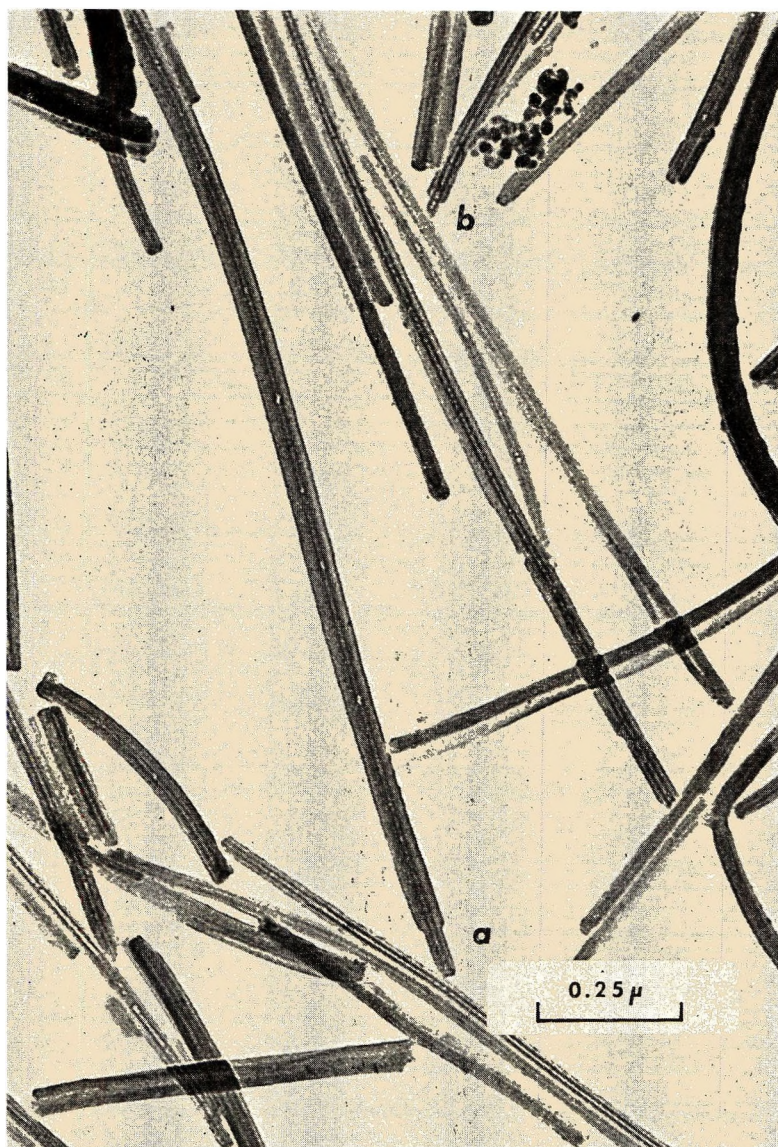
Fig. 8. Chrysotile polymer fibers with ends of reduced diameter, (a) and (b).

Figures 6 and 7. (Lattice images as clear as these were seldom found, in part, of course, because of the required precise vertical alignment of the sections.) Similar direct confirmation of the layer nature of chrysotile fibers has been furnished by lattice images of mineral fiber cross sections.[10]

These micrographs indicate that many of the individual layers are incomplete. The occurrence of such layers supports the assumption made above that the semirings of Figures 3 and 4 are associated with pieces of scrolls. Incomplete layers have also been found in the mineral fibers,[10]
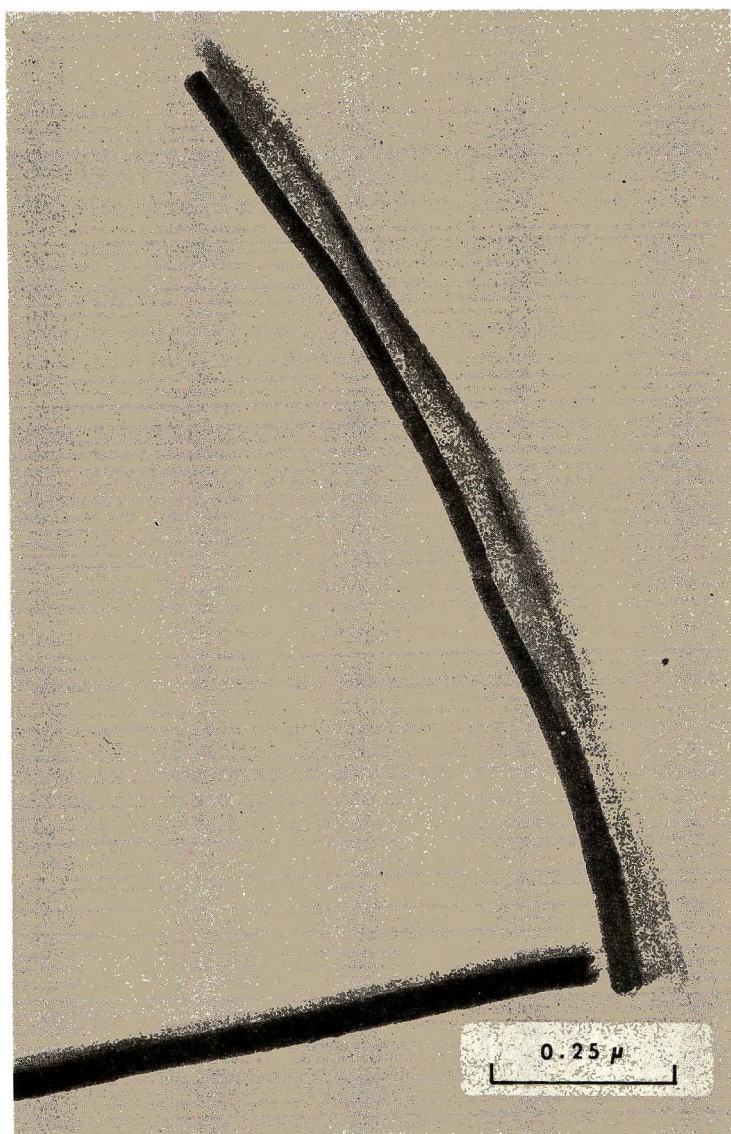
Fig. 9. Chrysotile polymer fiber with a parallel ribbon.

and it is assumed that the incomplete layers observed here were derived from similar incomplete mineral layers. (The formation of such layers during the conversion process seems unlikely.) That these incomplete layers did not get separated from the main parts of the fibers suggests that elsewhere they were more complete.

Somewhat puzzling is the fact that the measured distance between the lattice image lines in Figures 6 and 7 is about 17 Å, while the interlayer spacing deduced for the fibers from earlier x-ray powder work[3] is about 15 Å. Perhaps this discrepancy is connected with the difficulty of interpreting

Fig. 10. Lattice image of a chrysotile polymer fiber in a horizontal position.

the diffraction results from these unusual fibers (the microscope calibration was checked).

In Figure 7 is seen direct evidence for scroll-like character in a tightly curled fiber. Interestingly, it appears that three layers are rolled up together in this scroll. These results find a direct parallel in the work of Yada[10] on the mineral fibers. This latter work shows without question that the mineral fibers are composed of scrolls with an interlayer spacing of 7.3 Å (thus incidentally making it quite clear that the present fibers

Fig. 11. Synthetic chrysotile polymer fibers.

are not unreacted mineral fibers) and that various numbers of layers can be rolled up in the scrolls.

Several other details of the polymer fibers are worth noting. One of these is the occasional appearance of fiber ends with reduced diameters. Figure 8 shows two such fiber ends. These probably arise from layers with partially set back edges curling up to form the fibers, or from additional layers wrapping around already former fibers. Since ends of this type are known for the parent mineral fibers,[11] it is presumed that the observed
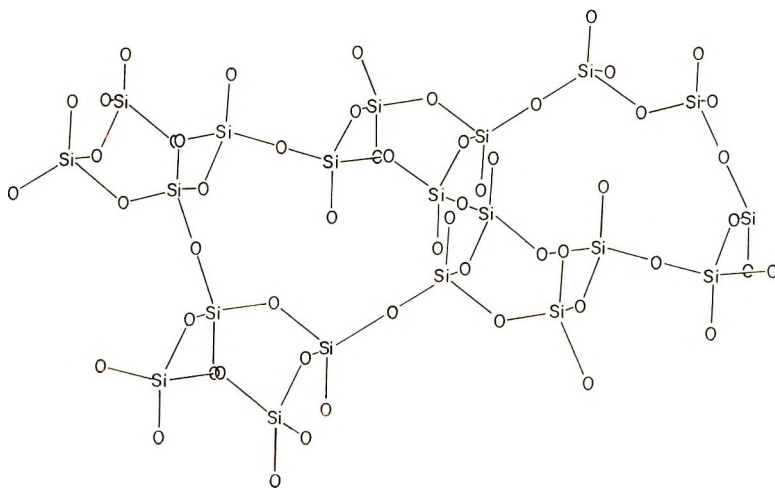
Fig. 12. Silicate sheet found in apophyllite.

ends with reduced diameter were derived from mineral fiber ends with similarly reduced diameters.

Also found (but rarely) are fibers with double cores (Figure 4). These could arise from a number of different types of unusual structure patterns. Two such patterns are suggested by Yada's[10] work on mineral fiber cross sections.

A feature of the fibers which is seen fairly often when the fibers are viewed horizontally is shown in Figure 9. It is presumed that the ribbon–fiber pair seen here is actually a partially unrolled fiber.

In Figure 10 is seen the lattice image of polymer fiber resting in a horizontal position. The spacing of the lines, about 17–19 Å, is that expected from the cross-section work. Similar lattice images (but spaced by 7.3 Å) have been observed for the parent mineral fibers by Yada. A complicating feature in the interpretation of this micrograph is that another fiber in the same micrograph shows more widely spaced lines. While the reason for this is not known, it may be that this second fiber was simply less tightly rolled than the first one.

The expected flexibility of the polymer sheets is reflected in the fact that the fibers are frequently seen in bent or curved configurations (e.g. Figure 5). It is also reflected in the ability of the sheets to uncurl when wetted with organic solvents and in the softness of the polymer on a macroscopic scale.

In Figure 11 is shown the product obtained from the synthetic chrysotile. The fibers in this product are much shorter and much less uniform in diameter than are those from the natural mineral. This is not at all surprising, since micrographs of the parent synthetic mineral show that it is also composed of short fibers of variable diameter. This product is of particular interest since it represents the full synthesis of an inherently fibrous poly-

Fig. 13. Bent (a) and stacked (b) sheets of the apophyllite polymer.

mer, both the framework-building stage and the grafting stage having been carried out in a deliberate fashion.

The previous work on the chrysotile-derived polymer fibers did not establish clearly the origin of the strain causing the sheets to bend nor the way in which they bent (i.e., with the methyl groups on the covex or concave side of the sheet). The present work does not provide direct evidence on this point either, but it is reasonable to suggest that the curl is caused by steric hindrance between methyl groups and that these are

Fig. 14. Lattice image of the apophyllite polymer embedded in Araldite resin and cross-sectioned.

therefore on the convex side of the sheet.   Perhaps the strongest point in favor of this view is the extremely hydrophobic character of the fibers.

A complement to this and earlier work on the chrysotile-derived polymer is provided by the work on the apophyllite-derived polymer.   While analytical difficulties prevented assessment of the degree of substitution in this polymer, the microscopic evidence indicates that the silicate sheets of the mineral were extracted and converted to organosilicon polymer sheets.   However, because of the nature of the parent Si_2O_5 = sheets[1e]

(Figure 12), the grafted groups must have been attached to both sides of the sheets thus giving balanced strains. Accordingly, flat sheets are expected. That such are obtained is shown clearly in Figures 13 and 14. The former figure shows in addition that the sheets are flexible, as expected.

Three methods were used to obtain information on the distance between the sheets; direct measurement of the distance between the lattice image lines, selected-area electron diffraction on the cross-section used to obtain the lattice images, and x-ray diffraction on similarly synthesized samples of the dry powder. Direct measurement indicated that the closest interlayer spacing was about 20–22Å. In agreement with this the selected area electron diffraction work gave a d spacing of ca. 22 Å, thus indicating an average spacing in the 22 Å range. The x-ray diffraction work gave a d spacing of ca. 16 Å and thus an average spacing of ca. 16 Å. Perhaps the first two methods gave larger spacings because the embedding process increased the spacing somewhat.

In accord with the flexibility of the sheets on a microscopic scale, the bulk powder is soft and exhibits somewhat waxlike behavior when ground. The chemical robustness of the sheets is demonstrated by their method of synthesis.

References

1. W. A. Deer, R. A. Howie, and J. Zussman, *Rock Forming Minerals,Vol. 3, Sheet Silicates*, Wiley, New York, 1962, (a) p. 191; (b) p. 1; (c) p. 121; (d) p. 170; (e) p. 258.

2. J. A. Bedford, S. E. Frazier, and M. E. Kenney, paper presented at 152nd National Meeting, American Chemical Society, New York, Sept. 1966; Abstracts, No. O59.

3. S. E. Frazier, J. A. Bedford, J. Hower, and M. E. Kenney, *Inorg. Chem.*, **6**, 1693 (1967).

4. J. J. Fripiat and E. Mendelovici, *Bull. Soc. Chim. France*, **1968**, 483.

5. J. L. Margrave, *Chem. Eng. News*, **48**, No. 2, 40 (1970).

6. W. Rüdorff, *Advan. Inorg. Chem. Radiochem.*, **1**, 230 (1959).

7. A. F. Wells, *Third Dimension in Chemistry*, Oxford Univ. Press, London, 1956, p. 19.

8. C. W. Lentz, *Inorg. Chem.*, **3**, 574 (1964).

9. R. A. Clifton, Jr., C. W. Huggins, and H. R. Shell, *Amer. Mineral.*, **51**, 508 (1966).

10. K. Yada, *Acta Cryst.*, **23**, 704 (1967).

11. T. F. Bates and J. J. Comer, *Proc. Nat. Conf. Clays and Clay Minerals*, **6**, 237 (1959).

Piezoelectricity, Pyroelectricity, and the Electrostriction Constant of Poly(vinylidene Fluoride)

KEN'ICHI NAKAMURA and YASAKU WADA,
*Department of Applied Physics, Faculty of Engineering,
University of Tokyo, Bunkyo-ku, Tokyo, Japan*

Synopsis

A new device for measuring the electrostriction constant of polymer films is described. Observed values for various polymers except poly(vinylidene fluoride) and poly(methyl methacrylate) agree well with those calculated from the Clausius-Mosotti equation. Elongational piezoelectricity, the pyroelectric current, and the electrostriction constant are measured for undrawn and roll-drawn poly(vinylidene fluoride) films. The piezoelectricity and pyroelectric current are attributed to space charges antisymmetrically distributed along thickness direction of the film for two reasons: (1) the polarity coincides between these two phenomena for all specimens, and (2) the piezoelectricity and the electrostriction constant have the same anisotropy for drawn films. Similarity of signs between piezoelectricity and pyroelectric current is observed also in poly(vinyl chloride) films. The electrical behavior of poly(vinylidene fluoride) is interpreted in terms of the ferroelectric nature of the β-form crystal.

Introduction

Poly(vinylidene fluoride) (PVDF) is distinguished among polymers by a very high dielectric constant. Melt-cast films of PVDF have an α-crystal form in which a molecule takes a planar *cis* conformation (2_1 helix) and the resultant dipole moment of the C—F bond is parallel to the chain axis.[1] When the film is drawn by rolling, the crystal is transformed into the β form, in which the molecular conformation is a planar zigzag and the dipole moment of the molecules is oriented perpendicularly to the chain axis. According to Lando, Olf, and Peterlin,[2,3] the unit cell of the β crystal (phase I in their work) is orthorhombic, belonging to space group *Cm2m;* and the dipole moment of two chains in the unit cell are oriented in parallel along the b axis. The β crystal of PVDF therefore exhibits the spontaneous polarization and this material may be classified as a ferroelectric polymer, if the polarization is proved to be reversed by an external field.

Various authors have studied the dielectric constant and dielectric loss of unrolled and rolled PVDF films as a function of temperature and frequency.[4–10] According to them, the polymer exhibits three relaxation regions, α, β, and γ, in the order of descending temperature. The α relaxation is assigned to the crystalline relaxation due to motion in the crystal.

161

The α relaxation markedly decreases in height and shifts to higher temperature when the crystal is transformed from the α to the β form.   The β and γ relaxations are assigned to primary and local-mode relaxations, respectively, both of which concern to motion in the amorphous phase.   The glass transition temperature of PVDF is around $-35°$C.

Piezoelectricity of PVDF was studied by Kawai[11] and Fukada[12] for PVDF films which had been drawn and then poled, that is, a high dc voltage was applied at a high temperature and then the film was cooled while the voltage was maintained.   The films show a very high piezoelectric constant, especially for elongation along the drawing direction.   The relation between the polarities of poling and piezoelectricity suggests that the film has a spontaneous polarization.   Asahina, Kakutani, and Wada[13] investigated the pyroelectric current in solvent-cast PVDF film in which β crystals are preferentially oriented.   The pyroelectric current denotes the short-circuited current that appears upon heating the capacitor constituted by the polymer film.   They observed that the current continues up to the melting point and that the integrated current agrees in sign and amount with the spontaneous polarization of the β crystal.

Elongational piezoelectricity of polymer films which have neither been drawn nor poled was found by Furukawa et al.[14] for a variety of polymers, including nonpolar and amorphous polymers.   This piezoelectric effect has been attributed to the space charge embedded in the polymer film.   If the charge distribution is antisymmetrical in the thickness direction (z axis), the film exhibits the polarization P_z which changes as the thickness changes in elongation.   An asymmetrical distribution can be in general decomposed into symmetrical and antisymmetrical distributions, and the latter component results in the piezoelectricity.   They also studied the pyroelectricity of poly(vinyl chloride) films and concluded that this phenomenon is also due to the antisymmetrical distribution of the space charge.   When the capacitor is short-circuited, the space charge in the dielectric is attracted to the nearer electrode on account of the image charge.   When the capacitor is heated and the charge attains sufficient mobility, the charge moves to the nearer electrode, and, if the charge distribution is antisymmetrical along the z axis, the resultant current appears.

The purpose of this paper is, first, to establish the correlation between pyroelectricity and piezoelectricity for undrawn and drawn films of PVDF. If both phenomena come from the antisymmetrical space charge distribution as described above, the same polarity must be observed for both phenomena in a given specimen.

The second purpose of this study is to investigate the origin of piezoelectricity of roll-drawn PVDF films.   Since the β crystal of PVDF has no symmetry center, the piezoelectricity might be due to internal strain as is the usual case in piezoelectric crystals.   Another possible origin of the piezoelectricity is the antisymmetrical distribution of space charge as in undrawn PVDF and other unoriented polymers.   These possibilities may be distinguished by anisotropy of the piezoelectricity, its correlation with the elec-

trostriction constant, and the correlation between polarities of piezoelectricity and pyroelectricity.

The study is part of a program to obtain a general understanding of piezoelectricity and other related electrical properties of polymer films which have been treated in various ways such as roll-drawing and poling.

Experimental Techniques and Samples

Techniques for measuring elongational piezoelectricity and pyroelectric current have been fully described in a previous paper.[14]

The electrostriction constant κ is defined by

$$\kappa = -\frac{1}{\epsilon}\left(\frac{\partial\epsilon}{\partial s}\right) \tag{1}$$

where ϵ is the dielectric constant and s the strain.   For an anisotropic material, κ is expressed as a tensor of fourth rank.   In this experiment, ϵ is the component along the z axis (thickness direction); and s the elongational strain in the xy plane.   Two methods for determining electrostriction are (1) to measure the change of ϵ with variation of s and (2) to measure the portion of strain that is proportional to the square of the electric field.[15] The latter method is, however, susceptible to errors for a piezoelectric material in which there is a strain contribution linearly proportional to electric field.   The first method, therefore, was adopted in this study.

The change of capacitance $C = \epsilon A/4\pi l$ of a parallel-plate capacitor due to elongational strain s is

$$\delta C/C = (\delta\epsilon/\epsilon) + (1 + \sigma_1 - \sigma_2)s \tag{2}$$

where A is the electrode area, l is the thickness of the dielectric, and σ_1 and σ_2 denote Poisson's ratio along the z axis and along the axis perpendicular to elongation in the xy plane, respectively.   If the material is elastically isotropic, σ_1 is identical with σ_2.   For a drawn polymer film, this is not exactly the case.   In the following, however, we always assume $\sigma_1 = \sigma_2 = \sigma$ for
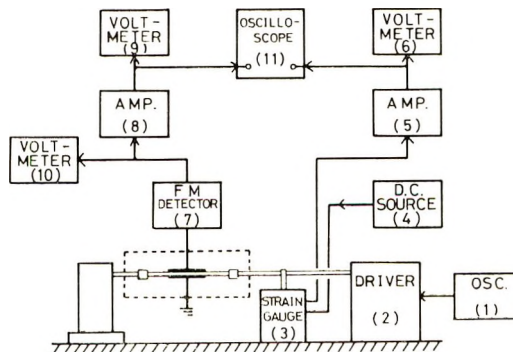

Fig. 1. Block diagram of apparatus for measuring electrostriction constants of polymer films.
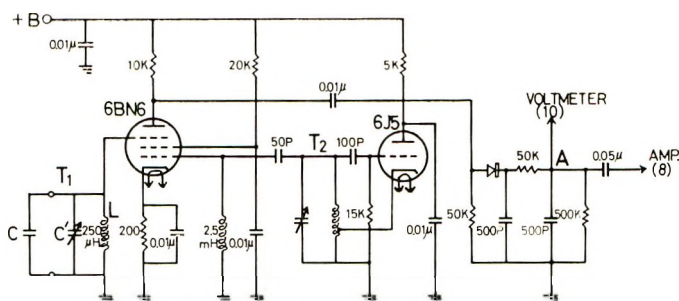
Fig. 2. Circuit diagram of the FM detector.

every case for simplicity because the difference $|\sigma_1 - \sigma_2|$ is presumably small compared with unity. Then, κ can be estimated from plots of $\delta C/C$ against s.

The electrical circuit for measuring κ is illustrated in Figures 1 and 2. Figure 1 is a block diagram of the entire system and Figure 2 is the circuit diagram of the FM detector.

The specimen (capacitor C) is mechanically vibrated by the moving-coil vibrator (2) at 130 Hz. The amplitude of displacement δL is detected by the strain gauge (3) and indicated by the voltmeter (6). The voltmeter reading V_1 is proportional to δL, i.e., $V_1 = K_1 \delta L$. The maximum of δL is limited to a few microns. The capacitor C forms a tuned circuit T_1 with the parallel inductance L and the variable capacitor C'. The resonant frequency f_1 of the circuit varies sinusoidally with time as the specimen is vibrated. The frequency f_2 of the oscillator T_2 is fixed at about 1 MHz and the maximum slope of the resonant curve of T_1 (without vibration) is adjusted to f_2 by means of the capacitor C'. When the specimen vibrates at 130 Hz, the 130 Hz output signal $\bar{V}_2$ at the point A is proportional to δC, i.e., $\bar{V}_2 = k\delta C$. The reading V_2 of voltmeter (9) is then $V_2 = K_2 k \delta C$.

Using eq. (2) with $\sigma_1 = \sigma_2$, we obtain

$$\kappa = -(\delta\epsilon/\epsilon)/s$$
$$= 1 - (\delta C/C)/s$$
$$= 1 - (K_1 L / K_2 k C)(V_2/V_1) \tag{3}$$

Here K_1 and K_2 are apparatus constants; L is the span-length; and k is proportional to the maximum slope of the resonant curve of T_1 and depends on the dielectric constant and dielectric loss of the specimen. The value of k for each specimen was obtained as follows. By varying the capacitance C' without vibrating the specimen, the resonant curve of circuit T_1 was obtained from the indication of the dc voltmeter (10) as a function of the capacitance C'. The maximum slope of the resonant curve thus obtained gives the value of k.

The oscilloscope (11) served as an indicator of phase relation between V_1 and V_2, that is, between s and δC. The capacity C of the specimen was
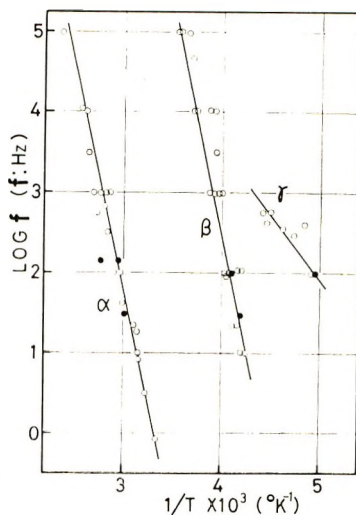
Fig. 3. Frequency of loss maximum plotted against reciprocal of absolute temperature for unrolled poly(vinylidene fluoride): (O) dielectric loss; (●) mechanical loss.

measured by a transformer bridge at 1 MHz (Ando-Denki TR-1B).   Silver electrodes were vacuum-deposited on both surfaces of the specimen.   The electrode dimensions were 1×1 cm^2.   Measurements of piezoelectricity and electrostriction constant were made at room temperature except as specially noted.

Films of PVDF were kindly supplied by Kureha Kagaku Co. Ltd.   Specimens used were films as-received, and roll-drawn films.   The as-received films proved to be almost isotropic so far as is indicated by measurements of Young's modulus.   The thickness of the undrawn film was 0.16 mm but was

TABLE I
Electrostriction Constants κ_0 of Polymers

| | κ_0 | |
Polymer	Observed	Calculated from Clausius-Mosotti equation
Poly(vinylidene fluoride) (undrawn)	0.29	1.14
Polystyrene	0.37	0.37
Poly(vinyl chloride)	0.32	0.29
Poly(methyl methacrylate)	0.25	0.41
Poly(bisphenol-A carbonate)	0.46	0.34
Poly(ethylene terephthalate) (amorphous)	0.40	0.38
Polypropylene	0.34	0.24
Polyethylene (high density)	0.27	0.26
Regenerated cellulose	0.93	0.88
Cellulose triacetate	0.35	0.35

decreased to 0.09 and 0.07 mm for draw ratios $\alpha = 1.6$ and $\alpha = 2.1$, respectively. The width of the film was kept almost constant during roll-drawing.

Dielectric constant and dielectric loss of the specimen were measured by the transformer-bridge. The dispersion map, a plot of loss-maximum temperature against frequency, is given in Figure 3, in which literature data[4-10] as well as the present data are compiled.

Electrostriction constants of several other polymers were measured for comparison and are listed in Table I.

Correlation between Pyroelectricity and Piezoelectricity

Pyroelectric current and piezoelectricity of polymer films should exhibit the same polarity, if both phenomena result from the same space charge in the film. Figure 4 shows a schematic representation of charges in the dielectric. In case (a) where the charge consists of true charges embedded in the dielectric, the charge will be pulled to the nearer electrode by attraction by the image charge and hence the upper electrode is positive for pyroelectric current in the load circuit. In case (b), on the other hand, where the charge consists of oriented dipoles, the pyroelectric current will have an opposite polarity to that for case (a).
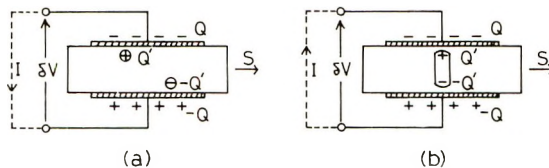

(a)   (b)

Fig. 4. Schematic representation of charges Q' in the dielectric, piezoelectric voltage δV for strain s and pyroelectric current I: (a) True charges embedded in the dielectric; (b) dipole orientation.

In the present study of elongational piezoelectricity, the piezoelectric charge Q_p is given by the voltage change δV due to elongational strain s multiplied by the capacitance,

$$Q_p = C \delta V \tag{4}$$

If charges in the film undergoes affine displacement with strain, no change in the charge on the electrodes will occur. However, since the metallic electrodes deposited on the polymer film have a much higher stiffness than the polymer film, surface layers are deformed only slightly with the deformation of the specimen. The non-uniform strain in the surface layers of specimen will act as a constant voltage source; and the equivalent circuit of the specimen consists of a dc voltage source E and a sinusoidally varying capacitance C connected in series. With sufficiently high input impedance in the measuring circuit, the charge Q on the electrode corresponding to

C is kept constant with strain and has the opposite sign to E; i.e., $Q = -CE$. Since $Q = CV$ and $\delta Q = 0$, it follows that

$$C\delta V = -V\delta C \tag{5}$$

This leads with eq. (4) to

$$Q_p = -V\delta C = -Q(\delta C/C) \tag{6}$$

Therefore, Q_p has the opposite polarity to Q and hence the same polarity as the charge in the dielectric. It is concluded, therefore, that piezoelectricity and pyroelectricity must exhibit the same polarity for an antisymmetrical distribution of true charges [case (a)] but opposite polarity for oriented dipoles [case (b)].

From eq. (2) with $\sigma_1 = \sigma_2$, it follows that

$$Q_p = -Q(1 - \kappa)s \simeq Q'(1 - \kappa)s \tag{7}$$

where $Q' \approx -Q$ is the charge in the dielectric.

Figure 5 shows the elongational piezoelectricity of three PVDF films and two poly(vinyl chloride) films. In the case of drawn films, the data for strain perpendicular to the draw axis is given, but the polarity is the same for all directions. The surface of the film is denoted as positive when the positive piezoelectric charge appears on this surface in elongation.

Figure 6 illustrates the pyroelectric current as a function of temperature (heating rate, 2.7°C/mm) for the same samples as in Figure 5. Positive current means current flow from the positive surface to the negative one in the load circuit.

The coincidence of the polarity of piezoelectricity and pyroelectricity affords evidence that both phenomena result from the same space charge in the film.
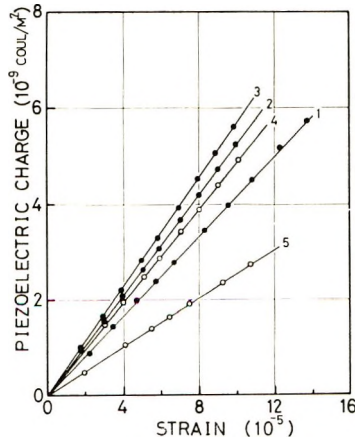

Fig. 5. Piezoelectricity versus elongation: (1) unrolled PVDF, (2) rolled ($\alpha = 1.6$) PVDF ($\theta = 90°$); (3) rolled ($\alpha = 2.3$) PVDF ($\theta = 90°$); (4), (5) poly(vinyl chloride).
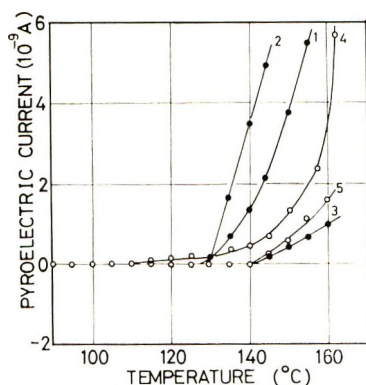
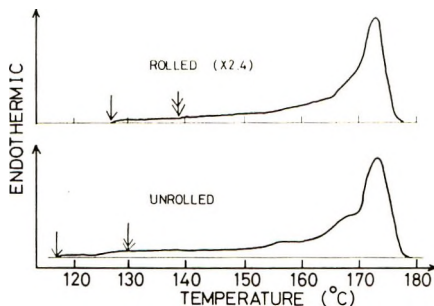Fig. 6. Pyroelectric current. Samples identified as in Fig. 5.

Fig. 7. Thermal analysis of PVDF by differential scanning calorimetry. Single arrows indicate start of partial melting and double arrows the threshold for pyroelectric current. Heating rate, 8°C/min.

The threshold temperature of the pyroelectric current in PVDF can be correlated with the onset of melting of crystallites. Results of the differential scanning calorimetry are shown in Figure 7, in which one can see the partial melting starts at 117°C and 127°C for undrawn and drawn (α = 2.4) films, respectively. The pyroelectric current begins at 130°C and 140°C for these two films, respectively, 13°C higher than the start of melting. This suggests that the trapped space charge can move only after melting of small crystallites has begun.

Electrostriction Constant

As has been shown in the preceding section, the piezoelectricity of PVDF, both undrawn and roll-drawn, seems to be attributable to the space charge embedded in the film. Equation (7) indicates that the apparent piezoelectric stress constant $e = Q_p/As$ is closely related to the electrostriction constant.

Assuming the Clausius-Mosotti equation,

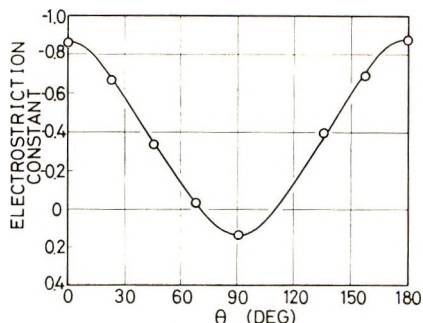$$\frac{1}{\rho}\left(\frac{\epsilon - 1}{\epsilon + 2}\right) = \text{const.} \tag{8}$$

Fig. 8. Electrostriction constant of roll-drawn PVDF ($\alpha = 2.3$) plotted against angle between elongational strain and draw-axis.

where ρ is the density, and assuming in addition that the dielectric constant depends on density variation alone, one can obtain the electrostriction constant κ_0 for elongational strain:

$$\kappa_0 = (1 - \sigma_1 - \sigma_2)[(\epsilon - 1)/(\epsilon + 2)]/3\epsilon \tag{9}$$

In Table I, electrostriction constants of various undrawn polymers are listed and compared with κ_0 calculated from eq. (9). In the calculation, ϵ at 1 MHz was used, and Poisson's ratios were assumed as $\sigma_1 = \sigma_2 = 0.35$ for all the polymers. This value was taken from data on polystyrene and poly-(methyl methacrylate).[16] The scatter in values of Poisson's ratio among glassy and semi-crystalline polymers is not so great as to affect the conclusion.

Except in PVDF and poly(methyl methacrylate), both of which exhibit dielectric relaxation at room temperature, the observed values of κ are reasonably close to κ_0, as can be seen in Table I. In the case of PVDF, however, the absolute value of κ is markedly larger than κ_0.

Figure 8 represents the anisotropy of the electrostriction constant of roll-drawn PVDF. The value is negative irrespective of strain direction and the absolute value is the highest for strain along the drawing axis.

In the case of polar polymers exhibiting dielectric relaxation, the dielectric constant ϵ' is expressed as

$$\epsilon' = \epsilon_\infty + \Delta\epsilon[1/(1 + \omega^2\tau^2)] \tag{10}$$

where ϵ_∞ is the instantaneous dielectric constant, $\Delta\epsilon$ is the relaxation strength, and τ is the relaxation time. The electrostriction constant defined by eq. (1) is given by

$$\kappa = -\frac{1}{\epsilon'}\left[\frac{\partial\epsilon_\infty}{\partial s} + \frac{\partial\Delta\epsilon}{\partial s}\frac{1}{1 + \omega^2\tau^2} - \Delta\epsilon\frac{2\omega^2\tau}{(1 + \omega^2\tau^2)^2}\frac{\partial\tau}{\partial s}\right] \tag{11}$$

Equation (11) suggests that the electrostriction constant may exhibit complicated behavior as a function of temperature and frequency. The first and second terms in the bracket of eq. (11) vary as the real part of di-

electric constant but the third term gives a maximum or minimum, depending on the sign of $\partial \tau / \partial s$, just as the dielectric loss which has a maximum when plotted against frequency or temperature. Such behavior has in fact been observed in temperature dependence of κ of PVDF, but detailed discussion will be given in a future report.

We now turn to the origin of the anisotropy of κ in drawn PVDF. The dielectric relaxation strength of a polar material is expressed in general by

$$\Delta \epsilon = (4\pi N f g \mu^2 / kT) F \tag{12}$$

where N is the number of dipoles per unit volume, μ is the dipole moment of a single dipolar unit, k is the Boltzmann constant, and T is the absolute temperature. The factor f is determined by the equilibrium orientation of the dipoles ($f = {}^1\!/_3$ for random orientation). The factor g originates from the hindering potential for dipole rotation ($g = 1$ for a free dipole). The factor F represents the ratio of the local field to the macroscopic electric field. Since the electrostriction constant κ_0 corresponds to variation of N with volume change, the remaining part ($\kappa - \kappa_0$) reflects variations of other factors, f, g, and/or F, with strain. The high negative value of ($\kappa - \kappa_0$) in PVDF indicates that the factor fgF appreciably increases with elongation.

We cannot say anything conclusive at present as to which factor is predominant in κ for PVDF. One possibility lies in the change of g with strain, because the short-range interaction among dipoles in PVDF is perhaps sensitive to strain. This possibility is supported by the fact that this polymer easily changes in conformation from a 2_1 helix to a planar zigzag during plastic deformation.

Elongational Piezoelectricity

Figures 9 and 10 show the piezoelectric charge as a function of elongational strain for two drawn samples of PVDF with $\alpha = 1.6$ and $\alpha = 2.6$, respectively. The slope of each straight line gives the apparent piezoelectric stress constant e. The piezoelectric strain constant d can be calculated from $d = e/E$, where E is Young's modulus.

The value of e is plotted in Figure 11 as a function of the angle θ between the draw axis and the direction of strain. The curve is approximated by

$$e = e_{31} \cos^2 \theta + e_{32} \sin^2 \theta \tag{13}$$

The value of e_{32} is very small and, in the case of the sample with $\alpha = 1.6$, nearly equal to the value for the undrawn PVDF film illustrated in Figure 5.

In the preceding discussion, the piezoelectricity of undrawn and roll-drawn PVDF films has been attributed to an antisymmetrical distribution of space charge in the polymer film. An alternative explanation, that the piezoelectricity might be brought about by orientation of β crystals which themselves have a spontaneous polarization, may be excluded because (1) the polarity of pyroelectricity would then be opposite to that of the piezo-
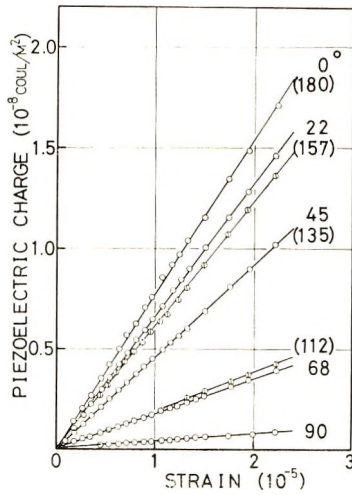
Fig. 9. Piezoelectricity of roll-drawn PVDF (α = 1.6) for various angles between elongational strain and draw-axis.
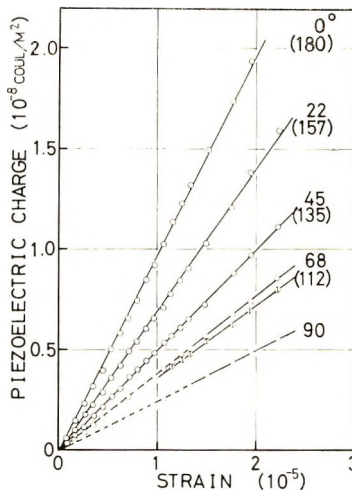

Fig. 10. Piezoelectricity of roll-drawn PVDF (α = 2.1) for various angles between elongational strain and draw-axis.
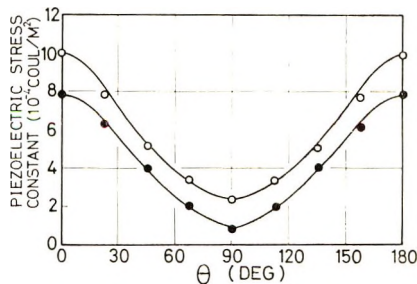

Fig. 11. Apparent piezoelectric stress constant of roll-drawn PVDF plotted against angle between elongational strain and draw-axis; (◯) α = 2.1; (●) α = 1.6.

electricity and (2) the orientation of β crystals produced by roll-drawing is not expected to be perpendicular to the film plane.

It must be noted that the piezoelectricity of drawn PVDF film has a quite different origin from that of uniaxially oriented proteins,[17] polypeptides,[18] and cellulose,[19] in which piezoelectricity does not appear for strain along the orientation axis but is strongest for strain along 45° direction.

The piezoelectricity of PVDF, therefore, can be classified into three cases as follows: (A) weak piezoelectricity in undrawn samples with the piezo-electric strain constant $d \approx 10^{-9}$ cgs esu; (B) medium, anisotropic piezo-electricity for drawn samples, $d_{31} \approx 10^{-3}$ cgs esu; (C) strong piezoelectricity for drawn and then poled samples, $d_{31} \approx 10^{-7}$ cgs esu, as observed by Kawai[11] and Fukada.[12]

Type A piezoelectricity is characterized by values of d similar to those for other undrawn polymers and can be attributed to space charge distrib-uted antisymmetrically along the z axis. Type B piezoelectricity may re-sult from a mechanism similar to that of type A, but anisotropy of the elec-trostriction constant plays an important role. The unit cell of the β-form crystal of PVDF has a permanent dipole but, in the case of roll-drawn films, the direction of polarization of individual crystallites may be random about the drawing axis and, hence, the specimen may have no net polariza-tion. After the film has been poled, however, the polarization of crystal-lites may have a preferential orientation along the z axis and the resultant polarization appears. Then, the strong type C piezoelectricity character-istics to the polar crystal may be observed.

Possibility of Ferroelectricity in Poly(vinylidene Fluoride)

As was indicated in the first section of this paper, the β crystal of PVDF has a spontaneous polarization P_s. Since the dipole moment of the repeat-ing unit ($-CH_2-CF_2-$) in a planar zigzag conformation is 2.1 D and the unit cell, which includes four repeating units, has a volume of 9.66 × 4.96 × 4.64 Å^{3},[2] the value of P_s is 1.32 × 10^{-2} coul/m^2.

When the polycrystalline, rolled PVDF has been poled at a high tem-perature, the material exhibits an extremely high value of piezoelectricity, indicating a high degree of orientation of the crystallites due to external field. The polarity of piezoelectricity agrees with the assumption that the polarization is due to dipole orientation in the crystal. Furthermore, it was shown by experiment that the polarity of piezoelectricity is reversed by the reversed poling. Therefore, such a material may be called ferroelectric.

The general features of ferroelectric materials are: (1) the hysteresis loop in the polarization, which disappears at the Curie point, (2) high dielectric constant, (3) a high electrostriction constant, and (4) pyroelectricity due to the temperature dependence of spontaneous polarization.

According to Asahina and his co-workers,[13] β-form PVDF shows a pyro-electric current up to the melting point (177°C) and the current integrated over time agrees with P_s in order of magnitude. This indicates that the Curie point of this material may be near the melting point or the spontane-

ous polarization may vanish at the melting point. As is well known, appearance of the Curie point is not a necessary condition of ferroelectricity.

In the case of a ferroelectric polymer, reversal of spontaneous polarization is brought about by the 180°C rotation of molecules around the chain axis and therefore encounters a high energy barrier. This means that the coercive field may be very high at room temperature, presumably higher than the breakdown field. This may be the reason why poling is possible only at high temperatures.[11,12]

References

1. Y. L. Gal'perin, Y. V. Strogalin, and M. P. Mlenik, *Vysokomol. Soedin.*, **7**, 933 (1965).

2. J. B. Lando, H. G. Olf, and A. Peterlin, *J. Polym. Sci. A-1*, **4**, 941 (1966).

3. K. Sakaoku and A. Peterlin, *J. Macromol. Sci.*, *B1*, 401 (1967).

4. Y. Ishida, M. Watanabe, and K. Yamafuji, *Kolloid-Z.*, **200**, 48 (1964).

5. A. Peterlin and J. D. Holbrook, *Kolloid-Z.*, **203**, 68 (1965).

6. A. Peterlin and J. Holbrook-Elwell, *J. Materials Sci.*, **2**, 1 (1967).

7. H. Sasabe, S. Saito, M. Asahina, and H. Kakutani, *J. Polym. Sci. A-2*, **7**, 1405 (1969).

8. N. Koizumi, S. Yano, and K. Tsunashima, *J. Polym. Sci. B*, **7**, 59 (1969).

9. H. Kakutani, *Kobunshi Kagaku*, **26**, 83 (1969).

10. T. Takamatsu and E. Fukada, *Polymer J.* (Japan), **1**, 101 (1970).

11. H. Kawai, *Japan J. Appl. Phys.*, **8**, 975 (1969).

12. E. Fukada and S. Takashita, *Japan. J. Appl. Phys.*, **8**, 960 (1969).

13. M. Asahina, H. Kakutani, and K. Wada, paper presented at the 18th Polymer Symposium, Japan, Tokyo, Nov. 1969.

14. T. Furukawa, Y. Uematsu, K. Asakawa, and Y. Wada, *J. Appl. Polym. Sci.*, **12**, 2675 (1968).

15. H. Kawai, *Oyobutsuri*, **39**, 413 (1970).

16. Y. Wada, H. Hirose, T. Asano, and S. Fukutomi, *J. Phys. Soc. Japan*, **14**, 1064 (1959).

17. E. Fukada and I. Yoshida, *J. Phys. Soc. Japan*, **12**, 1158 (1957).

18. E. Fukada, M. Date, and N. Hirai, *Nature*, **211**, 1079 (1966).

19. E. Fukada, M. Date, and N. Hirai, in *Macromolecular Chemistry, Tokyo-Kyoto* **1966** (*J. Polym. Sci. C*, **23**), I. Sakurada and S. Okamura, Eds., Interscience, New York, 1968, p. 509.

Equilibrium Melting Points of the Low-Melting and High-Melting Crystalline Forms of *trans*-1, 4-Polyisoprene

EDWARD G. LOVERING and DAVID C. WOODEN, *Research and Development Division, Polymer Corporation Limited, Sarnia, Ontario, Canada*

Synopsis

Equilibrium melting points in *trans*-1,4-polyisoprene were calculated from plots of crystallization temperature versus the experimentally measured melting points. The melting points were found to be 78 ± 1.7°C for the low-melting crystalline form and 87 ± 1.3°C for the high-melting form. Within the experimental error, melting points were independent of molecular weight above a number-average weight of 33,000.

Introduction

The equilibrium melting point T_m^0 of a polymer is defined as the melting point of crystals in which surface energies have no effect on the melting temperature.[1] This quantity cannot at present be determined directly and must be calculated by an extrapolation procedure. The most widely used of these involves plotting T_c, the temperature at which crystals form against T_m the temperature at which these same crystals melt, and extrapolating to the point where T_m and T_c are equal.[1-3] We have applied the technique to melting data obtained for *trans*-1,4-polyisoprene and obtained new values for the equilibrium melting points of the low-melting (LM) and high-melting (HM) crystalline forms.

Experimental and Results

Natural *trans*-1,4-polyisoprene (*mimusops balata*) was fractionated by preparative precipitation chromatography,[4] and molecular weights were determined by gel-permeation chromatography. The chromatograph was calibrated against viscosity-average and number-average molecular weights.[5,6]

Melting points were measured by means of a Dupont 900 differential thermal analyser, calibrated as described previously.[7] The materials to be studied were packed into the specimen tubes designed for the instrument and the thermocouples inserted into the polymers. The polymers were allowed to crystallize in a constant temperature bath after heating for 10 min or longer at 100°C to ensure complete melting. A single specimen of each fraction was used to determine the melting point associated with each

175

TABLE I
Melting Points of LM Crystals

$\bar{M}_n{}^a$	Melting Point, T_m, °C							
	$T_c = 27.5°C$	$T_c = 30.0°C$	$T_c = 32.5°C$	$T_c = 35.0°C$	$T_c = 37.5°C$	$T_c = 40.0°C$	$T_c = 42.5°C$	$T_c = 45.0°C$
33,000	44.0	45.0	46.8	47.8	50.0	51.3	53.5	55.0
	43.8	45.0	46.5	48.3		51.3		54.5
49,000	42.3	46.8	47.3	48.3	50.0	51.5	53.5	55.3
59,000	45.0	46.5	48.0	49.5	50.5	52.0	53.5	55.0
	45.5	47.3	48.3	49.3		52.0		55.0
70,000	45.5	47.3	48.3	49.3	50.3	51.8	53.8	55.0
77,000	45.3	46.5	48.0	49.0		52.0		55.3
94,000	45.3	47.3	48.3	49.3	50.0	51.5	53.8	55.0
116,000	45.0	46.5	48.3	49.0	50.3	51.5	53.8	56.0
	45.3	46.8	48.0	49.0		51.8		55.5

^{a} $\bar{M}_n$ calculated from GPC.

crystallization temperature in the series of crystallization temperatures studied.

Previous work showed that the thermograms of *trans*-1,4-polyisoprene depend upon the heating rate.[7] The rate used must be rapid enough to differentiate the melting of crystals formed at T_c from those formed by subsequent recrystallization during heating but the rate must not be high enough to shift the apparent melting point to higher temperatures. A rate of 1.35°C/min was found to be satisfactory.[7] Melting points of LM and HM crystals are given in Tables I and II, respectively. The absolute error in measurement is estimated to be ±0.5°C, except at temperatures below 35°C where nonisothermal crystallization is thought to become significant.

TABLE II
Melting Points of HM Crystals

M_n[a]	$T_c =$ 47.5°C	$T_c =$ 50.0°C	$T_c =$ 55.0°C	$T_c =$ 57.5°C	$T_c =$ 62.5°C
33,000	60.5	62.4	66.0	66.5	70.3
59,000	60.8	62.5	66.0	67.0	70.8
77,000	60.8	62.8	66.0	67.5	71.0
116,000	60.8	63.3	66.0	67.8	71.0
280,000	61.5	63.0	66.0	68.0	70.5

[a] M_n calculated from GPC.

Discussion

Within the experimental error, the observed melting point of the LM and HM crystalline forms does not vary with the molecular weight. Below 35°C, the experimental error in LM melting points is greater than 0.5°C, because the rapid rate of crystallization makes it probable that crystallization is nonisothermal and that the real crystallization temperature differed from that of the bath and varied from sample to sample. The melting points of each crystalline form were fitted to a straight-line plot of T_c versus T_m by a least-mean-squares procedure. LM points at 35.0°C and lower were excluded from the computation because of nonisothermal crystallization. For the LM crystals,

$$T_m = 0.693T_c + 24.037 \tag{1}$$

and for the HM crystals,

$$T_m = 0.658T_c + 29.706 \tag{2}$$

These equations, extrapolated to $T_m = T_c$, are plotted in Figure 1.

The equilibrium melting points calculated from eqs. (1) and (2) are 78 ± 1.7°C for the LM crystals and 87 ± 1.3°C for the HM crystals at the 95% confidence level. The error at the melting points, beyond the limits of the experimental data, was calculated from the least-mean-squares equations.[8]

The best previously reported values of the melting points were 64° and 74°C for the LM and HM forms, respectively.[9] They were determined
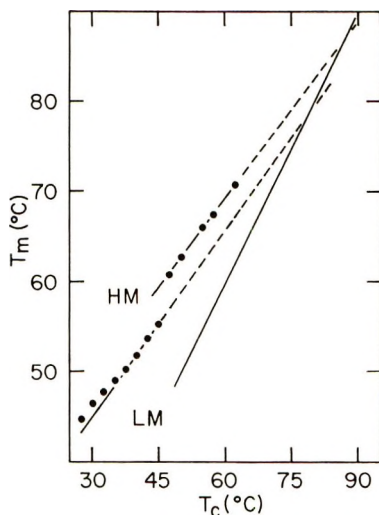
Fig. 1. Plot of eqs. (1) and (2) showing the extrapolation to $T_c = T_m$. The points shown are the average of melting points observed at each crystallization temperature.

dilatometrically by using very slow heating rates and, in terms of current theory, are not regarded as equilibrium melting points. Although the new melting points are 14 and 13°C higher than the old ones they are not uncorroborated. Rijke has found that spin-crystallized TRANS-PIP (registered trade mark of Polymer Corporation Limited), which x-ray diffractometry shows to be in the LM form, melts at 81°C.[10]

Previously we reported DTA extrapolated melting points of 66 and 77°C for the LM and HM forms, respectively.[7] The results were too low for two reasons, first because the fractions studied contained about 1% of enchained 3,4-polyisoprene and secondly because too much weight was given to melting points arising from crystallization at lower temperatures when carying out the extrapolation. In comparing our earlier results with those presented here, we discovered an error in Figure 5 of the previous paper.[7] The HM melting points are plotted 5°C too high, and as such are in disagreement with the results in Figures 3 and 6 of that paper. For example the HM melting point, after crystallization at 52°C (Fig. 3), is about 63.5°, not 68.5° as indicated in Figure 5. The actual DTA experimental points, neglecting those at the lower crystallization temperatures, in the preliminary work are well within 2°C of those reported here.

In studying the molecular weight dependence of the melting point of polyethylene it was necessary to carry out experiments on samples which were only a few per cent crystalline.[1] If this was not done plots of T_c against T_m with slopes of ca. 0.2 were obtained, and these, upon extrapolation, yielded abnormally low melting points. The slope of our T_c versus T_m plot is well above 0.5, even though the samples were about 30% crystalline. There is no indication that our results were adversely affected by not working at very low levels of crystallinity, but if they were, it would mean

the equilibrium melting points of *trans*-1,4-polyisoprene are even higher than those reported here.

A theoretical relation between T'_m and T_c has been derived by Gopalan and Mandelkern.[1] They found

$$T_m = (a/2n)T_c + T_m^0[1 - (a/2n)] \tag{3}$$

where $a = \sigma_{ec}/\sigma_{en}$ and $n = \zeta/\zeta^*$. The interfacial free energies of the 001 crystal face, σ_{ec} and σ_{en}, refer to mature crystals and the crystal nuclei, respectively. The thickness of the mature crystal is ζ, the thickness of the crystal nucleus is ζ^*, both expressed in chain units. From eqs. (1) and (2), a/n is 1.396 for the LM form and 1.316 for the HM form. In agreement with the work on polyethylene,[1] our results show that the interfacial free energy and the crystallite thickness of *trans*-1,4-polyisoprene crystals change as the nucleus grows into a stable crystal. As expected, the ratio a/n is a function of the crystal form growing from the melt, whether it is the LM or HM form, and not of the melt itself.

References

1. M. Gopalan and L. Mandelkern, *J. Phys. Chem.*, **71**, 3833 (1967).

2. L. Mandelkern, *J. Polym. Sci.*, **47**, 494 (1960).

3. J. D. Hoffman and J. J. Weeks, *J. Res. Nat. Bur. Stand.*, **66A**, 13 (1962).

4. J. F. Henderson and J. Hulme, *J. Appl. Polym. Sci.*, **11**, 2349 (1967).

5. E. G. Lovering and W. B. Wright, *J. Polym. Sci. A-1*, **6**, 2221 (1968).

6. E. G. Lovering, paper presented at IUPAC International Symposium on Macromolecular Chemistry, Toronto, 1958, Paper A6:16.

7. E. G. Lovering and D. C. Wooden, *J. Polym. Sci. A-2*, **7**, 1639 (1969).

8. O. L. Davis, *Statistical Methods in Research and Production*, Hafner, New York, 1961, Chap. 7.

9. L. Mandelkern, F. A. Quinn, and D. E. Roberts, *J. Amer. Chem. Soc.*, **78**, 926 (1956).

10. A. M. Rijke, private communication.

γ–α Transformation in Isotactic Polypropylene

B. A. NEWMAN and S. SONG, *Department of Mechanics and Materials Science, Rutgers University—The State University of New Jersey, College of Engineering New Brunswick, New Jersey 08903*

Synopsis

A γ-phase to α-phase transformation in a specimen of isotactic polypropylene crystallized under conditions of high pressure was induced by drawing at 100°C. X-ray studies showed that the unoriented component remained in the γ-phase, and that the oriented component was found only in the α-phase. This evidence supports a previous suggestion that the phase transformation is martensitic in character. The consequences of such an assumption are discussed. The role of dislocations in polymeric systems is generally believed to be not too significant, but since martensitic reactions involve cooperative movements of atoms, an exception in this case is suggested. A possible mechanism for the phase transformation is suggested.

Introduction

Crystallization of low molecular weight isotactic polypropylene fractions under certain conditions can yield a triclinic crystal phase, or γ-phase.[1–3] The same crystal phase can also be produced by the crystallization of whole polymer at high pressures.[4,5] Solid-state phase transformations from this γ-phase to the more commonly occurring monoclinic phase[6] or α-phase have been observed, both for the low molecular weight fractions[2,3] and the samples crystallized at high pressure.[5,7]

In a previous study,[3] needle-like crystalline entities prepared from a low molecular weight fraction of polypropylene, which contained single-crystal regions of both α-phase and γ-phase with the common crystallographic direction *b*,* were observed. Electron diffraction indicated that the γ-unit cell could be derived from the α-unit cell by a simple shear on (010) planes, confirming the suggestion first made by Kardos et al.[5] On the basis of these results, it was suggested that the γ–α phase transformation was probably martensitic in character. This possibility would imply a number of interesting consequences. Martensitic reactions involve cooperative movements of atoms (similar to those required for mechanical twinning), and indeed such transformation can usually be induced by the application of stress in a particular direction with respect to the crystal lattice. It has been observed that low molecular weight fractions of polypropylene crystallized very slowly from the melt crystallized in the γ-phase and do

---

* Notation for a direction in reciprocal space.

not transform to α-phase at elevated temperatures, but do transform to α-phase upon application of tensile stress.[2,3] During extension, orientation occurs, and the oriented polymer is observed to be in the α-phase. A "stable" form of γ-phase polypropylene, prepared by crystallization at low degrees of supercooling at high pressure, has been reported.[8] It was observed that samples crystallized in this way did not transform to α-phase either at elevated temperatures or upon application of compressive stress. However, it should be noted that if the stress-induced transformations are indeed martensitic in character, then since the changing orientation of crystallites with respect to the direction of stress is different for tension than compression, a phase transformation would not necessarily be anticipated in this case. It therefore seemed appropriate that this experiment should be repeated with the use of tension rather than compression.

A second question concerns the mechanism for the transformation. Martensitic phase transformations require dislocation motions. Since there are restrictions on the types of dislocations and their motions in crystalline polymers, this subject must also be considered. It should be clearly understood that no consideration is given here to the question of which structural features would explain the relative stabilities of the two crystal phases prepared in different ways. Rather, the question as to the mechanism of the transformation, when it occurs, is considered and possible implications of this.

Experimental

Samples of isotactic polypropylene crystallized under pressure at low degrees of supercooling ($\Delta T < 40°C$) were kindly provided by Dr. K. D. Pae. The x-ray diffractometer scans at room temperature and at 170°C confirmed that the sample had crystallized in the γ-phase and did not transform to α-phase at elevated temperatures. The sample was then compressed at 100°C to give a flat film, approximately 1 mm thick. An x-ray diffractometer scan showed that no transformation to α-phase had taken place at this stage. A tensile specimen was then cut from this film and a tensile test run at 100°C in an Instron testing machine. The elevated temperature was used both for compression and extension, since the material did appear to lack integrity and only limited amounts of sample were available for experimentation. It should be noted however, that the temperature used was well below the melting temperature of isotactic polypropylene. Moreover, the temperature was controlled to within 1°C in both cases. The specimen was drawn to fracture. The specimen yielded after the stress reached a level of approximately 4500 psi. Some small extension took place before fracture, and inspection of the fracture showed that some necking had taken place on a small scale, a number of small fibrils being observed. Some irregularities in the stress–strain curve after yielding was observed, but the type of fracture indicated that the integrity of the sample was questionable and hence the stress-strain results are not presented.

Flat film x-ray photographs in the position of front reflection were taken of the sample. In the region of the point of fracture the sample had transformed to α-phase oriented in the direction of the applied tensile stress. At a large distance from point of fracture, where the material was essentially unstrained, the sample was still in the γ-phase and was not oriented. At intermediate regions closer to the fracture surface, both γ-phase and α-phase were present, but the α-phase was found only in the oriented form and the γ-phase only in the unoriented form. This result is shown in Figure 1.

ORIENTED α-PHASE (130)

UNORIENTED γ-PHASE,(130) AND (140)
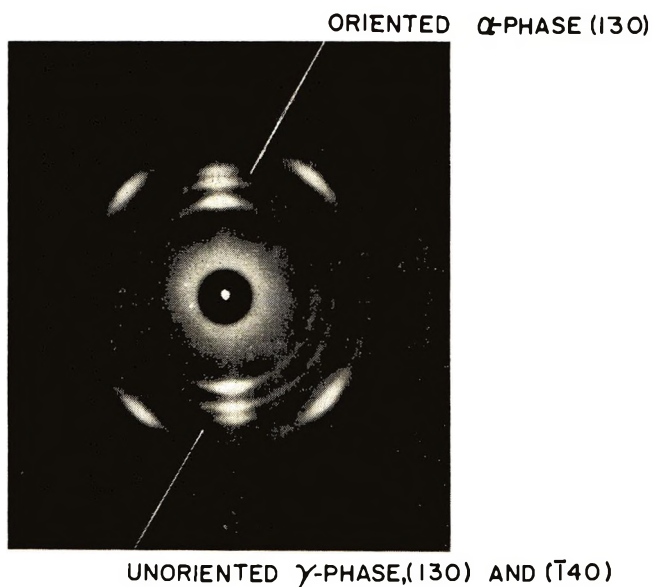
Fig. 1. X-Ray diffraction pattern showing the transformed oriented α-phase and the untransformed unoriented γ-phase.

The principal difference in the diffraction patterns of α- and γ-phase polypropylene is that, in the γ-phase, no reflection in a Bragg angle of $18.6°$ corresponding to the (130) reflection of the α-phase is observed, but a new reflection at a Bragg angle of $20.1°$ is present. Accordingly, in Figure 1, all lines contain intensity contributions both from α- and γ-phase, with the exception of the two lines mentioned. These are labeled on Figure 1. It should be noted that the α-phase line indicates orientation, while the γ-phase line shows no appreciable orientation. All other lines show some indication of orientation which presumably arises from the contribution of the α-phase. Thus, it was clearly established that the "stable" γ-phase material also transforms to α-phase under appropriate application of stress, and that this transformation is closely related to the orientation process.

Discussion

The question under consideration is whether the $\gamma-\alpha$ phase boundary is glissile or nonglissile. The shear relation between the unit cells; the common crystallographic direction between adjoining crystal phases; the observation that the phase transition can be induced by stress; the data presented here that the transition can also be induced in the high-pressure-crystallized samples and that the direction of stress is important; all these observations imply a glissile interface between α- and γ-phase polypropylene and that the transformation is martensitic in character. The consequences of such an interpretation are now examined.

A martensitic phase transformation implies cooperative movements of atoms usually described in terms of dislocation motions. In the case of polymer crystals, the anisotropic bonding and the phenomenon of chain folding imposes considerable restrictions on the types of dislocation motions possible, and generally, the role of lattice defects in plastic deformation of polymers is not thought to be relevant. A review by Keith and Passaglia[9]
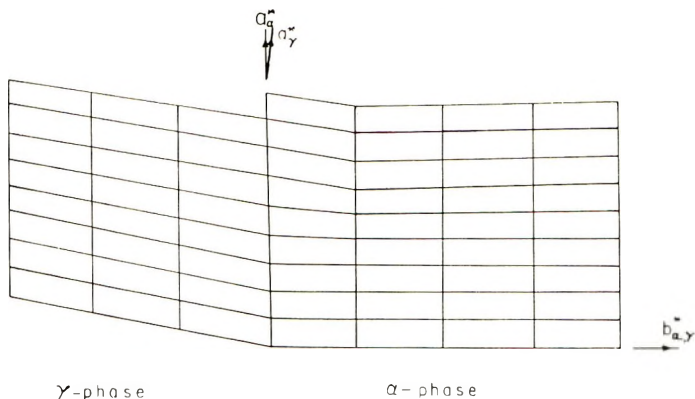
Fig. 2. Lattice distortion surrounding step in $\alpha-\gamma$ interface.

of the types of dislocations expected in polymer crystals leads to the conclusion that dislocations are not expected to play a significant role in the deformation processes in polymer single crystals. However, Keith and Passaglia also point out that twinning has been observed in polyethylene chain-folded crystals, and since twinning is a cooperative process, successive generation and motion of dislocations on adjacent glide planes may occur in this case. The essential similarity between a twinning process and a transformation of phase by a martensitic process, both cases involving a cooperative mechanism for slight translation of one polymer chain relative to its neighbors, should be noted.

Some consideration, therefore, was given to an interpretation of the $\gamma-\alpha$ martensitic transformation in this light. It is usually assumed that in martensite reactions, the transformed regions are lenticular in shape, the noncoherent boundary consisting of stepped coherent interfaces. In the

case considered, the boundary would consist of stepped (010) interfaces. This would then account for the common b^*-direction observed in both α- and γ-regions. Figure 2 shows the lattice projection perpendicular to the c direction (that is, the molecular axis) and shows the lattice distortion surrounding a step in the (010) interface. The α-phase being monoclinic is rectangular in projection, the γ-phase being triclinic is oblique. From Figure 2 it can be seen that such a distortion would be regarded as a partial dislocation. The Burger's vector could be defined as the closure failure of a circuit that would close across a nonstepped interface.[10] In which case, if we assume zero lattice shear in the c direction, the Burger's vector would be in the direction a_α^*. One phase would then grow at the expense of the other by movement of the step in the a_α^* direction, i.e., by the movement of the partial dislocations in the a_α^* direction. Keith and Passaglia observe that in polyethylene twinning takes place on the fold planes where the restrictions to the movement of dislocations would be least. For polypropylene chain-folded crystals it is now believed that the folds are restricted to (010) planes. For regularly folded arrangements we might expect some hindrance to the dislocation motion in the a_α^* direction proposed. The $\gamma-\alpha$ transitions are observed in cases when there is reason to believe that the chains are extended (low molecular weight fractions and samples crystallized at high pressure). One observation of an $\alpha-\gamma$ transition has been made, this in the case of a poly(ethylene–propylene) copolymer.[8] In this case it seems likely that there may well be some disorder associated with the folded regions of the chains. Thus, it would appear that in the particular case of the $\gamma-\alpha$ phase transformation in isotactic polypropylene, a situation is presented where dislocation motions might play an important role.

If the transformation is indeed martensitic a second fundamental question can be raised concerning the origin of the driving force for the reaction. In a metallurgical system the difference in lattice-free energy usually provides the largest contribution to the driving force of the reaction. In a polymer it seems likely that this contribution is small, the driving force arising mainly from morphological features (crystallite size, chain-folds, defects, etc.). This would not be surprising since these morphological features influence even the melting point (when the free energy difference between crystal lattice and melt must be much larger than the free energy difference between α-phase and γ-phase lattices). This point has been previously somewhat obscured by discussion of the relative "stability" of the α-phase versus the γ-phase. It should be noted that free energy differences between perfect crystals of either phase at room temperature and pressure are probably small in comparison with the free energy difference between the morphological features associated with either phase. It is well known that martensitic reactions are accompanied by morphological changes, but in the case under consideration irreversible changes in microstructure occur due to the deformation to fracture of the specimen. The relationship between the stability of the γ-phase and specific morphological features is not considered

here.   Rather the mechanism of the transformation, when it occurs, is discussed.

Conclusions

The data establish a second observation of a case where the $\gamma-\alpha$ phase transformation in polypropylene is induced by application of stress.   Moreover, in this case, it is clear that the direction of the applied stress is important.   Some investigators suggest that a complete "melting" and recrystallization occurs during the necking process, and it might be thought that this would provide an alternative explanation.   However, it should be pointed out that no extensive necking occurred in this case, and the x-ray data indicated a transformation to α-phase where the material had oriented but not necked, away from the region of fracture.

A mechanism for the transformation is suggested.   It is not intended to imply that this mechanism necessarily operates in the detailed way described, but merely to demonstrate that dislocation motions compatible with the anisotropic bonding and chain folding can be found in this particular case, which would be used to interpret the transformation.

References

1. E. J. Addink and J. Beintema, *Polymer*, **2**, 185 (1961).

2. A. Turner-Jones, J. M. Aizlewood, and D. R. Beckett, *Makromol. Chem.*, **75**, 134 (1964).

3. D. R. Morrow and B. A. Newman, *J. Appl. Phys.*, **39**, 4944 (1968).

4. K. D. Pae, D. R. Morrow, and J. A. Sauer, *Nature*, **211**, 514 (1966).

5. J. L. Kardos, A. W. Christiansen, and E. Baer, *J. Polym. Sci. A-2*, **4**, 5, 777 (1966).

6. G. Natta, P. Corradini, and M. Cesari, *Atti. Acad. Naz. Lincei Rend. Classe Sci. Fis. Mat. Nat.*, **21**, 365 (1956).

7. K. D. Pae, *J. Polym. Sci. A-2*, **6**, 657 (1968).

8. D. R. Morrow, *J. Macromol. Sci. (Phys.)*, **B3**, 53 (1969).

9. H. D. Keith and E. Passaglia, *J. Res. Nat. Bur. Stand.*, **A68**, 513 (1964).

10. W. T. Read, *Dislocations in Crystals*, McGraw-Hill, New York, 1953.

NOTES

Multiple Phases in Filled Polymers Detected by Nuclear Spin Relaxation Studies

Physical properties of filled polymers have been studied extensively in recent years. There are several indications that when polymers are blended with high surface area fillers, the polymer phase in the composite sometimes displays properties different from those of the unfilled polymer. It has been observed that with increasing filler concentration: the glass transition temperature of the polymer increases,[1-3] the transition peaks in dynamic mechanical properties are shifted to higher temperatures,[4] and lowering of water vapor sorption takes place.[5] Most of these physical changes can be explained qualitatively in terms of a simple two-phase model, in which one phase, namely the polymer portion near the filler interface, has different conformational properties and is restricted in its molecular flexibility by interaction with the filler. The other phase represents the polymer farther away from the filler interface and has molecular properties similar to those of the pure polymer. Nuclear spin relaxation studies of filled polymers have indicated effects of the filler on overall molecular mobility[6] but have failed to give direct evidence of multiple phases.[7] The feasibility of using nuclear spin relaxation measurements to study composite materials in order to detect multiple phases and differences in their molecular motion was investigated in this work.

The polymer chosen was Phenoxy PKHH with the structural formula $\{OC_6H_4C-(CH_3)_2C_6H_4OCH_2CH(OH)CH_2\}_n$, where $n \approx 100$, giving a molecular weight around 30,000. It is amorphous, linear except for a slight amount of branching, and thermoplastic with $T_g = 371°K$. One of the fillers used was Attapulgus clay, Attagel-40, of rodlike morphology, with a BET specific surface area of 150–200 m²/g. Chemically, Attagel-40 is principally SiO_2. The composite was prepared by first heating the filler at 600°C for 12 hr to drive off water and organic sizings. Next the appropriate amounts of polymer and filler (30% by weight of filler) were blended dry in a roller mill at an elevated temperature. Finally the blend was compression molded into strips under pressure at 240°C.[8]

Conventional pulse techniques were used to study the proton spin-lattice relaxation of both the pure and the filled polymer. The basic pulsed-NMR apparatus has been described elsewhere.[9,10] The resonant frequency was 20.0 MHz. The temperature control employs a gas-flow cryostat[11,12] permitting measurements between −100°C and 300°C; control is to within about ±0.5°C. A digital computer employing nonlinear regression methods was used to fit relaxation curves to the data.[13]

The pure phenoxy resin can be characterized by a single spin-lattice relaxation time T_1 throughout the entire temperature range studied. These data are represented in the uppermost curve in Fig. 1. The spin–spin relaxation time T_2 is of the order of 20 μsec at temperatures much below T_g, limiting the accuracy of the measurement. Above T_g, there is a rapid rise in T_2, permitting the use of digital techniques in data acquisition.[10] The two T_1 minima are due to different kinds of molecular motions: the low-temperature minimum is due to the rotation of the CH_3- groups about their symmetry axis; the high-temperature minimum arises from the overall motion of the polymer chain.[14,15]

The filled polymer had to be characterized by a non-first-order spin-lattice relaxation process. Although a distribution of relaxation times is probably more realistic, the data could be represented to an adequate approximation as the sum of two exponential decays with time constants T_{1a} and T_{1b}, corresponding to fractions α and β of the total
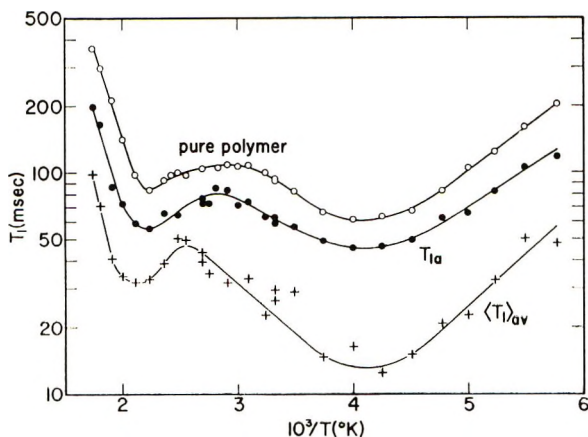
Fig. 1. T_1 vs. $10^3/T$ in Phenoxy PKHH: (○) pure polymer; (●) longer component in system filled with 30% Attagel-40; (+) average relaxation time in filled system.

signal ($\alpha + \beta = 1$). The longer of these times T_{1a} is plotted as the middle curve in Figure 1; about 75% of the signal (unchanging over the entire temperature range) is accounted for in this way. Because, over much of the temperature range, T_2 is near the limit of detectability of the apparatus, and because the shorter T_{1b} corresponds to a relatively small fraction (25%) of the signal, a plot of T_{1b} shows too much scatter to be edifying. To give some indication of the behavior of T_{1b}, the weighted average of the two relaxation times $\langle T_1 \rangle_{av}$, defined by $\langle T_1 \rangle_{av}^{-1} = \alpha(T_{1a})^{-1} + \beta(T_{1b})^{-1}$, is plotted instead as the bottom curve in Figure 1. This parameter, which corresponds to the initial rate of relaxation of the total system, may be contrasted to the longer T_{1a} which corresponds to the asymptotic rate of relaxation of the total system. Although T_{1b} is dominant in $\langle T_1 \rangle_{av}$, the scatter is less since a small difference between uncertain quantities is not involved. It is planned to postpone further NMR studies of this kind until a data acquisition technique suited to a short T_2 can be employed.

The simplest interpretation of the behavior of the filled polymer is that two distinct phases are present, in much the same way as in a partially crystalline polymer.[16] If we associate the 25% of the signal with shorter T_1 with that portion of the polymer near the filler interface, we can calculate that, if the filler particles are completely dispersed, the filler affects the polymer to a depth of about 30 Å. The 75% of the signal with longer T_1 is presumed to be largely unaffected by the filler. This is supported by the similarity between the T_1 data for this fraction and the pure polymer. The presence of ca. 5% of Fe_2O_3 in the Attagel-40 may account for the fact that these data are not identical. Alternatively, the discrepancy may be the result of representing a distribution of relaxation processes by two discrete processes. A similar study on the same resin filled with 20% synthetic mica with platelike morphology, averaging 200 Å thick and 2×10^4 Å in diameter and free of Fe_2O_3, revealed 90% of the polymer to be indistinguishable from pure polymer. The data for the remaining 10% suggested the results quoted here.

It can be seen that for all three curves shown in Figure 1, the minimum associated with CH_3-group reorientation is unshifted, indicating little effect on this motion from the filler. The high temperature minimum in $\langle T_1 \rangle_{av}$ is slightly shifted to higher temperatures indicating that chain reorientation in the surface phase is restrained, possibly by interactions with the filler surface. This minimum may also be slightly broader than the two above it; it is clearly shallower in relation to the CH_3-group minimum than the others. Since $\langle T_1 \rangle_{av}$ is the weighted combination of T_{1a} and the shorter T_{1b}, the indication is that the minimum in the shorter T_1 is much more displaced to higher temperatures, but not enough to produce two distinct minima in $\langle T_1 \rangle_{av}$.[17]

Another composite was prepared by using the same resin and 40% soda lime glass beads of mean diameter 29 μ, giving a calculated specific surface area of 0.07 m^2/g. Only one spin-lattice relaxation was detected, identical to that of the pure polymer. Clearly much less of the polymer is altered by the small surface area. The glass beads affect the long-range mobility of the polymer chains (ca. 50 monomer units are involved), as is indicated by both thermodynamic and viscoelastic measurements.[8] The NMR measurement is affected by the mobility of smaller segments of the polymer chain (ca. 1 monomer unit).

References

1. R. F. Landel, *Trans. Soc. Rheol.*, **2**, 53 (1958).

2. V. A. Kargin, T. I. Sogolova, and T. K. Metelskaya, *Vysokomol. Soedin.*, **5**, 921 (1963); *ibid.*, **4**, 601 (1962).

3. D. H. Droste and A. T. DiBenedetto, *J. Appl. Polym. Sci.*, **13**, 2149 (1969).

4. L. E. Nielsen, R. A. Wall, and P. G. Richmond, *SPE J.*, **11**, 22 (1955).

5. T. K. Kwei, *J. Polym. Sci. A*, **3**, 3229 (1965).

6. Y. S. Lipatov and F. G. Fabulyak, *Vysokomol. Soedin.*, **A10**, 1605 (1968).

7. M. A. Waldrop and G. Kraus, *Rubber Chem. Technol.*, **42**, 1155 (1969).

8. D. H. Droste, D. Sc. Thesis, Washington University, St. Louis, Missouri, 1969.

9. J. C. Buchta, H. S. Gutowsky, and D. E. Woessner, *Rev. Sci. Instr.*, **29**, 55 (1958).

10. E. O. Stejskal, *Rev. Sci. Instr.*, **34**, 971 (1963).

11. L. G. Alexakos, Ph.D. Thesis, University of Wisconsin, Madison, Wisconsin, 1963.

12. S. B. W. Roeder, E. O. Stejskal, and W. E. Vaughan, *J. Chem. Phys.*, **43**, 1317 (1965).

13. B. D. Boss, Ph.D. Thesis, University of Wisconsin, Madison, Wisconsin, 1967.

14. T. Kawai, *J. Phys. Soc. Japan*, **16**, 1220 (1961).

15. G. P. Mikhailov and V. A. Shevelen, *Polym. Sci. USSR*, **8**, 840 (1966).

16. D. W. McCall, D. C. Douglass, and D. R. Falcone, *J. Phys. Chem.*, **71**, 998 (1967).

17. T. M. Connor, *Trans. Faraday Soc.*, **60**, 1574 (1964).

D. H. Droste*
A. T. DiBenedetto

Materials Research Laboratory
Washington University
St. Louis, Missouri 63130

E. O. Stejskal

Central Research Department
Monsanto Company
St. Louis, Missouri 63166

* Present address: E. I. du Pont de Nemours & Co., Inc., Film Department, Experimental Station, Wilmington, Delaware 19898.

INFORMATION FOR CONTRIBUTORS

This *Journal* Does Not Carry a Page Charge for Contributions

1. Manuscripts should be submitted to H. Mark, Polytechnic Institute of Brooklyn, 333 Jay Street, Brooklyn, New York 11201, or for Part A-1 (Polymer Chemistry) to C. G. Overberger, Department of Chemistry, University of Michigan, Ann Arbor, Michigan 48104, or for Part A-2 (Polymer Physics) to T. G. Fox, Mellon Institute, Pittsburgh, Pennsylvania 15213. Address all other correspondence to Periodicals Division, Interscience Publishers, John Wiley & Sons, Inc., 605 Third Avenue, New York, New York 10016.

2. It is the preference of the Editors that papers be published in the English language. However, if the author desires that his paper be published in French or German, it is necessary that a particularly complete and comprehensive English synopsis be furnished.

3. Manuscripts should be submitted in triplicate (one *original*, two carbon copies), typed *double space* throughout and on one side of each sheet only, on a *heavy* grade of paper with margins of at least one inch on all sides.

4. A short synopsis (maximum length 200 words) is required for papers in Parts A-1 and A-2. No synopsis is published for Part B or for "Notes" in Parts A. This synopsis should be carefully prepared, for it is automatically the source of most abstracts. The Synopsis should be a summary of the entire paper; not the conclusions alone.

5. The paper should be reasonably subdivided into sections and, if necessary, subsections. Please refer to any issue of this *Journal* for examples.

6. The references should be numbered consecutively in the order of their appearance and should be complete, including authors' initials and—for unpublished lectures or symposia—the title of the paper, the date, and the name of the sponsoring society. Please compile references on a separate sheet at the end of the manuscript. Abbreviations of journal titles should conform to the practices of *Chemical Abstracts*.

7. Please supply numbers and titles for all tables. All table columns should have an explanatory heading.

8. It is particularly important that all figures be submitted in a form suitable for reproduction. Good glossy photographs are required for halftone reproductions. For line drawings (graphs, etc.), the figures must be drawn clearly with India ink on heavy white paper, Bristol board, drawing linen, or coordinate paper with a very light blue background. The India ink lettering of graphs must be large, clear, and "open" so that letters and numbers do not fill in when reduced for publication. It is the usual practice to submit drawings that are twice the size of the final engravings; the maximum final size of figures for this *Journal* is $4^1/_2 \times 7^1/_2$ inches.

It is the author's responsibility to obtain written permission to reproduce material which has appeared in another publication.

If in doubt about the preparation of illustrations suitable for reproduction, please consult the publisher at the address given above in paragraph *1* and ask for a sample drawing.

9. Please supply legends for all figures and compile these on a separate sheet.

10. Authors are cautioned to type—wherever possible—all mathematical and chemical symbols, equations, and formulas. If these must be handwritten, please print clearly and leave ample space above and below for printer's marks; please use only ink. All Greek or unusual symbols should be identified in the margin the first time they are used. Please distinguish in the margins of the manuscript between capital and small letters of the alphabet wherever confusion may arise (e.g., k, K, κ). Please underline with a wavy line all vector quantities. Use fractional exponents to avoid root signs.

The nomenclature sponsored by the International Union of Chemistry is requested for chemical compounds. Abbreviations should follow the American Chemical Society *Handbook for Authors*. Chemical bonds should be correctly placed, and

double bonds clearly indicated.   Valence is to be indicated by superscript plus and minus signs.

11. Authors will receive 50 reprints of their articles without charge.   Additional reprints can be ordered and purchased by filling out the form attached to the galley proof. Page proofs will not be supplied.

12. No manuscript will be returned following publication unless a request for return is made when the manuscript is originally submitted.

Manuscripts and illustrations not conforming to the style of the *Journal* will be returned to the author for reworking, thus delaying their appearance.